KU LEUVEN

ARENBERG DOCTORAL SCHOOL
FACULTY OF SCIENCE

HYDROTHERMAL DOLOMITE IN THE CANTABRIAN ZONE (NORTHERN SPAIN):
geometry and porosity distribution, paleothermometry and Mg-isotope geochemistry

Robin Honlet

Supervisor:
Prof. Dr. Rudy Swennen

Dissertation presented in partial fulfilment of the requirements for the degree of Doctor of Science (geology)

January 2018

HYDROTHERMAL DOLOMITE IN THE CANTABRIAN ZONE (NORTHERN SPAIN): GEOMETRY AND POROSITY DISTRIBUTION, PALEOTHERMOMETRY AND MG-ISOTOPE GEOCHEMISTRY

Robin HONLET

Supervisor:
Prof. Dr. Rudy Swennen

Members of the Examination Committee:
Prof. Dr. Patrick Degryse (chair)
Prof. Dr. Philippe Muchez
Prof. Dr. Jan Elsen
Prof. Dr. Olivier Namur
Prof. Dr. Marta Gasparrini
(IFP Energies nouvelles)
Prof. Dr. Anneleen Foubert
(Université de Fribourg)

Dissertation presented in partial fulfilment of the requirements for the degree of Doctor of Science (PhD): Geology

January 2018

Onderzoek gefinancierd met een doctoraatsbeurs van strategisch basisonderzoek door het Agentschap voor Innovatie door Wetenschap en Technologie (IWT).

The research was financially supported by the Institute for the promotion of Innovation through Science and Technology in Flanders (IWT-Vlaanderen).

Uitgegeven in eigen beheer, Robin Honlet, Heverlee.

Front cover: Dolomitized limestones exposed in the Bodón Unit of the Cantabrian Zone, close to the town of Viadangos de Arbas, on a sunny morning in April. Dolomite is characterized by a dark gray color, which contrasts with the light gray platform limestones of the Bashkirian Valdeteja Formation.

Dankwoord

Het werken aan een masterthesis, van een literatuurstudie over terreinwerk tot het afdrukken van het proefschrift, was een aangename kennismaking met geologisch wetenschappelijk onderzoek. De lokroep van een 4-jarig doctoraatsproject in mijn geliefde Geo-Instituut in mijn geliefde stad Leuven was dan ook groot, en bood een uitdaging die ik ten alle koste wou aangaan. De leuke mix van literatuurstudie, terreinwerk, labowerk (al dan niet in het buitenland), wetenschappelijke conferenties en het neerpennen van dat alles, stelde niet teleur, en leidde tot de doctoraatscriptie waarvan u momenteel het dankwoord leest. Ik maakte kennis met een type gesteente met wel zeer bijzondere eigenschappen. Een type gesteente dat ik enkel kende door een vakantie in de zuidelijke Alpen, in de Dolomieten. De voorbereiding van een doctoraatsaanvraag, het 4-jaar durend onderzoek, en alles wat erbij komt kijken, krijg je niet alleen gebolwerkt. Daarom dien ik mijn dank te uiten aan een heleboel mensen, die bijgedragen hebben tot de resultaten van dit doctoraat.

Allereerst wil ik mijn promotor Rudy Swennen bedanken. Hij gaf me zijn zegen en vertrouwen, zowel tijdens mijn masteropleiding als tijdens mijn doctoraat. Zijn expertise en steun zorgden ervoor dat het toenmalig IWT (nu opgenomen bij FWO) mijn beursaanvraag goedkeurde en mij van budget voorzag voor een 4-jaar durend onderzoek. Dankzij het uitgebreide netwerk van Rudy kwam ik in contact met interessante collega's zoals Marta Gasparrini en Cédric John, hetgeen leidde tot de uiteindelijke inhoud en kwaliteit van mijn doctoraat. De deur van Rudy stond steeds open, waarvoor dank.

Marta Gasparrini, my Paris connection, has played a very important role during my four years of scientific research. Since our first meeting in 2014, she has shown a strong interest in my PhD and has provided me with indispensable support. First of all, this support consisted of fine-tuning my research goals and strategies, based on her experience and knowledge of our common study area. She has guided me on fieldtrips and introduced me to the Bodón Unit by showing me the most interesting dolomite exposures. She also proved to be a good Spanish translator, which came in handy at the hospital of León during the summer of 2016. I was invited to IFPEN in Paris numerous times and these visits boosted my motivation and filled me with new knowledge. She introduced me to Daniel Pillot and Géremie Letort, whom I would like to thank for assisting me during Rock-Eval pyrolyis measurements. Marta has also introduced me to the French prince of clumped isotopes: Xavier Mangenot. Xavier supported me whenever I had a question concerning clumped isotopes, and was always ready for an interesting discussion. Marta, I would like to thank you for the last four years, for all your support, both during fieldwork and at IFPEN.

Een persoon die ook in zeer belangrijke mate heeft bijgedragen aan de publicatie van mijn onderzoek is Philippe Muchez. Zijn grondige kennis en expertise omtrent diagenese en vloeibare insluitsels, en zijn optimisme en ondersteuning, zorgden voor een leuke samenwerking, vooral tijdens de laatste 2 jaar van mijn doctoraat. Philippe, bedankt voor het vele verbeterwerk, voor de snelle feedback en voor uw interesse in mijn geliefde dolomietstalen.

I would like to express my greatest gratitude towards Cédric John, senior lecturer at Imperial College London. He introduced me to the world of clumped isotopes, which is a fantastic world full of powder samples, valves, acid, lines, glass vessels, camels, liquid nitrogen, Spanish ships, Easotope

and an unintelligible (at least to me) Simon. Simon, thank you for answering my questions and for filling my liquid nitrogen tank on a daily basis. Amelia, Claire and Carl, thank you for your kindness and help during my stays in London. Cédric, I hope the world of clumped isotopes will keep on exciting the coming years. I will cherish fond memories of my stays in London.

I would like to thank Hartmut Jäger from GeoResources STC in Heidelberg for performing vitrinite reflectance analyses on my samples. Your insights and ideas have helped a great deal in fine-tuning our scientific publication. Dieter Buhl and Adrian Immenhauser from the Institut für Geologie, Mineralogie und Geophysik at the Ruhr-University Bochum are thanked for performing Mg-isotope measurements. Thank you Dieter for answering my emails and questions. I would also like to thank An De Cleyn for performing Mg-isotope measurements on a small selection of my samples. Two researchers, whom I should thank for their interest in my PhD and for their kindness, are Juan Bahamonde from the University of Oviedo in Spain and Elias Samankassou from the University of Geneva in Switzerland. Juan and Elias, I was always welcome with questions and ideas. Both of you are examples of generous geoscientists, always ready to provide help to young and inexperienced colleagues. Juan, I would like to thank you in particular for providing me with the document that explained the Guardia Civil why I was hammering and drilling into rock. Elias, thank you for the professional cooperation during the proposal of a masterthesis subject and the guidance of Sami.

Steven Claes, bedankt voor de introductie in de wereld van CT, zowel tijdens mijn masterthesis als tijdens mijn doctoraat. Door de gangen van het UZ Leuven rollen met een kist vol stenen was werkelijk een vreemde maar leuke ervaring. Walter Coudyzer van het UZ Leuven, bedankt voor de hulp en bijstand bij het uitvoeren van medische CT metingen. Nick Janssens, mijn goede collega, bedankt voor het uitvoeren van microfocus CT op mijn stalen, en voor de hulp bij het verwerken van data op onze helikopter, en erna op ons nieuw supersonisch ‘machien’.

Velen van de honderden stenen die ik meebracht uit Spanje, groot en klein, werden met liefde en passie behandeld door Herman Nys. Herman leerde me, met harde hand, hoe je gesteentestalen verwerkt zonder de vloer vuil te maken, en hoe je op een goede manier stalen nummert en stockeert. Graag bedank ik ook Dirk, Elvira, Erika, Ria, Petra, Gerty, Hilde en Johan voor de hulp en samenwerking gedurende de voorbije 4 jaar. Dirk, uw kennis van de kathodeluminescentie-microscoop (uw creatie) was van groot belang voor mijn petrografische studie. Ik bewonder uw bereidheid tot hulp en vooral uw geduld. Elvira, bedankt om mij wegwijs te maken in het laboratorium. Erika, wij spendeerden talloze uren aan het organiseren van excursies, en kennen zo mogelijk elke slaapgelegenheid voor grote groepen van Namen tot Dinant (het zijn er dan ook niet zo veel). Ria, Petra en Gerty, ik waardeerde ten zeerste jullie openheid en hulpvaardigheid bij kleine en grote problemen. Hilde en Johan, bedankt voor de hulp bij alle IT-gerelateerde problemen. Dans cette liste, il y a une personne qui ne peut pas manquer. Rachid, tu as nettoyé mon bureau comme si c’était le tien. Merci pour la camaraderie et pour les journaux quotidiens.

Met weemoed denk ik terug aan de verscheidene weken die ik doorbracht in het Cantabrisch Gebergte in Noord-Spanje, een prachtig maar relatief onbekend gebied. Het terreinwerk verliep zeer gemoedelijk door de hulp en het gezelschap van Rudy, Marta, Steven, Jente en Sami. Steven, bedankt voor het harde labeur, voor het wegjagen van bloeddorstige Spaanse Mastiffs en voor je taak als engelbewaarder van mijn hamer. Jente, samen verkenden we de steile bergflanken in het oosten van het studiegebied, wat resulteerde in een interessante masterthesis. Ik was blij dat ik je niet alleen

mentaal iets kon bijbrengen, maar je ook aan je conditie en armspieren kon werken door het dragen van boorkoppen en vaten vol water. Sami, we explored an incredible outcrop in the central part of the Bodón Unit (our triangle). I was impressed by your motivation and knowledge and wish you all the best for the future. I will never forget the most bizarre diner I have ever had: a quarter of a pig, with fries and ketchup.

Bij de start van mijn doctoraat aan de Afdeling Geologie van de KU Leuven, werd ik verwelkomd door een leuke groep grappige en zorgzame collega's. Ze leerden mij wat het inhoud om een doctoraatstudent te zijn, tijdens een noodzakelijke koffiepauze (of twee). Bedankt Julie, Tom, Rieko, Jorik, Tine, Kim, Sofie, Bene, Steven, Hannes, Jeroen, David, Koen V. en Koen T. Un grand merci à Johan, pour l'amitié et la camaraderie. De oude garde vertrok, en de nieuwe kwam, met Nick, Bram, Michaël, Johanna, Buruk, Rik, Eva, Alicia en Sarah. Jong leven in de brouwerij! En dan zijn er die collega's waarmee ik een lange periode van mijn doctoraat doorbracht: Wim, Katreine, Dominique, Niels, Alexander, Ophélie, Marcelle, Asefeh en Ági. Bedankt!

Of the many offices in the first tower of the Geo-Institute, I am convinced that room 02.214 was the ideal breeding ground for great scientific accomplishments. Julie, bedankt voor de introductie in de wereld van dolomiet, de hulp bij het opstellen van mijn beursaanvraag en je vriendelijkheid en hulpvaardigheid. Ik koester de herinneringen aan spectaculair terreinwerk in Oman en Marokko, waar ik leerde hoe je op een professionele manier terreinwerk voorbereid én uitvoert. Mahtab, you were always in the mood to answer questions and to discuss the reflectance of vitrinite. Steven, bedankt voor de hulp bij de start van mijn doctoraat en de vele tips. Nick, laat ik toch wel stellen dat jij een meer dan waardige opvolger was van Julie. Maosong, I hope working in our office has given you a lot of new (cultural) insights. Mahtab and Maosong, I am deeply sorry for the numerous weeks of cold wind and freezing conditions in our office.

Mijn doctoraat zou niet hetzelfde geweest zijn zonder sport. Daarom wil ik eerst en vooral hulde brengen aan een groep echte mannen met haar op de benen. Mannen die door weer en wind gaan (behalve in de Jura) en altijd rijden om te winnen. Mannen die er niet voor terugdeinzen om 's avonds diep in het glas te kijken, en om elkander de volgende dag een kloot af te trekken tijdens de koers. Die mannen zijn Tom, Jorik, Koen V., Koen T., Karel, Iggy en De Smits. Samen Het Groot Verzet. Bedankt jongens voor de vele duizenden kilometers en tienduizenden hoogtemeters, maar vooral voor de mooie herinneringen. Daarnaast moet ik ook beloftenploeg Club De Ronde Wielen (#CDRW) bedanken voor de motivatie op de fiets en de leuke gespreksonderwerpen tijdens de koffiepauze. Nick en Michaël, laten we elkaar nog vaak bekampen in het mooie Hageland en op menig andere ijzerzandstenen heuvels. Next to cycling, regular running trainings intensified my heart rate. Julie, Johan, Bura, Nick and Michaël, thanks for the competition, the motivation and lots of fun. And last but not least I should thank the ping pong squad: The Windmill, The Wizard, Bura, The Donkey Slicer, Sir Spin-a-lot, Sneaky Balls, Hannanas, Rieko, Dominique, Jeroen, The Chinese Dragon and Jacek.

Tijdens mijn bachelor- en masteropleiding aan de KU Leuven leerde ik een groep jonge en gemotiveerde studenten kennen, met een gemeenschappelijke interesse: geologie. Doorheen de jaren ploegden we door opdrachten en examens, en maakten we plezier tijdens excursies en op de Oude Markt. Bedankt Mathieu, Joris, Nicole, Ellen, Jana, Ruben, Katherine, Minnen, Tuur, France, Pieter, Ruth, Arnaud, Nelis (De Tank) en Cryns (De Eightpack van Leuven). Klara, ook jij bedankt voor de leuke tijd in Zürich en voor de vriendschap.

Na jaren van avontuur en plezier zijn The Four Legendary Belgians een begrip geworden in Leuven en omstreken (en ook in Hasselt). Mannen, na al die jaren zijn we nog steeds beste maten, hoewel onze wegen zich af en toe scheiden. Laat ons er nog minstens evenveel jaar bijkappen, samen met een goed streekbierke en een welriekend glas whiskey.

Mijn opleiding geologie en mijn doctoraat zouden er niet gekomen zijn zonder de steun van mijn familie, die steeds klaarstond en -staat wanneer dat nodig is. Hoewel ze zich de afgelopen 4 jaar vaak afvroegen wat ik juist deed op de universiteit, en waarom ik geen 3 maanden vakantie had tijdens de zomer, kon ik altijd rekenen op hun steun. Mijn ouders duwden mij in de goede richting, ondersteunden mij en brachten en brengen steeds begrip op voor mijn levenskeuzes. Mijn grootouders staan altijd klaar met goede raad of met een kookpot lekkere ossentong, choucroute, moambe of konijn met pruimen. Ook de deur van mijn broer en zijn kersvers vrouwtje staat altijd open, voor een etentje of een gezellige spelletjesavond. In Leefdaal kon ik dan weer op steun rekenen van mijn meter en Eva, die oprecht geïnteresseerd zijn in mijn studies. En sinds enkele jaren word ik ook steeds met open armen ontvangen door mijn schoonfamilie in het verre Alken.

De afgelopen zes jaar bracht ik door met Ine aan mijn zij. Een geografe en een geoloog bleek tegen alle verwachtingen in toch een spetterende combinatie te zijn. Ine, tijdens de laatste jaren van onze opleiding ontfermde jij je over mij als een moeder over haar kind, wat af en toe broodnodig was na een cantus of een match van de Rode Duivels. Na mijn opleiding geologie steunde je mij door dik en dun bij de zoektocht naar uitdagingen, bij het behalen van deadlines en bij het structuur brengen in mijn dagelijkse leven. We beleefden reeds heel wat avontuur in binnen- en buitenland, en onze fietstochtjes zijn hoogdagen van liefde, plezier en gastronomie. Als ik ’s avonds thuiskom in de Mezenlaan vergeet ik de dagelijkse sleur, en vliegt de avond voorbij, met Liefke op onze schoot. Ik kijk uit naar de toekomst, en liefst met jou aan mijn zij.

Summary

Carbonate rocks represent important reservoirs for oil and gas. Due to the increasing global energy demand and current efforts to reduce CO_2 emissions, they are now also considered for new and sustainable energy applications such as geothermal projects and CO_2 sequestration. The reservoir properties of marine carbonate rocks are complex and are defined by both their predominant biological nature and the variety of diagenetic modifications that affected them. In carbonate systems, dolomite rocks diverge from limestone as they often form the best reservoir rocks. Dolomite is more brittle (e.g. Williams and McNamara, 1992) and less reactive compared to limestone, which results in better preservation of porosity and permeability. Many hydrothermal dolomite geobodies formed and occur in the subsurface. In order to understand and predict the properties of such geobodies, outcrop analogues are studied.

Geobodies of hydrothermal dolomite exposed in the Cantabrian Mountains in Northern Spain provide ideal outcrop analogues. The Cantabrian Mountains represent the Variscan foreland fold-and-thrust belt on the Iberian Peninsula, which is referred to as the Cantabrian Zone and is subdivided into several thrust units. In one of the latter, the Bodón Unit, hydrothermal dolomite rocks are spectacularly exposed on mountainsides and along road sections. Dolomitization affected several Paleozoic carbonate successions, but was most intense in Carboniferous limestones. Dolomitizing fluids were marine-derived brines which circulated through thermal convection following Late-Variscan orocline formation and subsequent lithospheric delamination (Gasparrini et al., 2006a). The petrography and geochemistry of the dolomite rocks, exposed in the Bodón Unit, have been characterized in previous studies (Gasparrini et al., 2006a, b; Lapponi et al., 2013).

This PhD thesis concentrates mainly on two underexplored aspects of the dolomitization process in the Bodón Unit. The first aspect is the geometry and associated distribution of porosity of hydrothermal dolomite geobodies. A detailed study of the geometry and petrophysical properties allows to understand the parameters controlling the dolomitization process and the resulting variation in reservoir properties. The second aspect is the thermicity of precursor limestones (which host dolomite) and over- and underlying siliciclastic rocks. A paleothermal study reconstructs the thermal history of Paleozoic rocks exposed in the Bodón Unit and of the dolomitizing fluids. The hydrothermal dolomite rocks of the Bodón Unit are then used as a test case for two new proxies in carbonate diagenesis: carbonate clumped isotope paleothermometry and Mg-isotope geochemistry.

The study concerning the geometry of dolomite geobodies and associated matrix porosity focuses on 3 key outcrops selected based on the divergent properties of exposed dolomite rocks. The geometry and petrophysical properties of these geobodies depend on different controlling factors such as the nature of fluid-migration pathways, the available volume of dolomitizing fluids and the lithology and sedimentological framework of the dolomitized limestone formations. Dolomitizing fluids migrated along dense fracture networks, whereby the availability of dolomitizing fluids defined the resulting petrophysical properties. Limited circulation of dolomitizing fluids along fracture zones resulted in tight dolomite rocks (average matrix porosity 1.8 %), as they are often affected by additional episodes of fluid expulsion and cementation as a result of fracture reactivation. Intense fluid circulation along fracture zones resulted in the creation of wide-spread and massive dolomite

geobodies. Fluid flow concentrated in fracture zones but intruded the neighboring limestone rocks. In these cases, the lithology and sedimentological framework of the precursor limestone rocks exerted an important control on the distribution of dolomitizing fluids. Intercalations of siliciclastics and silicifications affected fluid flow, and dolomite pore types strongly depend on the depositional facies of the precursor limestones. The resulting matrix porosity in these massive dolomite geobodies averages around 3.8 %. A unique dolomite geobody is exposed in the eastern part of the Bodón Unit. Here, fluids migrated along a deeply-rooted thrust which allowed more intense water-rock interactions, and which was affected by several reactivations. The fault zone associated with this thrust is characterized by Fe-rich and coarse-crystalline dolomite, which likely resulted from overprinting and/or recrystallization of a previous dolomite phase. The dolomitized fault gouge yields exceptionally high porosities (average matrix porosity 9.6 %). Analysis of log data indicates a higher amount of fractures in dolomite compared to precursor limestones. Permeability values for dolomite plugs are generally low (average matrix permeability 0.10 mD) and are only higher in samples strongly affected by exposure and associated telogenetic dissolution.

A paleothermal study of precursor limestones and over- and underlying siliciclastic rocks is based on a detailed literature study with additional Rock-Eval pyrolysis and vitrinite reflectance analysis. Bulk rock paleothermometers, such as Rock-Eval and illite crystallinity overestimate the thermal maturity of siliciclastic rocks due to the incorporation of reworked detrital sediments. Optical kerogen analysis of vitrinite in these siliciclastic rocks yields paleotemperatures around 100 °C, significantly higher compared to precursor limestone paleotemperatures based on the alteration index of conodonts (60 °C). This deviation is likely a result of method-specific variation between analytical techniques and empirical equations, but could also be related to a difference in mechanical deformation between limestone and siliciclastic successions, which caused fluids to circulate in a different manner. The paleothermal study confirms the hydrothermal nature of fluid flow and associated dolomitization, and indicates the occurrence of temperature anomalies, which can be used as an exploration tool in similar subsurface settings. The carbonate clumped isotope temperatures derived from dolomite cement correlate to temperatures obtained from fluid inclusion microthermometry, hereby illustrating the validity of high-temperature clumped isotope applications. Offsets in temperature between both techniques were observed and were interpreted in terms of pressure during carbonate crystallization, opening up the possibility for geobarometry. Dolomite crystals in zebra dolomite formed during pressure buildup, while thick dolomite cement rims in breccia textures likely formed in response to a sudden decrease in fluid pressure.

Mg-isotope geochemistry reveals expected signatures for limestone samples from the Bodón Unit, but documents a strong enrichment in heavy Mg isotopes in dolomite samples. The enrichment is a result of water-rock interactions between the circulating fluids and detrital siliciclastic rocks. This highlights the strong control of dolomitizing fluids on the Mg-isotope signature of resulting dolomite. Dolomite cement is slightly less enriched in heavy Mg isotopes compared to replacive dolomite, suggesting a change in fluid chemistry during dolomitization or the influence of unknown kinetic processes.

The results of this PhD thesis can be used for research and development of subsurface dolomite reservoirs in similar geodynamic settings, such as Variscan foreland fold-and-thrust belts elsewhere in Europe, and for high-temperature carbonate rocks occurring in a variety of environments.

Samenvatting

Carbonaatgesteenten vormen belangrijke conventionele koolwaterstofreservoirs. Omwille van de wereldwijd stijgende vraag naar energie en de huidige transitie naar een groene economie, wordt de reservoircapaciteit van carbonaatgesteenten nu ook aangewend voor duurzame applicaties zoals diepe geothermie en de ondergrondse opslag van CO_2. De reservoireigenschappen van mariene carbonaatgesteenten zijn complex en worden beïnvloed door hun voornamelijk biologische oorsprong en door de verscheidenheid aan diagenetische alteratieprocessen. In carbonaatsystemen zijn het voornamelijk dolomietgesteenten die de beste reservoireigenschappen vertonen, door hun brosse karakter (bv. Williams en McNamara, 1992) en lagere chemische reactiviteit in vergelijking met kalksteen. Het bestuderen van de reservoireigenschappen van dolomietgesteenten gebeurt vaak via de studie van analoge ontsluitingen, zoals ook in dit onderzoek.

Hydrothermale dolomietlichamen ontsloten in het Cantabrisch Gebergte in Noord-Spanje vormen ideale analogen. Dit gebergte is deel van de Variscische plooibreukgordel op het Iberisch Schiereiland, en is opgedeeld in verschillende tektonische eenheden. De meest spectaculaire ontsluitingen van dolomietgesteenten bevinden zich in de Bodón Eenheid. Dolomitisatie tastte verscheidene Paleozoïsche carbonaatafzettingen aan maar is het meest uitgesproken in afzettingen uit het Carboon. Laat-Variscische lithosferische delaminatie veroorzaakte thermale convectie van dolomitiserende mariene fluïda via gereactiveerde Variscische breukzones (Gasparrini et al., 2006a). De petrografische en geochemische eigenschappen van de dolomietgesteenten in de Bodón Eenheid werden uitvoerig bestudeerd in eerdere studies (Gasparrini et al., 2006a, b; Lapponi et al., 2013).

De voornaamste doelstellingen van deze doctoraatscriptie hebben betrekking tot twee onderbelichte aspecten van het dolomitisatieproces in de Bodón Eenheid. Het eerste aspect is de geometrie en de porositeit van de dolomietgesteenten, die in deze scriptie onderzocht worden op basis van een uitgebreide petrografische studie met porositeits- en permeabiliteitsmetingen. Een tweede onderbelicht aspect is de thermische maturiteit van kalksteen en siliciklastisch gesteente in het studiegebied. Een paleothermische studie van deze gesteenten laat toe de thermische geschiedenis van het studiegebied te ontrafelen. Tot slot vormen de dolomietgesteenten ontsloten in de Bodón Eenheid het onderwerp voor carbonaat *clumped isotope* thermometrie en Mg-isotopengeochemie, twee nieuwe en innovatieve technieken binnen het vakgebied van de carbonaatdiagenese.

De studie naar de geometrie en porositeitverdeling van dolomietlichamen is toegespitst op drie sleutelontsluitingen, die geselecteerd werden op basis van de uiteenlopende eigenschappen van hun dolomietlichamen. De geometrie en reservoireigenschappen van deze lichamen blijken in zeer belangrijke mate af te hangen van de aard van de permeabele breukzones, het volume aan dolomitiserende vloeistoffen en de lithologische opbouw en kenmerken van het gastgesteente. De meeste ontsloten dolomietlichamen in de Bodón Eenheid zijn gevormd rond kleinschalige breuken die de gastgesteenten doorsnijden. Beperkte volumes aan dolomitiserende vloeistoffen zorgden voor nauwe gedolomitiseerde breukzones met een lage matrixporositeit (gemiddeld 1,8 %) als gevolg van verscheidene reactivaties en gerelateerde cementatie. Belangrijke fluïda-circulatie langsheen breuken resulteerde in de vorming van grotere en massieve dolomietlichamen waarbij dolomitisatie ook de gastgesteenten langsheen breukzones aantastte. In dit geval beïnvloedden de lithologie en de

sedimentologische opbouw van de gastgesteenten in belangrijke mate de kenmerken van de resulterende dolomietlichamen, wat meestal zorgde voor een hogere matrixporositeit (gemiddeld 3,8 %). Fluïda-circulatie werd in belangrijke mate beïnvloed door intercalaties van siliciklastisch materiaal en de aanwezigheid van chert, terwijl poriëntypes in het dolomietgesteente werden beïnvloed door de sedimentologie van het gastgesteente. In het oosten van het studiegebied circuleerden dolomitiserende fluïda via de breukzone van een belangrijk overschuivingsfront. Deze fluïda werden sterk beïnvloed door water-gesteente interacties, en het overschuivingsfront werd verscheidene keren gereactiveerd. De dolomietlichamen ontsloten langsheen de breukzone zijn Fe-rijk en grof kristallijn, en ontstonden waarschijnlijk door rekristallisatie van een eerdere dolomietfase. Dit resulteerde in een poreuze breukbreccia (gemiddeld 9.6 % matrix porositeit). Een analyse van loggegevens bevestigt het brossere karakter van dolomiet, maar plug-metingen tonen een gemiddeld lage matrixpermeabiliteit (gemiddeld 0.10 mD).

De studie naar de thermische maturiteit van het kalksteen gastgesteente en siliciklastisch gesteente is gebaseerd op een gedetailleerde literatuurstudie met aanvulling van nieuwe Rock-Eval pyrolyse en vitriniet-reflectiviteitsmetingen. Methodes gebaseerd op volledige stalen, zoals Rock-Eval pyrolyse en illiet kristalliniteitsmetingen, overschatten de thermische maturiteit door de incorporatie van detritisch materiaal met een hogere maturiteit. Vitriniet-reflectiviteitsmetingen met optische analyse van kerogeen leveren paleotemperaturen rond 100 °C op voor siliciklastisch gesteente, significant hoger in vergelijking met conodont alteratie index temperaturen voor het kalksteen gastgesteente (rond 60 °C). Dit verschil in temperatuur is voornamelijk te wijten aan de gebruikte analytische methodes en empirische vergelijkingen, maar kan ook verklaard worden door het verschillend mechanisch gedrag van kalksteen en siliciklastisch gesteente hetgeen resulteerde in een intensere circulatie van fluïda in het siliciklastisch gesteente. De paleothermische studie bewijst het hydrothermale karakter van dolomitisatie en het voorkomen van temperatuursanomalieën in het gastgesteente, die gebruikt kunnen worden als exploratievector. De toepassing van carbonaat *clumped isotope* thermometrie levert temperaturen op die correleerbaar zijn met temperaturen bekomen via microthermometrie op vloeibare insluitsels, wat de validiteit aantoont van *clumped isotope* thermometrie naar hogere temperaturen (> 100 °C). De temperatuurswaarden bekomen via beide technieken laat bovendien toe de druk te bepalen waarop de dolomietkristallen gevormd werden. Kristallen in zebradolomiet vormden bij opbouwende drukken, terwijl cement kristallen in breccia vormden na een plotse daling van de fluïda druk.

Mg-isotopengeochemie toont een gemiddeld geochemisch signatuur voor het kalksteen gastgesteente uit de Bodón Eenheid, en een belangrijke aanrijking van zware Mg isotopen in dolomiet stalen. Deze aanrijking is het resultaat van belangrijke water-gesteente interacties. Een iets lager Mg-isotopen signatuur in dolomiet cement in vergelijking met matrixdolomiet, suggereert een lichte verandering in fluïda samenstelling tijdens dolomitisatie, of een mogelijke invloed van complexe variabelen (zoals kinetische factoren).

De resultaten van deze doctoraatscriptie kunnen aangewend worden bij het onderzoek naar ondergrondse dolomietlichamen in vergelijkbare geodynamische omgevingen, zoals andere Variscische plooibreukgordels in Europa, en bij studies van carbonaatgesteente in een variatie aan geologische omgevingen.

List of abbreviations

Δ_{47}	offset (‰) between the amount of the $^{18}O^{13}C^{16}O$ isotopologues in a carbonate sample compared to a stochastic distribution
ΔT	offset (°C) between T_h and $T\Delta_{47}$
µm	micrometer
AFT	apatite fission-track
ANOVA	analysis of variance
BO17	clumped isotope calibration of Bonifacie et al. (2017)
ca.	circa
CAI	conodont color alteration index
CDES	Carbon Dioxide Equilibrium Scale (reference frame Δ_{47})
cfr.	compare with
CI	clumped isotope
CL	cathodoluminescence
CM	Ciñera-Matallana (Basin)
cm	centimeter
CO	confidence level
CR	Canseco-Rucayo (Basin)
CT	computed tomography
CZ	Cantabrian Zone
dm	decimeter
DSM3	Dead Sea Magnesium (reference frame $\delta^{25}Mg$ and $\delta^{26}Mg$)
e.g.	for example
EK	empirical Klinkenberg (correction)
FFTB	foreland fold-and-thrust belt
FI	fluid inclusion
FIA	fluid inclusion assemblage
FL	fluorescent light
Fm.	formation
HI	hydrogen index
HTD	hydrothermal dolomite
i.e.	that is
KI	Kübler index (illite crystallinity)
KL15	clumped isotope calibration of Kluge et al. (2015)
km	kilometer
KO	key outcrop
kV	kilovolt
LCQ	Los Chábanos quarry
M	molar concentration
m	meter
mbar	millibar
mD	millidarcy

mg	milligram
mm	millimeter
MPa	megapascal
MQ	Millaró quarry
OI	oxygen index
OM	organic matter
PP	parallel polars
ppb	parts per billion
RE	Rock-Eval
Rm%	mean vitrinite reflectance
SE	standard error
$T\Delta_{47}$	Δ_{47}-derived temperature
T_h	homogenization temperature
Tmax	S_2 peak temperature in a Rock-Eval pyrolysis oven
TOC	total organic carbon
VR	vitrinite reflectance
WS	water saturation
XP	crossed polars

Table of contents

Chapter 1 Introduction

1.1. The holy grail: porous and permeable carbonate rocks

The ever increasing global energy demand results in an ever increasing quest to understand the formation and occurrence of porous and permeable rocks. These can form reservoirs in which hydrocarbons (oil or gas) can accumulate, and are in this respect often referred to as reservoir rocks. Reservoir rocks cannot only accumulate hydrocarbons, but can also be used as a storage site for captured CO_2 (e.g. Leung et al., 2014) or for geothermal projects (e.g. Lund and Boyd, 2015; Bertani, 2016). The latter applications are gaining importance given the global efforts to reduce the emissions of CO_2 and the transition to clean energy (IEA, 2017).

The petrophysical characteristics (i.e. porosity and permeability) of carbonate reservoir rocks are more complex compared to their siliciclastic counterparts (Choquette and Pray, 1970). This complexity arises from the predominant biological nature of many carbonate constituents and their high chemical reactivity, resulting in a variety of diagenetic modifications affecting primary reservoir characteristics (Moore, 1989). The diagenetic modifications can be grouped in eogenetic, mesogenetic and telogenetic stages (Choquette and Pray, 1970), depending on their timing during the burial history of the carbonate rocks. Reconstructing the burial history of carbonate rocks and their diagenetic modifications is thus essential to understand their formation, occurrence and reservoir characteristics.

Carbonate rocks currently contain more than 60 % of the world's oil and 40 % of the world's gas reserves (Schlumberger, 2017). A large amount of these reserves (50 % in 1980; Zenger et al., 1980) are hosted in dolomite rocks (Sun, 1995). Dolomite reservoir rocks have been described in North America, Russia, northwestern and southern Europe, northern and western Africa, the Middle East and the Far East (Al-Awadi et al., 2009). The formation, occurrence and petrophysical characteristics of dolomite rocks have been classically investigated through outcrop analogue studies, which allow detailed studies of otherwise deeply buried reservoirs (e.g. Grammer et al., 2004; Vandeginste et al., 2005; Gasparrini et al., 2006a; Wilson et al., 2007; López-Horgue et al., 2010; Sharp et al., 2010; Lapponi et al., 2011; Nader et al., 2012; Ronchi et al., 2012; Swennen et al., 2012; Lapponi et al., 2013; Dewit et al., 2014; Beckert et al., 2015; Jacquemyn et al., 2015).

1.2. Dolomitization and porosity

1.2.1. Dolomite: a rock and mineral

Dolomite refers to both the mineral with formula $CaMg(CO_3)_2$ as well as the carbonate rock composed largely (> 75 %) of the mineral dolomite (Machel, 2004). The name 'dolomite' is derived from the French geologist Déodat de Dolomieu (1750-1801), who was the first one to describe dolomite (the rock) in the southern Alps in the late 18^{th} century (de Dolomieu, 1791). It was the Swiss chemist Nicolas-Théodore de Saussure (1767-1845) who called the newly described

carbonate rock '*dolomie*' in honor of his colleague (de Saussure, 1792). Kirwan (1794) translated '*dolomie*' to the English equivalent 'dolomite', thereby referring to the mineral instead of the rock. Since then, 'dolomite' has been used for both rock and mineral. Throughout the 19th century, the southeastern part of the Alps, where the discovery was made, became known as the Dolomite Mountains (McKenzie and Vasconcelos, 2009). In the 20th century, the term 'dolostone' was introduced to refer to dolomite as rock (Shrock, 1948). It failed to become popular (e.g. Machel, 2004) and will not be used in this PhD thesis.

The mineral dolomite is composed of alternating layers of Ca^{2+} and Mg^{2+} cations, with layers of CO_3^{2-} anions in between. It can form through direct precipitation or cementation (eq. I), or through secondary replacement of $CaCO_3$ (i.e. dolomitization; eq. II; Machel, 2004).

$$Ca^{2+}(aq) + Mg^{2+}(aq) + 2CO_3^{2-}(aq) \rightarrow CaMg(CO_3)_2(s) \quad \textbf{(eq. I)}$$

$$(2-x)CaCO_3(s) + Mg^{2+}(aq) + xCO_3^{2-}(aq) \rightarrow CaMg(CO_3)_2(s) + (1-x)Ca^{2+}(aq) \quad \textbf{(eq. II)}$$

1.2.2. Modern dolomite and the dolomite problem

Dolomite is a major rock-forming mineral in carbonates throughout the Phanerozoic rock record (Given and Wilkinson, 1987), and has been studied intensively since the first description by de Dolomieu (1791), for both academic and economic purposes. Nevertheless, dolomite formation in modern marine environments is rare, despite the oversaturation of seawater with respect to dolomite. The precipitation of negligible amounts of primary dolomite has only been reported during the last 50 years (e.g. Deffeyes et al., 1965; McKenzie, 1981; Vasconcelos and McKenzie, 1997). Moreover, synthesis of dolomite in a laboratory environment at ambient temperature and pressure has not been successful (Land, 1998). This apparent paradox became known as 'the dolomite problem' and has not been solved to date (Arvidson and Mackenzie, 1999; Gregg et al., 2015). Slow precipitation kinetics have been proposed as the main reason for the lack of modern dolomite (Land, 1998), as well as the existence of a sort of catalyst yet to identify. Recent studies have been focusing on the catalytic effects of bacteria in the precipitation of dolomite (e.g. Vasconcelos and McKenzie, 1997). However, none of these studies managed to precipitate ordered dolomite, with ideal alternations of Ca^{2+} and Mg^{2+} layers. Instead they precipitated very high-magnesium calcite, which is believed to be the precursor for the nucleation and growth of true ordered dolomite (Gregg et al., 2015; Kaczmarek et al., 2017). As long as the step between the formation of very high-magnesium calcite and true ordered dolomite cannot be deciphered, the dolomite problem remains.

1.2.3. Hydrothermal dolomite

Most of the dolomite rocks in the Phanerozoic rock record are replacive, and almost all of them formed during burial (Machel, 2004). Several dolomitization models (the so-called dolomitization bandwagons) have been proposed to explain their formation mechanisms. Some of these bandwagons became popular while others quickly lost interest. Land (1998) refers to the latter as 'bandwagons lying upended, wheels still slowly spinning, along the side of the road'. Popular models are focused on explaining the force necessary to drive the flow of fluids rich in Mg, without which dolomitization would not be possible. The importance of fluid flow is illustrated by Land

(1985), who calculated that 650 m³ of seawater is needed to dolomitize 1 m³ of limestone with 40 % initial porosity at temperatures around 25 °C.

A dolomitization model which gained a lot of interest during the last 4 decades, is the 'hydrothermal dolomite (HTD) model' (Davies and Smith, 2006). 'Hydrothermal' refers to dolomitizing fluids which are warm or hot relative to their surrounding environment (White, 1957). Hydrothermal dolomitization commonly occurs under burial conditions at shallow depths by saline fluids with a temperature higher than that of surrounding rocks (Machel and Lonnee, 2002; Davies and Smith, 2006). Several textural features can be found in HTD, such as zebra textures (Fontboté, 1993; Nielsen et al., 1998; Vandeginste et al., 2005; Merino et al., 2006) and saddle or baroque dolomite crystals (Radke and Mathis, 1980; Searl, 1989; Davies and Smith, 2006).

1.2.4. Dolomite porosity

Since the first discovery of hydrocarbons in dolomite reservoir rocks in the middle of the 20th century, geologists were struck by the fact that dolomite often forms the best reservoir rocks in carbonate systems (Allan and Wiggins, 1993). Ever since, the influence of dolomitization on the petrophysical characteristics of carbonate rocks became a major research topic in carbonate diagenesis. Early works suggested that a volume decrease during replacement of calcite by denser dolomite results in a 13 % porosity increase during dolomitization (Warren, 2000). It soon became clear that this is only valid for closed systems, and does not take into account continuing influx of Mg-rich fluids in open systems. The beneficial petrophysical properties of dolomite are mainly due to dolomite being less chemically reactive, but more brittle, compared to limestone (Robertson, 1955; Handin, 1966). Because they are less reactive, they are more resistant to porosity loss with depth (Schmoker and Halley, 1982). Their more brittle nature will result in more intense fracturing compared to limestone (Hugman and Friedman, 1979; Williams and McNamara, 1992; Gale et al., 2004).

Pores in dolomite rocks can have several origins (Purser et al., 1994). Some of them are primary, and inherited from the precursor limestones. Prior to dolomitization, the dolomitizing fluids intruding limestone rocks can also generate porosity, mainly due to dissolution (Merino and Canals, 2011). The dolomitization process itself increases the crystal size and pore throat sizes, thus increasing the permeability of carbonate rocks (Allan and Wiggins, 1993). Continuing precipitation of dolomite can result in occlusion of existing pores, a process called overdolomitization (Lucia, 1983). Following dolomitization, dissolution of metastable dolomite, relict calcite or evaporite minerals can result in porosity creation.

1.3. Problem statements and research aims

Despite intensive research on dolomite, several aspects of the dolomitization process remain unclear (e.g. the dolomite problem). Especially the genesis and characteristics of massive bodies of dolomite in burial environments, such as HTD, are still not fully understood (Machel, 2004; Lapponi et al., 2011). This PhD thesis uses HTD rocks exposed in the Cantabrian Mountains in northern Spain as analogues to gain more insights into three main topics of interest, which are listed below (sections 1.3.1, 1.3.2 and 1.3.3). In the Cantabrian Mountains, Carboniferous limestone platforms have been intensely dolomitized (Gasparrini et al., 2006a), resulting in spectacular exposures of HTD which can

be observed on mountainsides and along road sections. These HTD geobodies represent outcrop analogues for dolomite rocks in Variscan foreland fold-and-thrust belts (FFTB; Suchý et al., 1996; Nielsen et al., 1998; Boni et al., 2000) and fracture-related dolomite geobodies in general (e.g. Cantrell et al., 2004; Smith, 2006; Sharp et al., 2010; Beckert et al., 2015).

1.3.1. HTD geometry and porosity distribution

HTD typically occurs associated with extensional or strike-slip faults (Lavoie and Morin, 2004; Davies and Smith, 2006; López-Horgue et al., 2010), or forms along structural discontinuities like fracture networks (Gasparrini et al., 2006a; Beckert et al., 2015). The geometries of HTD geobodies can be complex and influenced by a variety of secondary controlling parameters, such as primary depositional fabrics in precursor limestones, bedding planes and stylolites (e.g. Sharp et al., 2010; Lapponi et al., 2011; Dewit et al., 2014; Gomez-Rivas et al., 2014; Beckert et al., 2015; Gasparrini et al., 2017; Martín-Martín et al., 2017). As a result, dolomite rocks often occur as tongues replacing specific horizons in precursor limestones (Lapponi et al., 2011; Dewit et al., 2014). These secondary parameters not only control the geometry of HTD dolomite, but also define the nature of heterogeneous pore networks in dolomite rocks. This results in a wide range of porosity and permeability values in subsurface HTD, and a complex distribution of reservoir characteristics. Such complexity in subsurface dolomite reservoir rocks can often not be covered through reservoir modeling because of a general lack or limited availability of well and seismic data (Lapponi et al., 2011). Therefore, analogue studies can provide geological information which allows more realistic modeling of complex carbonate systems. In the Cantabrian Mountains, a detailed reservoir characterization of HTD geobodies has not been performed so far, except for a limited amount of observations of dolomite pore types in the study area by Gasparrini et al. (2006a), and a reservoir study of dolomite textures performed by Muñoz Quijano (2015). This PhD thesis uses the HTD reservoir analogues exposed in the Cantabrian Mountains to better understand the parameters controlling the geometry of massive HTD, and the related distribution of porosity and permeability, in similar geodynamic settings.

1.3.2. Dolomite paleothermometry and the application of clumped isotopes

The thermicity of Paleozoic rocks exposed in the southern Cantabrian Mountains has been investigated in previous studies through a variety of paleothermometry techniques (e.g. Raven and van der Pluijm, 1986; Aller et al., 2005). These techniques have been mainly used to map thermal isograds in order to understand the thermal history experienced by the Paleozoic rocks. A lack of knowledge exists on the true maximum temperatures experienced by precursor limestone rocks (which host dolomite) and over- and underlying ambient siliciclastic rocks. This PhD thesis aims to better understand the temperatures experienced by the Paleozoic rocks exposed the southern Cantabrian Mountains.

An emerging thermometer in carbonate sedimentology and diagenesis is clumped isotope paleothermometry (Ghosh et al., 2006). Clumped isotope paleothermometry is concerned with the state or ordering of rare and heavy O and C isotopes in the crystal lattice of carbonate minerals. The amount of carbonate ions containing two or more heavy isotopes is directly related to precipitation temperature. Carbonate clumped isotope paleothermometry has been applied in several studies to obtain the crystallization temperature of carbonate minerals (usually calcite) formed at low temperatures (< 100 °C; e.g. Ferry et al., 2011; Dale et al., 2014). Based on a detailed paleothermal

study of the precursor limestone and ambient siliciclastic rocks, the HTD rocks in the southern Cantabrian Mountains are used in this PhD thesis as a test case for high-temperature (> 100 °C) clumped isotope paleothermometry in dolomite crystals.

1.3.3. The application of Mg-isotope geochemistry

The nature and source of fluids which formed dolomite in burial environments are often unclear. Several proxies exist to characterize the type of fluids and the possible sources of Mg, such as stable O and C isotopes (Allan and Wiggins, 1993). A newly introduced proxy is the stable isotopic composition of Mg (Lavoie et al., 2010; Geske et al., 2015), which has been proposed as interesting future research by previous PhD studies on HTD rocks performed at KU Leuven (e.g. Dewit, 2012; Jacquemyn, 2013). Although the technique has been put forward as a new proxy to characterize the source of Mg in burial dolomite, so far it has not turned out to be as powerful as expected (Geske et al., 2015). This PhD thesis uses the HTD rocks exposed in the southern Cantabrian Mountains as a test case for Mg-isotope geochemistry, and tries to understand the potential implications of the new technique in the field of carbonate diagenesis.

1.4. Thesis outline

The PhD thesis consists of three main chapters (chapters 3, 4 and 5) which each focus on the main problem statements introduced above (sections 1.3.1, 1.3.2 and 1.3.3). Each of these chapters contains an introduction and methodology section, followed by results and a discussion. At the start of each chapter, a 'HIGHLIGHTS' box provides a brief overview of the main findings and results. The three main chapters are preceded by an introduction of the geology of the study area (chapter 2) and are complemented with an overview of general conclusions and future perspectives (chapter 6).

A detailed overview of the geodynamic history of the Cantabrian Mountains is provided in chapter 2 (section 2.2). This chapter also introduces the stratigraphy of the specific study area (section 2.3), as well as an overview of its thermal history (section 2.4). The chapter concludes with a section (section 2.5) combining information derived from previous studies performed on the HTD bodies exposed in the study area.

Chapter 3 of this PhD thesis aims to unravel the main parameters controlling the geometry of the exposed HTD geobodies and the associated distribution of matrix porosity networks. Hence, this chapter is focused on the dolomitization style and on the distribution of petrographic and petrophysical properties. A detailed account on the geometry and pore networks of HTD geobodies is elaborated, based on samples derived from 3 key outcrops. The chapter starts with an introduction on the lithology and internal structure of these key outcrops (section 3.3). A paragenetic sequence of diagenetic events is reconstructed based on petrographic observations (section 3.4), and different dolomite pore types are described (section 3.5). The porosity evolution is reconstructed based on the described diagenetic modifications and pore types (section 3.6), and the dolomitization style and matrix porosity and permeability distribution for each of the 3 key outcrops is discussed in detail, based on the previous sections (section 3.7).

Chapter 4 provides a detailed paleothermal study of precursor limestones, ambient siliciclastic rocks and HTD rocks. In order to better constrain the thermal conditions of the dolomitizing fluids, the

thermal history of precursor and ambient rocks has been reconstructed based on a detailed literature study with additional Rock-Eval pyrolysis and vitrinite reflectance analyses (section 4.2). The thermicity of the dolomite rocks has been assessed through fluid inclusion microthermometry and the novel technique of carbonate clumped isotope paleothermometry (section 4.3). A comparative study between both paleothermometers resulted in the establishment of a new approach to geobarometry for carbonate minerals. Both temperature and pressure are important parameters when assessing the burial history of HTD and their precursor and ambient rocks.

The main aim of chapter 5 is to understand the full potential of the new isotope technique and to provide more insights in the advantages and/or disadvantages of Mg-isotope geochemistry in dolomitization studies. The Mg-isotope signatures of a sample set of limestone, replacive dolomite and dolomite cement are reported and discussed in light of the current knowledge on Mg-isotope geochemistry and the available petrographic and geochemical data from previous studies in the southern Cantabrian Mountains.

The last chapter of this PhD thesis, chapter 6, gives a concise overview of the general conclusions of chapters 3, 4 and 5. It is followed by 7 appendices in which additional data can be found. Throughout the thesis, 4 text boxes provide complementary information on interesting features in the study area.

Chapter 2 Geological setting

2.1. Location of the study area

The study area is located in the Cantabrian Mountains in northern Spain. The E-W trending Cantabrian Mountains represent one of the main mountain ranges on the Iberian Peninsula, stretching over 480 km along the Cantabrian Sea, the southern part of the Bay of Biscay. They are made up of Paleozoic sedimentary rocks, locally covered by minor Mesozoic and Cenozoic successions. These Paleozoic rocks represent the foreland fold-and-thrust belt (FFTB) of the Iberian Variscan Massif, referred to as the Cantabrian Zone (CZ; figure 2.1A; Julivert, 1971).

The CZ is subdivided into several tectonostratigraphic units (Julivert, 1971; Pérez-Estaún et al., 1988), of which the Bodón Unit (see section 2.2) represents the study area for this PhD thesis (figure 2.1A & B). The Bodón Unit has a surface area of approximately 550 km² and is sparsely populated (see box 1). Inhabitants live in small villages with populations of a few hundred (figure 2.1B).

2.2. Geodynamic history of the Cantabrian Zone

The Iberian Variscan Massif was originally a N-S oriented east-verging thin-skinned mountain range, which evolved into a secondary thick-skinned orocline during the Upper Carboniferous (ca. 310-295 Ma; Gutiérrez-Alonso et al., 2004, 2012, 2015; Weil et al., 2013). The lithospheric material underneath the orocline centre, roughly corresponding to the CZ, thickened and created a lithospheric root. This root became unstable, detached (i.e. lithospheric delamination) and sunk away into the asthenosphere (ca. 295-285 Ma; Gutiérrez-Alonso et al., 2004, 2012). The delaminating lithosphere was replaced by hot upwelling asthenospheric material resulting in extension and increased crustal heat flow (Gutiérrez-Alonso et al., 2004; Weil et al., 2013).

Precambrian rocks exposed in the core of the Narcea Antiform (figure 2.1A) separate the CZ from the metamorphic internal zones of the Variscan Orogen, located to the southwest. The tectonostratigraphic units of the CZ include (Julivert, 1971; Pérez-Estaún et al., 1988): the Somiedo-Correcilla, La Sobia-Bodón, Aramo, Esla, Valsurvio, Ponga, Central Coal Basin, Picos de Europa and Pisuerga-Carrión units. The Somiedo-Correcilla and La Sobia-Bodón units are often subdivided into the Somiedo and Correcilla units and the La Sobia and Bodón units, respectively. The Bodón Unit is located south of the León Fault (a major tectonic lineament that crosscuts a large part of the CZ: figure 2.1A & B). Recently, the classical subdivision of the CZ has been modified by Alonso et al. (2009), based on a new interpretation of the León Fault, being an out-of-sequence breaching thrust, duplicating tectonic units. However, in this PhD thesis the former subdivision is used, to enable the correlation of new thermal data with thermal data from previous studies (see chapter 4). The Bodón Unit is subdivided into three structural nappes: the Gayo, Bodón and Forcada nappes (figure 2.1B; Evers, 1967; Marcos, 1968).

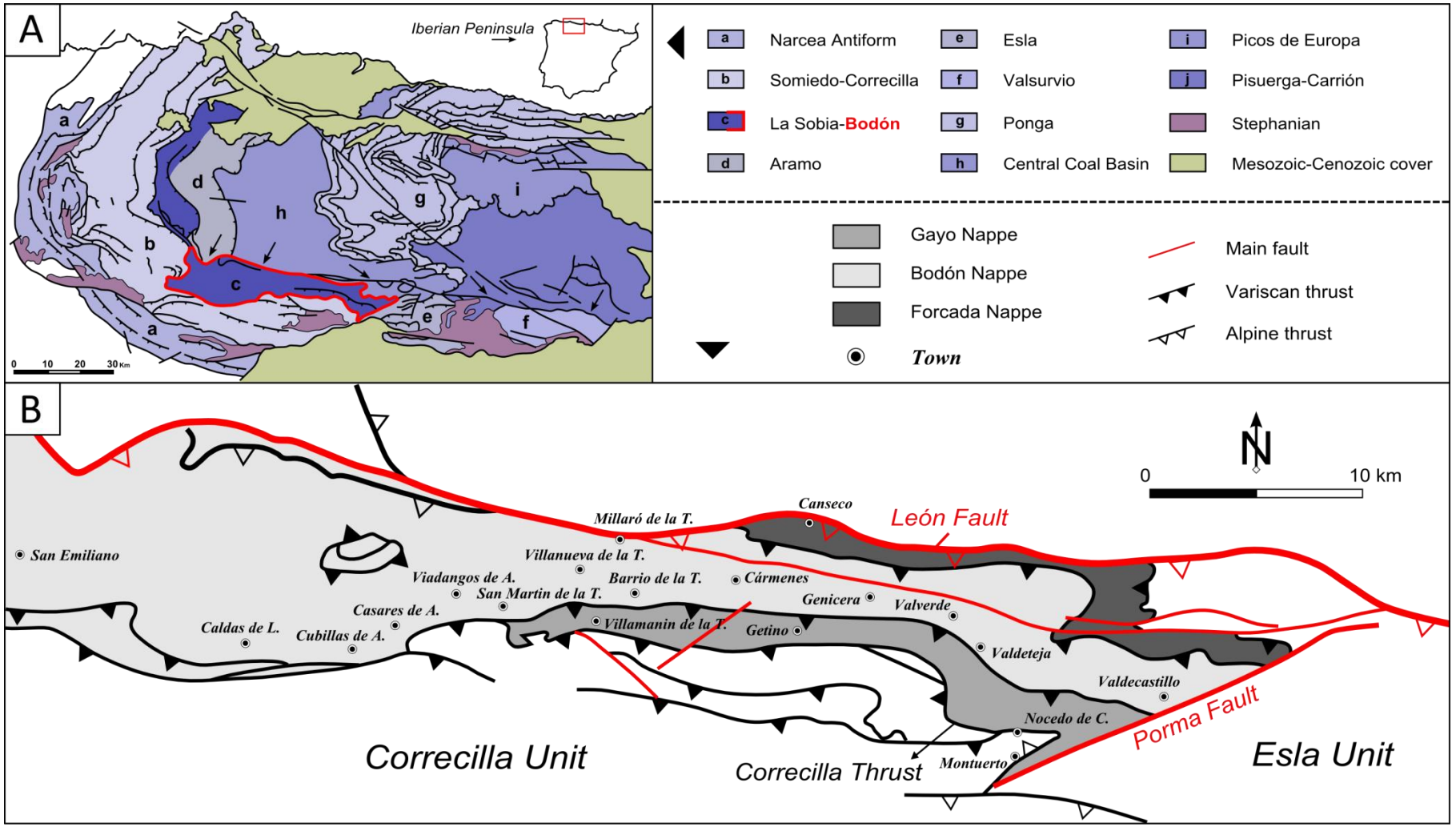

Figure 2.1: (A) Geological map of the CZ with indication of the main fault systems and tectonostratigraphic units (modified after Dallmeyer and Martínez-García, 1990). Unconformable Stephanian and Mesozoic-Cenozoic successions have been indicated. The Bodón Unit is encircled in red and the León Fault is indicated with black arrows. Inset shows the location of the CZ on the Iberian Peninsula. **(B)** Geological map of the Bodón Unit modified from Lobato et al. (1984), Alonso et al. (1990), Suárez Rodríguez et al. (1991) and Alonso et al. (2009). The Gayo, Bodón and Forcada nappes are indicated, as well as the most important faults and thrust systems. Alpine thrusts are created during the Alpine uplift, or represent reactivations of Variscan thrusts or faults. The main villages in the Bodón Unit have been indicated.

Box 1 : A trip to the abandoned Bodón Unit

Geographically, the Bodón Unit is located in the northern and mountainous part of the Spanish region of Castilla y León. It borders the region of Asturias, but in contrast to the green and wet coast of Asturias, it is characterized by dry summers. San Emiliano and Villamanín de la Tercia are the most important municipalities in the western and central parts, respectively, of the Bodón Unit. These villages are rather small (Villamanín de la Tercia has a current population of around 340 villagers; www.aytovillamanin.es) and have a desolate appearance, which is even more expressed in the numerous small towns (of a couple of 10 to 100 villagers) spread out over the Bodón Unit. The landscape is characterized by abandoned buildings and old ruins (figure box 1) together with impressive carbonate mountains. The area of the Bodón Unit has been the centre for mining activities during several centuries, but was abandoned by many after the closure of the most important mines in the course of the 20th century. And the old ruins? They are silent witnesses of the Spanish Civil War (1936-1939).

Figure box 1: Ruins of an old ore processing plant, close to Villamanín de la Tercia, which has been demolished during the Spanish Civil War (1936-1939).

During the Middle Cretaceous (Albian), an extensional episode occurred related to the opening of the northern Atlantic Ocean and the Bay of Biscay located northeast of the CZ (Gong et al., 2008). Overall, the extensional tectonics affecting the CZ at the end of the Paleozoic and during the Mesozoic are not well constrained due to a lack of preserved sediments (Martín-González et al., 2012).

The last important tectonic event that affected the CZ is related to the Alpine Orogeny, leading to uplift and exhumation of the Variscan basement (39 – 29 Ma; Alonso et al., 1996; Fillon et al., 2016). This created much of the present topography (i.e. the Cantabrian Mountains). The Alpine Orogeny caused minor internal deformation in the CZ, except for reactivation of faults and thrusts, block tilting and some further shortening (Pulgar et al., 1999).

2.3. Stratigraphy of the Bodón Unit

In the Bodón Unit, as in most tectonostratigraphic units of the western and southern CZ, Paleozoic rocks were thrust along a *décollement* level located in carbonate rocks of the Lower Cambrian Láncara Fm. (Julivert, 1971).

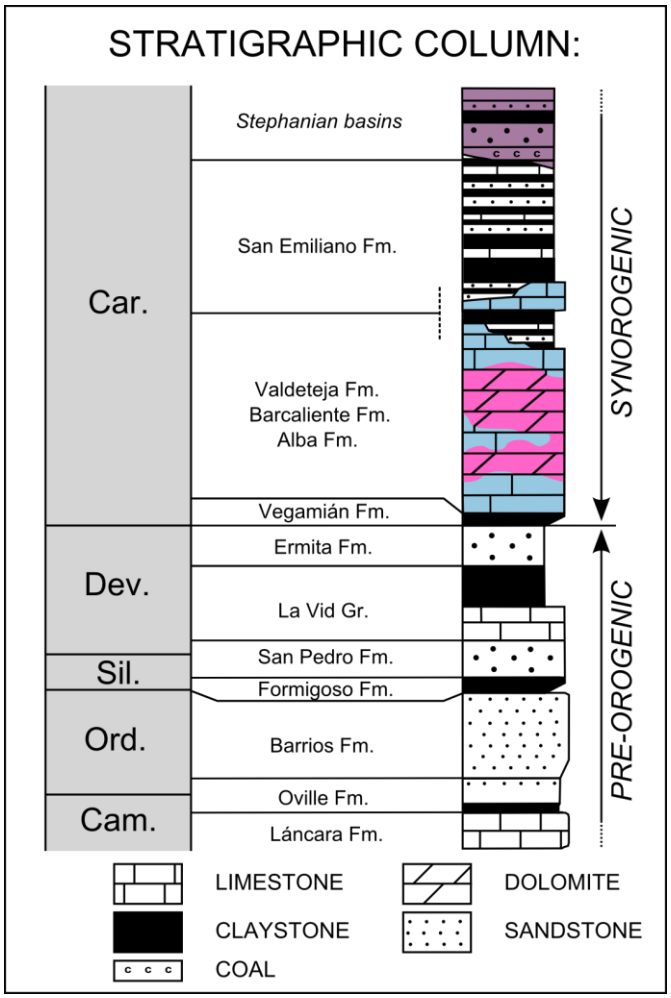

Figure 2.2: Stratigraphic column of the Bodón unit (modified from Aller et al., 2005; Pérez-Estaún et al., 1988) showing Carboniferous precursor carbonate successions in light blue and dolomite geobodies in pink. Stephanian siliciclastics are indicated in purple. Pre-orogenic and synorogenic successions are distinguished.

The CZ is subdivided into a pre-orogenic (pre-Carboniferous) and a synorogenic rock succession (Carboniferous), developed during the Variscan Orogeny (figure 2.2; Marcos and Pulgar, 1982). Due to the Variscan and Alpine compression, the rock successions in the Bodón Unit were tilted and presently dip subvertically, leading to excellent outcropping conditions, particularly along road sections (figure 2.3).

The Láncara Fm. is subdivided into a lower member composed of synsedimentary to early diagenetic beige dolomite and gray limestone and an upper member composed of glauconitic limestone overlain by nodular red limestone (figure 2.3A; Evers, 1967; Zamarreño, 1972; Lapponi et al., 2013). Upper Cambrian to Silurian deposits are composed of siliciclastic rocks, with the Silurian Formigoso Fm. composed of dark shales. The Devonian is characterized by an alternation of carbonates and siliciclastic rocks, with the La Vid Group representing the thickest stratigraphic unit (figure 2.3B). The Ermita Fm. is a transgressive sandstone unit of a few meters thick (but up to 140 m thick in the type locality; Comte, 1959) deposited during the Upper Devonian (figure 2.3B). The Vegamián Fm. at the base of the Lower Carboniferous is a thin succession (5 to 10 m) of black shales and siltstones with phosphate, manganese, marcasite and chert nodules (figure 2.3B). Thin silt- to sandstone intercalations can occur, as well as carbonate lenses of a few cm in thickness. The Vegamián Fm. was deposited below wave base at low sedimentation rates under anoxic conditions (Raven, 1983). Seibert (1986) correlates the deposition of the Vegamián Fm. with eustatic sea-level rise and subsidence. The Vegamián Fm. represents the transition to thick carbonate successions filling the Variscan foreland basin during the Lower to Middle Carboniferous (Bahamonde et al., 2014). These successions are divided into three formations: the Alba, Barcaliente and Valdeteja Fm. The Alba Fm. (Late Tournaisian to Late Serpukhovian) is usually less than 30 m in thickness and is composed of two nodular limestone packages, interpreted as condensed units deposited on a well oxygenated carbonate platform (figure 2.3B & C). A member composed of bedded cherts can be found between the two limestone packages and represents an episode of pelagic sedimentation (figure 2.3B & C; Wagner et al., 1971; Sanchez de Posada et al., 1990). The overlying Barcaliente Fm. (Late Serpukhovian to Early Bashkirian) is composed of thinly bedded dark mudstones (figure 2.3C & D) showing a remarkable consistency in both thickness (ca. 300 m) and depositional facies over most of the CZ. It reflects a period of uniform carbonate sedimentation in a shallow water, low energy, anoxic environment (Evers, 1967; Wagner et al., 1971; Eichmüller, 1986; Dietrich, 2005). The Bashkirian Valdeteja Fm. (up to 1500 m thick) is composed of microbial carbonate platforms developed in the Variscan foreland basin (figure 2.3E; Winkler Prins, 1968; Wagner et al., 1971; Dietrich, 2005; Chesnel et al., 2015), whose sedimentation is strongly influenced by the approaching Variscan orogenic front. The prevailing anoxic conditions in the restricted foreland basin provided optimal conditions for microbial and algal carbonate factories (Della Porta, 2003; Bahamonde et al., 2014). The Valdeteja Fm. is diachronically overlain by siliciclastic rocks of the Late Bashkirian to Early Moscovian San Emiliano Fm. (figure 2.3F; Bowman, 1982; Lobato et al., 1984; Alonso et al., 1990), which filled up the foredeep of the Variscan Orogen (Brouwer and van Ginkel, 1964). It is composed of claystones, locally with abundant sandstone and carbonate lenses, and coal seams (van Ginkel, 1965; Wagner and Bowman, 1983; Eichmüller, 1985; Samankassou, 2001). Unconformable Stephanian siliciclastic successions occur in local intramontane pull-apart basins (figure 2.1A), of which the Ciñera-Matallana (CM) and Canseco-Rucayo (CR) basins are located closest to the Bodón Unit (figure 2.4; Colmenero et al., 2008). Permian to Cretaceous sediments are absent in the southern CZ and crop out only locally in the northern CZ (figure 2.1A; Dallmeyer and Martínez-García, 1990). They might have been initially deposited and eroded later on (Alonso et al., 1996; Gómez-Fernández et al., 2000; Frings et al., 2004; Botor, 2012). For the CM Basin, just south of the Bodón Unit, a total overburden of some 1000 m has been attributed to eroded sedimentary cover (Frings et al., 2004).

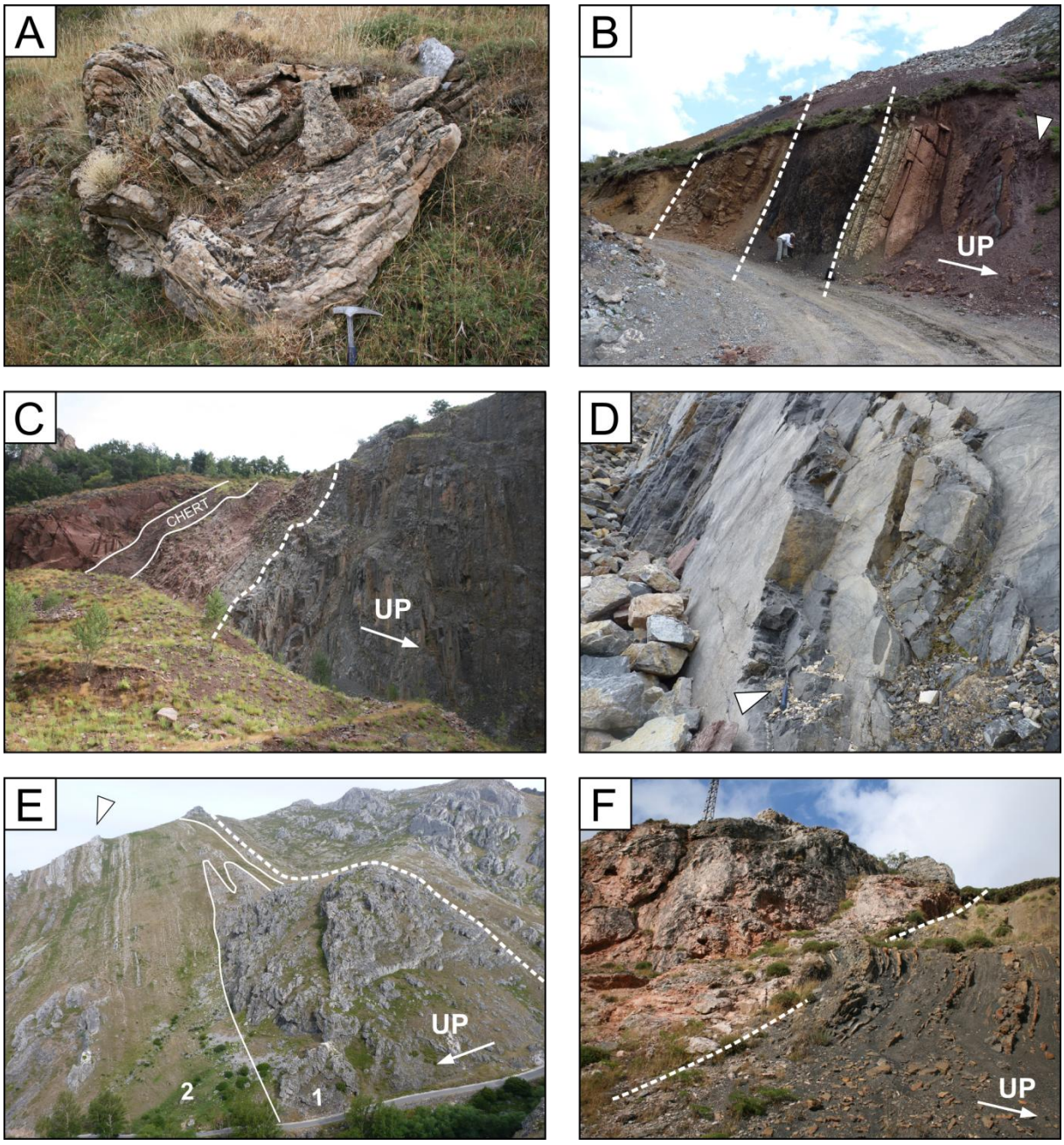

Figure 2.3: Outcrop photographs of important stratigraphic successions exposed in the Bodón Unit. **(A)** Limestone beds of the Cambrian Láncara Fm., folded and exposed in the southeastern part of the Bodón Unit, close to Montuerto. Hammer for scale (32 cm). **(B)** Exposure of Devonian and Carboniferous successions in the Las Chábanos quarry in the northern central part of the Bodón Unit, close to Villanueva de la Tercia. Formation boundaries are indicated with white dashed lines. Siliciclastic rocks of the Devonian La Vid Group are exposed on the far left, followed by brown sandstones of the Ermita Fm. The black succession in the centre of the picture represents the Lower Carboniferous Vegamián Fm. which is overlain by nodular limestones of the Alba Fm. On the far right side, the central chert member of the Alba Fm. can be seen (white arrow). Person for scale. **(C)** Transition between the Alba (left) and Barcaliente Fm. (right) exposed in the Las Baleas quarry north of La Pola de Gordón (Correcilla Unit). The chert member of the Alba Fm. has been indicated, as well as the contact between both formations (white dashed line). The thickness of the succession visible on the photograph is approximately 80 m. **(D)** Exposed limestone beds of the Barcaliente Fm. in the Los Chábanos quarry. Hammer for scale (32 cm; white arrow). **(E)** Carbonate successions of the Valdeteja Fm., exposed close to Millaró de la Tercia. The contact with the underlying Barcaliente Fm. has been indicated with a white dashed line. The first massive Valdeteja deposits (depositional unit 1; see chapter 3) have been completely dolomitized, while younger successions (depositional unit 2; see chapter 3) are less affected by dolomitization (white arrow). Road for scale. **(F)** Contact between the massive limestones of the Valdeteja Fm. and the overlying siliciclastics of the San Emiliano Fm., exposed close to Villanueva de la Tercia. Not utility pole (3 m) in upper left corner for scale.

2.4. Thermal history of the Cantabrian Zone

The Paleozoic rocks of the CZ have been affected by several thermal episodes related to the complex geodynamic history of the area (Bastida et al., 2002). Peak burial prior to the onset of Variscan thrusting was the most important event causing the metamorphic grades recorded by Paleozoic rocks in most of the CZ (Bastida et al., 2002; Aller et al., 2005). This is indicated by the following: (1) metamorphic grades increase with rock age, (2) the distribution of metamorphic grades is not influenced by major thrusts and (3) metamorphic patterns are discontinuously inverted (i.e. rocks recording higher metamorphic grades are thrust over rocks recording lower metamorphic grades; Brime, 1981; Bastida et al., 1999; Aller et al., 2005). Burial resulted in diagenetic (up to 200 °C) to locally anchizonal (200 to 300 °C) conditions. The thermal peak occurred when the Paleozoic successions reached their maximum thickness (Bashkirian-Moscovian), preceding the emplacement of the tectonostratigraphic units (Bastida et al., 2002). Based on conodont color alteration index (CAI) data from Devonian rocks in the Somiedo Unit, a paleogeothermal gradient of about 35 °C/km is estimated for this episode of peak burial (Brime et al., 2001).

Regional orogenic metamorphism, due to Variscan thrusting and folding, has only locally been recognized in the CZ (Bastida et al., 2002). It is generally recorded closer to the internal areas of the Variscan Orogeny (e.g. in the northwestern part of the Somiedo Unit; Brime et al., 2001). It is of minor importance in the southern CZ and did not affect the Paleozoic rocks presently exposed in the Bodón Unit (Bastida et al., 2002; Aller et al., 2005).

Lithospheric delamination, initiated after the orocline formation, led to the upwelling of the asthenosphere and to a concomitant increase in crustal heat flow (Gutiérrez-Alonso et al., 2004; Weil et al., 2013). The upwelling also caused uplift of the CZ, accompanied by near-surface extension (Muñoz-Quijano and Gutiérrez-Alonso, 2007). Two thermal events have been recognized in the CZ, corresponding respectively to the orocline formation and the subsequent lithospheric delamination, both accompanied by dominant extensional tectonics (Bastida et al., 2002; Aller et al., 2005).

The first event, often referred to as the Late-Variscan extensional event (Bastida et al., 2002) and likely associated with the orocline formation, has been recorded in the southern part of the Central Coal Basin and in the Pisuerga-Carrión and Valsurvio units (Aller and Brime, 1985; Aller et al., 1987; Bastida et al., 2002). Here, the Paleozoic rocks record anchizonal to locally epizonal conditions (above 300 °C) typically associated with the occurrence of a subhorizontal cleavage (Aller et al., 1987; Marín, 1997; García-López et al., 1999). The distribution of both anchizonal and epizonal metamorphism (affecting pre-Permian rocks only), as well as the cleavage development, do not correspond to the location of the main Variscan structures. Intrusions of small sills and stocks, which occur mainly in the western and eastern units of the CZ (Corretgé and Suárez, 1990), accompanied this event. Close to these intrusions, contact metamorphism resulted in epizonal grades and the development of skarn deposits (Bastida et al., 2002 and references therein). Since subhorizontal cleavage associated with high metamorphic grades or intrusions has not been reported in the Bodón Unit (Aller et al., 1987), the Late-Variscan extensional event was likely of minor importance.

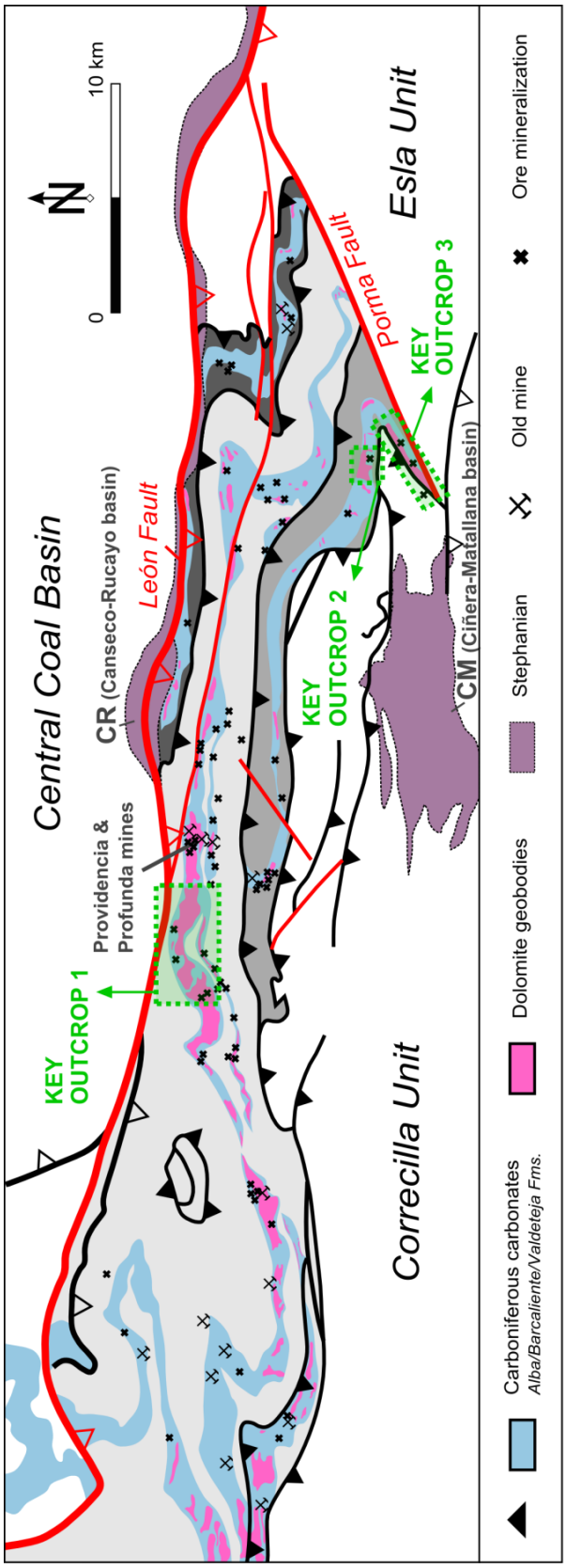

Figure 2.4: Geological map of the Bodón Unit modified from Lobato et al. (1984), Alonso et al. (1990), Suárez Rodríguez et al. (1991) and Alonso et al. (2009), with indication of Carboniferous carbonate outcrops and the location of dolomite geobodies (based on Muñoz Quijano, 2015) and ore mineralizations. The locations of 3 key outcrops, which are discussed in chapter 3, have been indicated.

The second thermal event, referred to as the Post-Variscan thermal event (Bastida et al., 2002), was responsible for the widespread occurrence of fracture-related dolomitization and ore mineralization (see box 2) in Paleozoic successions (Martínez-García, 1983; Crespo et al., 2000; Gómez-Fernández et al., 2000; Gasparrini et al., 2006a; Muñoz-Quijano and Gutiérrez-Alonso, 2007). Several anomalies in CAI values occur within the Bodón and Picos de Europa Units, in areas with a dense fault pattern and abundant ore mineralization, and are interpreted to be due to this thermal episode (Raven and van der Pluijm, 1986; Bastida et al., 2002). In the southern CZ, anchi- to epizonal conditions recorded in the Stephanian pull-apart basins are probably related to intrusions of diorite during the same thermal episode (Bastida et al., 2002). These intrusions resulted in re-equilibration of fluid inclusions in quartz veins in the CM Basin (Ayllón et al., 2003). The Post-Variscan thermal event is dated at 270 Ma based on K-Ar ages from illite (Weh et al., 2001). These ages correspond with U-Pb dating of dolomite-hosted ore minerals from the Bodón Unit (Paniagua et al., 1993, 1996). Therefore, the Post-Variscan thermal event correlates temporally with lithospheric delamination following the orocline formation. Based on apatite fission-track (AFT) thermochronology, Carrière (2006) and Botor and Anczkiewicz (2015) concluded that although this thermal event was likely short-lived, temperatures remained high within Stephanian siliciclastic successions (above 60 °C), at least until the Middle Triassic.

2.5. Dolomite in the Cantabrian Zone

Dolomite geobodies, some of them with associated ore mineralizations, have been reported in most of the tectonostratigraphic units of the CZ (e.g. Gómez-Fernández et al., 2000; Grimmer et al., 2000; Kenter et al., 2002) and their outcrops cover an area of over 1000 km² (Muñoz Quijano, 2015). The most spectacular occurrences can be studied in the Bodón and Picos de Europa Units, and have been generally associated with the Post-Variscan thermal event (Martínez-García, 1983; Crespo et al., 2000; Gómez-Fernández et al., 2000; Gasparrini et al., 2006a; Muñoz-Quijano and Gutiérrez-Alonso, 2007; Lapponi et al., 2013). This implies that they are related to fluid flow following the Post-Variscan lithospheric delamination, in contrast with Albian dolomite occurrences in the Basque-Cantabrian Basin (east of the CZ; López-Horgue et al., 2010; Shah et al., 2010; Nader et al., 2012; Dewit et al., 2014). The Providencia and Profunda mines (figure 2.4) were the most productive sites of ore extraction in the Bodón Unit, but are currently abandoned (see box 2).

In the Bodón Unit, dolomitization mostly affected the Carboniferous Barcaliente and Valdeteja Fm. (figures 2.4; 2.5A & B; Gasparrini, 2003; Gasparrini et al., 2006a; Muñoz Quijano, 2015). Smaller dolomite geobodies occur in the Láncara Fm. (figure 2.5C; Lapponi et al., 2007, 2013), in the top layers of the Alba Fm. (Gasparrini, 2003) and in Devonian successions (Muñoz-Quijano, 2015). Based on the work of Muñoz Quijano (2015), combined with results from aerial photographs and mapping, the occurrence of dolomite geobodies in Carboniferous carbonates in the Bodón Unit has been indicated on figure 2.4. Dolomite is mostly fracture-associated, but the geometry of the dolomitization front was locally affected by rock anisotropies such as bedding and stylolite planes (figure 2.5A; Gasparrini et al., 2006a).

Box 2: Ore minerals in the Bodón Unit

The Cantabrian Mountains are characterized by over 300 localities of epithermal ore mineralizations which include Cu, Au, Co, Ni, Pb, Zn, Hg, Sb, As, F, Ba and talc. Approximately 75 % of these mineralizations are hosted in fractured carbonate rocks, and some of them are associated with Late- to Post-Variscan volcanics (Dallmeyer and Martínez-García, 1990). The formation of ore deposits post-dates the massive dolomitization of limestones in the Bodón Unit (Gasparrini et al., 2006a), but is associated with the same episode of hydrothermal fluid circulation following Late- to Post-Variscan lithospheric delamination. The Bodón Unit contains several old mines, mine shafts and numerous reported occurrences of ore minerals (figure 2.4). The two most important mines in the Bodón Unit are the Providencia and Profunda mines (see locations on figure 2.4) where exploitation commenced in pre-Roman times (Gómez et al., 1996) and intensified during the Roman occupation of Spain (Fernández-Martínez et al., 1996). During the 1930s, the Providencia and Profunda mines produced large amounts of Cu, Co and Ni. The mines constitute the type locality of a new mineral first described in 1920 (Schoeller and Powell, 1920). Villamaninite, named after the village of Villamanín de la Tercia, is a disulphide of Cu, Ni, Co and Fe ($(Cu, Ni, Co, Fe)S_2$). It has a black to dark green color and occurs disseminated in crystalline dolomite as small crystals or nodular aggregates.

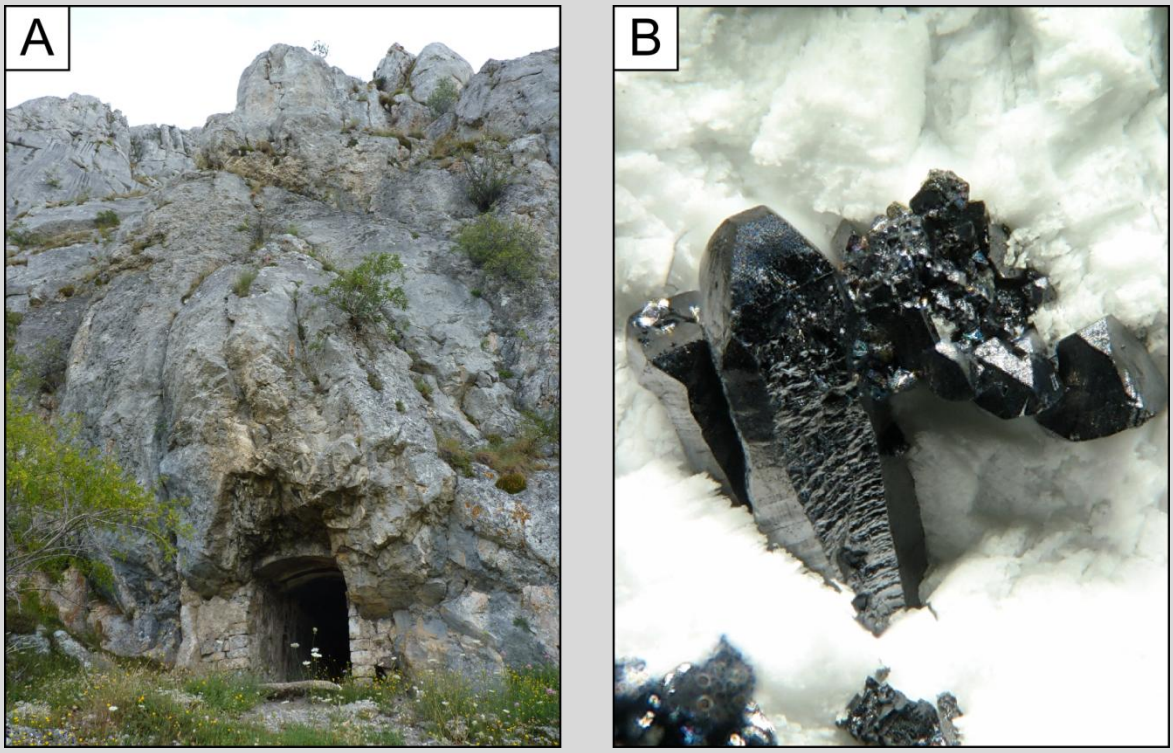

Figure box 2: (A) One of the many entrance shafts (currently sealed-off) of the abandoned Profunda mine, in carbonate rocks close to Cármenes. Width of the entrance is approximately 1.5 m. **(B)** Small crystals of dark green to black villamaninite disseminated in a matrix of dolomite crystals. The scale of this photograph is unclear, but the large villamaninite crystal is probably around 1 cm in length (www.mindat.org).

The dolomite rocks show a typical succession of replacive and void-filling dolomite, followed by calcite cementation (figure 2.5D; Gasparrini, 2003; Gasparrini et al., 2006a; Lapponi et al., 2013). Inclusions within the dolomite crystals are two-phase aqueous with consistent liquid to vapor ratios, which is a diagnostic feature for high-temperature diagenesis (Goldstein and Reynolds, 1994). Raman spectroscopic measurements on the gas bubbles did not detect gases such as CO_2, CH_4 or N_2 (Gasparrini, 2003). Fluid inclusion microthermometry on void-filling dolomite in Carboniferous precursor limestones yielded T_h values between 110 to 150 °C (Gasparrini et al., 2006b). Salinity calculations were based on cryo-Raman spectroscopy, in order to overcome metastability problems during low-temperature microthermometry, and revealed salinities around 26 eq. wt% $CaCl_2$. The dolomitizing fluids were hypersaline brines derived from evaporated seawater, and affected by water-rock interactions, as evidenced based on radiogenic Sr-isotope signatures and high Li contents in fluid inclusions (Gasparrini et al., 2006a; Lapponi et al., 2013). Towards the end of the Post-Variscan thermal event (ca. 270 Ma), Cu-Ni-Co-Fe sulfides with homogenization temperatures up to 200 °C precipitated in fracture damage zones (Paniagua et al., 1993).

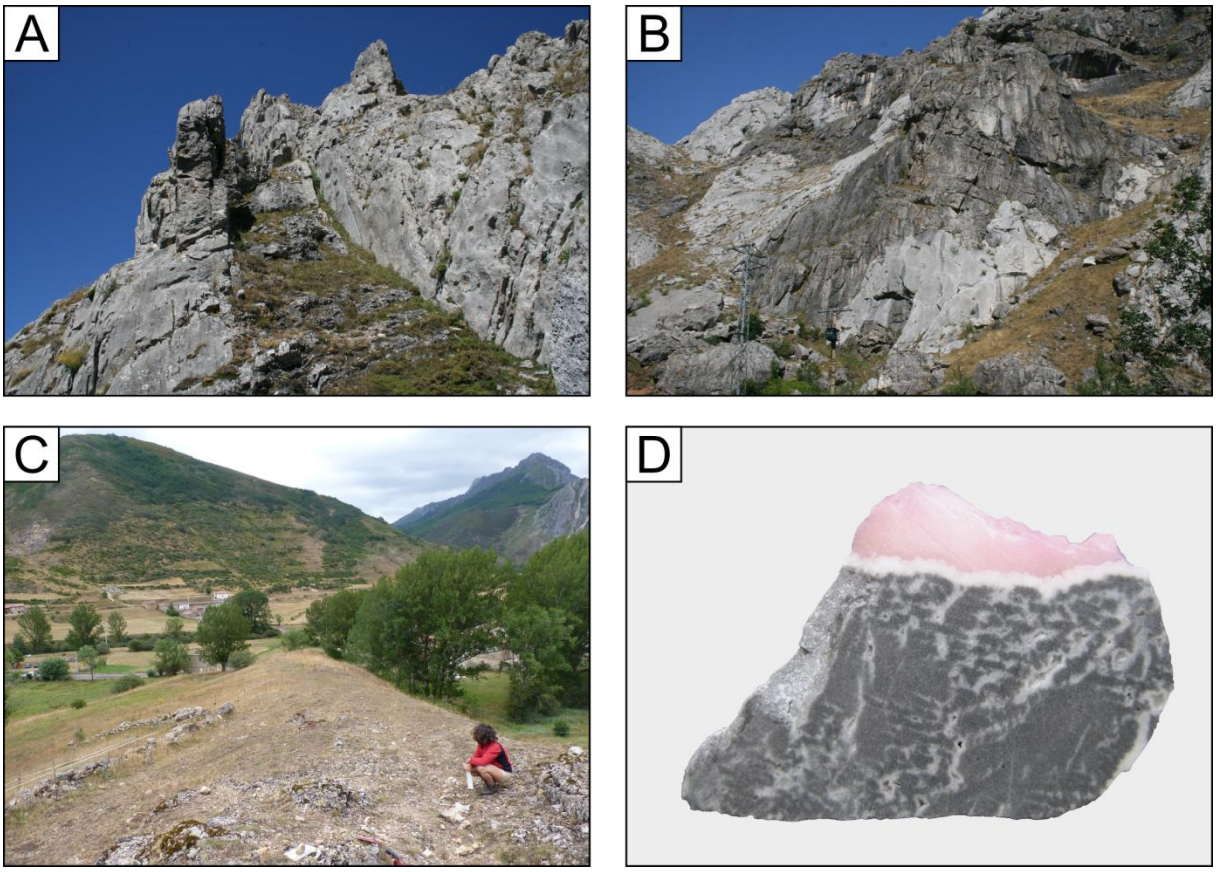

Figure 2.5: Outcrop photographs of dolomite rocks exposed in the Bodón Unit. **(A)** Dolomite geobody in Barcaliente limestones close to Millaró de la Tercia. Light gray rocks are the precursor limestones, whereas dark gray rocks are dolomites. The geobody is aligned according to bedding planes, and its thickness is approximately 4 m. **(B)** Example of dolomitized limestones of the Valdeteja Fm. in the southeastern part of the Bodón Unit, close to Nocedo de Curueño. Iron utility pole (7 m) on lower left side for scale. **(C)** Dolomitized limestone layers of the Láncara Fm. located north of Cármenes and creating a topographic high. **(D)** A typical succession of replacive (dark gray) and void-filling dolomite (white cement), followed by calcite cementation (red stained). The sample has dimensions of 3 by 4 cm.

Chapter 3 HTD geometry and porosity distribution

3.1. Introduction

Although the geochemical properties of HTD exposed in the Bodón Unit have been studied by several authors (see section 2.5), few studies focused on the geometry and/or petrophysical characteristics of the dolomite geobodies. Gasparrini (2003) reports the occurrence of both massive irregular and fracture-associated HTD geobodies. Precursor limestones are tight, while the dolomitized Barcaliente and Valdeteja Fm. display zebra pores and vuggy pores, respectively (Gasparrini, 2003; Gasparrini et al., 2006a). Muñoz Quijano (2015) investigated the distribution of dolomite in the Bodón Unit, and concluded that the western part (around the village of San Emiliano; figure 2.1B) is most intensely affected by dolomitization due to a combination of a large reservoir of dolomitizing fluids, a high local fracture abundance and an increased geothermal gradient. The petrophysical properties of HTD are found to be most prolific in the western part of the Bodón Unit, which Muñoz Quijano (2015) attributes to zebra and vuggy pores which are more abundant in this area. She reports matrix porosities ranging from 0.6 to 12 % (with an average of 3.5 %) and matrix permeability values from 0.01 to 11.3 mD (with an average of 0.76 mD) for the entire Bodón Unit based on plug measurements.

Several questions on the geometry and petrophysical properties of HTD exposed in the southern Cantabrian Zone remain unanswered. Although the local influence of stylolites and bedding planes on the geometry of dolomitization fronts has been reported (Gasparrini et al., 2006a), no explanations have been proposed for the highly variable geometries of HTD geobodies visible in several exposures of Carboniferous carbonates. Variation in the geometry and associated petrophysical characteristics of burial dolomite in other study areas has been assigned to the occurrence of bodies of synsedimentary dolomite (e.g. Cantrell et al., 2004), the occurrence of impermeable limestone beds (e.g. Dewit et al., 2014) or to the influence of early meteoric diagenesis affecting precursor limestones (e.g. Gasparrini et al., 2017). The influence of these controlling parameters makes the evaluation of subsurface dolomite reservoirs and associated porosity networks difficult (Al-Awadi et al., 2009; Lapponi et al., 2011; Gomez-Rivas et al., 2014; Jacquemyn et al., 2015).

The aim of this chapter is to investigate the geometry of HTD geobodies and hence the dolomitization style which affected several Carboniferous precursor limestone successions in the central and eastern parts of the Bodón Unit. What are the controlling parameters in the dolomitization process resulting in these irregular geometries? The chapter also investigates petrophysical properties associated with the different HTD geobodies, and specifically tries to understand the range and distribution of matrix porosity throughout the study area. Muñoz Quijano (2015) reports that dolomite textures (e.g. zebra texture or massive texture) are the main controlling parameters in the distribution of porosity and permeability, but does not explain the distribution of these dolomite textures. A better understanding of the correlation between HTD geobody architecture and the distribution of porosity networks can enhance the knowledge of complex dolomite reservoirs in similar geodynamic settings and can refine reservoir models.

Although observations have been performed on numerous outcrops in the Bodón Unit, this chapter mainly focuses on 3 key outcrops located in the central and eastern parts. The general properties of these key outcrops are introduced, as well as their sedimentological and stratigraphic framework (section 3.3). In order to understand the geometry of HTD geobodies and the distribution of their petrophysical characteristics, a paragenetic sequence of diagenetic events affecting the limestone successions in the Bodón Unit is reconstructed (section 3.4). An overview of the different pore types recognized in the dolomite rocks is elaborated (section 3.5) as well as the development of porosity during the diagenetic and geodynamic evolution of the carbonate rocks (section 3.6). The last section of this chapter (section 3.7) gives an integrated overview of petrographic characteristics, petrophysical data and dolomitization style for each of the three key outcrops. In this chapter, and throughout this PhD thesis, the terms 'outcrop' and 'exposure' are used interchangeably. Box 3 explains the subtle difference between both.

Box 3: Outcrop *versus* exposure

Outcrop and exposure are two terms which are often confused in geological literature. In this PhD thesis, the terminology of Kearey (2001) is followed. An outcrop refers to the total area over which a particular rock unit occurs at the surface, whether it has a covering of soil and vegetation or not. An exposure is that part of an outcrop which is free of soil and vegetation and where rocks can be studied *in situ*.

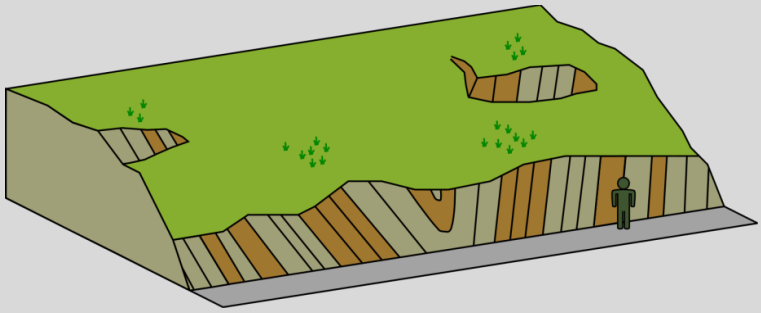

Figure box 3: Sketch illustrating the difference between outcrop and exposure. The sketch shows an outcrop, which is exposed along a road section. The top of the outcrop is covered with vegetation, except for 2 uncovered exposures.

CHAPTER 3 ***HIGHLIGHTS:***

- Chapter 3 provides a study on the **geometry** and **porosity distribution** of HTD geobodies exposed in the Bodón Unit, based on **three key outcrops** of **Carboniferous** carbonate successions.
- The chapter starts with an introduction on the **stratigraphy** and **lithology** of the precursor **limestone** rocks exposed in each of the three key outcrops.
- **Three depositional growth phases**, described by Chesnel et al. (2015) for the Bashkirian Valdorria carbonate platform in the eastern part of the Bodón Unit, have been recognized in the platform limestones of the first key outcrop.
- Fieldwork and petrography allowed to reconstruct the **paragenetic sequence of diagenetic events** which affected the Carboniferous carbonate successions in the Bodón Unit.
- Eo- and mesogenetic **porosity-destructive processes** resulted in **tight limestones** prior to Early Permian lithospheric delamination and related hydrothermal fluid flow.
- Dolomitization is mostly **fracture-controlled**, but secondary controlling factors influencing the dimension and geometry of dolomite geobodies are the nature of **fluid-migration pathways**, the **available volume of dolomitizing fluids** and the **lithology and sedimentological framework** of the dolomitized precursor limestone successions.
- Fluid-migration pathways in the three key outcrops correspond to **dense fracture networks**, except for the southeastern extremity of the Bodón Unit, where the fault zone of an important **thrust** has been dolomitized. Fluid circulation along the fault zone resulted in coarse-crystalline Fe-rich dolomite, which likely overprinted and/or recrystallized a previous dolomite phase. The **dolomitized fault gouge** has average matrix porosity values of ± 9.6 %, being the highest of all dolomite rocks exposed in the Bodón Unit.
- A low volume of fluids available for dolomitization resulted in **tight fracture-bounded** dolomite geobodies, while a high volume of available fluids yields **large bodies** of dolomite with better reservoir properties (average matrix porosity 3.8 %). **Log data**, **medical CT** and **image analysis** reveal higher porosities compared to plug measurements for dolomitized microbial boundstones, which is attributed to large pore sizes exceeding the size of small plugs used for porosity and permeability measurements (diameter of ± 3.3 cm). An increase of the **representative elementary volume** for petrophysical measurements of dolomitized microbial boundstone is needed to quantify its porosity and permeability.
- In massive dolomitized outcrops, the **sedimentological framework** of the precursor limestones influenced the dolomitization style and hence the geometry of HTD geobodies. The influence of the mechanical behavior of precursor limestone facies on dolomitization seems to be limited.
- Matrix permeability values obtained for dolomite from the Bodón Unit are often very low (average matrix permeability 0.10 mD) due to the **bad connectivity** between pores.
- **Recent exposure** results in a significant increase in petrophysical properties due to meteoric dissolution and karstification.
- **Fractures** are omnipresent in HTD rocks exposed in the Bodón Unit. Log data indicate that fracture abundance is more important in **dolomite** compared to precursor limestones. The exact influence of fractures on reservoir quality has not been addressed in this study.

3.2. Methodology

3.2.1. Sampling strategy

Limestone and dolomite samples were mostly obtained from three key outcrops which have been studied in detail and which are introduced in section 3.3. Additional samples were collected from numerous Carboniferous exposures in the central and western parts of the Bodón Unit during several field campaigns. A limited amount of samples was collected from exposures in the western part of the Bodón Unit. Samples were hammered from exposed rocks, while large cores (diameter of ± 9 cm) were drilled directly in the field using a modified Stihl drilling machine. Small plugs (diameter of ± 3.3 cm) were drilled out of larger samples and cores using a fixed HILTI DD 130 diamond core drilling machine at KU Leuven.

3.2.2. Logging and data analysis

Most of the collected samples originate from key outcrop 1 (KO 1; see section 3.3.1), the largest of the three studied outcrops. During a field campaign, five stratigraphic sections across the Carboniferous successions of KO 1 were logged in detail (see Appendix I). During logging, the following properties were visually assessed: precursor limestone sedimentary facies, bed thickness, dolomite quantity, dolomite texture, dolomite crystal size, dolomite color, abundance of calcite cement, abundance of fractures, size and abundance of pores, and pore type. Semi-systematic sampling was performed across the sections by taking samples every time an important change in visual properties occurred. The subvertical bedding of the successions allowed the calculation of the exact thicknesses of all formations based on the log data.

Each of the visual properties assessed during logging was converted into numerical codes (e.g. dolomitized layers were given numerical code 1 while non-dolomitized layers received code 0). These log data were processed using Easytrace software for well data treatment developed at *IFP Energies nouvelles* in Paris. The numerical codes corresponding to each property are introduced into Easytrace which displays the original dataset as histograms. These histograms reveal relationships between different properties (e.g. precursor limestone sedimentary facies *versus* dolomite texture) for a single log, or for all five logs combined (see Appendix II).

3.2.3. Petrography

Samples, collected during fieldwork, were cut and polished at KU Leuven. Rock slices were stained with a mixture of Alizarine Red S and potassium ferricyanide, in order to allow differentiation between calcite and dolomite, and Fe-poor and Fe-rich phases, respectively (Dickson, 1966). Based on careful observations, specific areas of the rock slices were selected for the fabrication of thin sections. These were investigated with standard optical microscopy (Leica DM LP microscope) and cold cathodoluminesence microscopy (Techosyn Model 8200 Mark II instrument mounted on a Nikon microscope). Thin sections were impregnated with a fluorescent resin, which allowed an improved identification of pores through a 12V/100W fluorescent light source mounted onto the Leica microscope.

3.2.4. Computed tomography

Computed tomography (CT) has been performed on large cores (diameter of ± 9 cm) and small plugs (diameter of ± 3.3 cm) to allow internal 3D visualization and description of pore types and pore connectivity. The obtained images help to bridge the important gap between 2D observations from petrography and petrophysical data from plug measurements (see section 3.2.5). Medical CT has been performed on large cores to allow a fast overview of pore networks at relatively low resolutions (voxel size of 230*230*500 µm). A total amount of 25 cores were scanned in a Siemens SOMATOM Definition Flash scanner at the university hospital in Leuven (UZ Leuven) in collaboration with Dr. Ir. Steven Claes. The X-ray beam of the scanner was set at 120 kV. Microfocus CT was performed on 14 small plugs in order to create high resolution images (voxel size of 16*16*16 µm). Scanning at 90 kV was performed by Drs. Nick Janssens with a GE Phoenix nanotom scanner at the Department of Metallurgy and Materials Engineering from KU Leuven. The obtained CT images were segmented in Matlab R2017a using hysteresis thresholding, after which pore networks were reconstructed and labeled using Avizo Fire 7.0 software. CT-based porosity values (see Appendix III) were calculated from segmented images based on pixel counting in Matlab. The obtained porosity values are compared with petrophysical data from plug measurements (see Appendix IV).

3.2.5. Petrophysical measurements

The porosity of small plugs (diameter of ± 3.3 cm) was measured through both helium (He) porosimetry and water saturation (WS) measurements. He porosimetry was performed by PanTerra Geoconsultants B.V. (The Netherlands) on 42 plugs. The porosity for each plug was determined by direct measurements of grain and bulk volume. Grain volume was measured trough helium expansion in a porosimeter. A reference cell with known volume is charged with helium at a pressure of ± 6.9 bar, which is then expanded into a sample chamber containing the plug. Bulk volume was calculated based on the length and diameter of the plug. WS measurements were performed at KU Leuven on 132 plugs. The plugs were saturated with water in a desiccator under vacuum conditions (< 2 mbar) for 24 hours. Measurements of the dry weight, wet weight and saturated weight of the plugs allowed to calculate their effective porosity (cfr. Crain, 2011). Porosity data displayed in this chapter are always accompanied by information on how the data have been obtained (He or WS porosity). Gas permeability measurements were performed on 42 plugs by PanTerra Geoconsultants B.V. using a nitrogen permeameter. Permeability values were corrected for gas-slippage by applying an empirical Klinkenberg (EK) correction. An overview of all petrophysical data, complemented by CT-based porosity values, can be found in Appendix III. A comparison between He porosimetry and WS measurements is provided in Appendix IV. In order to test for significant variation between the petrophysical properties of several groups (e.g. the porosity of different dolomite textures), one-way analysis of variance (ANOVA) has been performed using Matlab R2017a. When the obtained p-value is smaller than 0.05, the null hypothesis of the ANOVA analysis (i.e. there is no significant variation) can be rejected. This implies that the variation between two groups is significant.

3.2.6. Image analysis

The porosity of rocks can also be assessed based on 2D-image analysis of pixel color and brightness on photographs or photomicrographs. Photographs of outcrops and samples were captured during

fieldwork or following sample processing at KU Leuven, and photomicrographs were taken using a camera mounted on the Leica DM LP microscope. Image analysis only provides a 2D analysis of petrographic images, but is a cost-effective and fast technique to get an estimation of the porosity. JMicroVision software (Roduit, 2007) was used for image analysis.

3.3. Key outcrops and their stratigraphy

The three key outcrops on which this chapter is based have been selected because of the contrasting geometries and characteristics of their HTD geobodies. These geobodies are excellently exposed along road sections and/or easily accessible on mountain sides. The general subvertical bedding of the successions in the Bodón Unit results in clear transect views which allow a detailed visualization both during fieldwork as well as on satellite images. This section introduces the key outcrops, of which the locations have been indicated on figure 2.4 in chapter 2, and describes their stratigraphic framework. A general stratigraphic column of the Paleozoic successions in the Bodón Unit can also be found in chapter 2 (figure 2.2). Section 3.7 will focus on the geometry and associated distribution of matrix porosity of the dolomite geobodies exposed in each key outcrop.

3.3.1. Key outcrop 1 (KO 1)

The first key outcrop covers an area of approximately 2 km² in the central part of the Bodón Unit (figure 2.4) and encompasses Upper Paleozoic successions starting with the Upper Devonian Ermita Fm., followed by the Carboniferous Vegamián, Alba, Barcaliente and Valdeteja Fm. (figure 3.1). The southern boundary of the outcrop is the diachronic contact between the Valdeteja Fm. and the overlying San Emiliano Fm. The western boundary is a WNW-ESE oriented valley draining the Río Bernesga at a nearly constant altitude of 1200 m. An important regional road (N-630) and a rail road connecting the cities of Oviedo and León run through the valley and provide an excellent road section of both the Barcaliente and Valdeteja Fm. The eastern boundary is a NE-SW oriented valley draining the small Arroyo de Millaró stream and connecting the village of Millaró de la Tercia with the regional road N-630. The small road climbing to Millaró de la Tercia (at an altitude of 1385 m) provides an exceptional road section of the entire Carboniferous succession. The Alba Fm. and lower part of the Barcaliente Fm. are excavated in quarries in the eastern (Millaró quarry; MQ) and western (Los Chábanos quarry; LCQ) parts of the outcrop (figure 3.1). On the outcrop itself, the carbonate successions are partly exposed and partly covered with soil (e.g. figure 2.3E). Since the sedimentological and stratigraphic framework of KO 1 has not been addressed in previous studies, a brief overview of fieldwork and petrographic observations is provided below (section 3.3.1.1). This descriptive overview is largely based on log data (see figure 3.1 for the exact locations of the logged sections). The depositional and sedimentological interpretation of the successions have been established based on these observations, and on a literature study of similar Carboniferous successions elsewhere in the Bodón Unit and the CZ (section 3.3.1.2).

3.3.1.1. Fieldwork and petrographic observations

The Upper Devonian Ermita Fm. is exposed in and above the MQ (figure 3.2A), and in the LCQ (figure 2.3B). On the outcrop, the presence of the Ermita Fm. is locally indicated by a subtle topographic high and the rare occurrence of small exposures. Its thickness ranges from 7 m in the MQ to 3 m in the LCQ. The Ermita Fm. is composed of sandstones, locally containing numerous

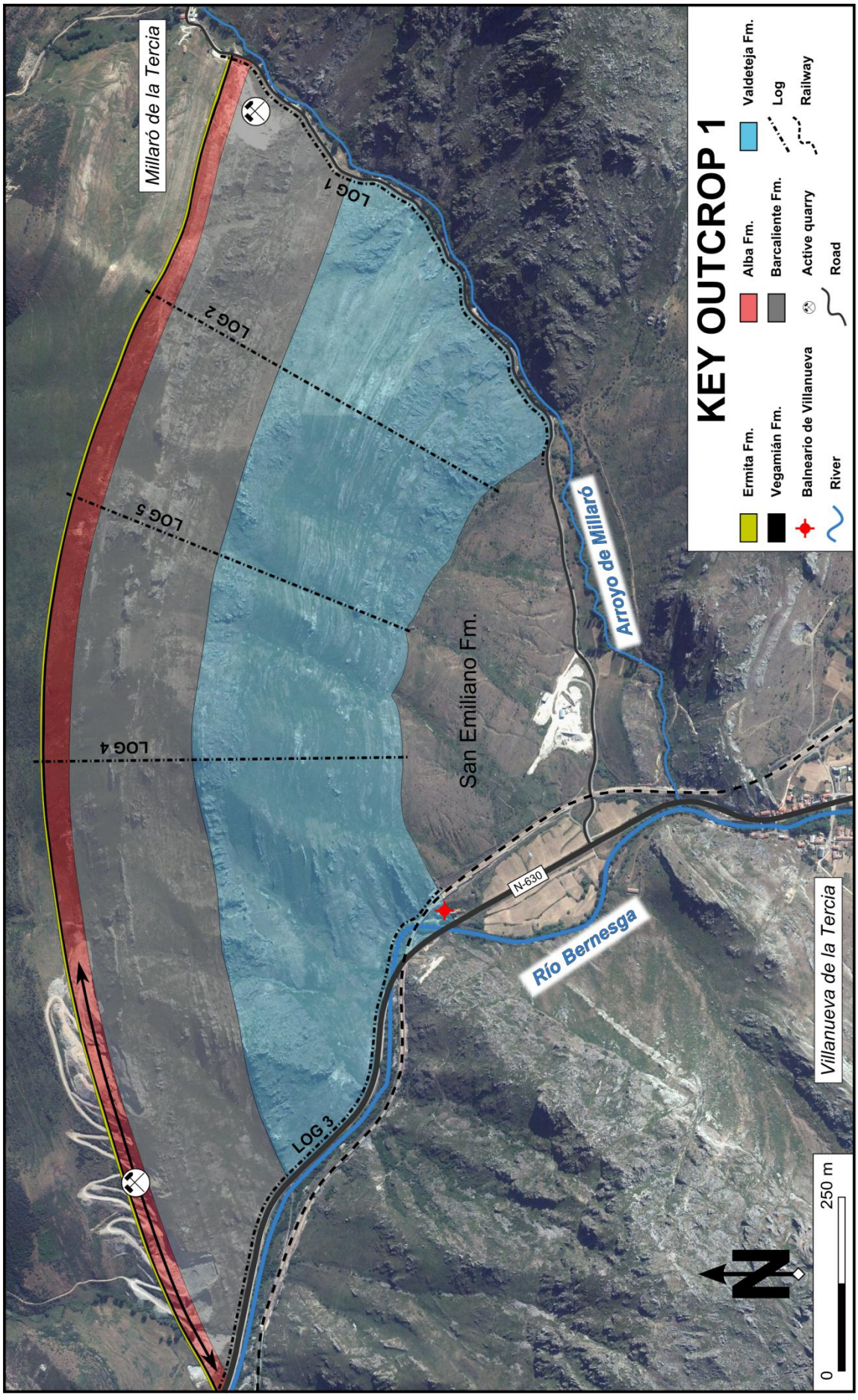

Figure 3.1: Satellite image of KO 1 with indication of the important Upper Paleozoic formations, villages, main roads and streams. The stratigraphic sections which have been logged are indicated. Logs 1 and 3 correspond to the stratigraphic sections exposed along the Millaró RS and Los Chábanos RS, respectively.

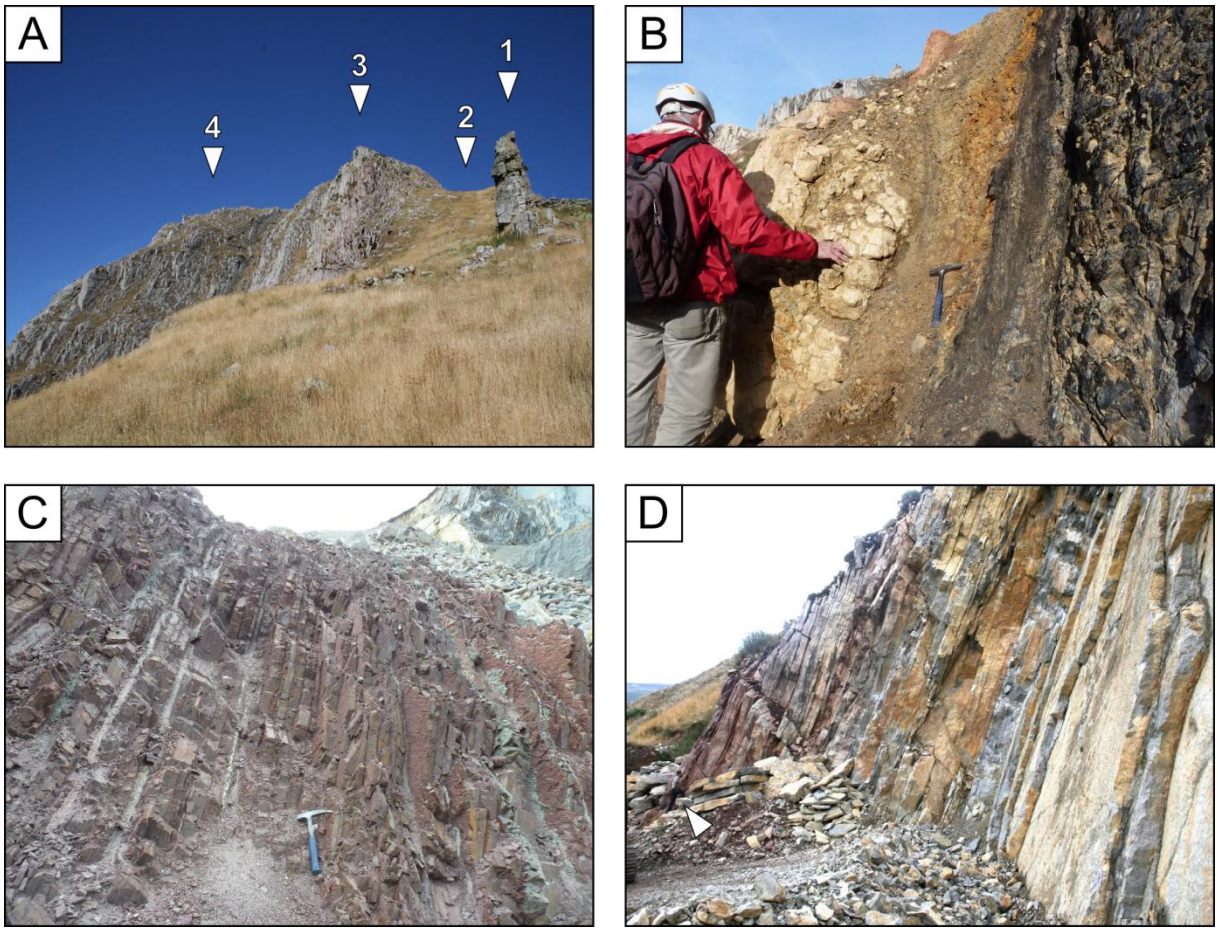

Figure 3.2: Upper Devonian and Lower Carboniferous successions in KO 1. **(A)** Exposure of Upper Devonian and Lower Carboniferous successions 400 m west of the MQ. From north to south: (1) Ermita Fm., (2) depression corresponding to the eroded Vegamián Fm. and the eroded lower and middle members of the Alba Fm., (3) third member of the Alba Fm. and (4) Barcaliente Fm. The exposed Ermita Fm. has a thickness of approximately 4 m. **(B)** Exposure in the MQ showing Vegamián shales (right) grading into beige nodular limestones of the first member of the Alba Fm. (left). **(C)** Thinly bedded chert layers of the middle member of the Alba Fm. exposed in the LCQ. Hammer for scale (32 cm). **(D)** Exposure of the upper member of the Alba Fm. (left) grading into the Barcaliente Fm. (right) in the LCQ. Person for scale on the left (white arrow).

bioclast molds, with a conglomerate basal level. The Lower Carboniferous Vegamián Fm. is intensely eroded and forms topographic lows within the outcrop (figure 3.2A). It is only exposed in both quarries (figures 2.3B & 3.2B), where it has a thickness of 2.5 (MQ) to 4 m (LCQ). The first member of the overlying Alba Fm. is composed of 3 m (MQ and LCQ) of beige to red nodular limestones (figure 3.2B), while the second member is composed of 6.5 (MQ) to 9 m (LCQ) of thinly bedded chert layers (figure 3.2C). Both first and second members are only exposed in the quarries, and are weathered on the outcrop (figure 3.2A). The third member is composed of 25 (LCQ) to 32 m (MQ) of red to gray limestones representing a gradual transition towards the overlying Barcaliente Fm. (figures 2.3C & 3.2D). The latter is exposed along both road sections, in the quarries, and on the outcrop itself. It has a thickness of 280 m along the Millaró road section increasing to 350 m along the Los Chábanos road section. The Barcaliente Fm. is made up of well-bedded dark mudstones with very little fossil content (figure 2.3D).

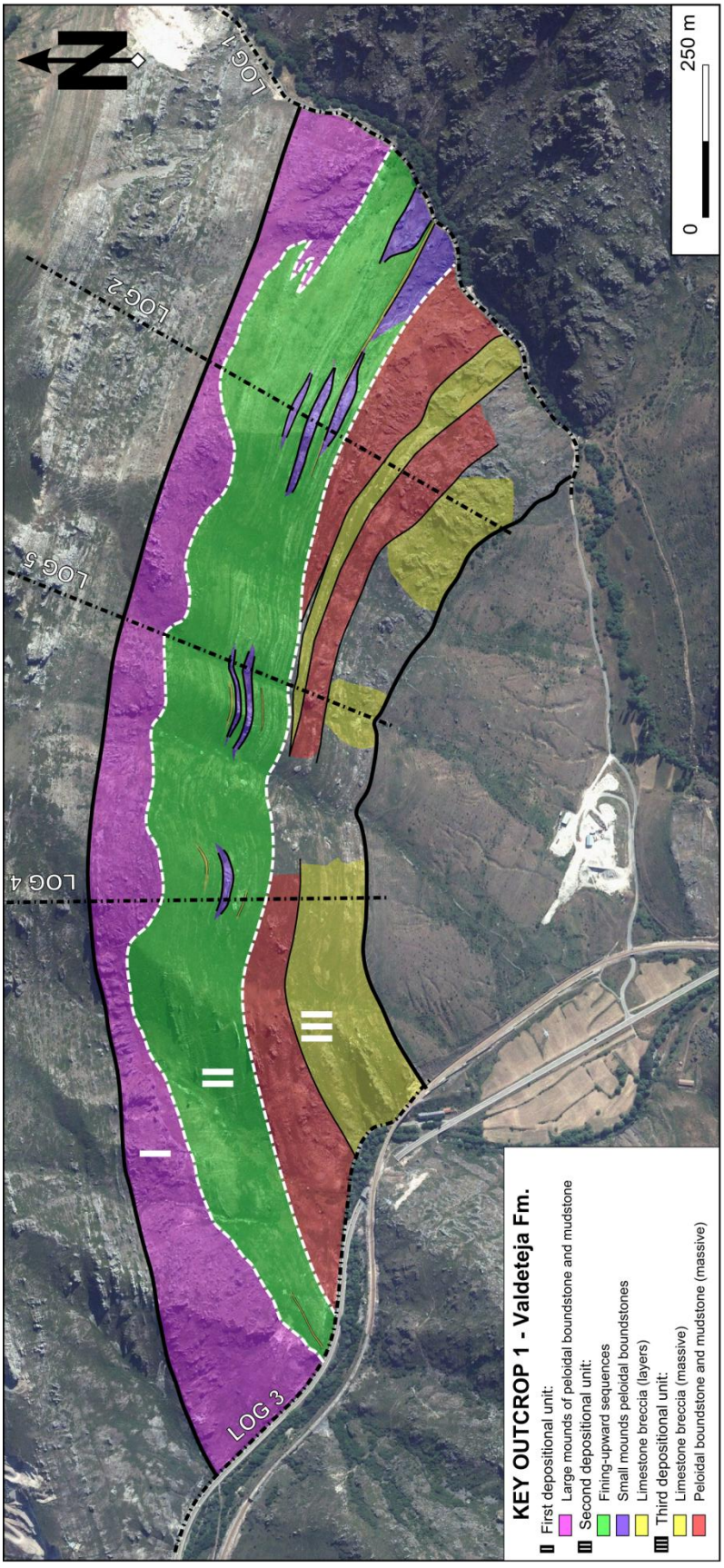

Figure 3.3: Satellite image of KO 1 with indication of stratal patterns and internal structure of the Valdeteja Fm. in KO 1. Based on fieldwork and petrography, the different depositional units have been highlighted.

The stratigraphic framework and internal structure of the Valdeteja Fm. in KO 1 are more complex compared to the Alba and Barcaliente Fm. Satellite images indicate that the Valdeteja Fm. has an irregular thickness, which is confirmed based on log data (see Appendix I). Its thickness approaches 770 m along the Millaró and 650 m along the Los Chábanos road section, but decreases to 480 m in the central part of the outcrop. Stratal patterns are clearly visible on satellite images and indicate a sequence of (1) a first depositional unit composed of large mounds, overlain by (2) a second depositional unit composed of well-bedded deposits with local occurrence of smaller mounds and (3) a third depositional unit made up of massive carbonate wedges along both road sections which pinch out towards the central part of the outcrop (figure 3.3).

The first depositional unit, made up of large mound-like structures, occurs directly on top of the Barcaliente Fm. and has a very irregular thickness (figure 3.3). The mounds are up to 250 m thick along both road sections and pinch out towards the central part of the outcrop, where they locally increase in thickness up to 100 m. The entire first unit is dolomitized, which makes it very hard to discriminate depositional facies or internal sedimentary structures, as they are obliterated. The mounds are characterized by steeply dipping flanks and a lack of obvious frame-building organisms such as corals. Based on the few stratal patterns and bedding surfaces recognizable within the mounds (figure 3.4A), it seems that they are composed of an amalgamation of smaller coalesced buildups. These buildups are characterized by pink (figure 3.4A) to white colors (figure 3.4B) upon dolomitization, and the local presence of large pores (figure 3.4A). In several samples of these buildups, sponge spicules have been observed, although they are often (partly) dissolved leaving behind molds. Deposits of dolomitized mudstone occur in between the porous deposits.

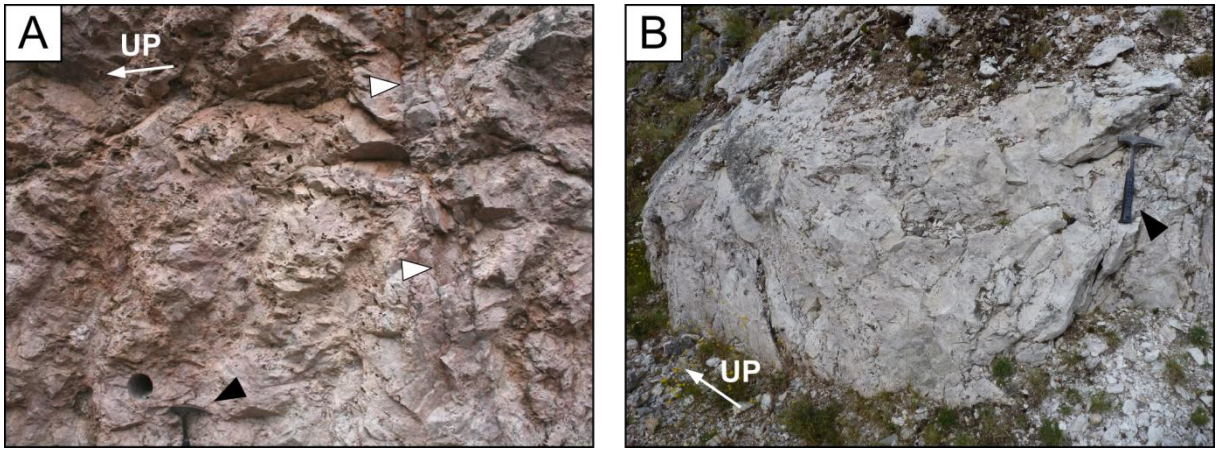

Figure 3.4: Outcrop photographs of the first generation of mounds in the Valdeteja Fm. of KO 1. **(A)** Massive dolomitized deposits exposed along the Millaró road section. They are porous and characterized by a typical pink color. In this particular exposure, a few bedding planes are present (white arrows). Hammer for scale (32 cm; black arrow). **(B)** Example of massive white dolomite, exposed along the Millaró road section. Hammer for scale (32 cm; black arrow).

The second depositional unit is composed of well-bedded carbonates characterized by subvertical bedding planes (figure 3.5A) and the local occurrence of small buildups (figure 3.3). The well-bedded carbonates represent numerous fining-upward sequences made up of bioclastic grainstone (with local levels of rudstone) evolving into wackestone or mudstone (figures 3.5B &

C). Bioclasts include echinoderm, brachiopod and gastropod fragments. Silicified bioturbations are often observed in these deposits (figure 3.5D). Locally, exposed layers of fine-grained siliciclastics can be found in between the carbonate sequences (figure 3.5E), as well as layers up to a few m thick composed of calcareous limestone breccia (figure 3.3).

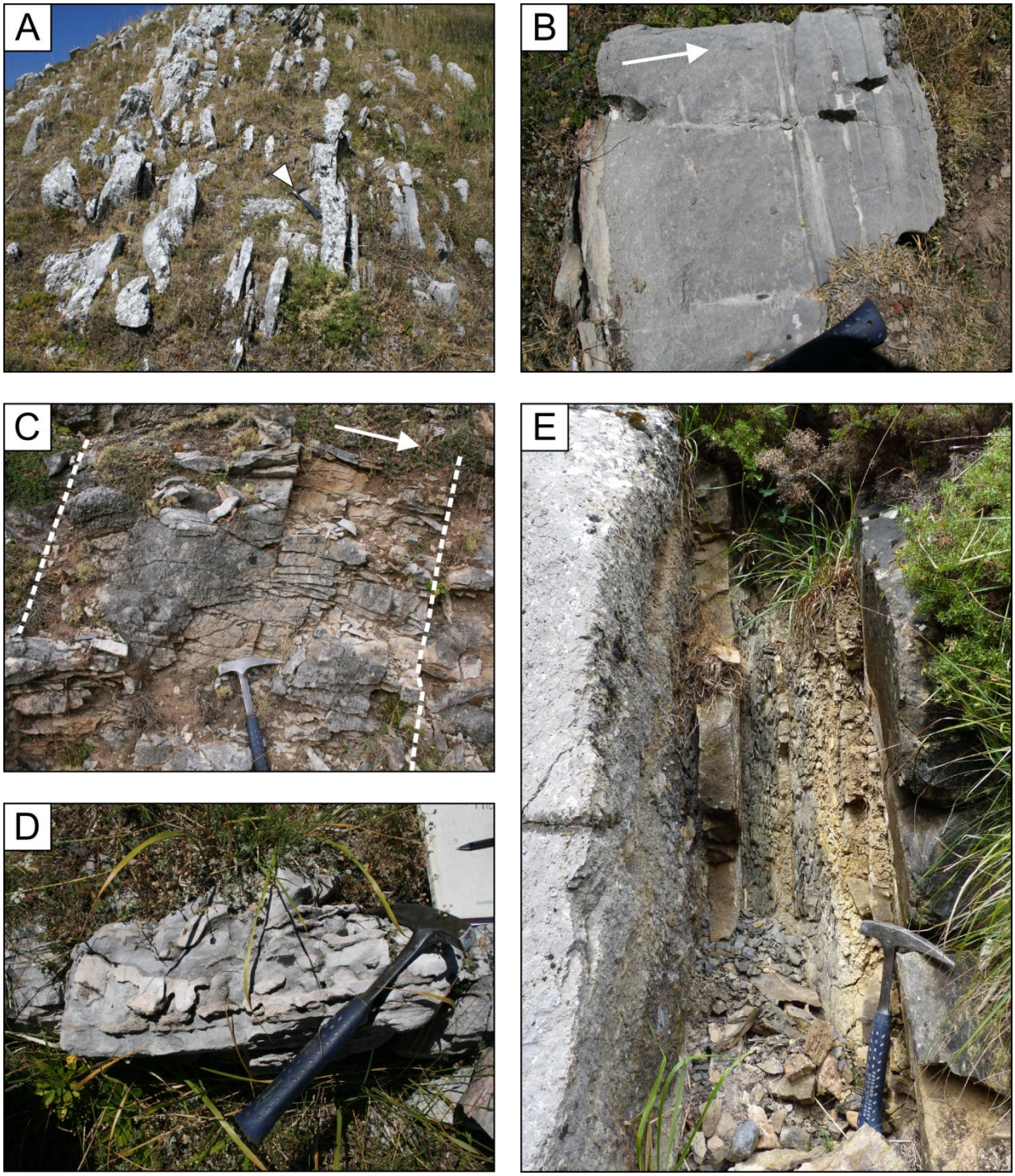

Figure 3.5: Outcrop photographs of well-bedded carbonates in KO 1. Hammer for scale (32 cm). **(A)** Exposure of bedded successions on top of the outcrop. Hammer for scale (32 cm; white arrow). **(B)** Example of a fining-upward sequence made up of pack- to rudstone (left) evolving into mudstone (right). Top of the outcrop. **(C)** Example of a dolomitized fining-upward sequence along the Los Chábanos road section. **(D)** Silicified bioturbations in a fine-grained bed. Top of the outcrop. **(E)** Exposure of finely laminated silt- and claystones in between carbonate beds along the Millaró road section.

Numerous small carbonate buildups occur in the fining-upward successions (figures 3.3 & 3.6A). These buildups are a few to 15 m thick and most of them resemble massive structureless beds (even though they have not been dolomitized) in between the bedded successions (figure 3.6B). Clear mound geometries with dipping flanks are only recognizable in the larger buildups (e.g. figures 3.6A & B). The buildups are composed of tight peloidal micrite-rich boundstones with *Donezella* (a characteristic carbonate mound builder during the Carboniferous; Choh and Kirkland, 2006), brachiopod, coral, sponge and foraminifera fragments. Abundant relics of fibrous cements occur in the boundstones (figure 3.6C), which indicate that they possessed a high primary porosity.

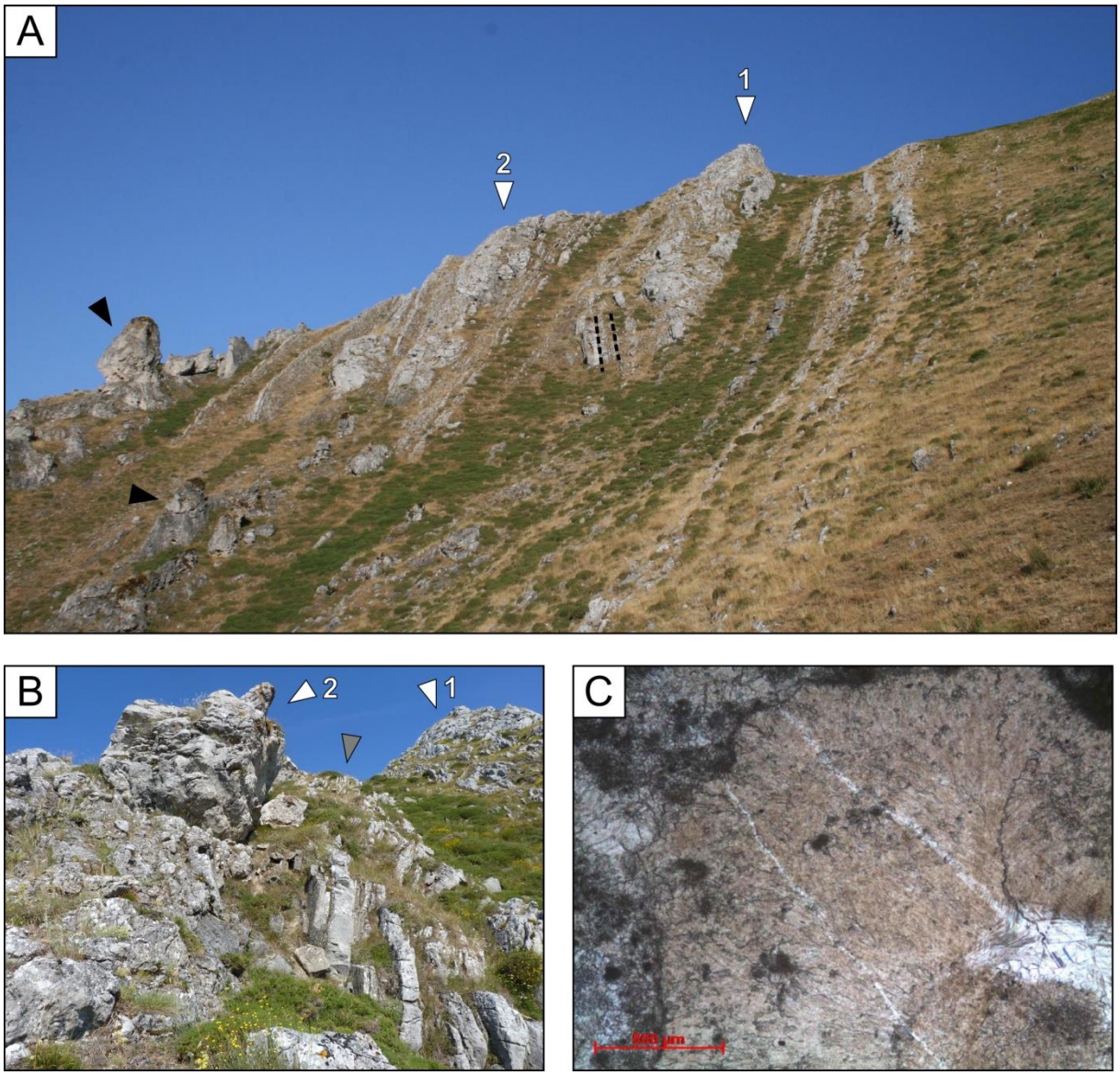

Figure 3.6: Outcrop and thin section photographs of small buildups in between the bedded carbonates of KO 1. **(A)** Two buildups (white arrows) exposed in between bedded successions 400 m west of the Millaró road section. Beds making up the flank of the lower buildup are indicated with black dashed lines. Black arrows indicate dolomitized successions. The two buildups are also visible in the upper left corner of figure 2.3E, where their size can be compared to the size of the larger mounds of the first depositional unit. **(B)** Detailed photograph of the bedded substrate of the second small buildup from figure A. The beds are approximately 20 to 30 cm in thickness (gray arrow). Both buildups from figure 3.6A are indicated with white arrows. **(C)** PP photomicrograph of brown fibrous cements filling a primary cavity in boundstone derived from the core of the second buildup of figures 3.6A and B. The fibrous cements have been neomorphosed but are still recognizable. Note the secondary blocky calcite cement filling the remaining pore space (right).

The massive carbonate wedges making up the third depositional unit of the Valdeteja Fm. in KO 1 (figure 3.3) are composed of carbonate mounds, thick packages of limestone breccia and local levels of grain- to rudstone. As these successions grade into each other and are almost entirely dolomitized, it is difficult to delineate stratal patterns or facies changes both on satellite images or during fieldwork. The carbonate mounds resemble those making up the first depositional unit of the Valdeteja Fm., with pink to white colors and the omnipresence of large irregular pores. In several locations on the outcrop, the paleosurface of the mounds in the third depositional unit can be recognized (figures 3.7A & B). The packages of limestone breccia are thick deposits of matrix-free breccias (figures 3.7C & D). Individual clasts are relatively large and have dimensions of a few cm to several dm (figure 3.7D).

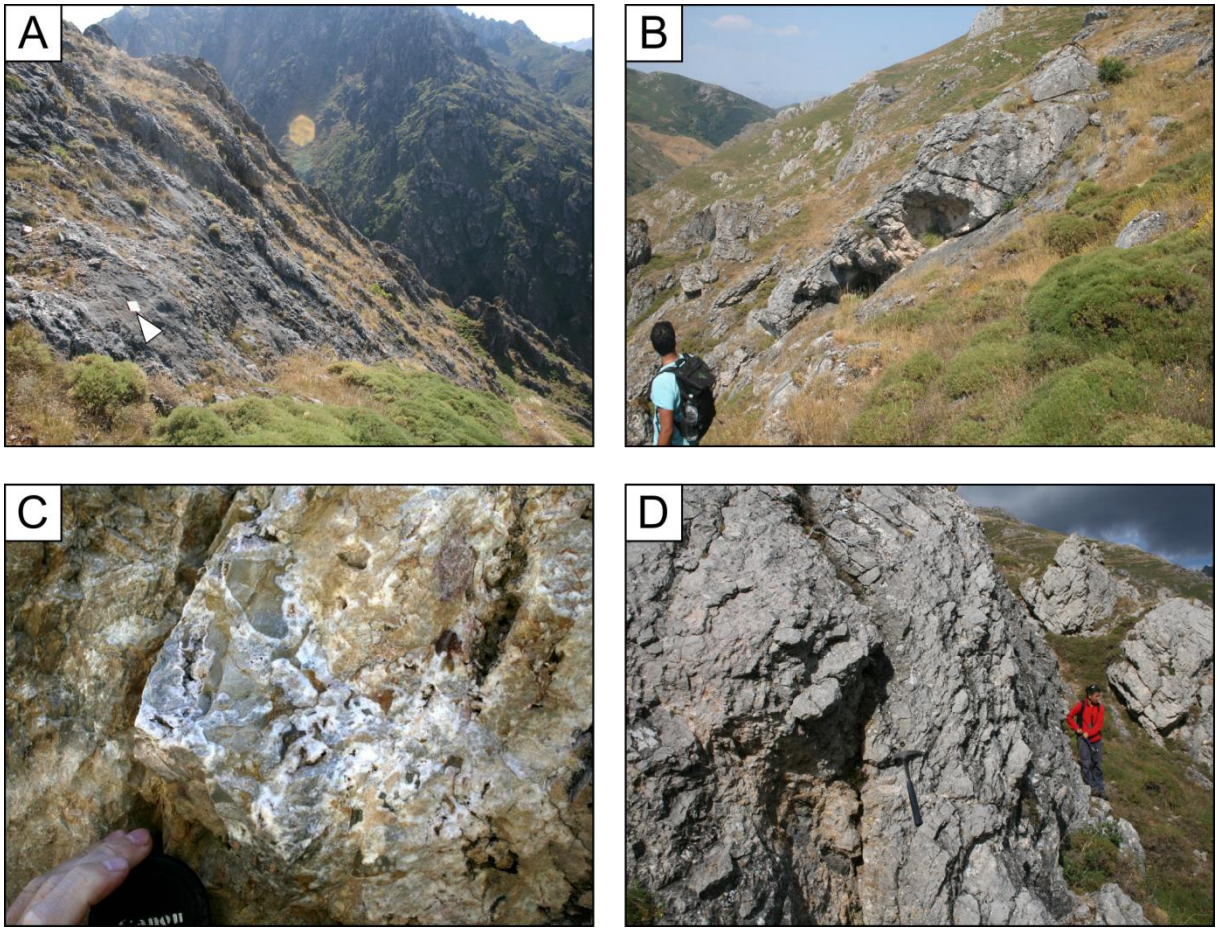

Figure 3.7: Massive carbonate wedges composed of carbonate mounds and limestone breccia in KO 1. **(A)** Large exposed paleosurface of a carbonate buildup in depositional unit three. Notebook for scale (20 cm; white arrow). **(B)** Smaller exposed paleosurface of a buildup. **(C)** Exposure of dolomitized limestone breccia along the Millaró road section. **(D)** Thick deposits of undolomitized limestone breccia on top of the outcrop. Hammer for scale (32 cm).

3.3.1.2. Depositional and sedimentological model

The stratigraphic and petrographic observations of the Ermita, Vegamián and Alba Fm. in KO 1, described in section 3.3.1.1, largely correspond to the results of previous studies on these successions in other exposures in the Bodón Unit (e.g. Wagner et al., 1971; Eichmüller, 1986). Only the thickness of formations tend to be variable throughout the Bodón Unit (e.g. the Ermita Fm.; Comte, 1959). These early Carboniferous successions have been interpreted as resulting from a sea level rise followed by a gradual transition to thick carbonate successions filling the Variscan foreland basin (i.e. the Alba, Barcaliente and Valdeteja Fm.; see section 2.3). The Barcaliente Fm. is composed of well-bedded mudstones representing a period of uniform carbonate sedimentation (see section 2.3). Breccia intervals described in the top of the Barcaliente Fm. elsewhere (e.g. the so-called Porma breccia; Dallmeyer and Martínez-García, 1990; Quijada et al., 2017) have not been observed, which might be due to the bad exposure of the top layers of the Barcaliente Fm. in KO 1.

Log data (e.g. orientation of bedding planes; figures 3.7A & B) and stratal patterns visible on satellite images (figure 3.3), indicate that the three depositional units which make up the Valdeteja Fm. in KO 1 have been deposited in an inter-platform basin in between high-relief carbonate structures which resemble flat-topped and high-relief Bashkirian carbonate platforms described elsewhere in the CZ (Kenter et al., 2002; Chesnel et al., 2015). These three depositional units likely represent 3 platform growth phases, which can be correlated with those recognized in the Bashkirian Valdorria carbonate platform studied by Chesnel et al. (2015) in the southeastern part of the Bodón Unit (see section 3.3.2).

The first depositional unit of the Valdeteja Fm. in KO 1 is likely similar to mounded structures described in the Valdorria platform (Chesnel et al., 2015), and to mounds exposed in platform successions in the Central Coal Basin (Samankassou et al., 2013). These latter structures have not (or only locally) been dolomitized and are made up of microbial boundstone dominated by peloidal and clotted micrite. Stromatactis-like cavities are omnipresent in these boundstones and although they are completely occluded, they must have produced primary porosities up to 40 % (Bahamonde et al., 2014; Chesnel et al., 2015). These cavities have been interpreted as biomoldic porosity resulting from corrosion of calcareous substrate triggered by changes in pH and action of organic acids derived from degradation of siliceous sponges. The peloidal textures are the result of calcification of siliceous sponge bodies (Bahamonde et al., 2014). The symbiosis between carbonate-precipitating microbes and siliceous sponges was widespread in Variscan foreland basins during the Upper Paleozoic (Brunton and Dixon, 1994; Wood, 1999). The carbonate mounds making up the third depositional unit in KO 1 likely have a similar origin.

The fining-upward sequences, typical for the second depositional unit, have been reported in several Pennsylvanian platforms elsewhere in the CZ. They have been interpreted as calciturbidites deposited in inter-platform basins and representing storm-triggered turbidity currents (Bahamonde et al., 2007, 2014, 2015). The small carbonate buildups in between the calciturbidites are potentially smaller equivalents of the larger mounds making up the first depositional unit. Similar small buildups have been described in a Pennsylvanian mixed terrigenous-carbonate ramp in the Central Coal Basin (Samankassou et al., 2013). The shape, size

and growth dynamics of these small buildups were mainly influenced by pre-existing paleohighs, sea-level fluctuations and episodic siliciclastic input.

The limestone breccias making up the third depositional unit in the Valdeteja Fm. of KO 1 resemble deposits of synsedimentary breccia. Similar breccias have been reported in other platform settings in the CZ have been interpreted as gravitational rock-fall deposits resulting from a collapse of depositional topography (Della Porta et al., 2003), potentially resulting from a major sea level fall.

3.3.2. Key outcrop 2 (KO 2)

The second key outcrop is a smaller outcrop (± 0.15 km² in area) located in the southeastern part of the Bodón Unit (figure 2.4), just north of Nocedo de Curueño. Key outcrop 2 (KO 2) represents part of a N-S oriented valley (figure 3.8), drained by the Río Curueño, cutting through the spectacular Valdorria carbonate platform (Valdeteja Fm.; figure 3.9). The Valdorria carbonate platform is a 14 km wide Pennsylvanian flat-topped and high-relief carbonate platform almost entirely exposed (figure 3.9A; Chesnel et al., 2015). The platform nucleated on top of the well-bedded mudstones of the Barcaliente Fm., but the platform limestones belong to the Valdeteja Fm. The Valdorria carbonate platform represents part of the northern fold limb of a large south-verging syncline, referred to as the Montuerto Syncline (Evers, 1967). The Montuerto Syncline formed as a result of multiphase deformation during the Variscan Orogeny (Potent and Reuther, 2000).

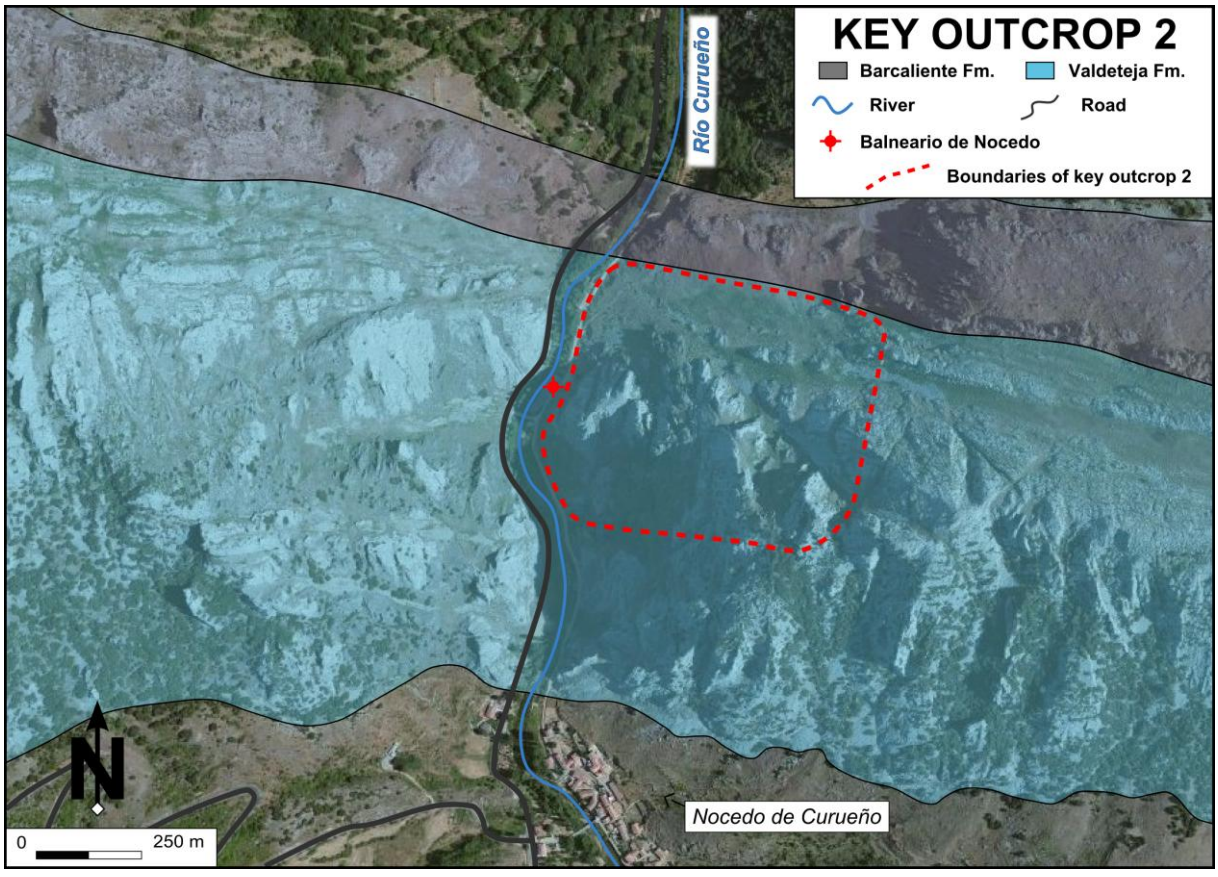

Figure 3.8: Satellite image of KO 2 on which the Barcaliente and Valdeteja Fm. have been highlighted. The town of Nocedo de Curueño, main roads and the Río Curueño stream have been indicated, as well as the location of the ancient Balneario de Nocedo (see box 4 in section 3.4.3.3).

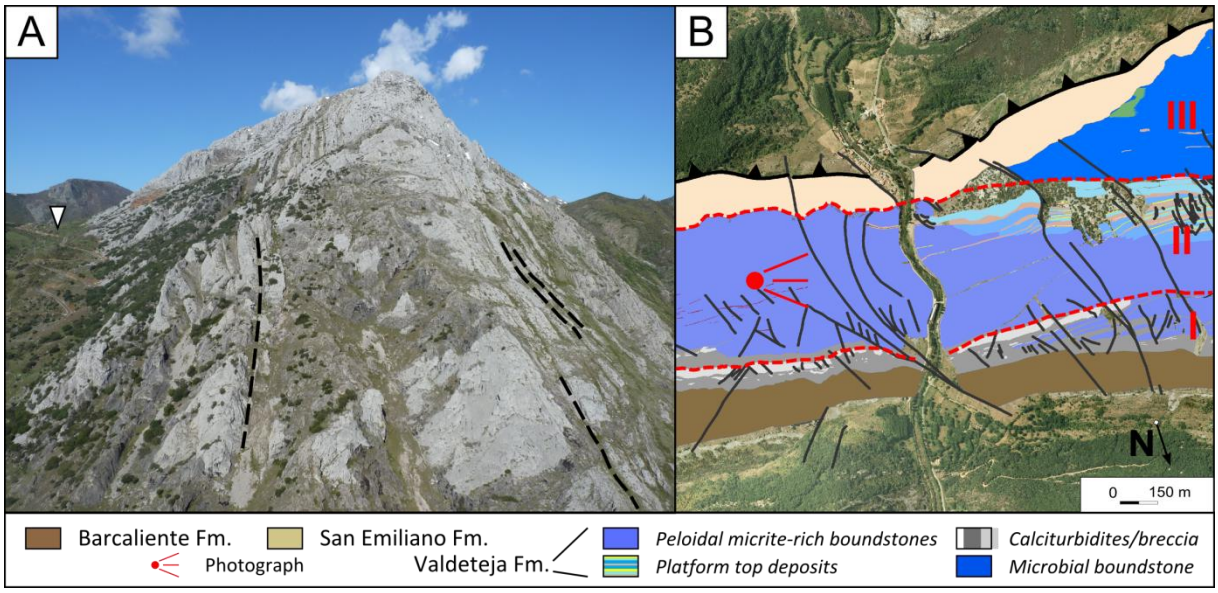

Figure 3.9: Outcrop photographs of the Valdorria platform exposed in KO 2. **(A)** Transect view of the Valdorria carbonate platform (Valdeteja Fm.) as seen from the other side of the valley. The stratigraphic top of the platform successions is on the left side of the picture. The platform limestones (light gray) have been partly dolomitized (dark gray rocks). Bedding planes have been indicated with black dashed lines. Road for scale on the left (white arrow). **(B)** Distribution of depositional facies in the Valdorria platform mapped on an aerial photograph by Chesnel et al. (2015). Red dashed lines represent major stratigraphic boundaries between the 3 major depositional units, and black lines are fractures. The underlying Barcaliente Fm. and overlying San Emiliano Fm. have been indicated.

The stratigraphic framework and sedimentological evolution of the Valdorria carbonate platform have been studied in detail by Chesnel et al. (2015). This study identified 3 platform growth phases based on laterally and vertically traceable stratal patterns (figure 3.9B). During a first (Early Bashkirian) growth phase, a 430 m thick platform to slope succession prograded over 6 km. The second growth phase (Middle Bashkirian) is characterized by progradation and aggradation, resulting in the production of prograding slope deposits and 180 m of cyclic platform top deposits. During the third growth phase (Late Bashkirian), a large mound-shaped structure, comparable to those observed in the first depositional unit of KO 1, nucleated on top of the platform top deposits. KO 2 is located in the prograding slope deposits of the second growth phase, which are almost exclusively made up of partly dolomitized peloidal micrite-rich boundstones (figure 3.9B; Chesnel et al., 2015). These boundstones have a massive field appearance (figure 3.10A), lacking bedding surfaces, similar to the boundstones observed in the carbonate buildups of KO 1. Microscopically, they are made up of peloidal micrite cemented with blocky calcite (figure 3.10B). The fossil content includes crinoid fragments (figure 3.10B) and in situ *Donezella* algae (Chesnel et al., 2015). The boundstones are rich in recrystallized sponge spicules, which occur as euhedral elongated quartz crystals. The boundstones have been formed by in situ precipitation of peloidal micrite and microbial crusts, and rapid early cementation. They have been interpreted as slope boundstones, forming clinoforms of the prograding second growth phase of the Valdorria platform (Chesnel et al., 2015).

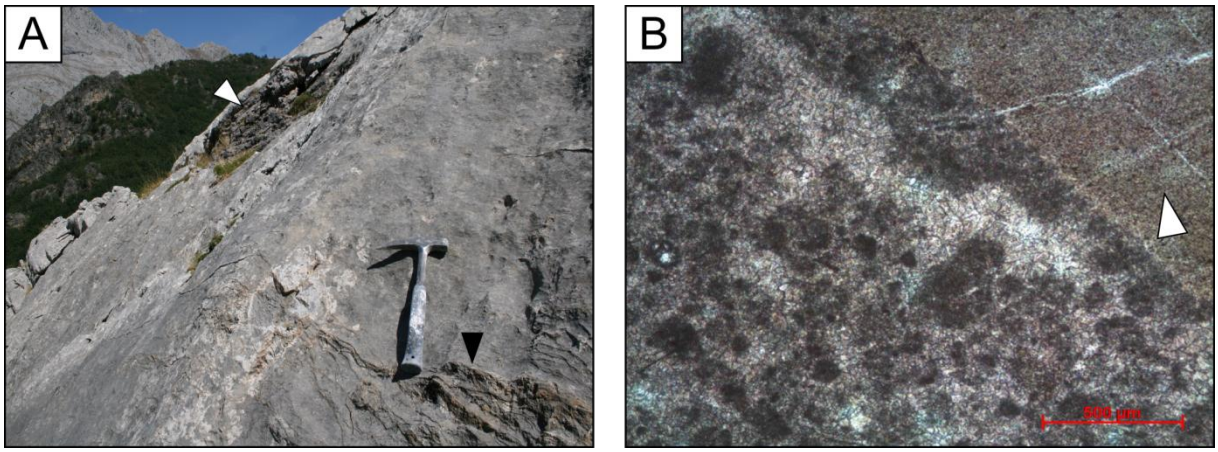

Figure 3.10: Outcrop and thin section photographs of peloidal micrite-rich boundstones in KO 2. **(A)** Field appearance of massive boundstones making up the prograding slope deposits of growth phase 2 in the Valdorria platform of KO 2. The boundstones on this photograph have been partly dolomitized (white arrow). Swarms of dolomite veins cut through the boundstones (black arrow). Hammer for scale (32 cm). **(B)** PP photomicrograph of boundstone showing a peloidal texture and an echinoderm fragment (white arrow).

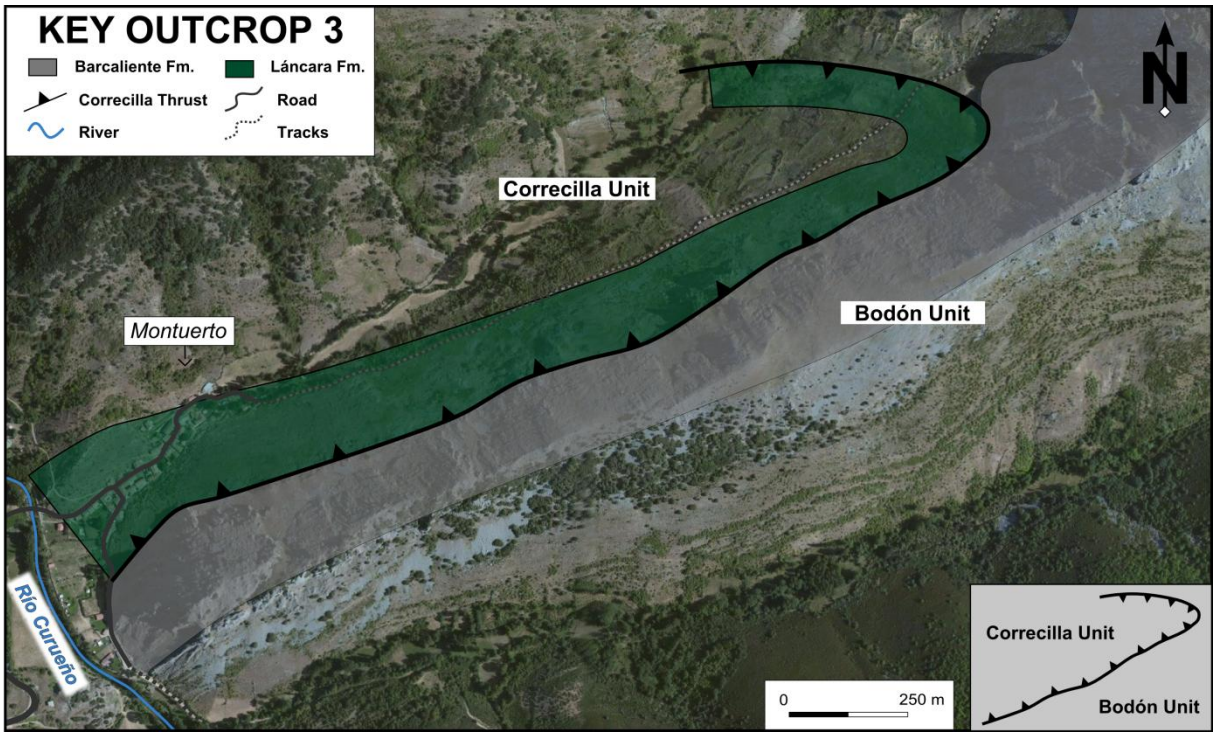

Figure 3.11: Satellite image of KO 3 on which the Cambrian Láncara and Carboniferous Barcaliente Fm. have been indicated as well as the fault trace of the important Correcilla Thrust. The village of Montuerto, main roads and tracks and the Río Curueño stream are indicated. Inset in the lower right corner of the figure shows a geodynamic sketch.

3.3.3. Key outcrop 3 (KO 3)

The third key outcrop (KO 3) is located close to the second outcrop, in the southeastern extremity of the Bodón Unit (figure 2.4). It is exposed on the N-oriented mountainside south of the village of Montuerto, and covers an area of approximately 0.4 km² (figure 3.11). The outcrop is part of the southern fold limb of the Montuerto Syncline (see section 3.3.2; Potent and Reuther, 2000). On the mountainside, the tectonic fault breccia of the Correcilla Thrust is exposed, representing a thrust contact between the Cambrian Láncara Fm. of the Correcilla Unit and the Carboniferous Barcaliente Fm. of the Bodón Unit (figures 2.1B; 3.11 & 3.12A). Exposures of the Láncara Fm. show yellow synsedimentary dolomite (figure 3.12B) as well as gray limestone (both belonging to the lower member of the Láncara Fm.; see section 2.3) and glauconitic and red nodular limestone (both belonging to the upper member of the Láncara Fm.). The Barcaliente limestones create the topography in the southern part of the Montuerto Syncline, and are exposed along the entire mountainside (figure 3.12A). They are composed of well-bedded dark mudstones (figure 3.12C).

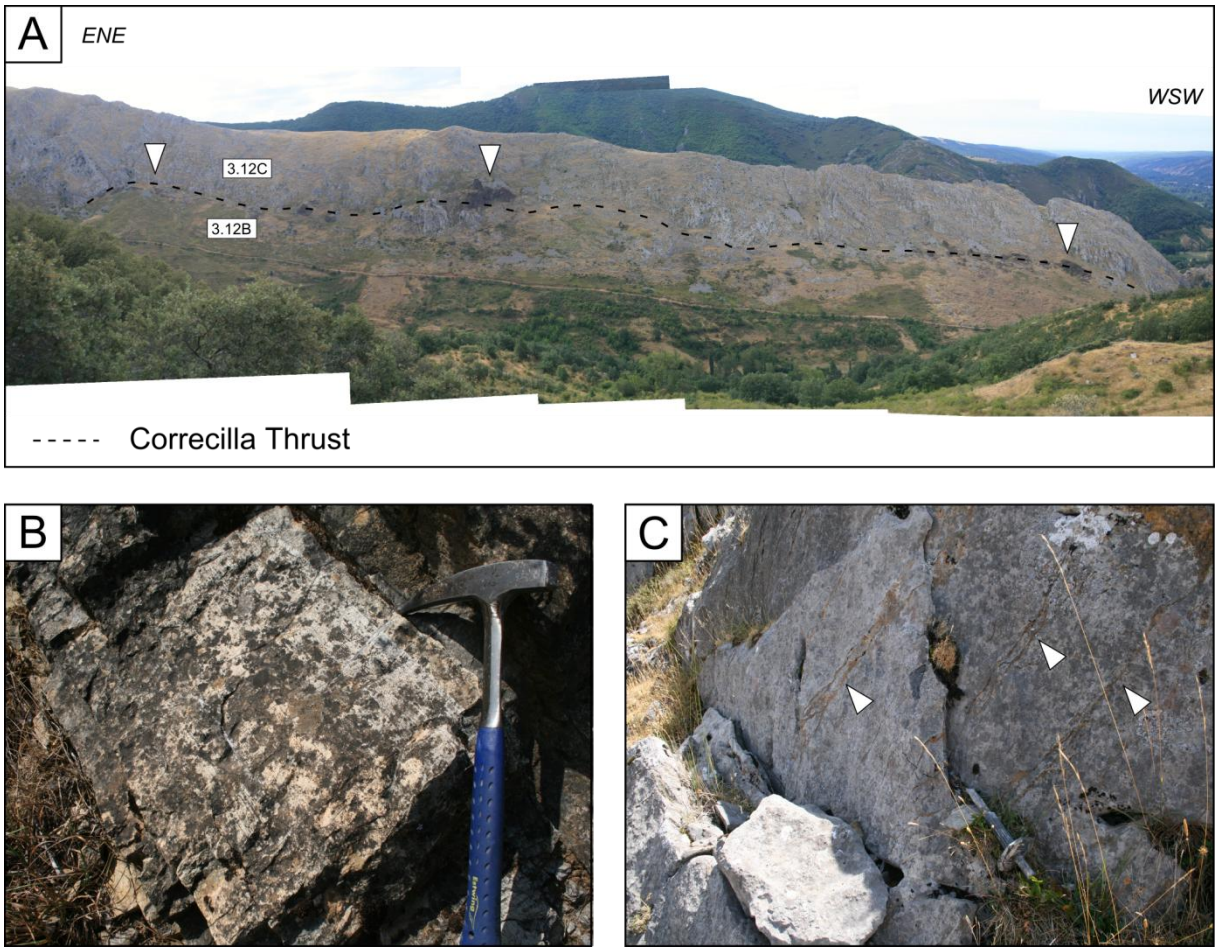

Figure 3.12: Outcrop photographs of KO 3. **(A)** Photograph of KO 3 with indication of the Correcilla Thrust and dark dolomite geobodies (white arrows) along the fault trace. **(B)** Exposure of beige synsedimentary dolomite belonging to the lower member of the Cambrian Láncara Fm. Hammer for scale (32 cm). **(C)** Exposure of gray limestones from the Barcaliente Fm., crosscut by orange dolomite veins (white arrows). Chisel for scale (25 cm).

3.4. Diagenesis

Diagenesis refers to all physical, chemical and biological processes which affect sediments after deposition and during burial until temperature and pressure reach the domain of low-grade metamorphism, or until the sediments are uplifted and exposed (Flügel, 2004). The boundary between diagenesis and low-grade metamorphism for this study is set at temperatures around 200 °C and pressures around 200 MPa. Most of the Paleozoic rocks in the Cantabrian Zone experienced diagenetic conditions, with local development of low-grade metamorphism (see section 2.4 and chapter 4). Based on field observations and a detailed petrographic study of limestone and dolomite samples collected from the three key outcrops and additional outcrops in the Bodón Unit, a paragenetic sequence of diagenetic phases has been reconstructed (section 3.4.1; figure 3.13). The paragenetic sequence is mostly based on Carboniferous limestone samples, as these form the main precursor limestones for the three important key outcrops. In section 3.4.1, each diagenetic phase is described and illustrated with outcrop photographs and thin section photomicrographs. This section has been subdivided into pre-dolomitization (section 3.4.1.1), dolomitization (section 3.4.1.2), and post-dolomitization subsections (section 3.4.1.3). The diagenetic products are then categorized and subdivided into eogenetic, mesogenetic and telogenetic processes (Choquette and Pray, 1970), and interpreted in light of the depositional history of the precursor limestones and the geodynamic history of the Cantabrian Zone (section 3.4.2; figure 3.21). A clear understanding of diagenetic processes and their products is crucial in assessing the geometry of HTD geobodies and the distribution of their petrophysical properties.

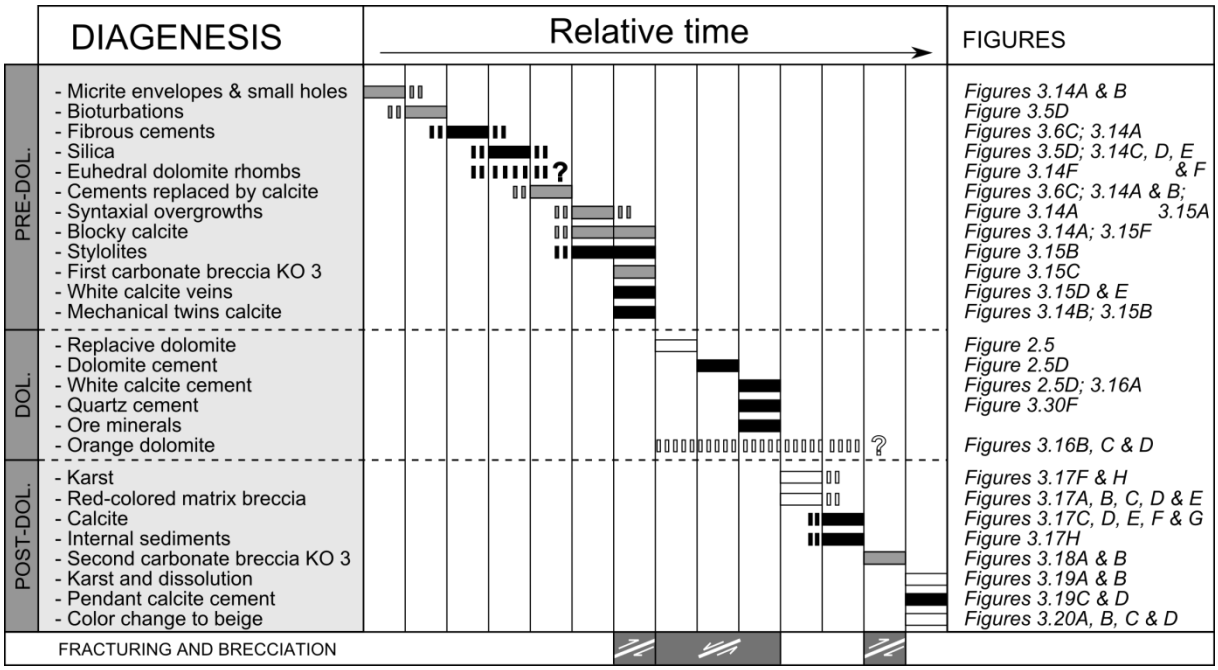

Figure 3.13: Schematic overview of the paragenetic sequence of diagenetic phases in Carboniferous limestone successions exposed in the Bodón Unit. The diagenetic phases are described in detail and illustrated in section 3.4.1. Diagenetic products increasing the porosity of the platform limestones have been indicated with white bars while porosity-destructive products have been indicated with black bars. Diagenetic phases with little effect on reservoir characteristics have been indicated with gray bars. Corresponding figures in section 3.4.1 illustrate the diagenetic products.

3.4.1. Fieldwork and petrographic observations

3.4.1.1. Pre-dolomitization

The earliest diagenetic products that have been observed occur in porous and grain-dominated Carboniferous limestones (e.g. in the Valdeteja Fm.), where bioclasts are selectively affected by micritization. Many bioclasts show relics of thin irregular micritic envelopes (figure 3.14A) and some of the clasts have been partly or completely replaced by micrite. Micritization did not affect ostracod, brachiopod, echinoderm or trilobite fragments (figure 3.14A). In the mudstones of the Barcaliente Fm., the few bioclasts present are not as intensely affected by micritization compared to bioclasts in grain-dominated facies of the Valdeteja Fm. Nevertheless, some bioclasts in Barcaliente mudstones show the occurrence of small holes filled with micrite (figure 3.14B). Calciturbidite successions in KO 1 show signs of bioturbation (figure 3.5D).

Depositional facies with high amounts of primary porosity, such as grainstones and microbial boundstones in KO 1, are affected by cementation, expressed as 2 phases of circumgranular and isopachous rims of fibrous cement (figures 3.6C & 3.14A). The cement rims themselves have been overgrown by blocky calcite and are only preserved as brown relics.

An omnipresent diagenetic product observed during fieldwork and petrography is silica. Silicified fossils were observed in numerous exposures of Valdeteja limestones and include gastropods (figure 3.14C), rugosa and syringopora corals, sponges (figure 3.14D) and bivalves, among others. Sponge spicules made up of silica occur in several depositional facies of the Valdeteja Fm. Silicified bioturbations occur in the calciturbidites of the Valdeteja Fm. in KO 1 (figure 3.5D), as well as elongated chert nodules oriented parallel to bedding surfaces. As the silica is more resistant to chemical weathering, the silicified bioclasts and nodules stick out of smooth limestone surfaces and are readily visible during fieldwork (e.g. figures 3.5D & 3.14D). Microscopic observations reveal that the different occurrences of silica are characterized by specific microtextures. Silicified bioclasts are composed of euhedral quartz crystals (figure 3.14C), while silicified bioturbations and chert nodules resemble porous layers cemented by chalcedony (figure 3.14E). In some thin sections, this pore-occluding chalcedony cement is associated with small euhedral dolomite rhombs which are never observed in non-silicified samples (figure 3.14F). The rhombs show distinctly zoned cathodoluminescence (CL) patterns, in contrast to crystals making up hydrothermal dolomite in the Bodón Unit.

The 2 phases of circumgranular and isopachous rims of fibrous cement around bioclasts are overgrown and replaced by blocky calcite which further fills primary pore space (figures 3.6C & 3.14A). Some bioclasts, such as phylloid algae (figures 3.14B & 3.15A) are replaced by blocky calcite. Cementation is complemented with syntaxial cements which occur as overgrowths on echinoderm fragments. Bedding-parallel dissolution seams in fine-grained facies such as the Barcaliente mudstones and stylolites in coarser grained limestones (figure 3.15B) crosscut bioclasts and calcite cement.

The limestone successions, occluded with calcite cement and with abundant stylolites, have been locally brecciated. The clearest example is the fault zone of the Correcilla Thrust, exposed in KO 3. The fault zone is made up of a noncohesive breccia composed of angular clasts of limestone from both the Cambrian Láncara and Carboniferous Barcaliente Fm. (figure 3.15C).

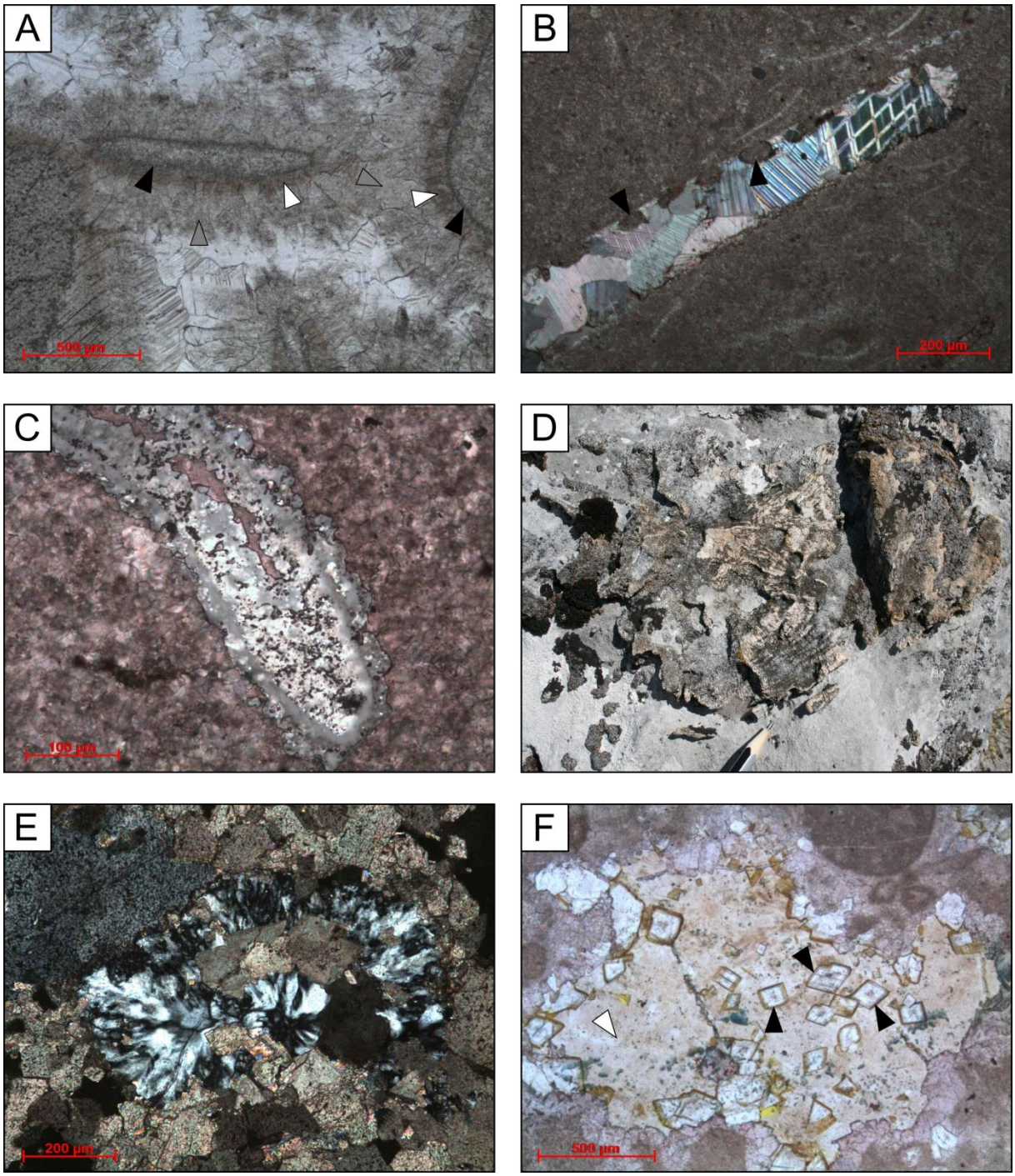

Figure 3.14: Early diagenetic products. **(A)** PP photomicrograph of thin micritic envelopes (black arrows) surrounding partly or completely micritized bioclasts. Echinoderm fragment in lower left corner is less affected by micritization. The pore space has been filled with 2 phases of circumgranular and isopachous rims of fibrous cement (white and gray arrows) and a later phase of clear blocky calcite. Syntaxial calcite cement overgrows previous cement phases in lower left corner. Grain-dominated calciturbidite sample from the Valdeteja Fm. in KO 1. **(B)** XP photomicrograph of a bioclast (likely a phylloid algal fragment) displaying small holes (black arrows). Barcaliente Fm. in KO 1. **(C)** XP photomicrograph of a silicified bioclast, likely a gastropod fragment, in fine-grained limestone from the Barcaliente Fm. in KO 1. The original bioclast has been replaced by euhedral quartz crystals. **(D)** Photograph of a silicified sponge in a small buildup from the Valdeteja Fm. in KO 1. **(E)** XP photomicrograph of a dolomitized sample from mound deposits in the Valdeteja Fm. of KO 1. The central pore is occluded with chalcedony. **(F)** PP photomicrograph of a pore filled with chalcedony (white arrow) and small euhedral dolomite rhombs (black arrows). Valdeteja Fm. north of Caldas de Luna.

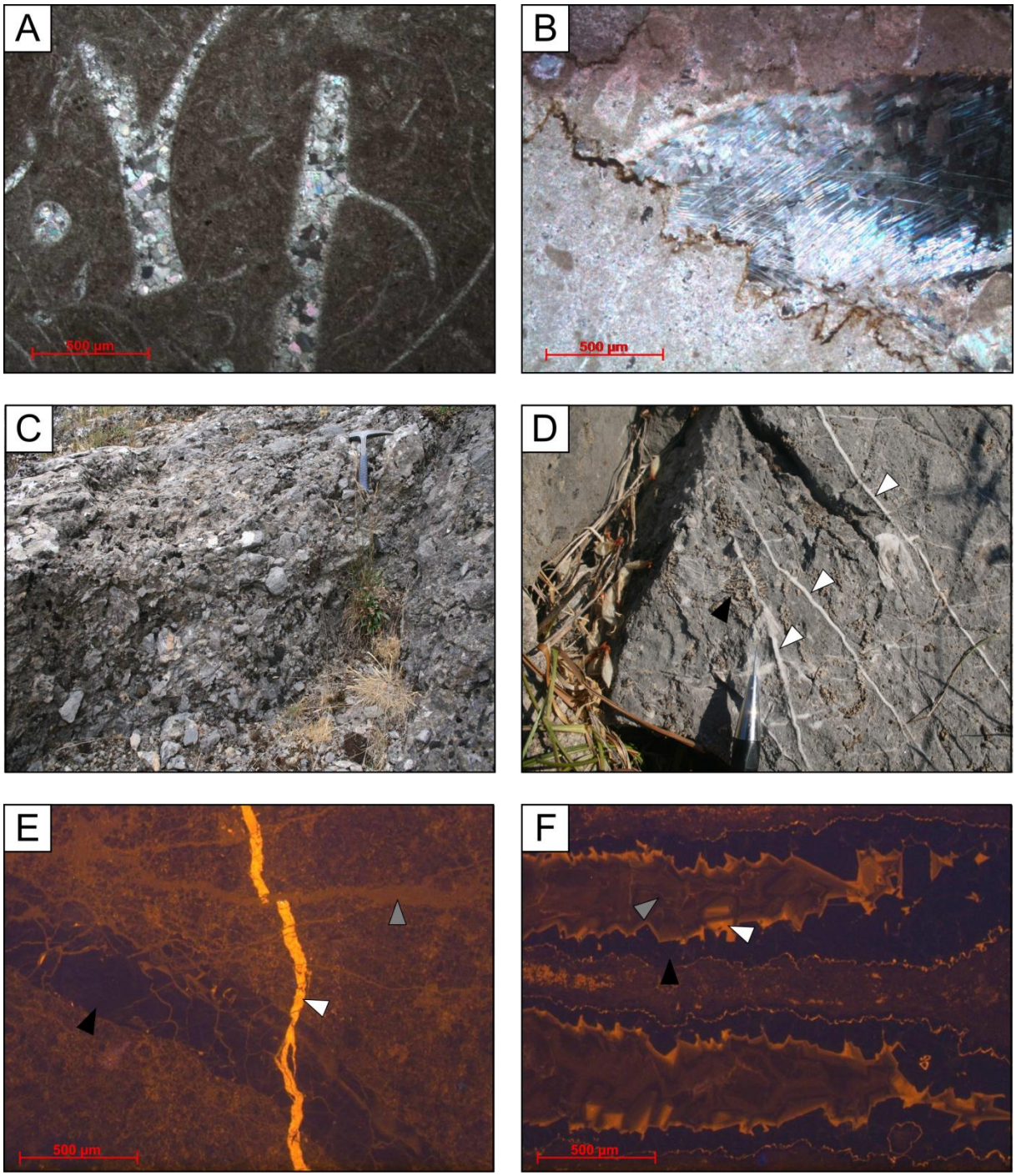

Figure 3.15: Early diagenetic products. **(A)** XP photomicrograph of phylloid algal fragments replaced by blocky calcite. Limestone sample from the Alba Fm. of KO 1. **(B)** XP photomicrograph of pressure dissolution of a brachiopod shell fragment along a stylolite in calciturbidites from the Valdeteja Fm. of KO 1. **(C)** Exposure of an undolomitized carbonate breccia along the fault trace of the Correcilla Thrust in KO 3. Hammer for scale (32 cm). **(D)** White calcite veins (white arrows) cutting through limestone with silicified coral fragments (black arrow) of the Valdeteja Fm. in KO 1. **(E)** CL photomicrograph of calcite veins displaying a non-bright-dull luminescence sequence (black, white and gray arrows respectively). Valdeteja Fm. close to Nocedo de Curueño. **(F)** CL photomicrograph of a *Chaetetes* sponge in which framework pores are occluded by cement displaying a similar non-bright-dull luminescence sequence (black, white and gray arrows respectively). Sample collected from a limestone buildup in the San Emiliano Fm. close to Casares de Arbas.

They range in size from a few dm to less than a mm. In some samples, clasts seem to float in a matrix of very fine-grained material resembling a fault gouge. Throughout the Bodón Unit, several generations of white calcite veins are associated with these breccias, and crosscut all previous diagenetic phases, including silicified fossil fragments, dissolution seams and bedding-parallel stylolites (figure 3.15D). Under the CL microscope, consecutive generations of calcite veins display the same non-bright-dull sequence (figure 3.15E) compared to calcite cement filling pores (figure 3.15F). Mechanical twins in calcite crystals are omnipresent (figures 3.14B & 3.15B). An additional phase of stylolitization affected the carbonate rocks and crosscuts calcite veins.

3.4.1.2. Dolomitization

Fabric-destructive dolomitization overprinted all previous diagenetic phases, such as silicifications, stylolites and calcite veins, and has been discussed in detail in previous studies (Gasparrini et al., 2006a; Lapponi et al., 2013; Muñoz Quijano, 2015). Replacive dolomitization was followed by cementation of white dolomite crystals (figure 2.5D), including abundant saddle dolomite displaying typical curved crystal boundaries. In some samples, the last thin phase of dolomite cement colors blue after staining. The specific style of dolomitization for each KO will be discussed in section 3.7.

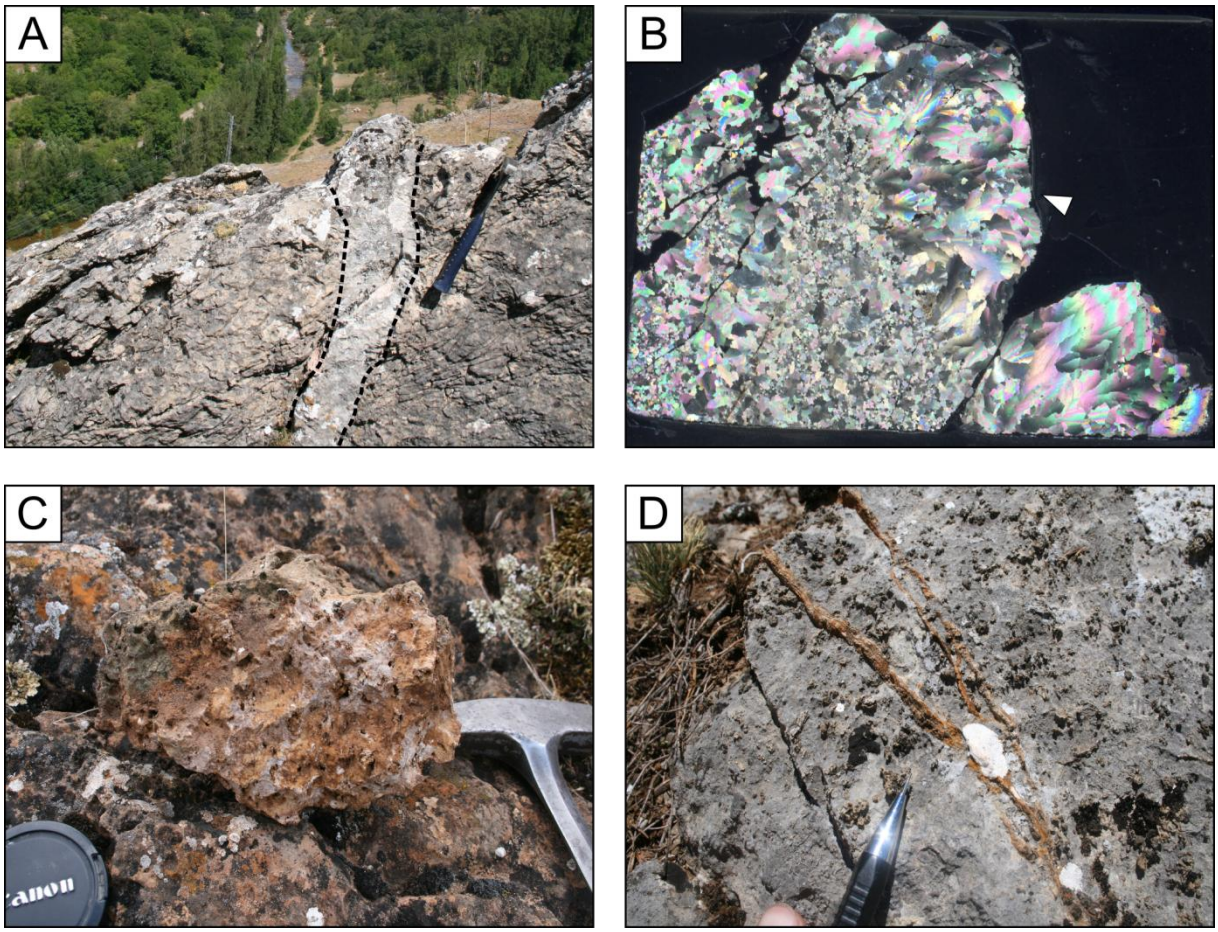

Figure 3.16: Dolomite field observations and thin section petrography. **(A)** Thick calcite vein (black dashed lines) crosscutting dolomitized boundstones exposed in KO 2. Hammer for scale (32 cm). **(B)** XP thin section scan of a coarse-crystalline dolomite sample characterized by a high abundance of feather-like saddle dolomite (white arrow). Length of the thin section is approximately 2 cm. Sample from dolomitized Barcaliente Fm. in KO 3. **(C)** Clast of porous coarse-crystalline dolomite in KO 3 displaying a typical orange patina. **(D)** Orange dolomite veins in a small carbonate buildup of the Vadeteja Fm. in KO 1.

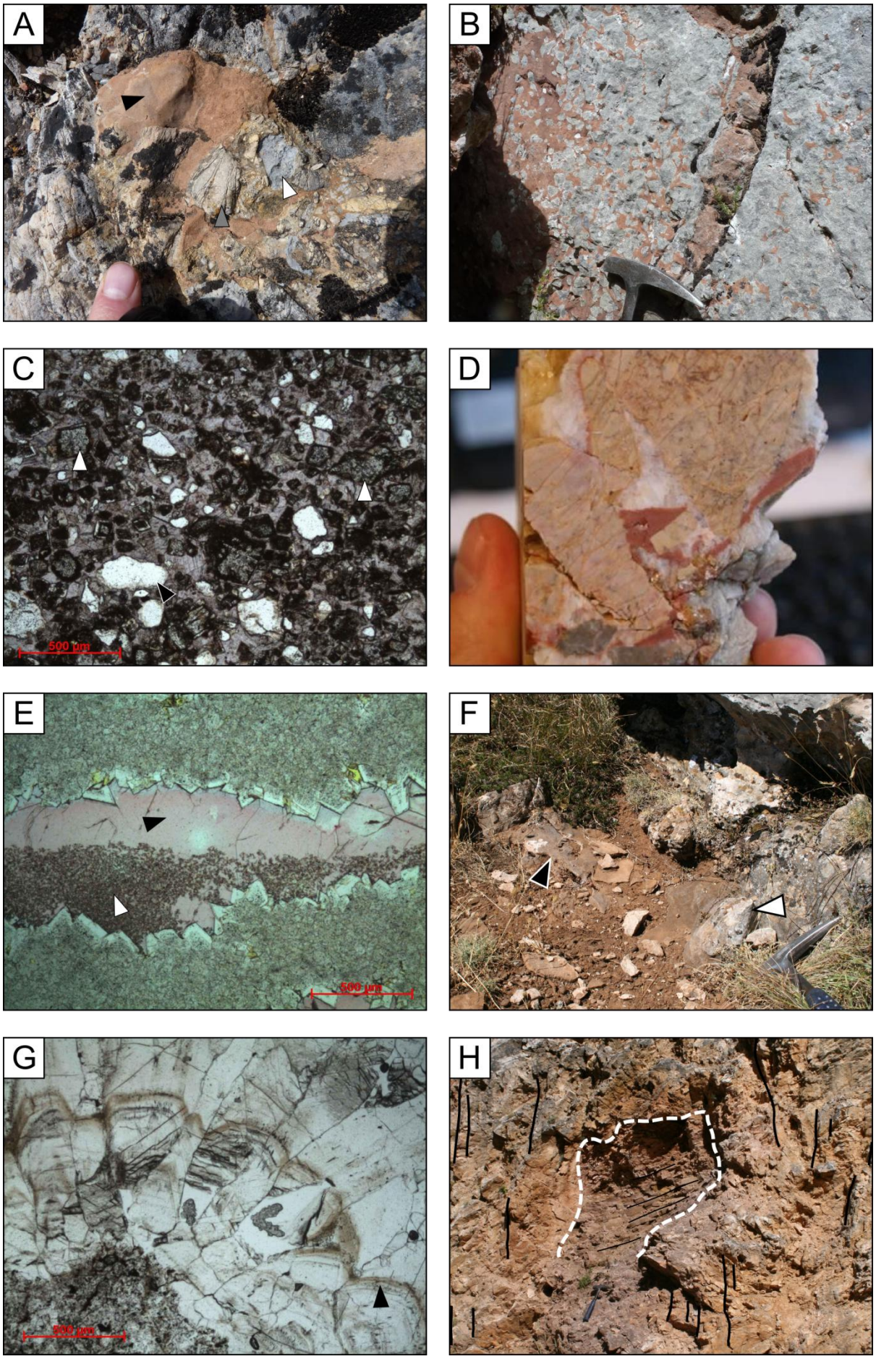
A
B
C
500 µm
D
E
500 µm
F
G
500 µm
H

Figure 3.17 (opposite page): Paleokarstification. **(A)** Clast-supported breccia with angular limestone (white arrow) and dolomite (gray arrow) clasts embedded in a red-colored matrix (black arrow). Exposure in the Valdeteja Fm. north of San Martin de la Tercia. **(B)** Fracture surface exposing large dolomite crystals (gray upon weathering) and red-colored matrix filling the intercrystalline pore space. Road section in the Valdeteja Fm. east of the town of Valdeteja. **(C)** XP photomicrograph of the red matrix composed of weathered dolomite clasts (white arrows) and quartz grains (black arrow) cemented by calcite. Valdeteja Fm. north of San Martin de la Tercia. **(D)** Clast-supported breccia with breccia porosity partly filled with red internal sediment and white calcite cement. Sample from the Valdeteja Fm. in San Martin de la Tercia. **(E)** PP photomicrograph of a zebra dolomite sample from the Valdeteja Fm. exposed in KO 1. Zebra pores are filled with internal sediment (white arrow) and cemented with clear calcite (black arrow). **(F)** Exposed paleocave with layered flowstones (black arrow) and broken stalagmite (white arrow) in the Barcaliente Fm. in KO 1. **(G)** PP photomicrograph of a stalagmite of KO 1 composed of radially-oriented bladed calcite crystals with red to brown dust laminations (black arrow). **(H)** Cavity in sub-vertical dolomitized Barcaliente limestones along the Millaró road section in KO 1. The cavity, delineated with a white dashed line, is filled with internal sediments dipping 20° south. Hammer (32 cm) below cavity for scale.

Dolomite cementation is postdated by white calcite cementation (figure 2.5D), which preferentially affected the most porous dolomite rocks. Calcite cementation occurred during a deformation event, as evidenced by the omnipresence of calcite-filled veins and fractures crosscutting fracture-associated dolomite (figure 3.16A). Calcite cementation is locally associated with quartz (see section 3.7.2.2), and with small amounts of pyrite and associated ore minerals.

A remarkable petrographic feature is the occurrence of a coarse-crystalline phase of replacive dolomite and dolomite cement made up of large (up to 2 mm) saddle or baroque crystals with a typical feather-like appearance (figure 3.16B). This coarse-crystalline phase of dolomite is omnipresent in KO 3 where it is characterized by an intense orange patina upon weathering (figure 3.16C; see section 3.7.3). The dolomite phase is locally highly porous, but the pores are not cemented with the typical white calcite cements postdating the fabric-destructive dolomitization phase introduced above (figure 2.5D). In KO 1, this additional orange-colored dolomite phase has only been observed as thin veins crosscutting undolomitized precursor limestones (figure 3.16D).

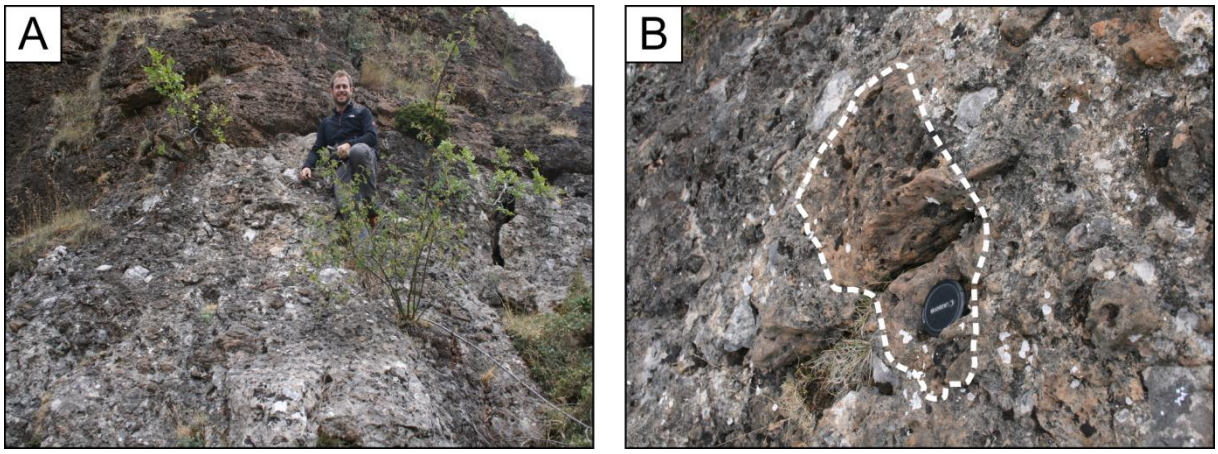

Figure 3.18: Second carbonate breccia in KO 3. **(A)** Undolomitized carbonate breccia exposed in KO 3 with limestone and coarse-crystalline dolomite clasts displaying an orange patina. **(B)** Detailed view of figure 3.18A with a porous clast of coarse-crystalline dolomite delineated with white dashed line.

3.4.1.3. Post-dolomitization

In several dolomitized fracture zones in the Bodón Unit, pockets of a specific type of clast-supported breccia overly the Carboniferous platform limestones. The breccia is composed of both angular limestone and dolomite clasts, generally embedded in a red-colored matrix (figure 3.17A). Exposures of these red-matrix breccias have been observed in the Valdeteja Fm. northeast of San Martin de La Tercia (see figure 2.1B for the locations of towns), in the Barcaliente Fm. in the central part of KO 1, and in a fracture zone in the Valdeteja Fm. east of KO 2. They typically occur at high altitudes, although limited amounts of red micritic matrix have been observed in some pores and fractures at lower altitudes (figure 3.17B). Microscopically, the red matrix is made up of small dolomite clasts, quartz grains and micrite, cemented with calcite (figure 3.17C). Geopetal infilling with laminated internal sediments is obvious from several samples where pores are partly filled with red internal sediments and partly with calcite cement (figures 3.17D & 3.17E). At the top of KO 1, a small cave with layered flowstones (i.e. laminated cement composed of coarse sparry calcite) and stalagmites has been observed in close association with the red-matrix breccia (figure 3.17F).

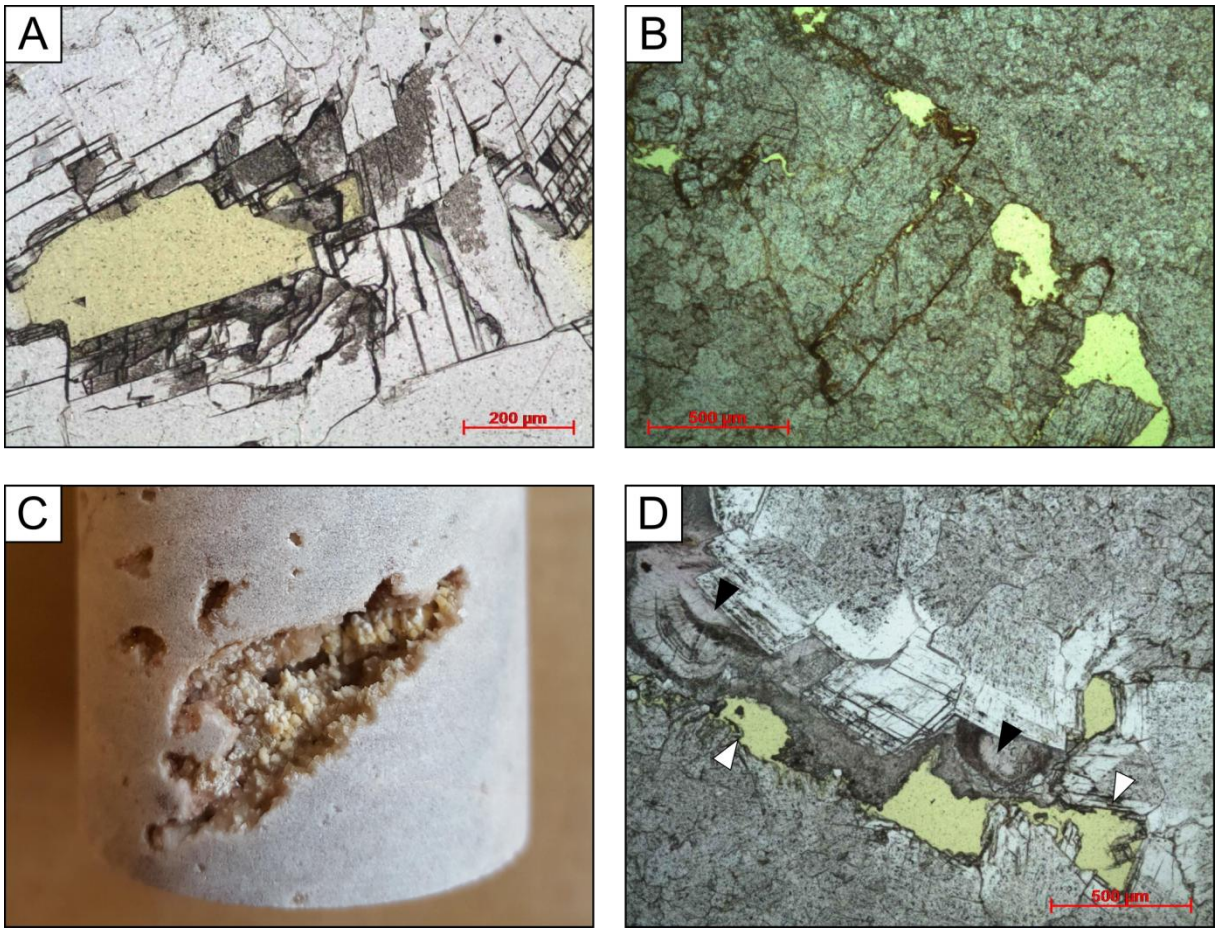

Figure 3.19: Dissolution and pendant calcite cementation. **(A)** PP photomicrograph showing partial dissolution of void-filling dolomite crystals. **(B)** PP photomicrograph showing dissolutional vugs (filled by yellow resin) along high-amplitude stylolite, creating channel porosity. Sample SL16RH031 from KO 1. **(C)** White to yellow calcite cement partially filling a vuggy pore in a dolomite plug. Sample SL16RH020 from KO 1. **(D)** PP photomicrograph of micro-stalactitic or pendant calcite cement (black arrows), stained red with Alizarine Red S. Note dark dust zonations. Void-filling dolomite crystals are partly dissolved (white arrows). Sample SL16RH011 from KO 1.

Microscopically, the stalagmites are made up of radially-oriented bladed calcite crystals which contain red to brown dust laminations (figure 3.17G). Along the Millaró road section in dolomitized limestone layers of the Barcaliente Fm., a karstic pocket filled with laminated internal clay sediments is exposed (figure 3.17H). The finely laminated sediments are dipping 20° S.

In the fault zone of the Correcilla Thrust in the Montuerto Syncline (KO 3), the dolomitized carbonate fault breccia has been locally affected by a second event of brecciation. Small pockets of undolomitized breccia containing clasts of both orange-colored coarse-crystalline dolomite and precursor limestone occur in the center of the fault zone (figures 3.18A & B).

Throughout the Bodón Unit, dissolution affected carbonate rocks, both limestone and dolomite. This gave rise to several natural thermal springs which were used for the construction of *balnearios*, or antique spas, during the 19th and 20th centuries (see box 4; figures 3.1 & 3.8). Cold-water springs are omnipresent and are often characterized by the occurrence of active tufa deposits (freshwater carbonates). On a smaller scale, calcite and dolomite samples are affected by dissolution along crystal boundaries or fractures and localized precipitation of pendant calcite cement.

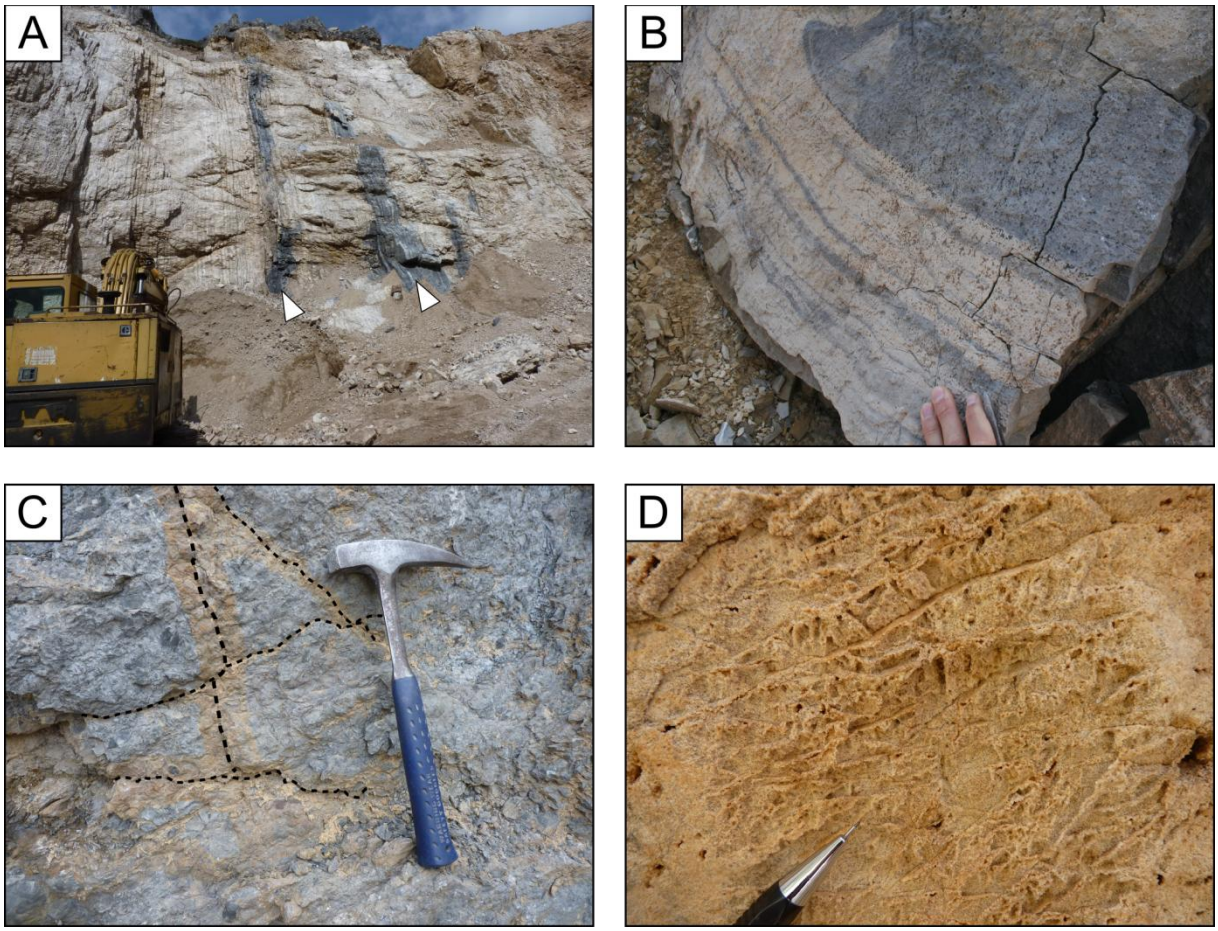

Figure 3.20: Color change affecting dolomite and limestone rocks. **(A)** Dolomitized limestones of the Barcaliente Fm. exposed in the MQ in KO 1. The color of the dolomite rocks altered to beige, except for 2 stratabound patches which still show the original dark gray color (white arrows). **(B)** Liesegang-banded patterns on a bedding plane in dolomitized limestones of the Barcaliente Fm. in the LCQ. **(C)** Alteration of dark gray undolomitized fossiliferous rudstones of the Devonian La Vid Group along small fracture planes close to the MQ. **(D)** Beige-colored dolomite of the Barcaliente Fm. exposed along the Millaró road section. Although the original zebra dolomite texture can still be differentiated, the dolomite is completely weathered up to the point where it mechanically disintegrates.

Partial dissolution of void-filling dolomite crystals (figure 3.19A), as well as dissolution along stylolites (figure 3.19B), are omnipresent in samples from the Bodón Unit. Pendant calcite cements are observed in porous samples of key outcrops 1 and 3. Macroscopically, the cement has a white to yellow color (figure 3.19C). It often shows a micro-stalactitic or pendant morphology under the microscope (figure 3.19D), including dust zonations, and is not luminescent.

In some areas, notably in both quarries and along both road sections of KO 1, the color of gray dolomite rocks changed to beige (figure 3.20A). The color change is slightly bounded by bedding surfaces or fractures, but not confined by piezometric surfaces. Several examples of Liesegang-banded patterns show alternations of beige and gray colors on bedding planes (figure 3.20B). Nearby the MQ, similar color changes have been observed in limestones of the Devonian La Vid Group, where the color change clearly represents an alteration process around fracture planes (figure 3.20C). Although the textural characteristics of the gray and beige dolomite rocks of the Barcaliente Fm. seem macroscopically similar at first sight, the beige rocks are often more coarse-crystalline and less cohesive up to the point where they mechanically disintegrate. In some locations, they are almost completely composed of a framework of loose dolomite crystals, resembling dolomite sand (figure 3.20D). Microscopically, gray-colored dolomite contains more intercrystalline insoluble residue compared to beige rocks, which have a higher intercrystalline porosity. Vuggy and zebra pores in the beige dolomite rocks are often affected by dissolution, and are partly occluded with pendant calcite cement.

3.4.2. Diagenetic evolution

3.4.2.1. Eogenetic stage

The eogenetic stage directly follows sedimentation and is the earliest stage of diagenesis (figure 3.21A). It is defined as the stage of relatively short duration during which sediments are still affected by surface-related processes and fluids (Choquette and Pray, 1970). For Carboniferous limestones from the Bodón Unit, the most important eogenetic processes identified through field observations and thin section analysis are micritization, cementation and silicification (figure 3.21A). Micritization selectively affected specific types of bioclasts, which were likely of aragonitic or high-Mg calcite composition, making them more prone to micritization (Flügel, 2004). The contacts between bioclasts and their micritic envelopes are irregular which points to destructive micritization, possibly related to microboring organisms (Bathurst, 1966). The action of microboring organisms can also be suspected based on the occurrence of small holes filled with micrite in bioclasts in the Barcaliente Fm. (figure 3.14B).

The early phases of carbonate cementation in porous and grain-dominated samples are characterized by a brown color and fibrous crystals, which suggests a primary aragonitic composition. Both fibrous and radiaxial fibrous cement rims are typical for marine phreatic environments (Scholle and Ulmer-Scholle, 2003; Flügel, 2004). Early marine cementation is well-documented in shallow and agitated environments of carbonate platforms in the CZ (figure 3.21A; Kenter et al., 2002; Bahamonde et al., 2014; Chesnel et al., 2015).

The source of silica for the important silicifications in the Bodón Unit is likely biogenic since the area was not affected by important volcanic or hydrothermal activity prior to Late- to Post-Variscan lithospheric delamination. Siliceous sponges and sponge spicules have been reported for numerous Pennsylvanian microbial boundstone-dominated carbonate platforms elsewhere in the Cantabrian Zone (Bahamonde et al., 1997, 2007, 2014, 2015; Della Porta et al., 2003; Samankassou et al., 2013; Chesnel et al., 2015, 2017). As reported in section 3.3.1, the association of microbial communities with siliceous sponges is characteristic for the Phanerozoic era (Brunton and Dixon, 1994; Wood, 1999). Accumulations of siliceous sponge spicules are usually observed in basinal settings, as in these settings the alkalinity and temperature of seawater are sufficiently low to allow preservation of siliceous organisms or precipitation of silica (Arp et al., 2003). This might explain the preferential occurrence of chert nodules and silicified bioturbations in the calciturbidite successions of KO 1, which are likely deposited in an inter-platform basin with restricted water circulation (see section 3.3.1). The association of silica and small dolomite rhombs suggests that the silicification process resulted in a local release of Mg. According to Kastner et al. (1977), dolomite rhombs can be formed by Mg released during the transformation of opal-CT to quartz. Several other studies assume that the Mg necessary to create dolomite rhombs must be derived from calcite during the replacement by silica (Jacka, 1974; Knauth, 1979; Mansour, 2004). An alternative source for Mg might be the conversion of high- to low-Mg calcite, but this mechanism cannot explain the close association of the dolomite rhombs with silica.

3.4.2.2. Mesogenetic stage

The mesogenetic stage is defined as the stage during which diagenetic modifications are not influenced by surface-related fluids, and is also known as the burial diagenetic stage (Choquette and Pray, 1970). The burial diagenetic stage of the Carboniferous limestone successions in the Bodón Unit can be subdivided into pre-Variscan (figure 3.21B), Variscan (figure 3.21C) and Late- to Post-Variscan substages (figure 3.21D).

The Pre-Variscan substage of burial diagenesis is mainly characterized by burial and associated compaction leading to pressure solution and further cementation of primary porosity (figure 3.21B). Bedding-parallel stylolites (figure 3.15B) and dissolution seams are related to increasing burial prior to the onset of Variscan thrusting, accompanied by higher temperatures and pressures. Pressure solution of calcite was likely a source of carbonate for further occlusion of pores by cementation.

Brecciation along thrust faults, intense fracturing, calcite twinning and the complete occlusion of any remaining pore space with calcite cement attest of Variscan thrusting (figure 3.21C). The best example of Variscan brecciation is the exposed fault breccia of the Correcilla Thrust in KO 3 (figure 3.15C; Potent and Reuther, 2000). Similar fault zones have been reported in several locations in the Cantabrian Zone (e.g. Grimmer et al., 2000). Throughout the Bodón Unit, several generations of white calcite veins are observed (figure 3.15D) and are assigned to fracturing associated with Variscan compression (cfr. Gasparrini et al., 2006a). The onset of Variscan thrusting and compression resulted in the creation of bedding-perpendicular stylolites and the complete occlusion of any remaining pore space. Under the CL microscope, consecutive generations of calcite veins display the same non-bright-dull sequence (figure 3.15E) compared to calcite cement filling pores (figure 3.15F), which suggests that complete occlusion of porosity occurred at this

stage. Mechanical twins are omnipresent in calcite crystals and are assigned to Variscan compression (figures 3.14B & 3.15B).

Box 4: *Balnearios* in the Bodón Unit

The thermal springs occurring in the area of the Bodón Unit have been intensively used already by the Romans. Their claimed medicinal and therapeutic value resulted in a modern revival in the 19th and 20th centuries, when several thermal spas or *balnearios* were built. Notable examples include the bathhouses of Villanueva de la Tercia and Nocedo de Curueño, which were called 'Caldas de Villanueva' and 'Caldas de Nocedo', respectively (see locations on figures 3.1 & 3.8). The *balneario* in Villanueva de la Tercia was built in 1848, when it was observed that a horse healed after drinking from the water. The *balneario* of Nocedo de Curueño (figure box 4) was built in 1900 by two brothers and included a guesthouse and a chapel. It is located along the Río Curueño, in the center of key outcrop 2. During the Spanish Civil War (1936-1939), the building was occupied for its strategic location in the steep valley north of Nocedo de Curueño. It was destroyed, together with many other important buildings, when the Republicans had to fled the territory. The *balneario* was rebuilt after the civil war. Visitors could enjoy the thermal waters and attend masses in a small chapel. Both the bathhouses of Villanueva and Nocedo were closed for public in the late 20th century. A modern *balneario* can currently be found in Caldas de Luna.

Figure box 4: An old photograph of the former bathhouse of Nocedo de Curueño.

The Late- to Post-Variscan substage of burial diagenesis in the carbonates of the Bodón Unit (figure 3.21D) is dominated by the circulation of hydrothermal dolomitizing fluids through thermal convection induced by Post-Variscan lithospheric delamination (Gasparrini, 2003; Gasparrini et al., 2006a). The exact timing of dolomitization has been inferred by Gasparrini (2003) who reported subhorizontal zebra textures in folded outcrops of dolomitized Barcaliente limestones. The orientation of the zebra textures is independent from the orientation and dip of the fold limbs, which has been an important argument to conclude that hydrothermal dolomitization postdates Variscan compression. Dolomitization was followed by white calcite cementation from the same hydrothermal fluids (Gasparrini et al., 2006a, b). The traces of pyrite and associated ore minerals, precipitated with the white hydrothermal calcite, are likely expressions of the important event of ore mineralization affecting the southern Cantabrian Zone. These ore mineralizations were dated

at approximately 270 Ma (Paniagua et al., 1993, 1996). A literature review of the occurrence of dolomite bodies in the Bodón Unit and an introduction to their petrographic and geochemical characteristics have been provided in section 2.5. The specific style of dolomitization for each KO will be discussed in section 3.7.

The orange patina of the coarse-crystalline phase of dolomite exposed in KO 3 (figures 3.12A & 3.16C) is likely a result of oxidation of high concentrations of Fe (Pauwels, 2016; see section 3.7.3.4). In KO 1, this dolomite phase must have been less important, as here only orange-colored veins crosscutting precursor limestones have been observed (figure 3.16D). The timing of this coarse-crystalline phase of Fe-rich dolomite is difficult to determine precisely. It could be associated with the important phase of Late- to Post-Variscan dolomitization which created the dolomite geobodies in KO 1 and 2 (figures 2.5A & B). Some dolomite samples from KO 1 and 2 display a thin late phase of blue-stained and thus Fe-rich dolomite cement. A similar Fe-rich phase of dolomitization has been described for dolomite samples from the Bodón Unit by Gasparrini et al. (2006a) and Lapponi et al. (2013). They observed a late Fe-rich phase of void-filling dolomite cement, often exhibiting Fe-oxyhydroxide coatings. On the other hand, the Fe-rich coarse-crystalline dolomite from KO 3 is not cemented with the typical white hydrothermal calcite which is omnipresent in dolomite pores in KO 1 and 2. This suggests that the Fe-rich dolomite rocks could have been formed from a later pulse of dolomitization, potentially overprinting or recrystallizing dolomite rocks from the Late- to Post-Variscan dolomitization event. In the Basque-Cantabrian Basin, approximately 160 km east of the Bodón Unit, Aptian carbonates have been affected by an important episode of Fe-rich dolomitization during the Late Albian (López-Horgue et al., 2010; Nader et al., 2012; Dewit et al., 2014). The coarse-crystalline Fe-rich dolomite rocks exposed in KO 3 could be associated with this Mesozoic episode of Fe-rich fluid flow.

3.4.2.3. Telogenetic stage

The telogenetic stage of Choquette and Pray (1970) refers to the stage during which long-buried and mineralogically stable rocks are exhumed and affected by fluids operating from the surface. The telogenetic stage is usually a consequence of uplift and erosion, and represents an important stage for the Paleozoic carbonates of the Bodón Unit. Following lithospheric delamination and fluid flow during the Early Permian, the Cantabrian Zone has been mainly affected by uplift during the Mesozoic and Cenozoic (see section 2.2), which had important telogenetic consequences.

The macro- and microscopic observations of the red-matrix breccias (figure 3.17) indicate that they are likely karstic collapse breccias postdating Late- to Post-Variscan dolomite formation (figure 3.21E). The dip of internal sediments indicates that they filled karstic cavities prior to Alpine steepening of the Variscan basement (see section 2.2; Pulgar et al., 1999). Similar red-matrix collapse breccias have been described in Carboniferous carbonate platforms in the Picos de Europa and northern Ponga units (Adrados-González et al., 2010) as well as in the northern part of the Central Asturian Coalfield (Bahamonde et al., 2014). Their close association with dolomitized fracture zones in Carboniferous carbonates and their red color suggests that these breccias might be of Permian age, since several red-colored rock exposures of the same age have been described in the northern part of the Cantabrian Zone (Martínez-García, 1983; Dallmeyer and Martínez-García, 1990). The upper part of the Permian succession in the Cantabrian Zone, referred to as the Villaviciosa Beds, is composed of red sandstones, shales and calcareous breccias

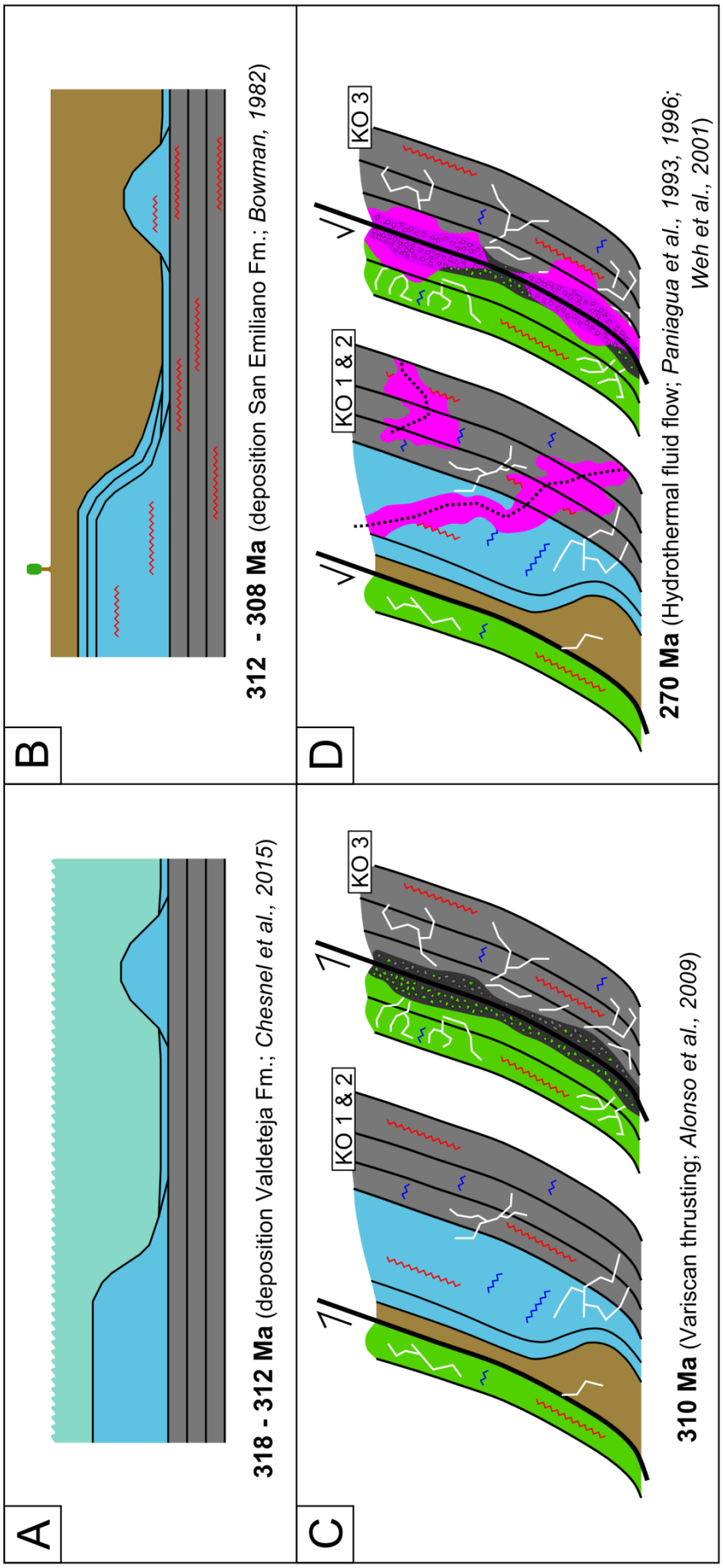

Figure 3.21: Illustration of the geodynamic evolution and associated diagenetic processes affecting Carboniferous successions exposed in the Bodón Unit. For each geodynamic stage, the approximate age is provided based on literature data. **(A)** Deposition of the Bashkirian Valdeteja Fm. and associated eogenetic processes such as micritization, early marine cementation and silicification. **(B)** Pre-Variscan burial of Carboniferous successions and onset of mesogenetic processes such as stylolitization and blocky calcite cementation. **(C)** Variscan thrusting and associated mesogenetic processes such as calcite veining around tectonic breccias. **(D)** Late- to Post-Variscan hydrothermal fluid flow and associated dolomitization along fracture networks (KO 1 & 2) and thrust faults (KO 3).

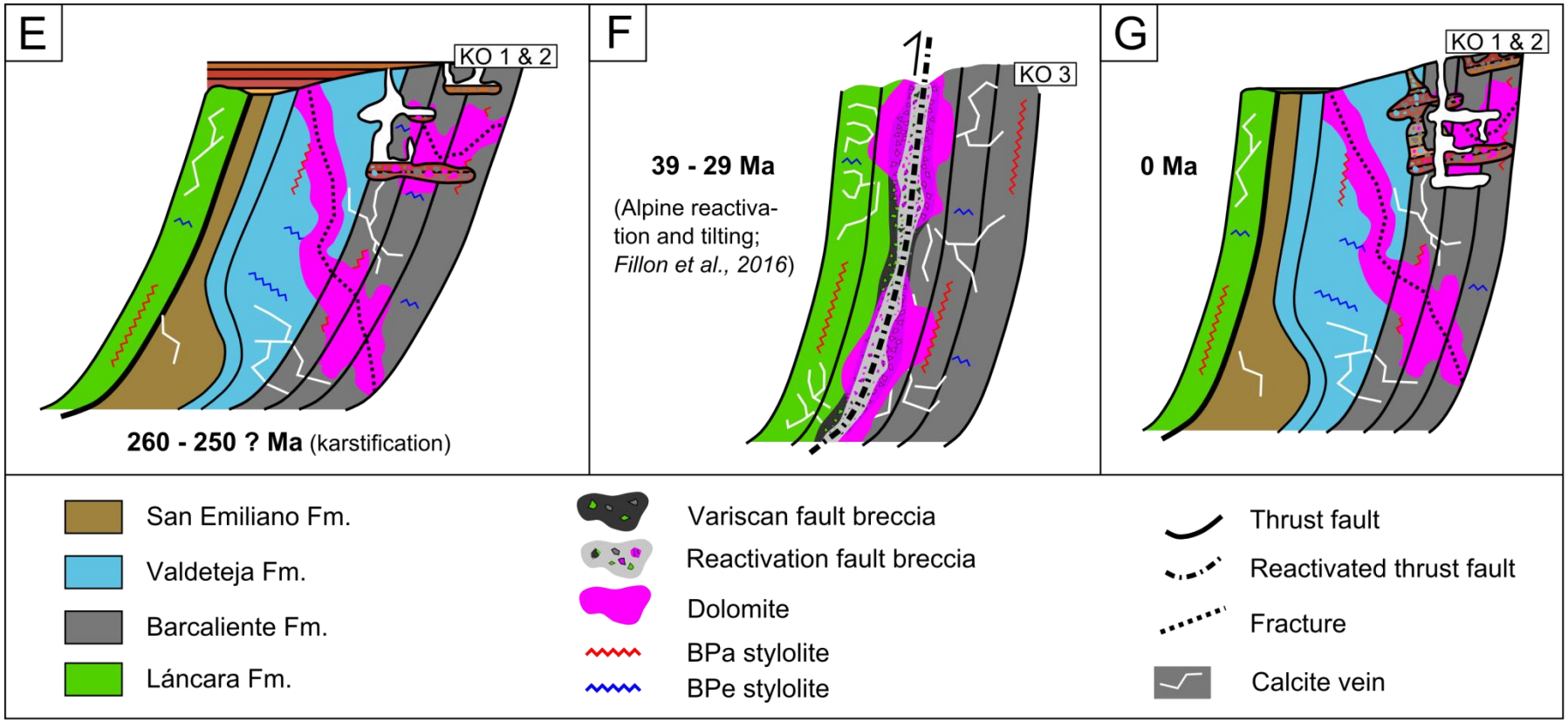

Figure 3.21 (continuation): (E) Telogenetic karstification and creation of red-matrix collapse breccia during Post-Variscan uplift and exposure of the Paleozoic carbonate successions. **(F)** Alpine reactivation of thrust faults (KO 3) and tilting of Paleozoic successions in the Cantabrian Zone. **(G)** Recent karstification and dissolution of exposed successions in the Bodón Unit. (BPa: bedding-parallel; BPe: bedding-perpendicular)

and often occurs unconformable on Carboniferous or pre-Carboniferous rocks (Martínez-García, 1983). The red-matrix breccias are possibly the result of Late Permian karstification of the uplifted and exposed Variscan Massif. The karstification resulted in the formation of paleocaves, some of which were filled with fine-grained sediments locally overlying the limestones.

The occurrence of brecciated Fe-rich dolomite along the Correcilla Thrust in KO 3 (figure 3.18) suggests an important episode of tectonic reactivation (figure 3.21F). The most important reactivation of Variscan faults and thrusts in the Cantabrian Mountains (not taking into account Late-Variscan orocline formation) occurred in response to the Alpine Orogeny (Pulgar et al., 1999; Potent and Reuther, 2000; Fillon et al., 2016).

Recent karstification affecting Paleozoic carbonates in the Bodón Unit can be split up in large-scale dissolution creating cave systems and small-scale dissolution accompanied by precipitation of pendant calcite (figure 3.21G). The morphology of the calcite cement and its non-luminescent nature suggest a meteoric fluid source. The famous Cueva de Valporquero in Barcaliente limestones close to the town of Valporquero de Torrío is one example of the numerous recent cave systems which developed in the Paleozoic carbonates of the Bodón Unit. Similar cave systems occur in the Picos de Europa Unit, and were created by recent karstification developed at least since the Middle Pleistocene in the Variscan basement rocks after they were uplifted during the Alpine Orogeny (Ballesteros et al., 2011; Jiménez-Sánchez et al., 2014). These cave systems and springs attest of recent karstification and fluid flow, in contrast with paleokarstification characterized by red-matrix breccias (figure 3.21E).

An additional observation related to recent karstification is the color change from gray to beige which is best expressed in dolomitized limestones of the Barcaliente Fm. (figures 3.20A & B). The beige color is likely related to chemical alteration in response to recent meteoric fluid flow, as attested by the Liesegang-banded patterns and the fracture-associated color changes. Chemical alteration can result in dissolution of specific components, resulting in the creation of a so-called ghost-rock (*sensu* Dubois et al., 2014). It was likely the insoluble residue in between dolomite crystals, as well as calcite cement, which were preferentially flushed out or dissolved in dolomite rocks from the Barcaliente Fm. The migration of meteoric fluids responsible for the chemical alteration was likely confined by bedding planes and fractures. Continuing alteration results in disintegration of crystals and the mechanical weakening of the rocks. Similar alteration processes possibly also affected the dolomite rocks of the Valdeteja Fm., but potential color changes are most likely obliterated due to the complex sedimentological framework of this formation.

3.5. Dolomite pore types

This section introduces the different pore types observed in the Carboniferous carbonate rocks exposed in the Bodón Unit during fieldwork and thin section petrography. Pores have only been observed in HTD rocks, and not in precursor limestones which are generally very tight and therefore not discussed in this section. The dolomite pore types are defined based on the classification system of Choquette and Pray (1970) and are listed in order of decreasing importance. Photographs of the different pore types have been assembled in figure 3.22. This section introduces each pore type, while section 3.6 focuses on the evolution of reservoir characteristics during the diagenetic history of the platform limestones, which has been elaborated in section 3.4. Section 3.7 describes the importance of each pore type for the dolomite matrix porosity in each of the three key outcrops.

3.5.1. Vuggy pores

Vuggy pores are defined by Choquette and Pray (1970) as mm- to m-sized non-fabric selective pores caused by early or late diagenetic dissolution. The origin of vugs in dolomite rocks has been assigned to the 13 % volume decrease upon dolomitization (see section 1.2.4), or to the occurrence of molds and intergranular pores present in the precursor limestones. According to Merino and Canals (2011), vugs in dolomite rocks are often generated through dissolution of calcite by dolomitizing fluids upon entering a limestone. In the current study, vuggy pores are defined as dissolutional vugs, following Merino and Canals (2011), associated with the dolomitization process. In contrast to the original definition of Choquette and Pray (1970), vuggy pores are found to be fabric selective in the Bodón Unit. They are typically associated with specific dolomitized facies such as microbial boundstones of the Valdeteja Fm. in KO 1 (figure 3.22A) and Fe-rich coarse-crystalline dolomite in KO 3 (figures 3.16C & 3.22B). Vugs can range from a few cm in size (figures 3.22A & B) to less than a mm (figure 3.22C). However, in case of small pores, it is often difficult to assign a precise origin.

3.5.2. Zebra pores

Diagenetic zebra textures, with associated zebra porosity, are made up of rhythmic alternations of replacive and void-filling dolomite and calcite (Nielsen et al., 1998). They form under high pore fluid pressures in low-permeability dolomite rocks (see chapter 4), and occur seldom in coarse-grained facies (Davies and Smith, 2006). The genesis of zebra textures has been assigned to focused flow of fluids at suprahydrostratic pressures, creating parallel fractures which are partly or completely filled with dolomite cement crystals (Nielsen et al., 1998; Vandeginste et al., 2005). Merino et al. (2006) introduced a new model of zebra dolomitization in which the textures are created by self-organization of layers of displacive dolomite and calcite crystals (instead of void-filling cement) that push aside replacive dolomite due to local induced stress generated by crystal growth. The calcite which occurs in between the dolomite crystals often dissolves leaving behind sheet-like pores, the so-called zebra pores. In the Bodón Unit, zebra textures and associated pores are omnipresent in the dolomitized mudstones of the Barcaliente Fm. (figure 3.22D) and occur locally in dolomitized microbial boundstones (figures 3.17E & 3.22E), where they are often associated with vuggy pores. Zebra pores can be up to several cm in length and a few mm in width.

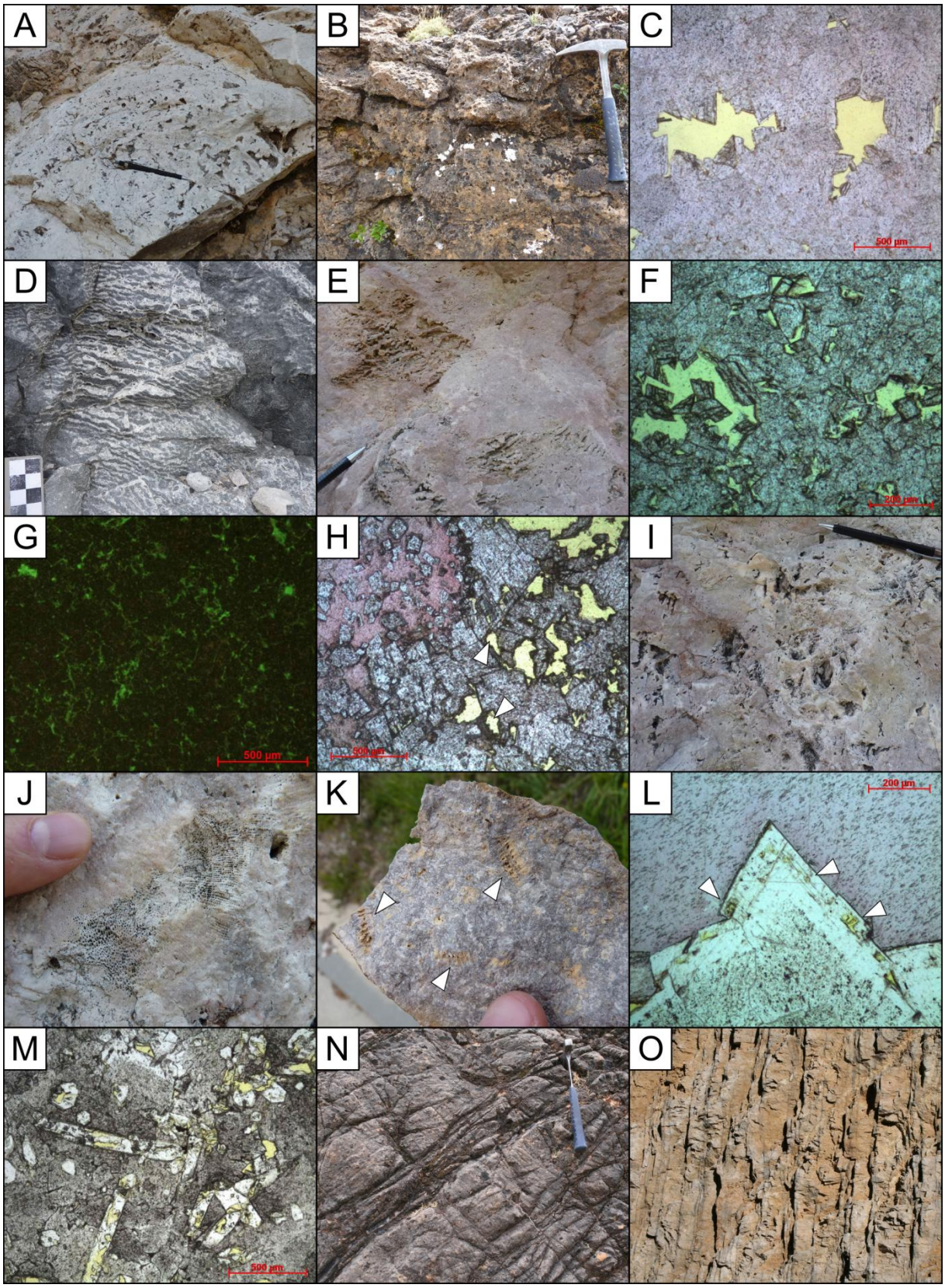
A
B
C
500 µm
D
E
F
200 µm
G
500 µm
H
500 µm
I
J
K
L
200 µm
M
500 µm
N
O

Figure 3.22 (previous page): Overview of dolomite pore types observed during fieldwork and petrographic observations. **(A)** Vuggy pores in white dolomitized microbial boundstone exposed along the Millaró road section in KO 1. Pencil for scale (14 cm). **(B)** Vuggy pores on a weathered surface of Fe-rich dolomitized fault gouge in KO 3. Hammer for scale (32 cm). **(C)** PP photomicrograph of small vuggy pores (filled by yellow resin) in a dolomitized carbonate mound in KO 1 (sample SL16RH028). **(D)** Zebra textures and associated zebra pores in the Barcaliente Fm. exposed in the LCQ in KO 1. **(E)** Zebra textures and associated zebra pores in dolomitized microbial boundstones in KO 1. **(F)** PP photomicrograph of intercrystalline pores in dolomitized mudstones in KO 1 (sample SL16RH063). **(G)** FL photomicrograph of intercrystalline pores in a dolomitized mudstone. Sample SL16RH011 from the Barcaliente Fm. in KO 1. **(H)** PP photomicrograph showing intercrystalline porosity in dolomite from KO 2. The pores are partly occluded with calcite cement (left; red stained) and partly dissolution-enlarged (right; filled by yellow resin). **(I)** Large and irregular pores in pink dolomitized microbial boundstone exposed along the Millaró road section of KO 1. Many of these pores resemble biomolds, although the exact origin of the molds cannot be determined. **(J)** Molds resembling a dissolved sponge in microbial boundstone exposed along the Millaró road section of KO 1. **(K)** Molds of crinoid stems (white arrows) in dolomitized grainstone exposed along the Millaró road section in KO 1. **(L)** PP photomicrograph of small crystal-moldic pores (white arrows) which formed after dissolution of a specific cement phase in a void-filling dolomite crystal. Sample SL16RH065 from KO 1. **(M)** PP photomicrograph of crystal-moldic pores in dolomitized microbial boundstone in KO 2. Large parts of the original quartz crystals are preserved. **(N)** Fracture sets on an exposed bedding plane of dolomitized Barcaliente limestones in KO 3. These fractures are generally filled with calcite. Hammer for scale (32 cm). **(O)** Example of well-bedded subvertical dolomitized Barcaliente limestones exposed along the Millaró road section, with superimposed subhorizontal fractures. Note the thin dark lines parallel to the bedding of the beige dolomite rocks. Width of view is approximately 1.5 m.

3.5.3. Intercrystalline pores

Pores occurring in between more or less equal-sized crystals are referred to as intercrystalline pores and are typically associated with dolomitization (Flügel, 2004). Intercrystalline pores are encountered in most dolomite samples in the Bodón Unit and their size ranges from a few µm to > 100 µm (figures 3.22F & G). The intercrystalline pores can be partly or completely occluded with insoluble residue or calcite cement, but can also be enlarged by dissolution (figure 3.22H).

3.5.4. Biomoldic pores

Biomoldic pores are created by selective dissolution of fossils or bioclasts. Many large and irregular pores in the dolomitized microbial boundstones of the Valdeteja Fm. of KO 1 resemble biomolds of which the origin is difficult to determine (figure 3.22I). They do not represent stromatactis-like cavities which are typically associated with microbial boundstones (see section 3.3.1.2; Bahamonde et al., 2014), as cavities of this kind were fully cemented prior to Late-Variscan hydrothermal dolomitization (e.g. figure 3.6C). Rare examples of sponge (figure 3.22J) and crinoid molds (figure 3.22K) have been observed, but are limited contributors to overall petrophysical properties.

3.5.5. Crystal-moldic pores

Crystal-moldic pores are formed by selective leaching of crystals. In the Bodón Unit, numerous void-filling dolomite crystals have been affected by leaching, resulting in intracrystalline dissolution and the creation of crystal-moldic pores. Dissolution often affects the last (sometimes Fe-rich, see section 3.4.1.2) growth phase in dolomite crystals (figure 3.22L), and is regularly associated with dedolomitization and oxidation of Fe-rich components. A distinct type of crystal-moldic porosity is encountered in dolomitized boundstones in KO 1 and KO 2. Here, molds are created by dissolution of elongated quartz crystals (figure 3.22M), which likely represent recrystallized sponge spicules (see sections 3.3.1 and 3.3.2).

3.5.6. Fractures

All pore types introduced above contribute to the matrix porosity of the dolomite rocks exposed in the Bodón Unit. Hydrothermal dolomite rocks are often affected by fracturing, given their brittle nature and typical fault-controlled settings (see chapter 1). Log data of KO 1 confirm a larger abundance of fractures in dolomite compared to precursor limestone rocks (see Appendix II figure A). Open fractures can strongly increase matrix porosity and many prolific hydrocarbon reservoirs in dolomite rocks are due to this association of matrix porosity and open fractures (Purser et al., 1994). The dolomite bodies exposed in the three key outcrops are crosscut by several fracture sets (figures 3.17H; 3.22N & O), which are discussed in more detail in section 3.7. Fractures are generally filled with calcite, or open and affected by dissolution resulting in channels.

3.5.7. Caverns and channels

Cavern and channel pores are large dissolutional vugs and elongated pores respectively, and are both typically associated with dissolution and karstification processes (Choquette and Pray, 1970). Caverns and channels are omnipresent in the Carboniferous platform limestones of the Bodón Unit, and contribute to spectacular cave systems (see section 3.4.2.3). Elongated channel pores are omnipresent in the limestone and dolomite rocks exposed in the Bodón Unit, and are caused by dissolution along stylolites (figure 3.19B) or fractures.

3.6. Porosity evolution

During their diagenetic and geodynamic history, the Paleozoic carbonate successions currently exposed in the Bodón Unit experienced both porosity-destructive and –constructive processes. Diagenetic products increasing the porosity of the platform limestones have been indicated with white bars on the paragenetic sequence in figure 3.13, while porosity-destructive products have been indicated with black bars. Diagenetic products with little effect on reservoir characteristics have been indicated with gray bars.

Most of the eogenetic and mesogenetic processes affecting the limestones, such as cementation and compaction, lowered their primary porosity. Prior to Late- to Post-Variscan hydrothermal dolomitization, the limestone successions had become extremely tight, with virtually all pores occluded with calcite cement. This is confirmed by petrographic observations (e.g. figure 3.6C) and by He porosimetry and WS measurements of limestone plugs from KO 2 (see section 3.7.2.3), indicating very low porosities. Open pores have never been reported in studies of Carboniferous limestone platforms in the CZ (e.g. Kenter et al., 2002; Bahamonde et al., 2014; Chesnel et al., 2015). It has only been the hydrothermal dolomitization process which induced a porosity (and permeability) increase of the platform limestones by creating mostly vuggy and zebra pores (see section 3.7).

Late- to Post-Variscan, Cretaceous and Alpine tectonic activity along dolomitized fractures and fault zones resulted in the creation of fracture sets, which are more abundant in the brittle dolomite rocks. Post-Variscan and recent karstification of the limestone platforms resulted in local pockets of high porosity and permeability due to the creation of cavern and channel porosity. Post-Variscan caverns and channels are usually occluded with sediments and clasts (figure 3.17H), while recent karstification is still dissolving carbonates to date. Infiltration of meteoric fluids, resulting in

dissolution of limestone and dolomite, strongly increases the petrophysical properties of dolomite rocks, as it enlarges existing pores. Intense dissolution, and associated local precipitation of meteoric calcite cement, are usually observed in samples already characterized by a high porosity, which suggest that these porous samples provide preferential pathways for infiltration of meteoric water.

3.7. Dolomitization in the key outcrops

This section concentrates on the HTD geobodies exposed in each of the three key outcrops, and is subdivided in three subsections which each focuses on one of the key outcrops. The size and geometry of the exposed dolomite geobodies are described, as well as their general petrographic characteristics and petrophysical data. The dolomitization style in each of the key outcrops is discussed based on the lithological and sedimentological framework of the different key outcrops (section 3.3), the reconstructed diagenetic history of the platform limestones (section 3.4), the description of the different pore types (section 3.5) and the discussion of the porosity evolution through time (section 3.6).

3.7.1. Dolomite in KO 1

3.7.1.1. Size and geometry

The occurrence of HTD in KO 1 has been indicated on a satellite image (figure 3.23) and is based on the stratigraphic logs, satellite images and additional observations made during fieldwork. Based on Easytrace analysis of the log data, it is estimated that approximately 75 % of the Barcaliente Fm. and 62 % of the Valdeteja Fm. in KO 1 have been dolomitized (see Appendix II figure B). In the Alba Fm., only the top layers have locally been affected by dolomitization. Dolomitization was most important in and along the valleys representing the western and eastern boundaries of KO 1 (figure 3.23). The successions exposed along both road sections have been completely dolomitized except for the Alba Fm. and some single limestone beds. Towards the centre of KO 1, large parts of both the Barcaliente and Valdeteja Fm. have not been dolomitized. Here, the distinctly different dolomitization style in both formations becomes apparent (figure 3.23). The dolomitization front is very irregular in the uniform mudstones of the Barcaliente Fm. on top of KO 1, resulting in a patchy occurrence of undolomitized areas which are creating topography with peaks up to 1692 m (figures 3.23; 3.24A & B). Dolomite occurrence is more stratabound in the platform limestones of the Valdeteja Fm. (figures 2.3E; 3.24C & D), indicating the importance of the lithological framework on dolomitization style. The first depositional unit is entirely dolomitized (figure 2.3E), while the second depositional unit, composed of calciturbidites with smaller carbonate buildups, is less affected by dolomitization (figures 2.3E; 3.23 & 3.24C). The third depositional unit as well is almost entirely dolomitized (figure 3.24C). The dolomitization front in the Valdeteja Fm. is less irregular compared to the Barcaliente Fm. and is often bounded by stratigraphic contacts (figure 3.24D).

3.7.1.2. Petrography

Dolomitized limestones in the Bodón Unit are characterized by a typical succession of replacive and void-filling dolomite, postdated by white calcite cementation (figure 2.5D; Gasparrini, 2003).

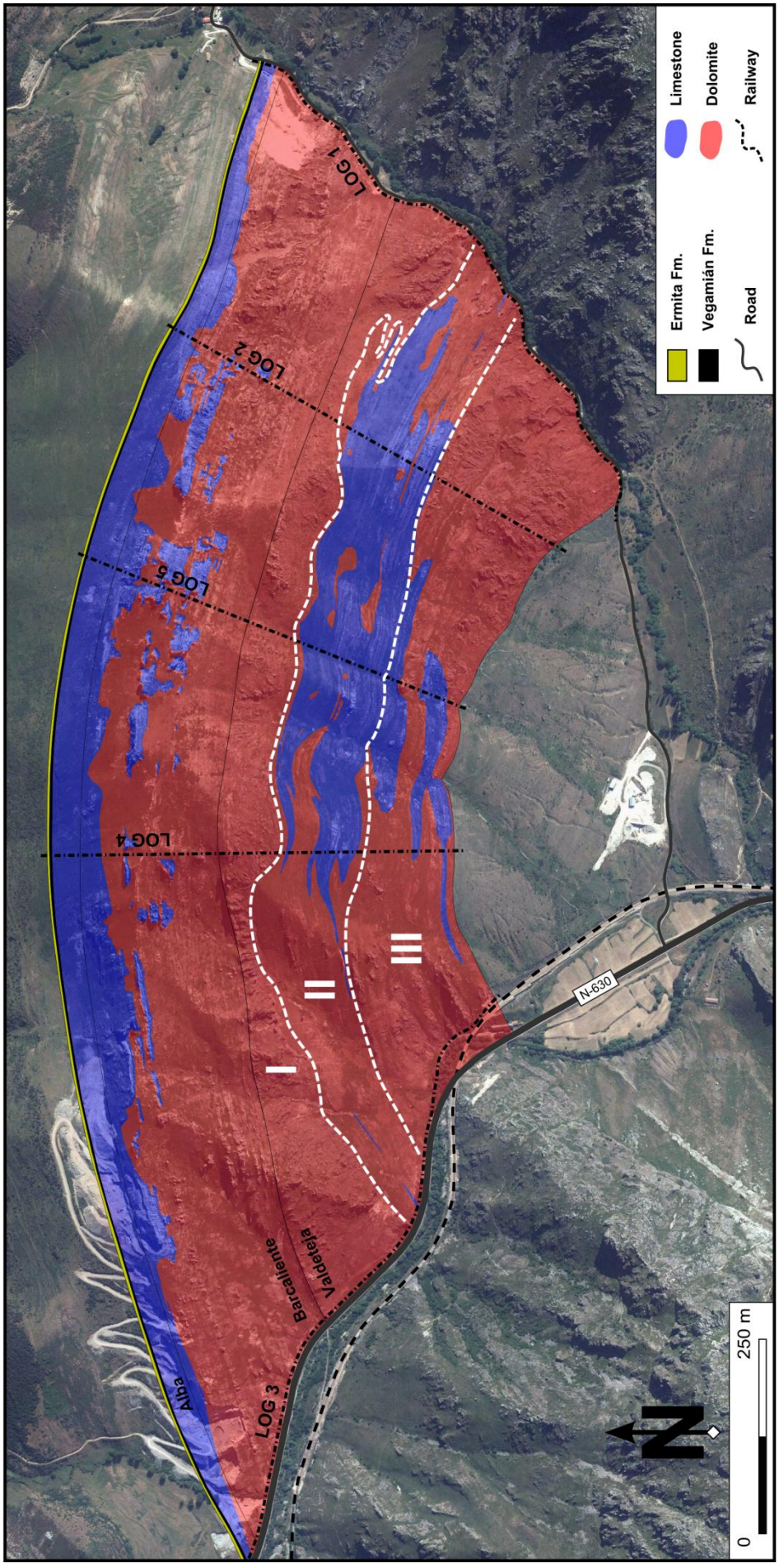

Figure 3.23: Satellite image of KO 1 on which the distribution of dolomite and undolomitized precursor limestone rocks has been indicated. This figure is based on the 5 stratigraphic logs, additional field observations and satellite images. The locations of the logged stratigraphic sections are indicated.

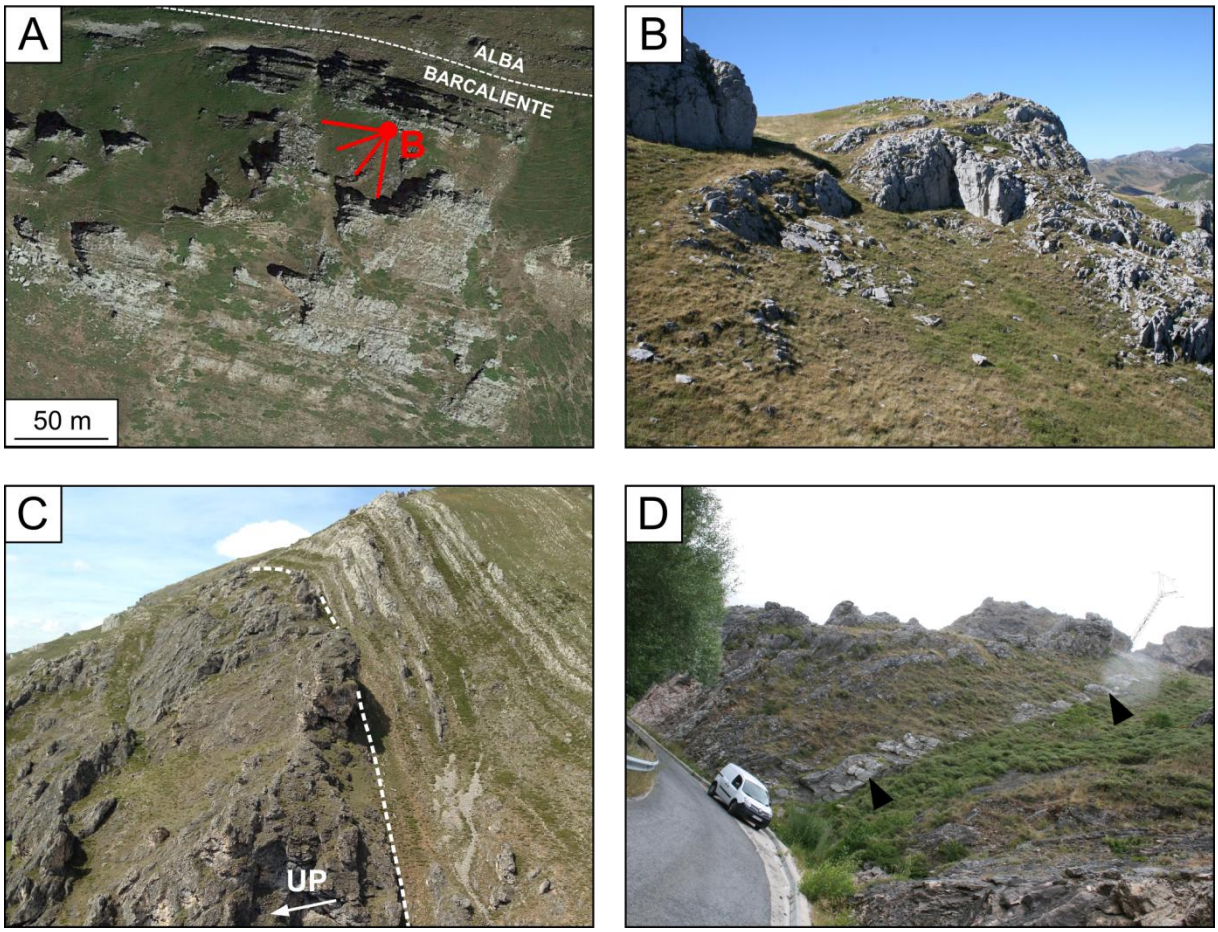

Figure 3.24: Size and geometry of dolomite exposed in KO 1. **(A)** Satellite image of the Barcaliente Fm. exposed on top of KO 1. The contact with the underlying Alba Fm. is indicated with a white dashed line. The dolomitization front is irregular, resulting in the patchy occurrence of undolomitized limestones which stick out of the topography. **(B)** View of undolomitized Barcaliente limestones exposed on top of KO 1. Dolomitized areas are covered with soil and low vegetation. **(C)** Partly dolomitized successions of the Valdeteja Fm., exposed along the Millaró road section. The right side of the photograph shows layered deposits of the second depositional unit composed of calciturbidites and small carbonate buildups. The left side of the photograph shows the massive deposits of the third depositional unit, which are completely dolomitized. Width of view is approximately 200 m. **(D)** Dolomitized small carbonate buildups and layered calciturbidites exposed along the Millaró road section. The bed indicated with black arrows is composed of synsedimentary breccia and is the only bed along the Millaró road section which has not been dolomitized. It overlays finely laminated silt- and claystones (figure 3.5E).

In the Barcaliente Fm. of KO 1, replacive dolomite has a dark gray color and a massive but fine-crystalline appearance (figure 3.25A) with abundant development of zebra textures (figure 3.25B; see Appendix II figure C). The dolomitization front is irregular (figures 3.23 & 3.24A) but sharp, and on a cm- to m-scale bounded by bedding planes, calcite veins and dissolution seams (figures 3.25C & D), which gives the dolomite bodies locally a stratabound nature (e.g. figure 2.5A). In limestones close to the dolomitization front, dolomite crystals occur aligned along parallel laminations (figure 3.25E). These laminations are likely bedding-parallel dissolution seams acting as preferential pathways for dolomitizing fluids. Microscopically, limestones close to dolomitization fronts are characterized by dolomite crystals which occur along these dissolution seams and also in calcite veins (figure 3.25F). Log data indicate that chemical alteration during telogenesis, which resulted in a color change to beige (see section 3.4.2.3), affected approximately 33 % of the exposed HTD rocks in the Barcaliente Fm. (see Appendix II figure D).

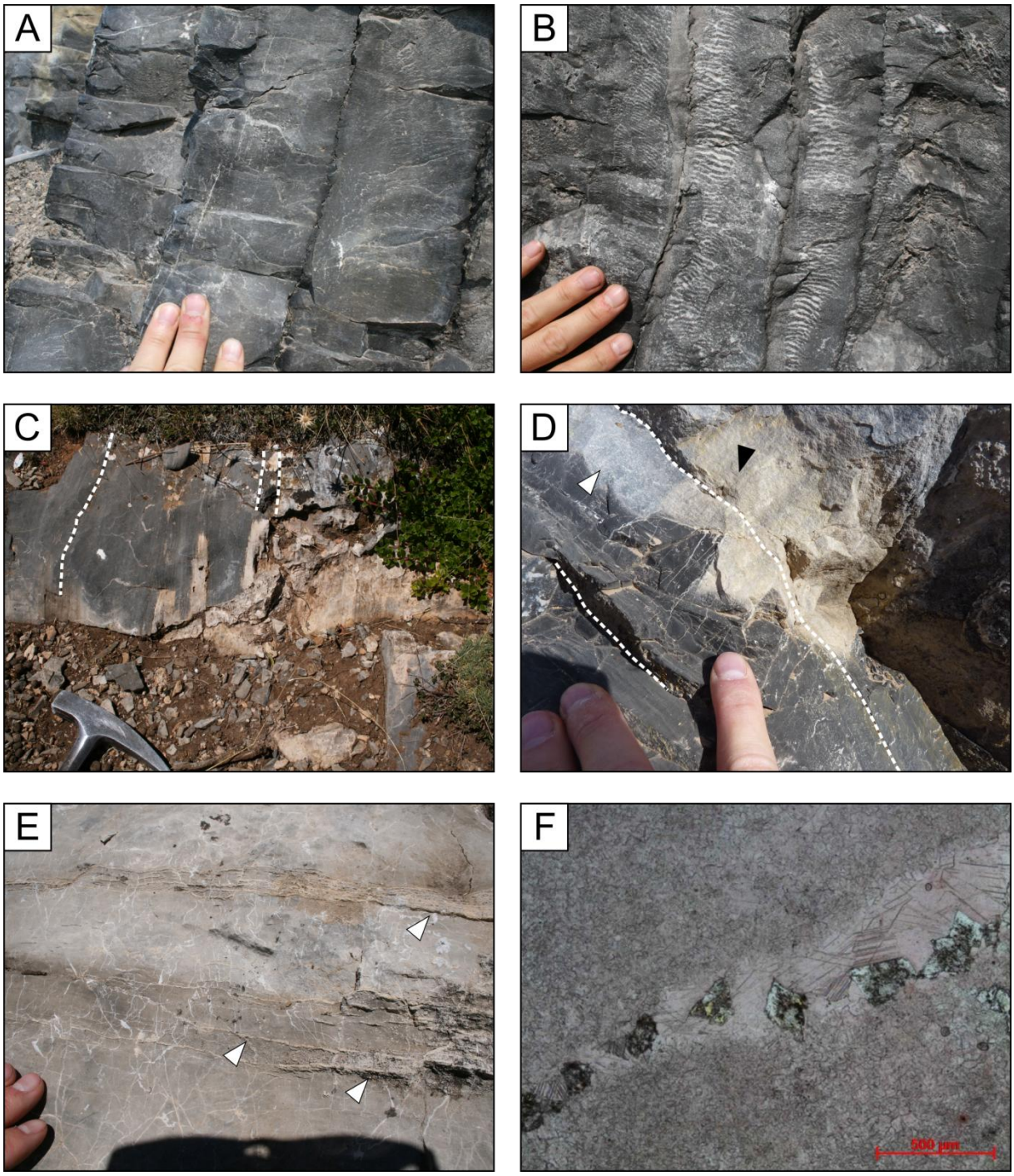

Figure 3.25: Dolomite petrography of the Barcaliente Fm. in KO 1. **(A)** Well-bedded layers of fine-crystalline dolomite in the LCQ. **(B)** Well-bedded layers with development of zebra textures in the LCQ. **(C)** Dolomitization front exposed on top of KO 1. Note the beige color of the dolomite (see section 3.4.2.3), and the influence of bedding planes (white dashed lines) on dolomite distribution. Hammer for scale (32 cm). **(D)** Dolomitization front exposed in the MQ. Dolomite shows gray (white arrow) and beige (black arrow) colors, and the front is bounded by thin Variscan calcite veins. Bedding planes are indicated with white dashed lines. **(E)** Smooth limestone surface close to a dolomitization front on top of KO 1. Note the preferential occurrence of dolomite crystals along bedding-parallel dissolution seams. **(F)** PP photomicrograph of a calcite vein in limestone close to a dolomitization front. Dolomite crystals preferentially replace the calcite vein.

Dolomitized limestones of the Valdeteja Fm. in KO 1 have a wide variety of appearances, reflecting the different precursor limestone depositional facies. The dolomitized mounds of the first depositional unit, as well as smaller buildups in between the calciturbidites and in the third depositional unit, are characterized by layered to massive deposits (figures 3.4A & B). They are generally white or pink (figure 3.26A), and are characterized by the presence of large vugs (figures 3.22A & 3.26A), usually in the massive deposits lacking bedding planes. Many of these vugs resemble molds of bioclasts (figure 3.22I), although their exact origin is hard to determine. Small pockets of zebra textures locally occur in these deposits (figure 3.22E), but they are less voluminous compared to zebra textures in the Barcaliente Fm. Large bodies of hydrothermal breccia often occur in the mounds of the first depositional unit (figure 3.26B).

Calciturbidites making up the second depositional unit are tight dolomitized wacke- to grainstones with gray to beige colors (figures 3.26C & D). Some calciturbidites are coarser, and can be classified as floatstones or rudstones. Bioclasts, mostly echinoderm fragments, are recognizable in some samples (figure 3.26C). Neither zebra textures nor hydrothermal breccia have been observed in dolomitized calciturbidites.

Figure 3.26: Dolomite petrography of the Valdeteja Fm. in KO 1. **(A)** Core of microbial boundstone (SL14RH125) drilled along the Millaró road section. The hole which remained after removing the drilled core can be seen on figure 3.4A. **(B)** Pocket of breccia in dolomitized microbial boundstone along the Millaró road section. **(C)** Sample of tight dolomitized calciturbidites. Dark relics of crinoid fragments are recognizable. **(D)** Plugs of fine (left; SL16RH027) and coarse (right; SL16RH028) dolomitized calciturbidites.

Dolomitized synsedimentary breccia has a gray color, and even though it has been dolomitized, one can often recognize individual clasts (figure 3.7C). The clasts making up the breccia can have a variety of origins, such as microbial boundstone or dolomitized grainstone. Pores can occur in between the clasts, which are usually tight.

3.7.1.3. Matrix porosity and permeability

WS porosimetry was performed on 40 dolomite plugs (diameter of ± 3.3 cm) of the Barcaliente Fm. and 67 dolomite plugs of the Valdeteja Fm., all collected along the 5 stratigraphic sections (see Appendix III). He porosimetry and gas permeability measurements were performed on 6 dolomite plugs of the Barcaliente Fm. and 13 dolomite plugs of the Valdeteja Fm. Medical CT measurements were performed on 4 cores (diameter of ± 9 cm) and microfocus CT was performed on 7 plugs. Porosity or permeability measurements were not performed on precursor limestone rocks, due to their tight nature.

The dolomite plugs of the Barcaliente Fm. have an average WS porosity of 3.7 % and an average permeability of 0.12 mD (table 3.1). They have been subdivided based on dolomite texture (normal replacive or zebra texture) and color (gray or beige; see section 3.4.2.3). The resulting 4 groups of plugs are characterized by significant differences in average matrix porosity values, as confirmed by ANOVA ($p < 0.05$). Both the presence of zebra textures and telogenetic chemical alteration, resulting in a color change from gray to beige (see section 3.4.2.3), greatly increase the porosity of normal replacive dolomite (figure 3.27A). Gray replacive dolomite has the lowest porosity, while beige dolomite with zebra textures has the highest porosity. The pore types encountered in gray replacive dolomite are small intercrystalline pores, which are often blocked with insoluble residue, and occasionally small vugs. Zebra textures and associated sheet-like pores are often arranged in parallel layers (figure 3.27B).

TABLE 3.1: KO 1 Petrophysical data KO 1

Formation	WS Ø (%)	# plugs	EK κ (mD)	# plugs
BARCALIENTE FM.	**3.7**	**40**	**0.12**	**6**
Replacive/gray	1.5	9	0.02	2
Zebra/gray	2.8	4	-	0
Replacive/beige	3.0	12	0.01	1
Zebra/beige	5.7	15	0.23	3
VALDETEJA FM.	**3.8**	**67**	**0.07**	**13**
Grainy	3.8	22	0.22	3
Muddy	4.5	13	0.07	3
Boundstone	4.1	23	0.02	4
Synsed. breccia	2.1	9	0.01	3

Table 3.1: Overview of petrophysical data for dolomite plugs from the Barcaliente and Valdeteja Fm. exposed in KO 1. The Barcaliente Fm. has been subdivided according to dolomite texture (replacive *versus* zebra) and color (gray *versus* beige). The Valdeteja Fm. has been subdivided based on texture of the precursor limestones. Results of water saturation (WS) porosimetry and gas permeability measurements (EK κ) are displayed, as well as the total number of plugs on which measurements have been performed.

The pore types observed in the dolomite plugs of the Barcaliente Fm. are generally too small to create well-connected pore systems (figures 3.27B, C & D), resulting in a very low permeability on average (table 3.1). Only plugs affected by chemical alteration have higher permeability values (e.g. 0.51 mD for plug SL16RH011; see Appendix III). Chemical alteration enlarged pores by dissolution, resulting in a higher porosity and a better connectivity. A remarkable feature observed along the Millaró road section and in the LCQ is the preferential occurrence of porosity in the central part of dolomitized limestone beds (figure 3.27E). Zebra textures and resulting pores seem to preferentially develop in the centre of a bed (figure 3.25B), and not in the dark areas which likely represent dolomitized dissolution seams.

Dolomite plugs of the Valdeteja Fm. have an average WS porosity of 3.8 % and an average matrix permeability of 0.07 mD (table 3.1). The plugs have been subdivided in 4 categories based on their texture (grainy, muddy, boundstone and synsedimentary breccia). The average porosity values of the grainy, muddy and boundstone categories are not significantly different (ANOVA $p > 0.05$; figure 3.28A). Muddy textures are characterized by intercrystalline pores and the development of small vugs and zebra pores (figure 3.29A). The pores are small but locally connected resulting in an average permeability of 0.07 mD. Boundstones are characterized by vuggy and/or biomoldic pores which are generally not well connected (figure 3.29B), resulting in an average permeability of 0.02 mD. The obtained porosity values for grainy textures are related to intercrystalline and vuggy pore types, and in some samples biomoldic (figures 3.22K & 3.29C). Microfocus CT images reveal that many of these pores are aligned along a preferred direction which does not correspond to the bedding of the deposits. This suggests that zebra textures and related pores also occur in more grainy facies, even though this is hardly recognizable during petrographic observations. The matrix permeability of grainy dolomite is low but locally increased due to dissolution. Plugs of synsedimentary breccia are characterized by the lowest matrix porosities (figure 3.28A), of which the significance is confirmed by ANOVA results. Microfocus CT reveals large irregular pores, which might represent pores in between tight clasts. In figure 3.28B, the petrophysical data of plugs from the Valdeteja Fm. have been subdivided according to the three depositional units. Although the boxplots on figure 3.28B suggest a porosity decrease from the first towards the third depositional unit, ANOVA results do not confirm the significance of this variance.

The porosity and permeability data presented above are based on petrophysical measurements performed on small plugs (diameter of ± 3.3 cm), which can be misleading. The plug measurements yield similar matrix porosity values for boundstones, grainy and muddy textures. However, during fieldwork, several exposures of dolomitized boundstone appear more porous (e.g. figures 3.4A; 3.22A & I; 3.26A) compared to grainy and muddy dolomite textures. This is confirmed by analysis of the log data, which indicate that the largest pores are generally observed in dolomitized microbial boundstones (see Appendix II figure E). Nevertheless, plug measurements do not confirm these field observations. This is attributed to the size of the pores (e.g. figures 3.22I; 3.26A; 3.29B), which often approaches the size of the small plugs used for porosity and permeability measurements. Dolomitized boundstones require a representative elementary volume (REV) larger than the small plugs, in order to quantify their porosity. Large cores (diameter of ± 9 cm) are more suitable to determine the petrophysical characteristics of porous dolomitized boundstones. Medical CT measurements on a large core (figure 3.28C) and image analysis of outcrop photographs (figures 3.28D, E & F) indicate that locally, the porosity in

dolomitized boundstones exceeds the matrix porosity values obtained from small plug measurements. The average matrix porosity of dolomitized boundstones (4.1 %; WS porosimetry; table 3.1) determined through plug measurements slightly underestimates the true porosity of porous exposures of dolomitized boundstones. Additional medical CT measurements, complemented with porosity and permeability calculations, would allow a more detailed porosity quantification.

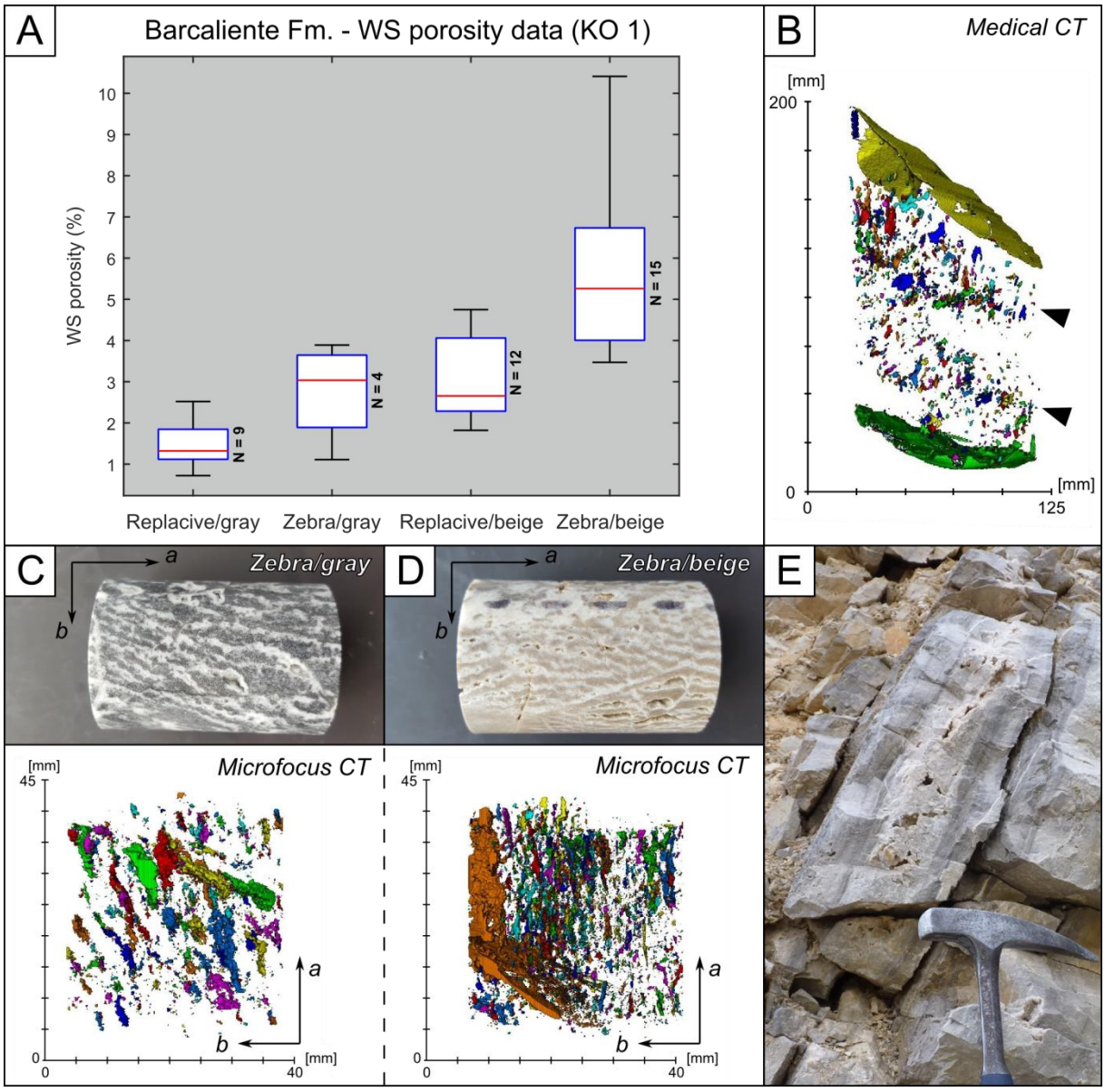

Figure 3.27: Overview of petrophysical data for dolomite samples of the Barcaliente Fm. in KO 1. **(A)** Boxplots showing the WS porosity data of replacive/gray, zebra/gray, replacive/beige and zebra/beige plugs. **(B)** Reconstructed and labeled pore network of a large core of beige zebra dolomite obtained through medical CT scanning. Zebra pores are oriented in 2 parallel layers (black arrows) running through the core. The large yellow top and green bottom of the core are artifacts. Core has been drilled in dolomite from the Barcaliente Fm. close to Caldas de Luna. **(C)** Reconstructed and labeled pore network of a small plug of gray zebra dolomite (SL16RH051b) obtained through microfocus CT scanning. **(D)** Reconstructed and labeled pore network of a small plug of beige zebra dolomite (SL16RH045a) obtained through microfocus CT scanning. **(E)** Example of a dolomitized limestone bed in the LCQ. Note the preferential occurrence of porosity in the central part of the bed, the overall beige color and the darker edges.

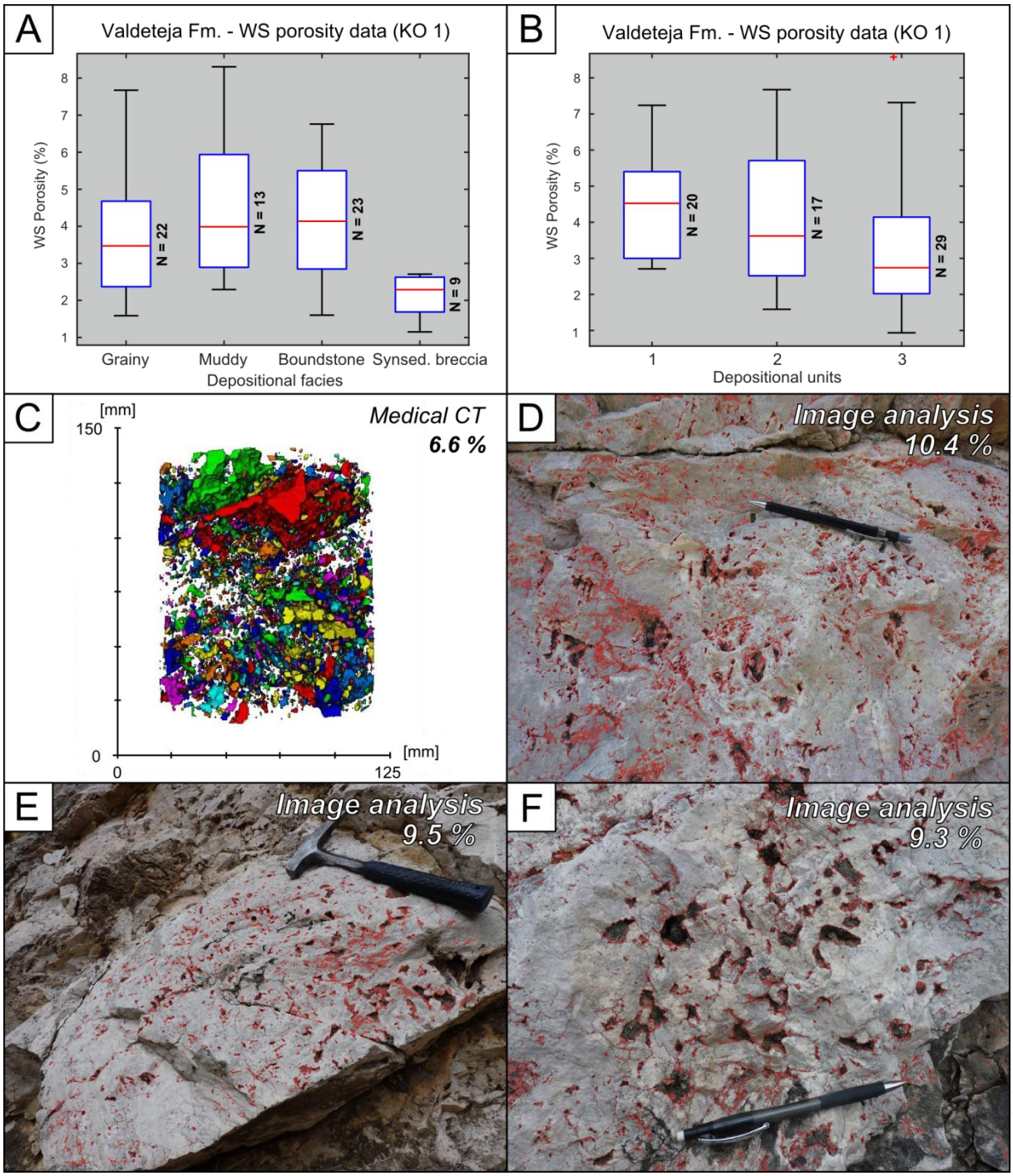

Figure 3.28: Overview of petrophysical data for dolomite samples of the Valdeteja Fm. in KO 1. **(A)** Boxplots showing the WS porosity data of grainy dolomite, muddy dolomite, dolomitized boundstone and dolomitized synsedimentary breccia. **(B)** Boxplots showing the WS porosity data of the plugs from the three depositional units. **(C)** Reconstructed and labeled pore network of a large core (SL14RH125) of dolomitized microbial boundstone obtained through medical CT scanning. An average of 6.6 % porosity is obtained through pixel counting in Matlab. **(D)** Photograph of dolomitized microbial boundstone (Millaró road section) on which pores have been delineated with red lines based on image analysis with JMicroVision. A total of 10.4 % porosity is obtained for the entire image. **(E)** Photograph of dolomitized microbial boundstone (Millaró road section) on which pores have been delineated with red lines based on image analysis with JMicroVision. A total of 9.5 % porosity is obtained for the exposed boundstone in the central part of the image. **(F)** Photograph of dolomitized microbial boundstone (Millaró road section) on which pores have been delineated with red lines based on image analysis with JMicroVision. A total of 9.3 % porosity is obtained for the entire image.

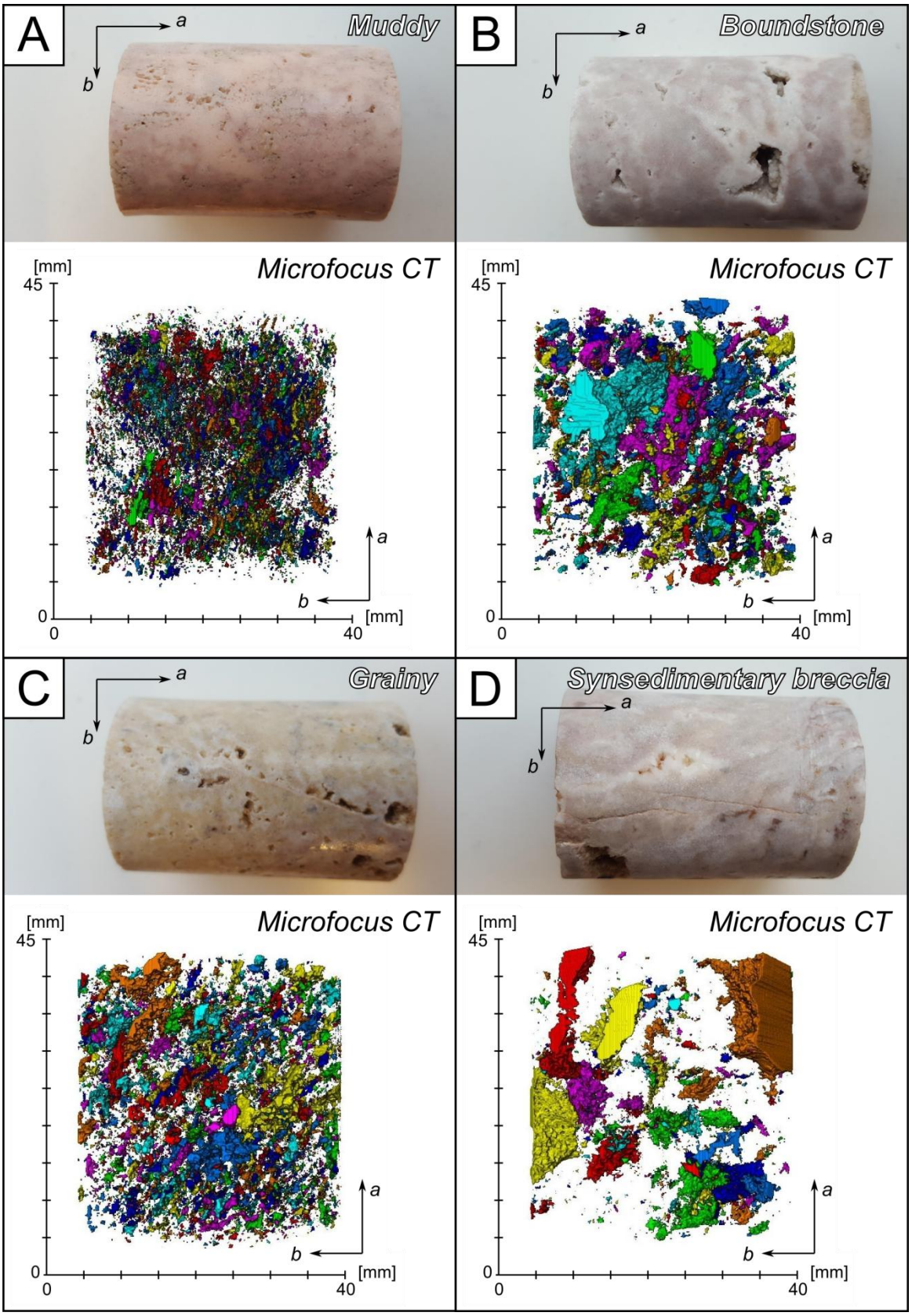

Figure 3.29: Reconstructed and labeled pore networks for dolomite plugs from the Valdeteja Fm. in KO 1, obtained through microfocus CT scanning. (A) Muddy dolomite. Sample SL16RH063. (B) Boundstone. Sample SL16RH015. (C) Grainstone. Sample SL16RH028. (D) Synsedimentary breccia. Sample SL16RH036.

Also for synsedimentary breccia, the pore sizes sometimes exceed the size of small plugs (figure 3.29D), which suggest that the plug size is smaller than the REV. Pore sizes in grainy and muddy textures are significantly smaller compared to the size of plugs. As a result, porosity data from plug measurements represent a close estimation of the true matrix porosity of these dolomite textures.

3.7.1.4. Dolomitization model

The massive circulation of dolomitizing fluids affecting KO 1 was likely controlled by fracture networks, after which the different lithology and stratigraphic frameworks of the Barcaliente and Valdeteja Fm. resulted in distinctly different dolomitization styles. Both valleys bordering the outcrop are most intensely affected by dolomitization, which suggests that they correspond to the most fractured areas, or potentially to the locations of larger fault systems.

In the uniform mudstones of the Barcaliente Fm., migration of dolomitizing fluids occurred along fractures. To a limited extent, fluids also migrated along bedding planes, which are essentially composed of diagenetic dissolution seams (figure 3.25E). In a later phase, these dolomitized dissolution seams might have acted as baffles for further dolomitization, resulting in the local stratabound nature of dolomite geobodies (figures 2.5A; 3.24A). Similar observations have been reported for dolomite occurrences in the Maestrat Basin in Eastern Spain (Martín-Martín et al., 2017), where stylolites play an important role in the distribution of dolomite. Both the uniform depositional facies of the Barcaliente Fm., as well as its uniform bed thickness, resulted in a uniform dolomitization style with zebra texture and associated porosity development in the central part of beds, in between dark-colored and usually coarse-crystalline dolomitized dissolution seams. The dark color of dolomitized dissolution seams in the beige dolomite successions exposed along both road sections (e.g. figures 3.22O & 3.27E) is likely the result of chemical alteration during exposure. Chemical alteration, and the associated color change, seems to preferentially affect the central parts of beds, which are more porous and fine-crystalline.

The complex stratigraphic framework and internal structure of the Valdeteja Fm. played a key role in the distribution of dolomite in this formation. Three depositional units have been recognized, and they likely correspond to the three growth phases described by Chesnel et al. (2015) for the Bashkirian Valdorria carbonate platform in KO 2 (figure 3.9B; see sections 3.3.1.2 & 3.3.2). The first and third depositional units in KO 1, mostly composed of microbial carbonate mounds and synsedimentary breccia respectively, are almost entirely dolomitized while the second depositional unit is not. Fluid circulation must have been more important in the first and third depositional units and restricted in the calciturbidites. This difference in fluid circulation cannot have been caused by the amount of primary porosity in the depositional units. The precursor limestones in all three units were tight prior to dolomitization, and although microbial carbonate mounds and bodies of synsedimentary breccia are known to have high primary porosities (see section 3.3.1), these primary pores were completely occluded during burial and Variscan compression. Stratigraphic properties which might have restricted fluid flow in the calciturbidites of the second depositional unit are fine-grained siliciclastic intercalations, as well as elongated chert nodules (section 3.4.1). The undolomitized limestone bed which can be observed in figure 3.24D, has been deposited on thin layers of siliciclastics (figure 3.5E), which is potentially the main

reason for the fact that this particular limestone layer has not been dolomitized. An additional feature which might influence fluid circulation is a difference in the mechanical and structural behavior of the precursor limestones in the different depositional units. The mechanical behavior of the precursor limestones has not been studied in detail, since the first and third depositional units have been intensely affected by dolomitization. However, undolomitized exposures and information from KO 2 suggest that massive microbial boundstones are not intensely fractured (e.g. figure 3.10A). On the other hand, the fracture abundance in undolomitized calciturbidite successions is higher (figures 3.5A & 3.6B). Nevertheless, dolomitization was most important in massive mounds composed of boundstones and synsedimentary breccia, which is illustrated by the preferential occurrence of hydrothermal breccia in these deposits. The variation in fluid circulation was thus likely the result of stratigraphic controls. Fine-grained siliciclastic intercalations acted as baffles for fluid flow in the second depositional unit composed of bedded calciturbidites. As a result, fluid circulation was more important in the massive deposits of boundstone and synsedimentary breccia.

3.7.2. Dolomite in KO 2

3.7.2.1. Size and geometry

The dark gray HTD geobodies exposed in KO 2 are narrow subvertical bodies of a few meters wide cutting through the light gray limestones of the Valdorria platform (Valdeteja Fm.; figures 3.30A & B). Some of the larger geobodies in KO 2 are stratabound and follow depositional contacts (figure 3.9A). The geobodies studied in this section are located at the eastern side of the Río Curueño valley (figure 3.8), in prograding slope deposits (peloidal micrite-rich boundstones) of growth phase 2 of the Valdorria platform (figure 3.9B; Chesnel et al., 2015). The geometry of the dolomite geobodies is controlled by subvertical fractures with a general orientation of 270/90 (figure 3.31A), similar to many important valleys and gorges cutting through the entire Valdorria carbonate platform (figure 3.9B). An additional fracture set, with subhorizontal orientations of 250/00, occurs throughout KO 2 (figure 3.31A).

3.7.2.2. Petrography

The exposed contact between dolomite and limestone rocks is very abrupt and sharp (figure 3.30B), and is locally bounded by subvertical fractures (270/90) and Variscan calcite veins on a cm- to dm-scale. Dolomite veins, with similar subvertical orientations, are observed in limestones bordering the dolomite geobodies (figure 3.10A). The crystal size of the dolomite samples is variable, ranging from unimodal fine-crystalline to coarse-crystalline. Coarse dolomite crystals show rare signs of a second dolomite phase overgrowing the first one. The dolomite samples are intensely fractured and brecciated, and cemented with hydrothermal calcite (figure 3.30C). Fracturing, brecciation and calcite cementation preferentially affected specific zones with similar subvertical orientations (270/90; e.g. figure 3.16A). The calcite cement partly dedolomitized dolomite clasts (figure 3.30D) and shows bright orange luminescence (figure 3.30E) which corresponds to the phase of hydrothermal calcite cementation following dolomitization (Gasparrini et al., 2006a). The calcite phase cementing fractures and breccias is locally associated with quartz. Calcite veins in the nearby precursor limestone rocks crosscut dolomite veins and are bounded by rims of quartz crystals sticking out of the limestone surface due to differential

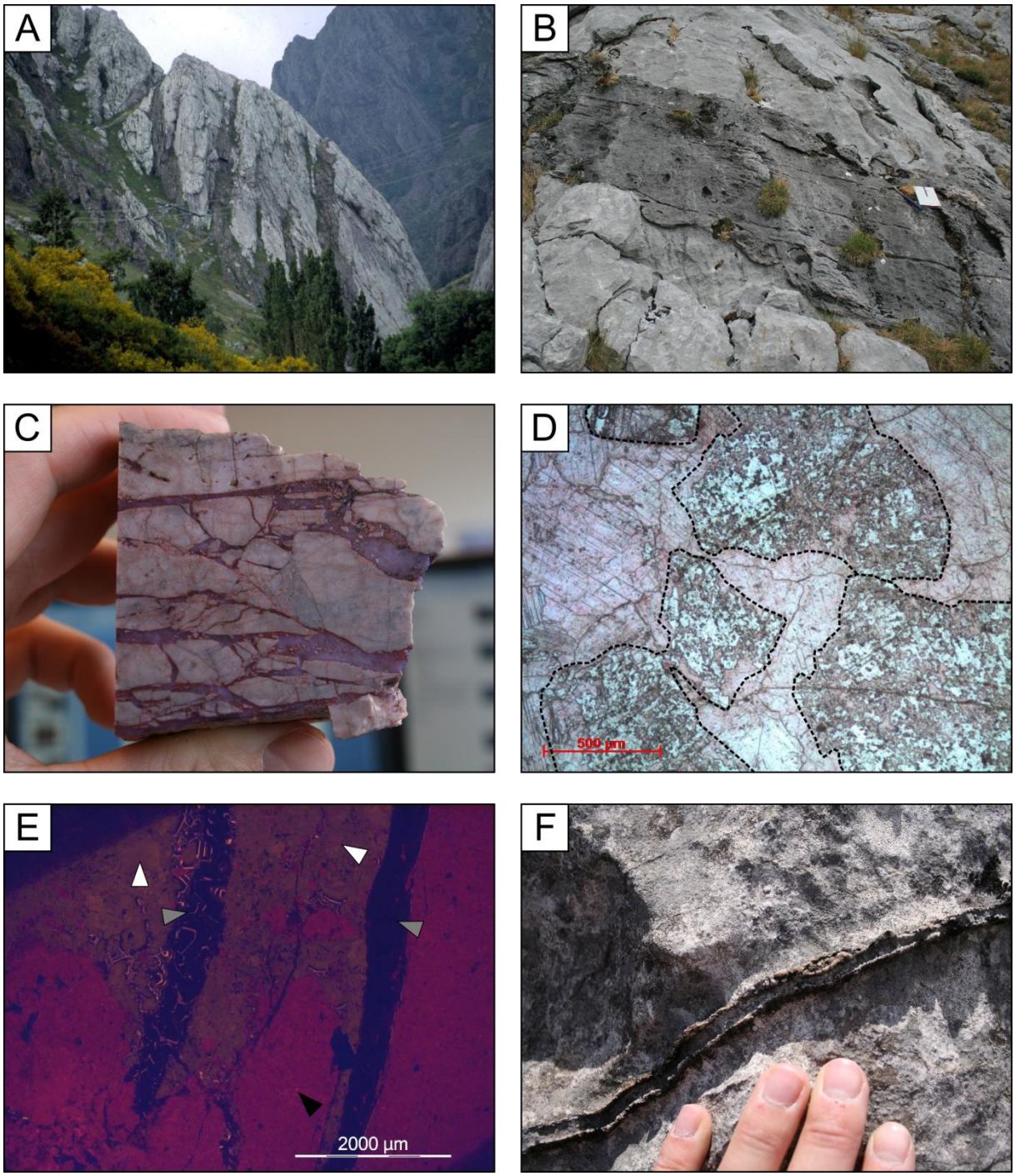

Figure 3.30: Geometry and petrography of dolomite geobodies exposed in KO 2. **(A)** Eastern valley side of KO 2 showing subvertical dolomite geobodies in dark gray cutting through light gray limestones. Photograph from Gasparrini et al. (2006a). **(B)** Exposed dolomite geobody approximately 1.5 m in width. Fieldbook for scale (22 cm). **(C)** Stained dolomite sample brecciated and cemented with calcite (red stained). **(D)** PP photomicrograph of brecciated dolomite sample cemented by calcite (red stained). Dolomite clasts have been partly dedolomitized and are delineated with black dashed lines. **(E)** CL photomicrograph of brecciated dolomite sample. Dolomite clasts (black arrow) float in a matrix of hydrothermal calcite (white arrows). A second fracturing event followed by meteoric calcite cementation affected the sample. **(F)** Vein of hydrothermal calcite crosscutting limestone and bounded by quartz crystals.

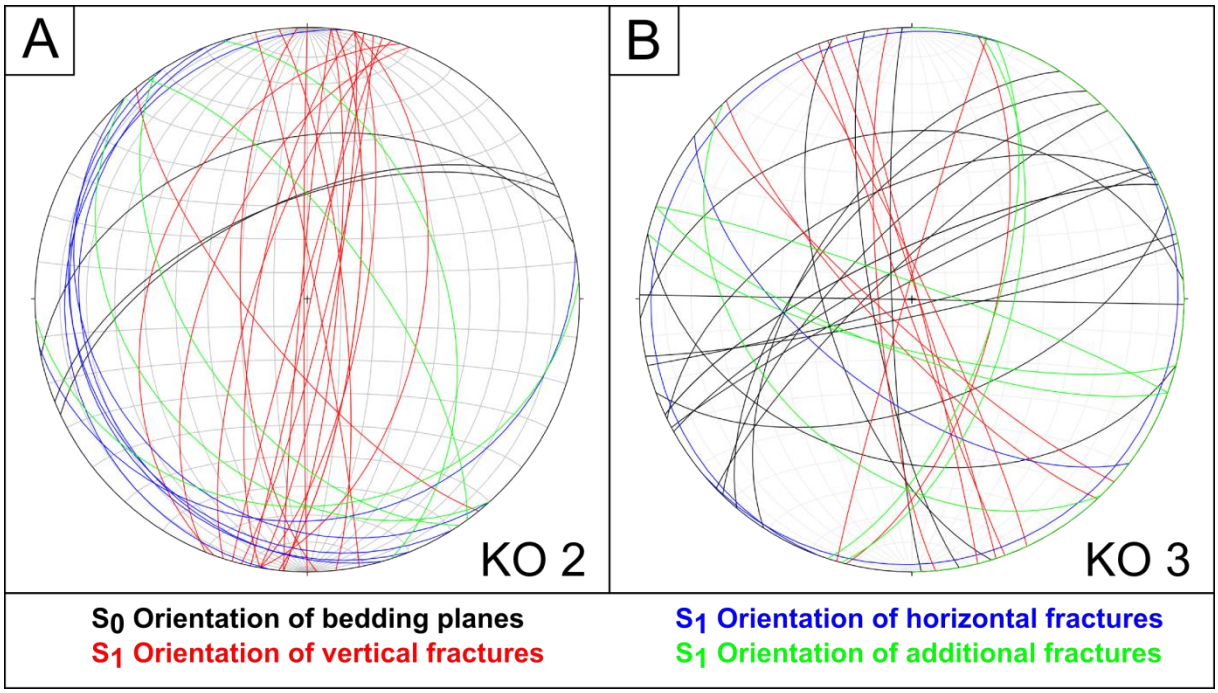

Figure 3.31: Stereographic projection of structural data. **(A)** Orientations of bedding planes and fractures measured in KO 2. **(B)** Orientations of bedding planes and fractures measured in KO 3.

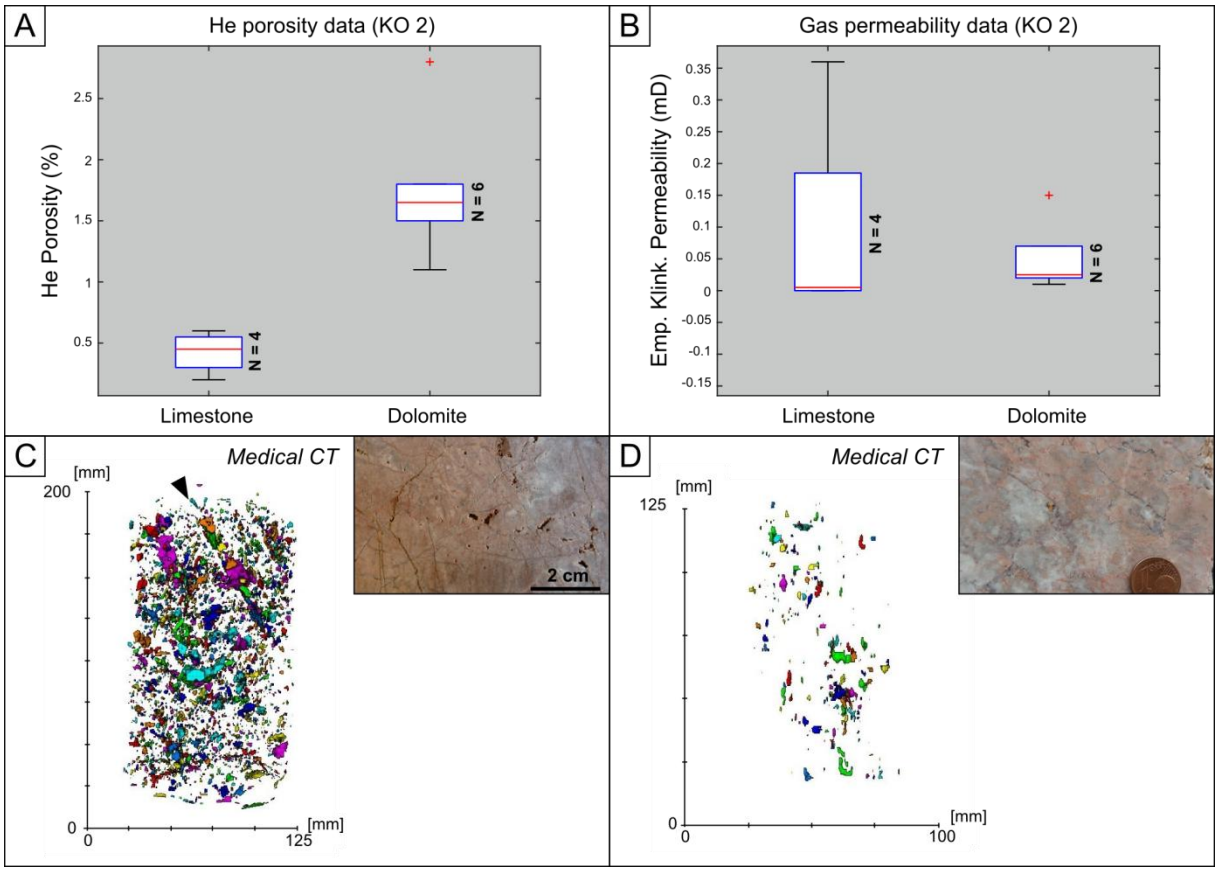

Figure 3.32: Overview of petrophysical data for limestone and dolomite plugs of the Valdeteja Fm. in KO 2. **(A)** Boxplots showing the He porosity data of limestone and dolomite plugs. **(B)** Boxplots showing the gas permeability data of limestone and dolomite plugs. **(C)** Reconstructed and labeled pore network of a large core of dolomite (SL14RH122) obtained through medical CT scanning. Note preferential dissolution along a small fracture (black arrow). **(D)** Reconstructed and labeled pore network of a large core of dolomite (SL15JP016) obtained through medical CT scanning.

weathering (figure 3.30F). The orientation of these calcite veins corresponds to both subvertical and subhorizontal fracture sets (figure 3.31A). Additional fracturing and cementation with meteoric calcite (figure 3.30E; cfr. Gasparrini et al., 2006a) further affected the brecciated dolomite bodies.

3.7.2.3. Matrix porosity and permeability

WS and He porosity measurements, as well as gas permeability measurements, were performed on 4 limestone plugs and 6 dolomite plugs from the Valdeteja Fm. in KO 2 (see Appendix III). Medical CT scanning was performed on 5 large cores.

The matrix porosity of the undolomitized peloidal micrite-rich boundstones ranges between 0.2 and 0.6 %, with an average porosity of 0.4 % (He porosimetry; figure 3.32A). The only visible pores in the limestone samples are caused by local dissolution along small fractures or stylolites. Matrix porosity values obtained for dolomite samples are significantly higher compared to the precursor limestone rocks (confirmed with ANOVA), and average around 1.8 % (1.1 – 2.8 % range; He porosimetry; figure 3.32A). These higher porosities are related to dissolution of dolomite crystals and calcite cement. Dissolution is apparent in all dolomite samples of KO 2 and creates dissolution-enlarged intercrystalline pores (figure 3.22H), crystal-moldic pores (figure 3.22M) or channel pores (figures 3.19B & 3.32C). The connectivity between these pore types is usually small, resulting in badly connected pore networks (figures 3.32C & D). The permeability of the dolomite samples is 0.025 mD on average, compared to 0.005 mD for the precursor limestone rocks (figure 3.32B). ANOVA results indicate that this difference is not significant. The skewing towards higher permeabilities in the limestone samples (figure 3.32B) is cause by a plug containing a dissolution-enlarged fracture.

3.7.2.4. Dolomitization model

The limestones of the Valdorria platform have been affected by dolomitization mostly along subvertical fractures predominantly N-S oriented and cutting perpendicular through the platform limestones. The pathways followed by circulating fluids were likely similar compared to KO 1 (i.e. fracture zones), but the available volume of dolomitizing fluids was less important in KO 2, resulting in relatively small fracture-controlled dolomite geobodies. Dolomitization, and associated hydrothermal calcite cementation, are likely caused by limited fluid expulsion related to separate episodes of fracture reactivation. This is indicated by the occurrence of dolomite- and calcite-cemented veins surrounding the fracture zones, which have similar subvertical orientations and were thus active fluid conduits at the moment of dolomitization. The coarse-crystalline dolomite samples showing overgrowths might have been recrystallized by a later dolomitization phase (see section 3.4.2.2). The fracture zones were shortly reactivated during their Post-Variscan history, and cemented by meteoric calcite (figure 3.30E). The timing of this reactivation is hard to constrain. Reactivation might have occurred in response to Alpine uplift, or in response to more recent tectonic activity. Current exposure of the dolomite geobodies results in dissolution along fractures and stylolites. Late- to Post-Variscan dolomitization along the fractures likely created vuggy porosity, which became occluded following limited dolomite overgrowth, brecciation and calcite cementation. The current pores are mainly the result of dissolution along fractures, which are more abundant in dolomite compared to the precursor limestone rocks.

3.7.3. Dolomite in KO 3

3.7.3.1. Size and geometry

The HTD geobodies exposed in KO 3 are unique in the Bodón Unit. They occur along the fault trace of the Correcilla Thrust exposed in the southern fold limb of the Montuerto Syncline (figures 3.11 & 3.12A; see section 3.3.3) and represent the dolomitized fault breccia. Two main HTD bodies, roughly of equal size (± 0.04 km²), can be distinguished (figure 3.33). One geobody is located in the western part of KO 3, directly south of the village of Montuerto, while the second body is located more to the east. In between both bodies, in the central part of KO 3, the fault zone has not been dolomitized and the tectonic fault breccia is exposed (figure 3.15C). The HTD bodies encompass parts of the Láncara and Barcaliente Fm., as well as the central part of the fault zone. The dolomitized formations are well-bedded but covered with soil and are only locally exposed (figure 3.34A), while the dolomitized central part of the fault zone sticks out of the mountainside (figures 3.12A & 3.34B). Due to their prominent appearance and dark color, they are referred to as *'las rocas negras'* ('the black rocks') by the villagers of Montuerto. Several mineralizations (e.g. galena, sphalerite and barite) have been mined along the fault trace of the Correcilla Thrust during the first half of the 20th century (Evers, 1967).

3.7.3.2. Petrography

The dolomitized Láncara and Barcaliente Fm. are generally coarse-crystalline with a typical gray to orange patina (figures 3.22N & 3.34A), which is unique for dolomite rocks in the Bodón Unit. Most of the exposed dolomitized beds are intensely affected by fracturing and calcite cementation (figure 3.22N), similar to the HTD exposures of KO 2. Subvertical and subhorizontal fracture sets occur throughout KO 3 and have mainly defined the occurrence and orientation of dolomite and calcite veins (figure 3.31B).

The fracturing intensity increases towards the main fault zone, along which the beds are intensely brecciated (figure 3.34B). Dolomite samples from the Láncara and Barcaliente Fm. show a distinct macroscopic mosaic of dark gray crystals in a light gray matrix (figure 3.35A). Microscopically, some dolomite crystals are clearly overgrown (figure 3.35B), and all dolomite samples from KO 3 are non-luminescent. Dolomite cement rims are thick and show featherlike crystals under the microscope (figures 3.16B & 3.35A).

The central parts of both dolomite bodies (*las rocas negras*), corresponding to the center of the fault zone, are made up of a coarse-crystalline matrix with a metallic gray color and strong orange to rust-colored patina (figures 3.16C; 3.22B & 3.34B). Macroscopically, the samples resemble the undolomitized central tectonic fault breccia of the Correcilla Thrust in between both dolomite geobodies (figure 3.35C). The dolomite crystals are enriched in Fe, as evidenced based on their blue stain (figure 3.35D) and orange patina. In several samples, ghosts of small clasts are visible in the coarse-crystalline matrix. Pores show little hydrothermal dolomite or calcite cementation, but are intensely affected by dissolution and meteoric calcite cementation during telogenesis (figures 3.35D & E). The orange patina is due to intense oxidation of Fe following dissolution of dolomite crystals (figure 3.35F).

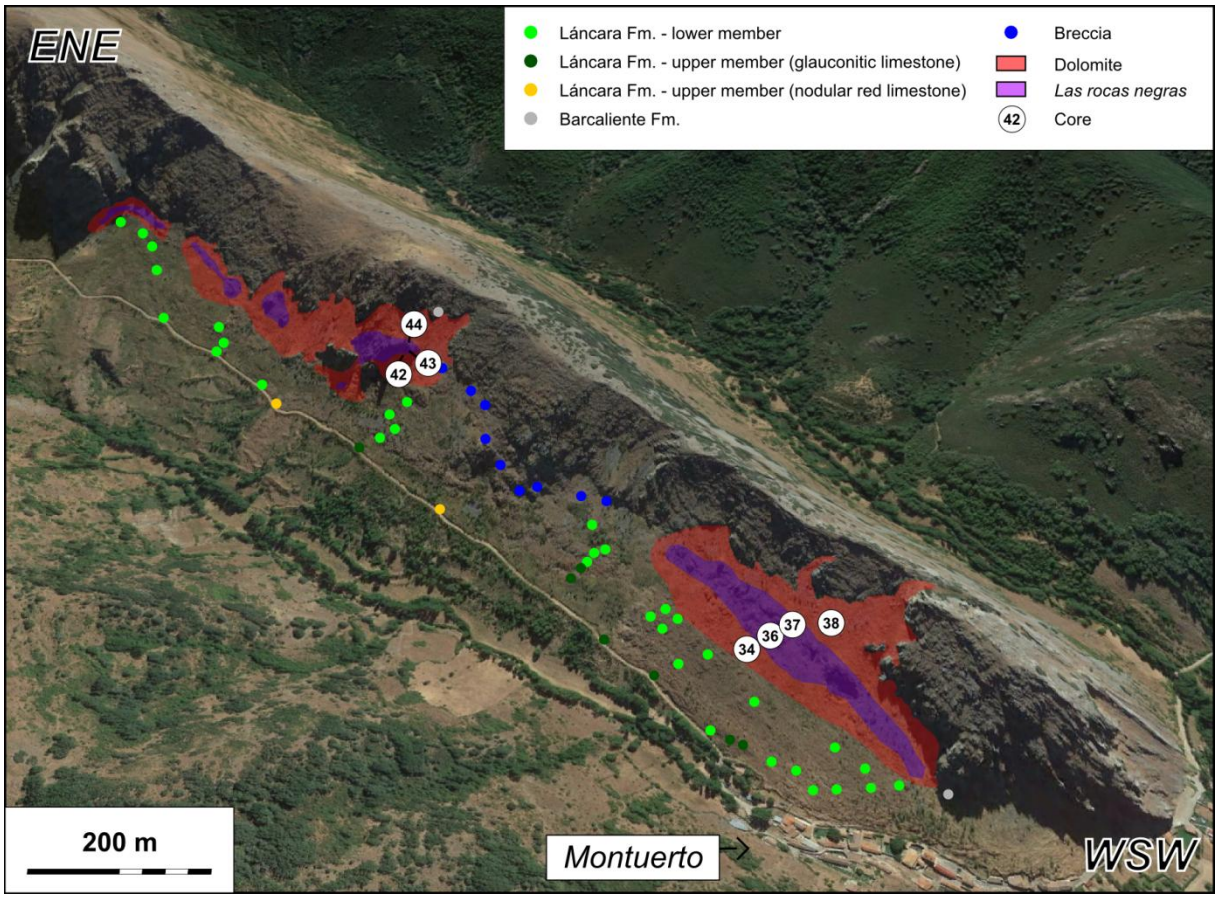

Figure 3.33: ENE-WSW aerial view of KO 3 with indication of the 2 main dolomite geobodies (colored in red and purple), precursor limestone stratigraphy (indicated with colored dots) and sample locations.

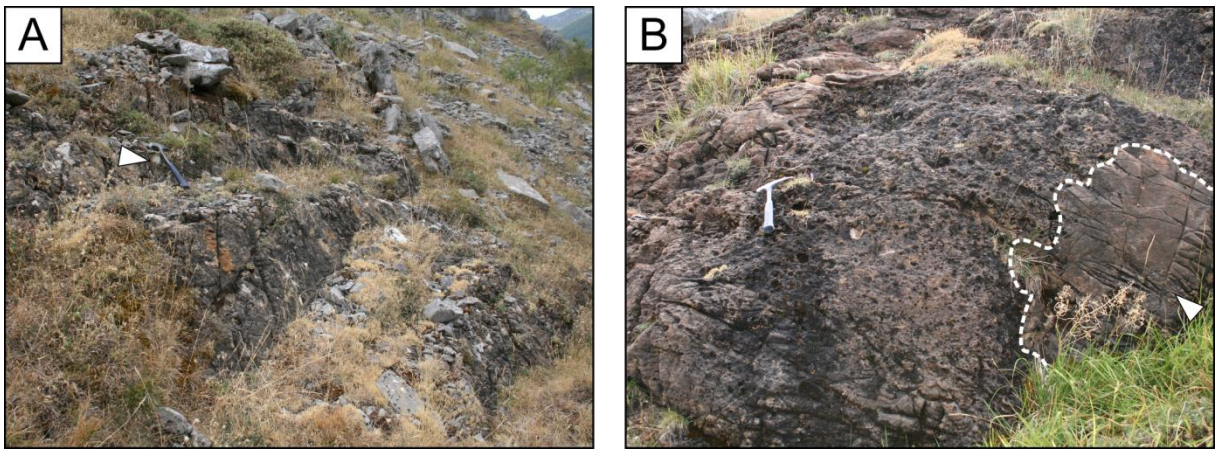

Figure 3.34: Exposures of dolomite in KO 3. **(A)** Bedded dolomitized limestones of the Barcaliente Fm. Hammer for scale (32 cm; white arrow). **(B)** Exposure of the dolomitized central fault gouge. In the lower right corner, a large dolomite clast belonging to the Barcaliente Fm. is exposed (white dashed line and arrow).

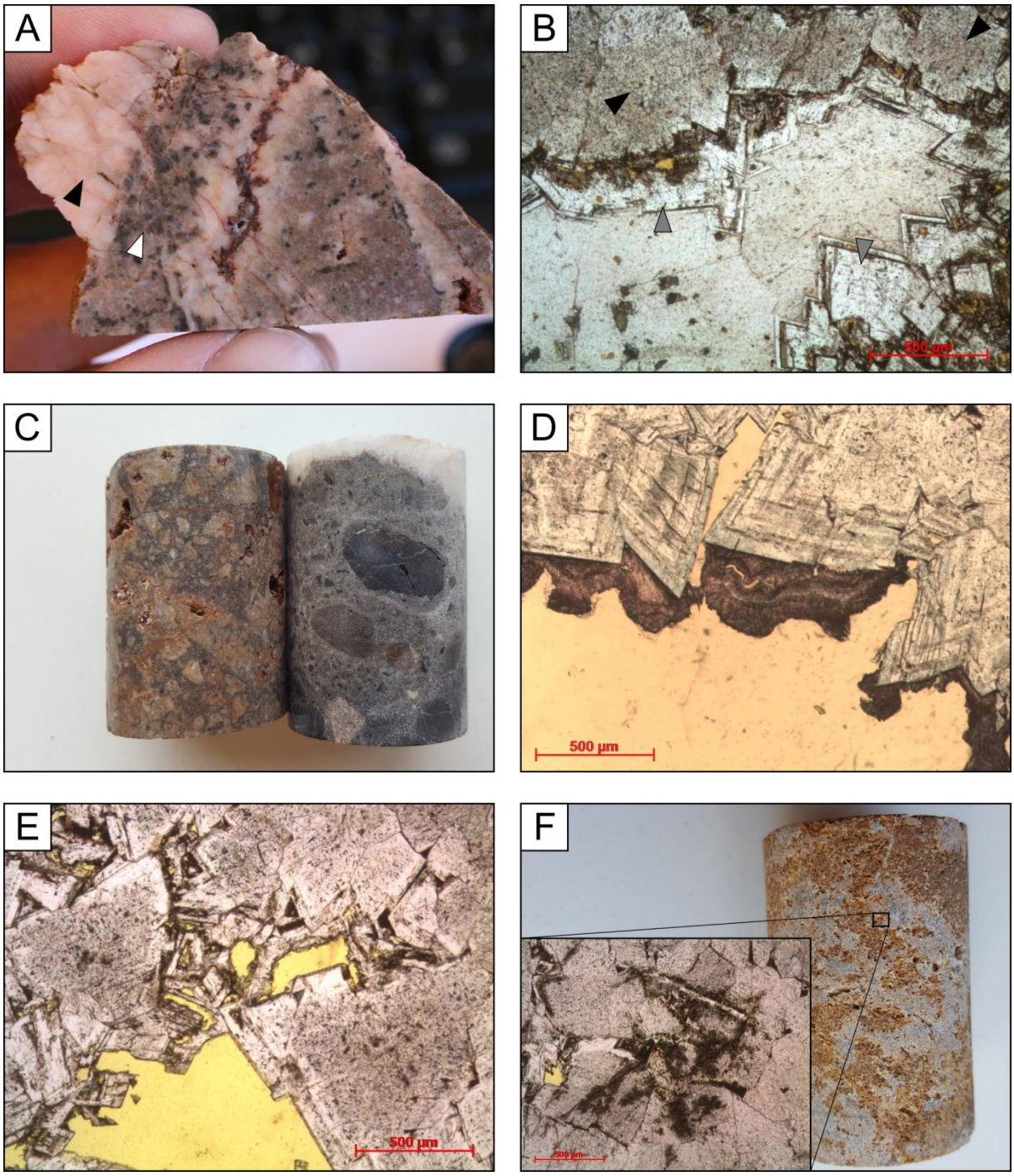

Figure 3.35: Petrography of dolomite samples collected in KO 3. **(A)** A sample of dolomitized limestone from the Barcaliente Fm., which is completely different compared to Barcaliente samples from elsewhere (e.g. figures 2.5D). The sample is composed of a mosaic of dark crystals in a light gray matrix (white arrow), and thick rims of feather-like cement crystals (black arrow). **(B)** PP photomicrograph of a dolomite sample from the Barcaliente Fm. (SL15JP038). The original dolomite crystals (black arrow) are overgrown by a second phase of transparent dolomite cement (gray arrows). **(C)** Plugs of dolomitized (left; SL15JP044) and undolomitized (right; SL15JP042) fault gouge. **(D)** PP photomicrograph of Fe-rich dolomite crystals with pendant meteoric calcite cements (stained red). **(E)** PP photomicrograph of dolomite crystals affected by dissolution. Sample SL15JP036. **(F)** Plug and PP photomicrograph of dolomitized fault gouge affected by dissolution and oxidation of Fe-rich dolomite. Sample SL15JP043.

3.7.3.3. Matrix porosity and permeability

WS, He porosity and gas permeability measurements were performed on 2 dolomite plugs from the dolomitized Láncara and Barcaliente Fm. and on 5 plugs from the central dolomitized part of the fault zone (*las rocas negras*; see Appendix III). Measurements were also performed on 1 sample of the dolomitized fault zone which was reactivated during the Alpine Orogeny (see section 3.4.3.2). Although the amount of plugs from KO 3 is low, the petrophysical data allow to make some important conclusions.

The dolomitized central part of the fault zone (*las rocas negras*) exhibits the highest matrix porosities observed for dolomite in the Bodón Unit. They range between 4.3 and 15.4 % with an average of 9.6 % (figure 3.36A; He porosity). The high porosity is caused by a combination of intercrystalline and vuggy pores, which are often dissolution-enlarged (figure 3.35E). The vugs likely represent dissolved clasts in the fault breccia. Both pore types are less important in the dolomitized Láncara and Barcaliente Fm. (figures 3.35A & 3.36A), resulting in lower matrix porosities of 4.3 % on average (range between 3.0 and 6.3 %; He porosity). The significance of the variation in porosity between the central part of the fault zone and the dolomitized Láncara and Barcaliente Fm. is not confirmed with ANOVA. This is likely a result of the low amount of plugs available for KO 3, and especially for the Láncara and Barcaliente Fm. The Alpine breccia sample has an average porosity of 2.2 % (figure 3.36A; He porosity). Despite the high porosity in the central part of the fault zone, the matrix permeability remains low (0.07 mD on average) due to a bad connectivity between pores (figure 3.36B). Open fractures locally increase the connectivity, in both the central dolomitized fault zone (figure 3.36C) and dolomitized Barcaliente limestones (figure 3.36D).

3.7.3.4. Dolomitization model

Dolomitizing fluids affecting the southern fold limb of the Montuerto Syncline migrated along the fault breccia of the Correcilla Thrust, which formed during the Variscan Orogeny and was reactivated during orocline formation (and during the Alpine Orogeny; Potent and Reuther, 2000). This is unique in the Bodón Unit, where dolomitization is mostly controlled by fracture networks (e.g. in KO 1 and KO 2). The fault breccia as well as the Láncara and Barcaliente limestones bordering it have been partly dolomitized. Fe-rich fluids likely overprinted and recrystallized primary dolomite rocks along the fault zone, which resulted in tight dolomite (e.g. figures 3.35A & 3.36D) but a very porous central part of the fault zone (e.g. figures 3.16A & 3.36C). This central part of the fault zone (*las rocas negras*) likely represents a dolomitized fine-grained fault gouge (figure 3.34B).

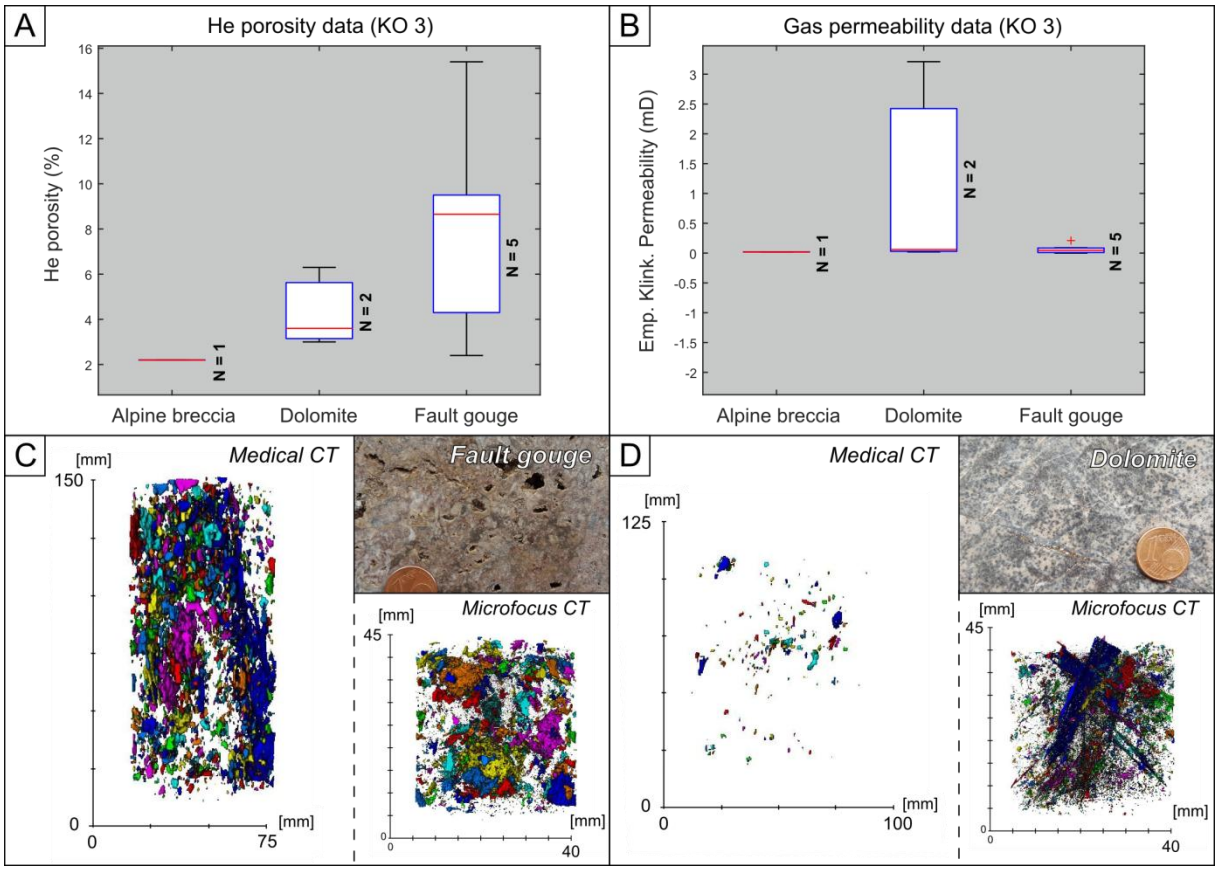

Figure 3.36: Overview of petrophysical data for samples of KO 3. **(A)** Boxplots showing the He porosity data from plugs of Alpine breccia, dolomitized Láncara and Barcaliente limestones and dolomtized fault gouge. **(B)** Boxplots showing the gas permeability data from the same samples. **(C)** Reconstructed and labeled pore network of both a large core and small plug of dolomitized fault gouge (SL15JP044) obtained through medical and microfocus CT scanning. An open fracture (colored in blue) crosscuts the core. **(D)** Reconstructed and labeled pore network of both a large core and small plug of dolomitized limestone from the Barcaliente Fm. (SL15JP038) obtained through medical and microfocus CT scanning. Several open fractures crosscut the core, but they are not visualized through medical CT because of the limited resolution.

The concentration of Fe in dolomite samples from KO 3 is 17000 ppm on average with concentrations around 30000 ppm for the dolomitized fault gouge (Pauwels, 2016). The average Fe concentration of dolomite rocks in KO 2 is 3500 ppm (Pauwels, 2016), and Gasparrini et al. (2006a) reported an average Fe concentration of 2500 ppm for HTD samples from various exposures in the Bodón Unit. The Fe in the dolomite bodies of Montuerto must be inherited from the late pulse of dolomitizing fluids, which has been less important elsewhere in the Bodón Unit. A possible source for the Fe can be the Late-Silurian to Early-Devonian San Pedro Fm. It is composed of iron-rich sandstone and was the main source of Fe for the precipitation of Fe-minerals in carbonates of the Devonian La Vid Group (Schneider et al., 2008). The limited importance of this last phase of Fe-rich dolomite elsewhere in the Bodón Unit indicates that the Correcilla Thrust in KO 3 likely penetrates the subsurface much deeper compared to the fracture networks of KO 1 and KO 2. Here, Fe-rich dolomite only occurs as veins or overgrowths on dolomite cement crystals.

3.8. Discussion

The three key outcrops studied in this chapter illustrate the diverse geometries and distribution of matrix porosity and permeability of the numerous HTD geobodies exposed in Carboniferous carbonate successions in the Bodón Unit. As such, they provide analogues for other dolomite geobodies exposed in the Bodón Unit and the Cantabrian Zone (figure 3.37). Hydrothermal dolomitization was generally fracture-controlled (Gasparrini et al., 2006a), but secondary controlling factors include the nature of fluid-migration pathways, the available volume of dolomitizing fluids and the lithology and sedimentological framework of the precursor limestone rocks.

In both KO 1 and KO 2, migration and circulation of dolomitizing fluids were primarily controlled by fracture networks cutting through the Carboniferous platform limestones (figures 3.38A & B). In KO 3, dolomitizing fluids migrated along the fracture zone of the deeply-rooted Correcilla Thrust (figure 3.38C), and this had important consequences for the formation and diagenetic evolution of corresponding HTD geobodies. The geobodies in KO 3 represent the dolomitized fault breccia between 2 different carbonate formations, and have been intensely overprinted and recrystallized by an important episode of Fe-rich dolomitization. Recrystallized Láncara and Barcaliente dolomite has an average matrix porosity comparable to KO 1 and 2, while the dolomitized fault gouge is characterized by a high matrix porosity of 9.6 % on average. The Correcilla Thrust has been reactivated several times following Late- to Post-Variscan orocline formation and is more deeply rooted compared to other fracture networks (Potent and Reuther, 2000). This allowed additional circulation of dolomitizing fluids following the general dolomitization episode which affected the limestones in the Bodón Unit. These secondary fluids were enriched in Fe following important water-rock interactions, possibly with iron-rich sandstones of the Late-Silurian to Early-Devonian San Pedro Fm. The timing of this additional pulse of coarse-crystalline Fe-rich dolomitization is unclear. It might be associated with the last phase of Late- to Post-Variscan dolomite cementation, which is often enriched in Fe (Gasparrini et al., 2006a; Lapponi et al., 2013). Evers (1967) reported the mining of several mineralizations along the fault trace, which suggests that the Fe-rich dolomitizing fluids are associated with the important episode of ore mineralization which affected several fracture zones in Paleozoic carbonates of the Bodón Unit (see section 2.5). Alternatively, the additional pulse of Fe-rich dolomitization which affected KO 3 could be associated with an important episode of Fe-rich fluid circulation and dolomitization in the Basque-Cantabrian Basin during the Middle Cretaceous (López-Horgue et al., 2010; Nader et al., 2012; Dewit et al., 2014). This episode of Cretaceous dolomitization is associated with the opening of the northern Atlantic Ocean and the Bay of Biscay. Hydrothermal dolomite with associated Zn-Pb ores affecting Late-Carboniferous limestones exposed in the Picos de Europa Unit (Cantabrian Zone; figure 2.1A) have recently been interpreted to originate from the same dolomitization event (Symons et al., 2015). The lack of white hydrothermal calcite cement in Fe-rich dolomite of KO 3 suggests that this additional dolomitization pulse might have postdated the Late- to Post-Variscan dolomitization event as described by Gasparrini et al. (2006a).

Circulation of dolomitizing fluids in KO 1 and KO 2 was controlled by fracture networks crosscutting the carbonate platforms (figure 3.38A & B). Nevertheless, burial dolomitization has been massive and widespread in the deposits of KO 1 and was less important in the platform limestones of KO 2. The massive nature of dolomite in KO 1 is potentially a result of more intense fluid circulation, likely due to the availability of a large volume of evaporated marine-derived brines. A combination of intense fluid circulation and dense fracture or fault networks in both valleys bordering the outcrop, resulted

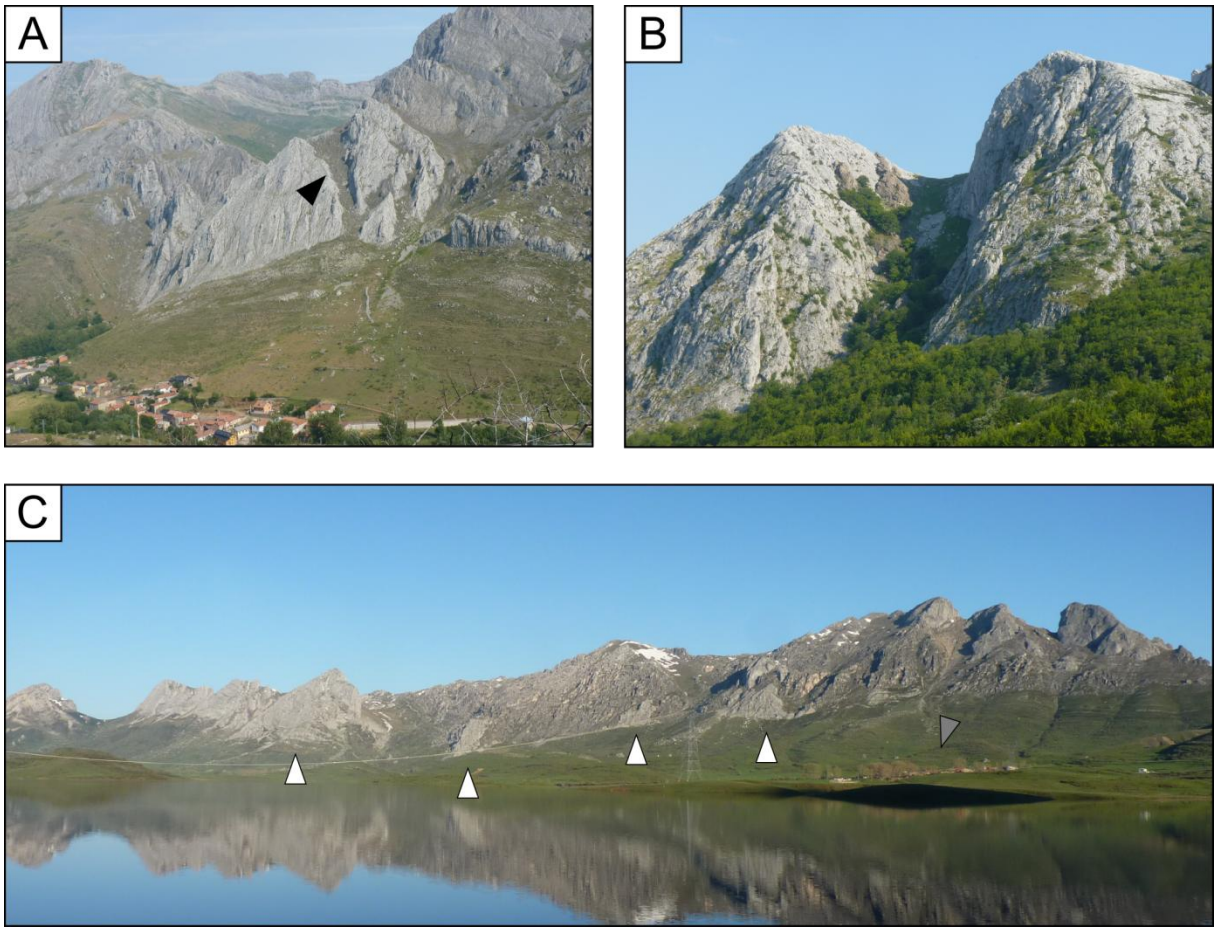

Figure 3.37: Examples of HTD geobodies exposed in the Bodón Unit, with similar geometries compared to the three key outcrops studied in this chapter. **(A)** A fracture-associated HTD geobody (black arrow) in a microbial carbonate mound of the Valdeteja Fm. exposed north of Caldas de Luna. **(B)** A fracture-associated HTD geobody exposed in limestones of the Barcaliente Fm. close to Cueva de Valporquero in the northern part of the Correcilla Unit. **(C)** Massive dolomitized limestones of the Valdeteja Fm. exposed north of Casares de Arbas (gray arrow). Undolomitized precursor limestone rocks are discernible based on their light gray color (white arrows).

in a large volume of dolomitized limestones (figure 3.38A). The latter are characterized by an average matrix porosity of 3.8 %. In KO 2, dolomitization was less intense, possibly because of a smaller available volume of dolomitizing fluids. This resulted in smaller volumes of dolomitized rocks and dolomite geobodies clearly bounded by fractures (figure 3.38B). Some of these fractures have been reactivated following the first phase of dolomitization, resulting in additional brecciation and calcite cementation of the dolomite rocks. The result is the predominant occurrence of tight dolomite in fracture zones with an average matrix porosity of 1.8 % and an average matrix permeability below 0.03 mD. According to Muñoz Quijano (2015), dolomitization intensity (and the resulting massive versus fracture-associated geometries) has not only been influenced by the available volume of dolomitizing fluids and local fracture behavior, but also by an increased geothermal gradient. The paleothermal data introduced in chapter 4 (e.g. figure 4.3A & table 4.3) yield comparable temperatures for both KO 1 and 2, suggesting a limited importance of a locally increased geothermal gradient in KO 1.

The Carboniferous platform limestone successions of the Valdeteja Fm. exposed in KO 1 and KO 2 have a similar sedimentological framework, composed of 3 major depositional units (figures 3.38A & B). These depositional units are defined based on stratal patterns which are clearly traceable on satellite images. They represent growth phases, which have been interpreted by Chesnel et al. (2015) for KO 2 to be controlled by flexural subsidence in the active foreland basin during the Variscan Orogeny. The depositional units recognized in the platform successions of KO 1 likely represent the same growth phases as those recognized by Chesnel et al. (2015) with the main exception that KO 2 belongs to the flat-topped and high-relief Valdorria carbonate platform while the successions exposed in KO 1 have been deposited in an inter-platform basin in between high-relief carbonate structures.

Pre-Variscan burial and Variscan compression resulted in decreasing primary porosities for the Carboniferous limestone successions of the Bodón Unit. Several eogenetic and mesogenetic porosity-destructive processes have been recognized through thin section petrography and suggest that the precursor limestones were completely tight prior to hydrothermal dolomitization. Even microbial boundstones, which are often characterized by high primary porosities (Bahamonde et al., 2014), were tight prior to dolomitization. This is confirmed by observations of tight precursor limestones during fieldwork and by the few porosity measurements performed on limestone plugs. None of the sedimentological studies performed on Carboniferous platforms exposed in the CZ mention open pores in the platform successions (e.g. Kenter et al., 2002; Bahamonde et al., 2014; Chesnel et al., 2015).

Notwithstanding the tight nature of the precursor limestones, their lithology and sedimentological framework influenced the dolomitization style. This is best expressed in the massive deposits of KO 1, where both the Barcaliente and Valdeteja Fm. have been dolomitized (figure 3.38A). In the Barcaliente Fm., dolomite occurrence is primarily controlled by small-scale fracture networks resulting in the patchy occurrence of dolomite geobodies and undolomitized precursor rocks. The dolomitized mudstones are characterized by the omnipresence of zebra textures. The dolomitization style was significantly different in the platform limestones of the Valdeteja Fm., where dolomitization was strongly influenced by the sedimentological framework. The massive units of microbial boundstone and synsedimentary breccia have been intensely dolomitized in contrast to well-bedded calciturbidites. Flow of dolomitizing fluids was likely restricted in the calciturbidites due to intercalations of fine-grained siliciclastics and the occurrence of elongated chert nodules.

Zebra textures and associated pores are rare in dolomite rocks of the Valdeteja Fm., which are characterized by a variety of other dolomite textures and pore types. Nevertheless, petrophysical data derived from plug measurements indicate that different textures do not significantly influence matrix porosity. Although the observed dolomite textures clearly differ (e.g. more zebra textures in the mudstones of the Barcaliente Fm.), the matrix porosity measured for the Barcaliente dolomites is 3.7 % on average and for the Valdeteja limestones 3.8 % on average. Field observations and log data suggest that dolomitized microbial boundstones in the Valdeteja Fm. are characterized by the highest porosity, but this is not confirmed by plug measurements. This apparent contradiction is attributed to the size of the plugs, which are relatively small (diameter of ± 3.3 cm) compared to the cm-sized vuggy and/or biomoldic pores in the dolomitized microbial boundstones. In order to meet the representative elementary volume (REV) for microbial boundstones, plugs for petrophysical measurements should have been larger. Medical CT porosity measurements on large cores and

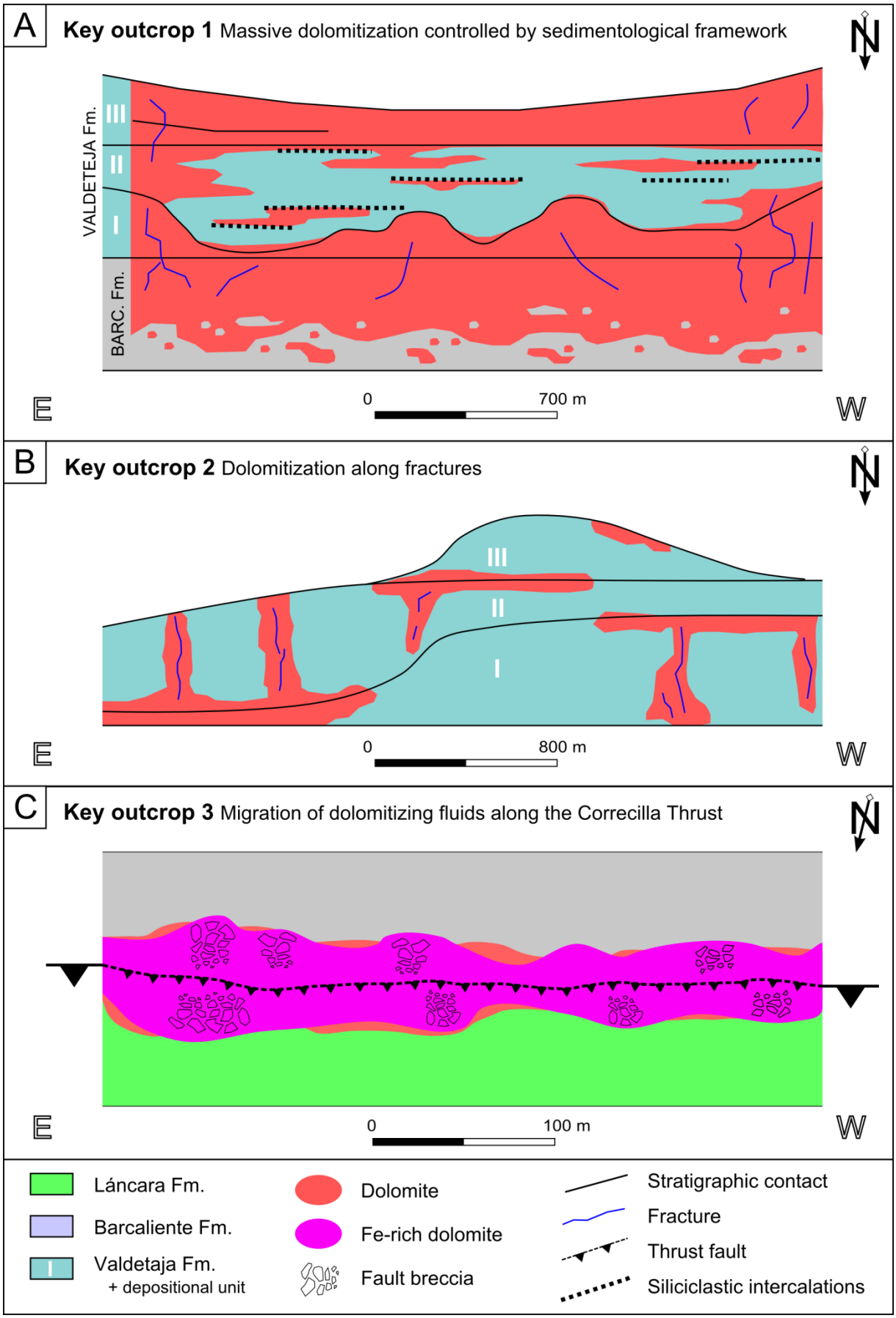
A
Key outcrop 1 Massive dolomitization controlled by sedimentological framework
N
VALDETEJA Fm.
III
II
I
BARC. Fm.
E
0
700 m
W
B
Key outcrop 2 Dolomitization along fractures
N
III
II
I
E
0
800 m
W
C
Key outcrop 3 Migration of dolomitizing fluids along the Correcilla Thrust
N
E
0
100 m
W
Láncara Fm.
Barcaliente Fm.
Valdetaja Fm.
+ depositional unit
Dolomite
Fe-rich dolomite
Fault breccia
Stratigraphic contact
Fracture
Thrust fault
Siliciclastic intercalations

Figure 3.38: Synthesis figure illustrating the geometry of HTD geobodies exposed in each of the three key outcrops. **(A)** Map view of the Barcaliente and Valdeteja Fm. exposed in KO 1. For clarity, the three depositional units of the Valdeteja Fm. have been indicated, as well as the occurrence of fractures and siliciclastic intercalations in the second depositional unit. Dolomitization (indicated in red) was mainly controlled by small-scale fracture networks in the uniform precursor limestones of the Barcaliente Fm. In the Valdeteja Fm., the dolomitization style is strongly influenced by the complex sedimentology of the precursor limestones. **(B)** Map view of the Valdeteja Fm. exposed in KO 2. Dolomitization (indicated in red) is clearly fracture-associated, and locally bounded by depositional surfaces. **(C)** Map view of the fault breccia in KO 3. Dolomitizing fluids migrated along the thrust and dolomitized (indicated in red) the fault breccia. An additional episode of Fe-rich dolomite (indicated in purple) likely affected the fault breccia.

image analysis of outcrop photographs indicate that the porosity of boundstones can locally be higher than the matrix porosity values obtained from plug measurements. Synsedimentary breccia is also characterized by large pores, which suggests the need for a better quantification of the REV. For other dolomite textures described in this study, pore sizes are significantly smaller compared to plugs, and the REV should not pose a problem. Similar observations have been reported by Dewit et al. (2014) for Albian dolomite geobodies exposed in the Basque-Cantabrian Basin.

Following the important episode of hydrothermal fluid circulation during the Early-Permian lithospheric delamination, the limestone platforms of the Bodón Unit were uplifted and exposed. Karst development, characterized by red-matrix collapse breccias, is possibly a result of Permian exposure. Reactivation of fault zones occurred during the Alpine Orogeny, however, this has only been recognized along the important Correcilla Thrust in KO 3. Following the Alpine reactivation, the Bodón Unit has been mainly affected by uplift, and this is expressed by recent karstification. Current telogenesis increased the petrophysical characteristics of the dolomite rocks through important dissolution, especially in dolomite rocks already characterized by a high porosity.

The overall matrix porosity and permeability data obtained for the dolomite rocks exposed in the Bodón Unit, excluding the anomalous values of KO 3 which has not been studied by Muñoz-Quijano (2015), are 3.7 % and 0.08 mD, respectively. Muñoz-Quijano (2015) reported a similar average matrix porosity value (3.5 %) but a higher average matrix permeability (0.76 mD). She obtained the best reservoir properties for dolomite geobodies exposed in the western part of the Bodón Unit (around the village of San Emiliano) where vuggy and zebra pores are omnipresent. This is likely due to massive dolomitization, comparable to KO 1, as the limestone successions in the vicinity of San Emiliano are intensely dolomitized. The higher average permeability reported by Muñoz-Quijano (2015) might be related to a lack, in this PhD study, of plugs from the western part of the study area, where permeability must be slightly higher. The low matrix permeability for dolomite rocks from the Bodón Unit is likely due to a bad connection between pores. Similar low matrix permeability values have been reported for stratabound Albian dolomite geobodies exposed in the Basque-Cantabrian Basin (0.6 mD; Dewit et al., 2014), and indicate the importance of fracture permeability in productive subsurface dolomite reservoirs (Purser et al., 1994; Aguilera, 1995).

The influence of mechanical stratigraphy on dolomite distribution in Carboniferous platform limestones in the Bodón Unit has not been studied in detail. Observations from the Valdeteja Fm. in KO 1, where dolomite distribution is mostly controlled by stratigraphy, suggest a limited importance of mechanical stratigraphy. Even though the well-bedded calciturbidite successions are intensely fractured, dolomitization preferentially affected massive boundstone and synsedimentary breccia.

Likewise, the fracturing behavior of dolomite rocks and the importance of fracture porosity has not been quantified in this chapter. Log data from KO 1 indicate that the fracture abundance is higher in dolomite rocks compared to precursor limestones. In KO 2, dolomite rocks are characterized by 2 distinct fracture sets which are absent in the massive precursor peloidal micrite-rich boundstones. Most of the observed fractures in KO 2 are filled with calcite and dolomite cement, and locally affected by telogenetic dissolution. These observations indicate the importance of fractures in the dolomite rocks. More detailed studies using scan lines and image analysis could result in a better quantification of these fractures in the overall reservoir quality of the dolomite rocks in the Bodón Unit.

The data presented in this chapter illustrate the complex distribution of dolomite and the associated increase in matrix porosity and permeability in dolomitized platform deposits. Digital reservoir models are usually build from well and seismic data, which do not cover the complexity of carbonate systems affected by such diagenetic processes (Lapponi et al., 2011). The Carboniferous limestone platforms with associated HTD geobodies exposed in the Bodón Unit provide seismic-scale examples of complex carbonate systems affected by hydrothermal dolomitization. As such, the outcrops studied in this chapter improve the understanding of complex dolomite geobodies, and the obtained petrographic and petrophysical data allow more geologically realistic modeling of dolomite reservoir occurrence.

3.9. Conclusion

Late- to Post-Variscan fluid flow resulted in intense hydrothermal dolomitization of Carboniferous limestone successions in the Cantabrian Zone, the Variscan foreland fold-and-thrust belt on the Iberian Peninsula. The resulting HTD geobodies are characterized by various geometries and associated distributions of reservoir properties. Outcrop studies of such complex carbonate systems provide geologically interesting information for reservoir modeling of similar subsurface systems. The dolomitization process in the Cantabrian Zone has been subject to several studies, which mostly focused on the geochemical properties of the dolomitized limestones. In this chapter, the geometry of HTD geobodies exposed in three key outcrops and the associated distribution of porosity were investigated in the Bodón Unit. The stratigraphic framework and diagenetic history of the precursor limestone rocks were studied, after which petrographic observations and petrophysical measurements on dolomite samples and plugs were performed.

The precursor limestone successions (most of which belong to important Carboniferous carbonate platforms) were affected by several porosity-destructive processes during Pre-Variscan burial and the Variscan Orogeny. As a result, virtually all primary porosity was obliterated prior to dolomitization. This resulted in dolomitization which is mainly fracture-controlled (Gasparrini et al., 2006a). The HTD geobodies have been formed following Late- to Post-Variscan orocline formation and associated lithospheric delamination, but their general characteristics are significantly different. One of the main controlling factors influencing dolomitization style are the migration and circulation pathways followed by the dolomitizing fluids. While most HTD in the Bodón Unit is formed due to fracture-controlled fluid circulation, the dolomite geobodies exposed close to Montuerto (key outcrop 3) are the result of intense fluid circulation along an important thrust fault. An additional phase of Fe-rich dolomitization was more important along the deeply rooted thrust, and recrystallized and

overprinted the original dolomite rocks. The recrystallized fault gouge is very porous, with an average matrix porosity of 9.6 %.

A second controlling factor influencing dolomitization style and reservoir characteristics is the intensity of fluid circulation. Limited circulation of dolomitizing fluids, possibly due to a small available volume of dolomitizing fluids, resulted in the creation of narrow geobodies around fractures (key outcrop 2). These geobodies are generally tight (average matrix porosity 1.8 %) following several reactivations of the fracture zones and associated cementation with calcite. Intense circulation of dolomitizing fluids resulted in the creation of massive dolomite geobodies (key outcrop 1), with large volumes of dolomitized rocks with an average matrix porosity of 3.8 %.

In these massive HTD geobodies, the control of fracture networks is still important, but the lithology and sedimentological properties of the dolomitized limestones are also of influence. In uniform mudstones of the Barcaliente Fm., the dolomitization front is highly irregular, and the influence of fractures can still be observed. The dolomitized mudstones are characterized by the omnipresence of zebra textures. In the Valdeteja Fm., which is composed of multiple depositional units, dolomitization style depends on the stratigraphy. Well-bedded calciturbidites are only partly dolomitized, while massive deposits of microbial boundstone or synsedimentary breccia are completely dolomitized. Fluid circulation was likely baffled by fine-grained siliciclastic deposits in between the carbonates and by elongated chert nodules.

The geometry and associated distribution of matrix porosity for HTD geobodies exposed in the Bodón Unit of the Cantabrian Zone are strongly influenced by the nature of fluid-migration pathways, the available volume of dolomitizing fluids and the sedimentological framework of the precursor limestone rocks. The highest matrix porosity is obtained in massive outcrops of HTD. Dolomitized fracture zones are generally tight. An exceptional dolomite geobody exposed in the Bodón Unit is a dolomitized thrust zone, which is characterized by matrix porosity values of 9.6 %. In order to fully characterize the reservoir quality of HTD geobodies exposed in the Bodón Unit, the influence of fractures on the permeability of the dolomite rocks should be quantified. Likewise, the representative elementary volume for pores in dolomitized microbial boundstones and synsedimentary breccia should be investigated to understand the effective matrix porosity and permeability of these particular dolomite facies.

Chapter 4 Paleothermometry

4.1. Introduction

Temperature is an important parameter affecting the evolution of carbonates and thus potential reservoir rocks. It influences geochemical reaction rates and corresponding diagenetic processes, such as cementation, dissolution and dolomitization. A clear understanding of the temperature experienced by rock successions allows to reconstruct their burial history, and provides input parameters for basin modeling. The temperatures recorded by sedimentary rocks and their diagenetic products can be assessed through a variety of geothermometers including the thermal maturity of organic matter (e.g. vitrinite reflectance analysis), clay mineral reactions (e.g. illite crystallinity) and fluid inclusion microthermometry.

This chapter aims to better constrain the thermal conditions of both the Paleozoic rocks exposed in the Bodón Unit as well as the diagenetic Mg-rich fluids which have caused widespread dolomitization and ore mineralization in the Bodón Unit of the CZ. To do so, the first part of this chapter focuses on the thermicity of the precursor and ambient rocks, which are subject to a detailed literature study and additional Rock-Eval pyrolysis and vitrinite reflectance analyses. This part of the chapter is based on Honlet et al. (in press). In the second part of chapter 4, the dolomite rocks are used as a high-temperature test case for the novel technique of carbonate clumped isotope paleothermometry. Clumped isotope signatures allow to determine the temperature at which crystals form and can be used, in combination with fluid inclusion microthermometry, to calculate the pressure of carbonate crystallization.

Throughout this chapter, and in the rest of the PhD thesis, a distinction is made between precursor rocks and ambient rocks (figure 4.1). Precursor rocks refer to Cambrian and Carboniferous limestone successions which have been partly dolomitized. Ambient rocks are siliciclastics or carbonate sequences under- and overlying the dolomitized Cambrian and Carboniferous limestones. They have not been affected by dolomitization.

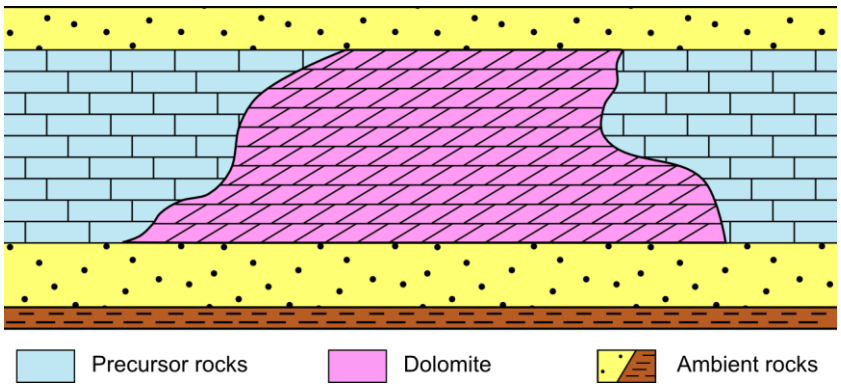

Figure 4.1: Schematic illustration of the concepts 'precursor rocks' and 'ambient rocks'.

CHAPTER 4 ***HIGHLIGHTS:***

- Chapter 4 aims to better constrain the **thermal conditions** of the Paleozoic rocks exposed in the Bodón Unit and of diagenetic Mg-rich fluids that have caused widespread dolomitization and ore mineralization.
- The thermal history of both **precursor and ambient rocks** has been investigated through a detailed **literature study** with additional **Rock-Eval and vitrinite reflectance analyses**. The **dolomite rocks** have been used as a test case for high-temperature carbonate **clumped isotope** paleothermometry.
- Bulk rock paleothermometers such as Rock-Eval pyrolysis and illite crystallinity tend to **overestimate** the thermal maturity of ambient siliciclastic rocks in the Bodón Unit, due to the **incorporation of reworked sediments** in synorogenic successions. **Optical kerogen analysis** during vitrinite reflectance studies allows to distinguish and exclude reworked kerogen populations, which results in a higher accuracy and reliability of maturity data.
- Paleotemperatures based on vitrinite reflectance (VR) analysis of ambient siliciclastic rocks (around 100 °C) are higher compared to temperatures obtained through conodont alteration (CAI) analysis of carbonate precursor rocks (around 60 °C). This variation in thermal maturity is likely related to the **analytical techniques** used to obtained VR and CAI data and the **empirical equations** applied to calculate corresponding paleotemperatures. A secondary cause might be a different response to **mechanical deformation** between siliciclastic and carbonate units during the Variscan and post-Variscan geodynamic evolution of the study area. This caused different patterns of fluid circulation and heat dissipation in both lithologies.
- The thermicity of precursor limestones and ambient siliciclastic rocks indicate that fluid circulation during Late- to Post-Variscan times was **hydrothermal** and associated with **positive temperature anomalies**, which can be used as an exploration tool for HTD geobodies in analogue sub-surface settings.
- Clumped isotope temperatures for dolomite cement samples correlate with fluid inclusion homogenization temperatures, confirming the **validity and applicability** of the **new paleothermometer** for high temperature carbonates.
- The new clumped isotope calibration of **Bonifacie et al. (2017)** yields slightly **lower** temperatures (102 – 154 °C) compared to those obtained from the calibration of **Kluge et al. (2015**; 107 – 168 °C). Increasing **inter-laboratory** communication and cooperation remain an important future challenge for clumped isotope paleothermometry.
- The obtained **clumped isotope temperatures** (102 – 168 °C) are on average slightly higher compared to homogenization temperatures for the same samples (95 – 145 °C). In case of primary fluid inclusions with known composition and pristine clumped isotope signatures, the observed offset between fluid inclusion and clumped isotope temperatures depends on the **pressure** of carbonate crystallization, and can be used for **geobarometry**.
- Dolomite crystals in zebra textures formed during **pressure buildup**, while thick dolomite cement rims in breccia precipitated in response to a **sudden decrease in fluid pressure**.

4.2. Precursor and ambient rock paleothermometry

4.2.1. Introduction

A variety of paleothermometers has been applied in previous studies to deduce the thermal history of the CZ, with the southern thrust units (e.g. the Bodón Unit) in particular. They include the conodont color alteration index (CAI; Raven and van der Pluijm, 1986; Bastida et al., 1999; Brime et al., 2001; Aller et al., 2005; Blanco-Ferrera et al., 2017), the Kübler Index (KI) of illite crystallinity (Brime, 1981; Aller et al., 1987; Marschik, 1992; Bastida et al., 1999; Brime et al., 2001; Blanco-Ferrera et al., 2017), vitrinite reflectance (VR; Colmenero and Prado, 1993; Frings et al., 2004; Colmenero et al., 2008), fluid inclusion (FI) microthermometry (Paniagua et al., 1993; Ayllón et al., 2003; Gasparrini et al., 2006a; Lapponi et al., 2013; Muñoz Quijano, 2015) and apatite fission-track (AFT) thermochronology (Carrière, 2006; Botor and Anczkiewicz, 2015).

The dolomite geobodies exposed in the Bodón Unit formed between 130 and 150 °C (based on FI microthermometry; Gasparrini et al., 2006b). The dolomitization has been interpreted as hydrothermal (i.e. formed at temperatures at least 10 °C higher than those of the precursor carbonate rocks; *sensu* Machel and Lonnee, 2002) based on CAI data from the Carboniferous precursor limestones (Gasparrini et al., 2006b), indicating that they experienced maximum temperatures between 70 and 95 °C (Raven and van der Pluijm, 1986). However, the temperatures derived from CAI data do not correspond to the common occurrence of ordered mixed-layer illite/smectite in ambient siliciclastic rocks of the southern CZ, indicating temperatures above 100 °C (Eberl, 1993; Brime et al., 2001; Aller et al., 2005). These observations highlight the need for a coherent interpretation of the paleothermal data available for the southern CZ, in order to better constrain the thermal conditions of dolomitization, the diagenetic process of prime importance in this area. Up to date, most of the paleothermometers listed above have mainly been used to map isograds in order to understand the different metamorphic events which affected the CZ. A more exhaustive understanding of the thermal history experienced by the Carboniferous precursor and ambient rocks in the southern CZ is thus necessary in order to address the thermal constraints of the dolomitization process in such a complex geodynamic setting.

The present study extends the published paleothermometry database by performing Rock-Eval (RE) pyrolysis and VR analysis on organic-rich clay- and mudstones from the Bodón Unit. The samples were taken from ambient siliciclastic rocks stratigraphically under- and overlying the massive dolomitized Carboniferous carbonate units (Alba, Barcaliente and Valdeteja Fm.) and the newly acquired data are integrated into the paleothermal framework of the southern CZ. The aim of this part of the PhD thesis is to deduce reliable maximum temperatures experienced by precursor and ambient rocks of the dolomite geobodies occurring in the study area, to improve the understanding of the paleothermal history of the Bodón Unit, as well as the thermal conditions (geothermal *versus* hydrothermal) which governed the occurrence of massive dolomitization. Finally, the regional distribution of the thermal maturity of precursor and ambient rocks was compared with the regional distribution of HTD geobodies, which allowed to correlate the spatial occurrence of dolomites and thermal anomalies in precursor and ambient rocks. This represents a potential new approach to detect hydrothermal subsurface carbonate geobodies in hydrocarbon and geothermal exploration plays.

4.2.2. Literature study

In the following sections, the different paleothermometry datasets published for the Bodón Unit in previous studies are introduced. The stratigraphic intervals sampled for each paleothermometer are indicated on the stratigraphic column of the Bodón Unit in figure 4.2. A brief explanation of the different paleothermometers is followed by an explanation on how the raw data have been converted to paleotemperatures. Most of the introduced paleothermometers are strongly affected by the duration of a thermal event, which has to be taken into account when comparing different paleothermal datasets. What also needs attention, is the fact that some datasets are available only from the precursor carbonate successions while others are derived from the ambient siliciclastic rocks. The calculated paleotemperatures have to be handled with care, because the empirical equations used for the different datasets have a specific accuracy and uncertainty regarding the parameters and preconditions applied, which might be a source of error and inaccuracy.

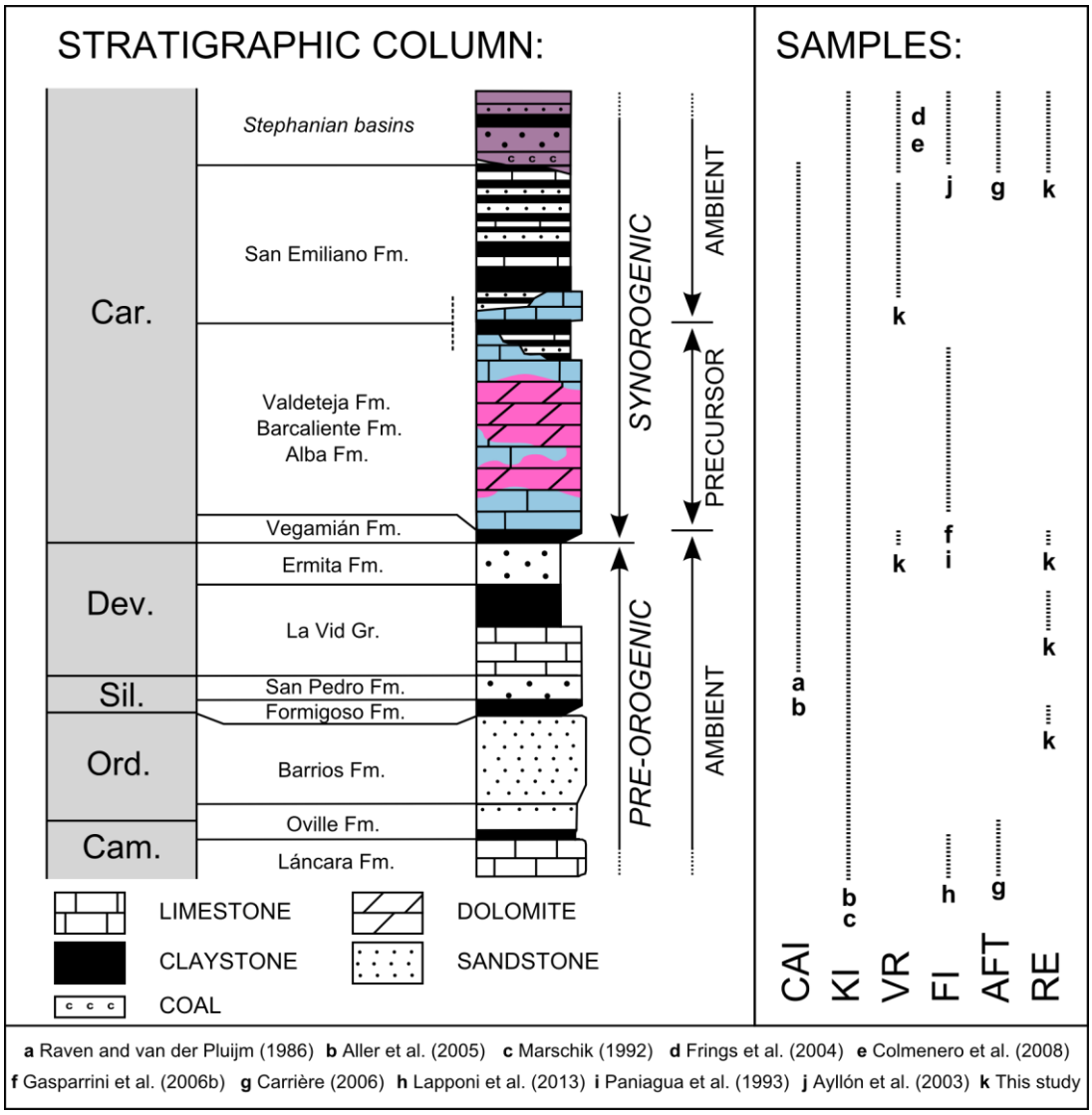

Figure 4.2: Stratigraphic column of the Bodón Unit (modified from Aller et al. (2005) and Pérez-Estaún et al. (1988)). The column shows Carboniferous precursor carbonate successions in light blue and dolomite geobodies in pink. Stephanian siliciclastics are indicated in purple. Pre-orogenic and synorogenic successions are distinguished, as well as precursor and ambient rocks. The stratigraphic intervals sampled for the different published paleothermometry datasets and sampled for this study are shown on the right (CAI: conodont alteration index; KI: Kübler index; VR: vitrinite reflectance; FI: fluid inclusions; AFT: apatite fission track; RE: Rock-Eval).

4.2.2.1. Conodont Color Alteration Index (CAI)

The color alteration of conodonts depends on the carbonization of organic matter (OM) traces and is controlled by maximum temperature and heating time (Epstein et al., 1977; Rejebian et al., 1987). Recalculated paleotemperatures are strongly influenced by the duration of the heating event, as a relatively long heating time is required for the carbonization of OM in conodonts. Confining pressure does not affect the alteration process, excluding tectonics from influencing the color of conodont fragments (Epstein et al., 1977). Nevertheless, the presence of fluids under pressure, which is important in hydrothermal systems, can retard alteration. In such settings, OM carbonization is replaced by oxidation and volatilization of oxides, resulting in a loss of OM which would affect the color alteration (Epstein et al., 1977; Rejebian et al., 1987).

CAI data for the Bodón Unit were obtained by Raven and van der Pluijm (1986) and Aller et al. (2005) and are derived from conodonts found in Devonian and Carboniferous rocks (figure 4.2). The data have been converted to temperature using the Arrhenius plot constructed by Epstein et al. (1977). A heating time of 10 Ma was used to convert the CAI data, based on the work of Carrière (2006) and Botor and Anczkiewicz (2015).

4.2.2.2. Kübler index (KI) of illite crystallinity and clay mineralogy

The KI of illite crystallinity allows the determination of the kinetic clay mineral reaction progress and thus metamorphic grades in pelitic sequences. The crystallinity of illite is determined by measuring the full width at half maximum height of the illite (001) X-ray diffraction peak (Kübler, 1967, 1968). Measurements are performed on oriented mineral aggregate samples of the < 2 µm grain size fractions. Increasing crystallinity and thus metamorphic grade results in decreasing KI values. Despite the important role of temperature in the reaction process of phyllosilicates, numerous other factors (such as permeability, potassium availability, weathering and mechanical and hydrothermal alteration) affect the crystallinity of illite (e.g. Junfeng and Browne, 2000; Fukuchi et al., 2014). As a result, phyllosilicates in diagenetic conditions often do not reflect thermodynamic equilibrium, which makes the use of the KI as a paleothermometer problematic (Guggenheim et al., 2002).

Despite the many factors possibly influencing the crystallinity of illite, general correlation charts (e.g. Merriman and Frey, 1999; Voldman et al., 2008) estimate that KI values lower than 0.42 correspond to temperatures above 200 °C (anchizone), whereas KI values lower than 0.25 correspond to temperatures above 300 °C (epizone). Marschik (1992) and Aller et al. (2005) analyzed the clay mineralogy and KI of clay-rich siliciclastic rocks in the Bodón and Correcilla units, ranging from Cambrian to Carboniferous in age (figure 4.2). Corresponding temperatures were calculated using the empirical formula of Mukoyoshi et al. (2007). This equation has been established based on a correlation between VR and KI data in an accretionary complex in southwestern Japan, and has been applied with caution.

Eberl (1993) identified 3 reaction zones for illite formation in sedimentary and diagenetic settings with the third zone corresponding to temperatures of at least 100 °C. Clay mineralogy of samples from the Bodón Unit suggests that all mixed-layer illite/smectite in the samples used for KI measurements appears to be ordered (e.g. Brime et al., 2001; Aller et al., 2005). These results allow to conclude that zone 3 of Eberl (1993) was reached.

4.2.2.3. Vitrinite reflectance (VR) analysis

Due to changes in optical properties, the reflectance of vitrinite increases with increasing temperature in a predictable manner (Karweil, 1956; Suggate, 1959; Teichmüller, 1982). Although suppression or retardation of vitrinite reflectance can occur under certain circumstances (e.g. in case of overpressure; Schito et al., 2016), the analysis of vitrinite reflectance is considered a reliable paleothermometry technique to assess the thermal maturity of sediments in diagenetic settings (Teichmüller, 1987).

Published VR data are only available for the Stephanian CM (Frings et al., 2004; Colmenero et al., 2008) and CR (Colmenero et al., 2008) basins (see section 2.3; figure 4.2). They have been converted to temperature by applying the formula proposed by Barker and Pawlewicz (1994) which, according to Frings et al. (2004), yields the most realistic temperatures for samples from the Stephanian CM Basin.

4.2.2.4. Fluid inclusion (FI) microthermometry

FIs are tiny vacuoles of fluid trapped in crystals during mineral precipitation (Goldstein and Reynolds, 1994). They provide information on the composition and temperature of the precipitating fluids through microthermometric measurements. Of most importance for this study is the homogenization temperature (T_h), which gives an estimation of the minimum trapping temperature of an inclusion. By applying a pressure correction, the true temperature of crystal precipitation can be derived from T_h (see section 4.3.4.2).

Primary FIs in fracture-related dolomites occurring in both Cambrian and Carboniferous precursors have been investigated in previous studies (figure 4.2; Gasparrini et al., 2006b; Lapponi et al., 2013; Muñoz Quijano, 2015), as well as FIs in late diagenetic calcite supposed to have precipitated from the same fluid system (Gasparrini et al., 2006b). FIs in quartz gangue minerals from ore deposits of the Providencia and Profunda mines (figure 2.4) have been investigated by Paniagua et al. (1993). Ayllón et al. (2003) performed a microthermometric study on quartz veins in the Stephanian CM Basin.

4.2.2.5. Apatite fission track (AFT) thermochronology

Fission track thermochronology is a suitable technique to investigate the low-temperature thermal history of sedimentary rocks (Price and Walker, 1963; Wagner and van den Haute, 1992). The technique is based on the natural decay of ^{238}U isotopes, producing radiation damage trails (so-called fission tracks) in U-bearing minerals. The spontaneous fission of ^{238}U isotopes produces fission tracks at a continuous rate throughout geological time. Fission-track thermochronology is mostly performed on apatite crystals (AFT thermochronology). Apatite fission tracks can undergo partial annealing (i.e. resetting) in a temperature range of 60 to 110 ± 10 °C, due to a measurable shortening of the fission tracks at these temperatures (Gleadow and Duddy, 1981). Complete annealing of fission tracks in apatite crystals occurs at temperatures higher than 110 ± 10 °C for 10 Ma.

Carrière (2006) successfully deduced the thermal history for 3 Cambrian samples and 1 Stephanian sample in or close to the eastern part of the Bodón Unit (figure 4.2). Recently, Botor and Anczkiewicz (2015) investigated the thermal history of the Stephanian Sabero Coalfield basin

(located southeast of the study area) through a combination of AFT thermochronology and VR analysis.

4.2.3. Methodology

In addition to the published paleothermal datasets introduced above, the thermal maturity of a new set of samples was investigated through RE pyrolysis and VR analysis. A total of 78 samples of clay- and mudstones from different stratigraphic levels in the study area were collected from road sections and quarries. During fieldwork and sampling, dark material was preferentially sampled in order to obtain samples rich in OM. Most of the samples were collected in the Bodón Nappe (figure 2.1B). Other samples were collected in the Forcada and Gayo nappes, north of the León Fault (in the Central Coal Basin as well as in the Stephanian CR Basin) and in the northern part of the Correcilla Unit (figure 2.1). Fresh material was preferentially sampled in order to minimize the influence of weathering (cfr. Copard et al., 2002).

RE pyrolysis is an analytical method used to characterize source rocks and evaluate their petroleum potential. It is based on the relative contents of free hydrocarbons and CO_2 generated during pyrolysis (i.e. artificial heating of a sample; Espitalié et al., 1977; 1985a, b, c). Pyrolysis of the collected samples was performed using the Rock-Eval 6 apparatus (Lafargue et al., 1998) which employs a temperature-programmed heating of a powdered sample (± 100 mg) in an inert atmosphere (helium or nitrogen). The sample is first placed in a pyrolysis oven to measure the quantity of free hydrocarbons (revealed by the so-called S_1 peak). Heating up to 650 °C allows the determination of the amount of hydrocarbons (S_2 peak) and CO_2 (S_3 peak) produced during thermal cracking of kerogen. The sample is then transferred to an oxidation oven where the residual organic carbon, remaining in the sample after pyrolysis, is oxidized (and revealed by the S_4 peak) at temperatures up to 850 °C. In this way, the Total Organic Carbon (TOC) content of the sample can be quantified. Of particular interest for this study is the Tmax parameter which corresponds to the S_2 peak temperature in the pyrolysis oven, which is used to estimate the thermal maturity of rocks (Tissot and Welte, 1978). In this study, Tmax values were converted to equivalent VR values (referred to as Tmax-derived VR values) using the equation of Jarvie et al. (2001). RE pyrolysis produced reliable results for 55 samples, which are listed in table 4.1. The other samples (including all samples from the Alba, Barcaliente and Valdeteja Fm.) were excluded due to low TOC values (< 0.3 %) which have a high risk to produce unreliable RE pyrolysis data. From the 55 productive samples, 40 are from OM-rich layers of the San Emiliano Fm. In the Central Coal Basin, north of the León Fault, 5 samples are from the Lena and Sama Groups (local equivalents of the San Emiliano Fm.) and 2 samples are from the CR Basin. The remaining 8 samples were collected from the Formigoso (2 samples) and Vegamián Fm. (4 samples), from the La Vid Group (1 sample) and from the Stephanian CM Basin (Roguera Fm.; 1 sample).

TABLE 4.1: VR and RE data

Formation	Location	Tmax (°C)	HI	OI	TOC (%)	VR (%) from Tmax	T (°C) RE	VR total (Rm%)	VR *in situ* (Rm%)	T (°C) VR
San Emiliano	Gete	504	36	129	0.45	1.91	188			
San Emiliano	Pedrosa	469	34	48	0.58	1.28	156	1.1	0.86	123
San Emiliano	Lavandera	464	40	32	0.57	1.19	150		0.93	130
San Emiliano	Lavandera	470	34	57	0.67	1.3	157			
San Emiliano	Genicera	469	41	96	0.69	1.28	156			
San Emiliano	Genicera	455	31	76	0.54	1.03	138			
San Emiliano	Genicera	454	53	49	0.68	1.01	136		0.71	108
San Emiliano	Valverde d. Curueño	462	30	64	0.44	1.16	147			
San Emiliano	Valverde d. Curueño	459	53	32	0.76	1.1	143		0.61	96
San Emiliano	Redilluera	486	31	79	0.87	1.59	173			
San Emiliano	La Braña	460	48	48	0.66	1.12	145		0.72	109
San Emiliano	La Braña	454	27	78	0.51	1.01	136			
San Emiliano	Valdecastillo	459	25	44	1.15	1.1	143	1.28	0.79	116
San Emiliano	Cármenes	473	37	25	0.71	1.35	160			
San Emiliano	Cármenes	484	33	12	0.76	1.55	171	1.1	0.79	116
San Emiliano	Cármenes	525	13	61	0.31	2.29	202		0.76	113
San Emiliano	Mina Profunda	467	30	63	0.27	1.25	153			
San Emiliano	Barrio de la Tercia	468	30	35	0.46	1.26	154			
San Emiliano	Barrio de la Tercia	475	38	38	0.68	1.39	162		0.8	117
San Emiliano	Villanueva d. l. Tercia	512	16	91	0.44	2.06	194			
San Emiliano	Villanueva d. l. Tercia	502	18	108	0.51	1.88	186			
San Emiliano	Villanueva d. l. Tercia	465	27	25	0.67	1.21	151			
San Emiliano	Rodiezmo d. l. Tercia	462	41	59	1.11	1.16	147		0.71	108
San Emiliano	San Martin d. l. Tercia	456	50	69	0.32	1.05	139			
San Emiliano	Poladura d. l. Tercia	511	30	79	1.26	2.04	193			
San Emiliano	Poladura d. l. Tercia	464	53	27	0.89	1.19	150		0.74	111
San Emiliano	Poladura d. l. Tercia	459	11	93	0.44	1.1	143			
San Emiliano	Viadongos de Arbas	521	24	66	2.81	2.22	200			
San Emiliano	Casares de Arbas	449	49	50	0.68	0.92	129			
San Emiliano	Casares de Arbas	466	36	123	0.64	1.23	152			
San Emiliano	Caldas de Luna	502	30	50	0.6	1.88	186			
San Emiliano	Casares de Arbas	470	14	241	0.37	1.3	157			
San Emiliano	Valdorria	573	9	98	0.65	3.15	228			
San Emiliano	Villamanin d. l. Tercia	467	23	88	0.4	1.25	153			
San Emiliano	Villanueva d. l. Tercia	510	39	37	3.32	2.02	192		0.63	98
San Emiliano	Villanueva d. l. Tercia	485	52	13	0.77	1.57	172			
San Emiliano	Caldas de Luna	505	21	21	0.57	1.93	189	1.64	0.87	124
San Emiliano	Casares de Arbas	450	56	13	0.63	0.94	130	0.83	0.7	107
San Emiliano	Casares de Arbas	493	48	10	0.58	1.71	179			
San Emiliano	San Martin d. l. Tercia	455	43	9	0.54	1.03	138		0.67	103
Lena/Sama	Valdehuesa	462	35	86	0.66	1.16	147			
Lena/Sama	Valdehuesa	459	78	19	0.97	1.1	143			
Lena/Sama	Rucayo	454	41	67	0.9	1.01	136			
Lena/Sama	Campo	496	2	63	0.65	1.77	181			
Lena/Sama	Campo	492	3	71	0.72	1.7	178			
CR Basin	Canseco	603	5	7	4.2	3.69	241			
CR Basin	Canseco	608	13	7	5.02	3.78	243			
Formigoso	Getino	464	32	45	0.75	1.19	150			
Formigoso	Aralla de Luna	602	5	33	1.28	3.68	240			
Vegamián	Hoces de Curueño	449	60	32	3.52	0.92	129		(0.45)	
Vegamián	Los Chábanos	465	8	56	6.07	1.21	151		0.69	106
Vegamián	Los Chábanos	471	13	81	4.65	1.32	158			
Vegamián	Millaró de la Tercia	485	30	1	9.38	1.57	172		0.69	106
La Vid	Aralla de Luna	591	8	55	0.38	3.48	236			
Roguera	Vegacervera	568	14	22	0.73	3.06	226			

Table 4.1 (opposite page): Results from RE pyrolysis and VR analysis. RE Tmax values are indicated, as well as hydrogen and oxygen indices (HI and OI), TOC, Tmax-derived VR values (cfr. Jarvie et al., 2001) and corresponding temperatures (cfr. Barker and Pawlewicz, 1994). HI and OI roughly correspond to the H/C and O/C atomic ratios for each sample. VR results are expressed in Rm%. The first column of VR data refers to the total vitrinite assemblage. The second and third columns of VR data represent *in situ* kerogen and corresponding temperatures (cfr. Barker and Pawlewicz, 1994).

VR analysis, including specific maturity analysis of dispersed kerogen, was performed on 18 samples out of the 55 productive RE samples of the San Emiliano (15 samples) and Vegamián Fm. (3 samples; table 4.1) through a method specifically applied in the GeoResources STC lab at the University of Heidelberg (Germany). The samples cover a wide range of TOC and Tmax values to evaluate the consistency between results from RE pyrolysis and VR analysis. Most samples are located within the Bodón Nappe and only 1 is located in the Forcada Nappe. Kerogen was isolated by the maceration technique (double acid treatment with HCl and HF) and concentrated and embedded in epoxy resin blocks, which were polished on the surface for reflectance analysis. VR analysis is based on digital image analysis, using high-resolution black/white images of vitrinite, obtained with a reflected-light microscope. Grey levels of the digital images represent the levels of reflectance and are recalculated to real VR values by specifically modified image analysis software. This enables high-resolution reflectance analysis of single vitrinite grains down to pixel-size (< 10 µm) providing highly accurate and reliable VR data, without any correction factor needed. It also supports the identification of *in situ* versus reworked and degraded vitrinite in mixed vitrinite assemblages and the separation of real vitrinite from vitrinite-like particles. In each sample 50 vitrinite particles were measured, if available. Additionally, one kerogen slide was made from each sample for optical analysis of kerogen composition, particularly the composition of the vitrinite assemblage, which was included in the detailed interpretation of the VR data. Several equations can be used for the calculation of exact paleotemperatures from VR data, leading to different paleotemperatures, with increasing variation towards higher maturation (table 4.2). In this study the equation of Barker and Pawlewicz (1994) was used to provide the maximum comparability between the new data of this study and the previous data by Frings et al. (2004). The equation of Barker and Pawlewicz (1994) is generally accepted as the standard equation for conversion of VR data to corresponding temperature, and is most often used.

TABLE 4.2: VR data and corresponding temperature (°C) based on different equations

Equation	VR 0.75 %	VR 1.0 %	VR 2.0 %	VR 3.0 %
Barker (1991)	118	148	220	262
Barker and Goldstein (1990)	120	155	241	291
Barker and Pawlewicz (1994)	112	135	189	225

Table 4.2: Paleotemperatures in °C calculated with common equations for increasing vitrinite reflectance levels. The difference in paleotemperatures obtained from different equations increases with increasing reflectance level.

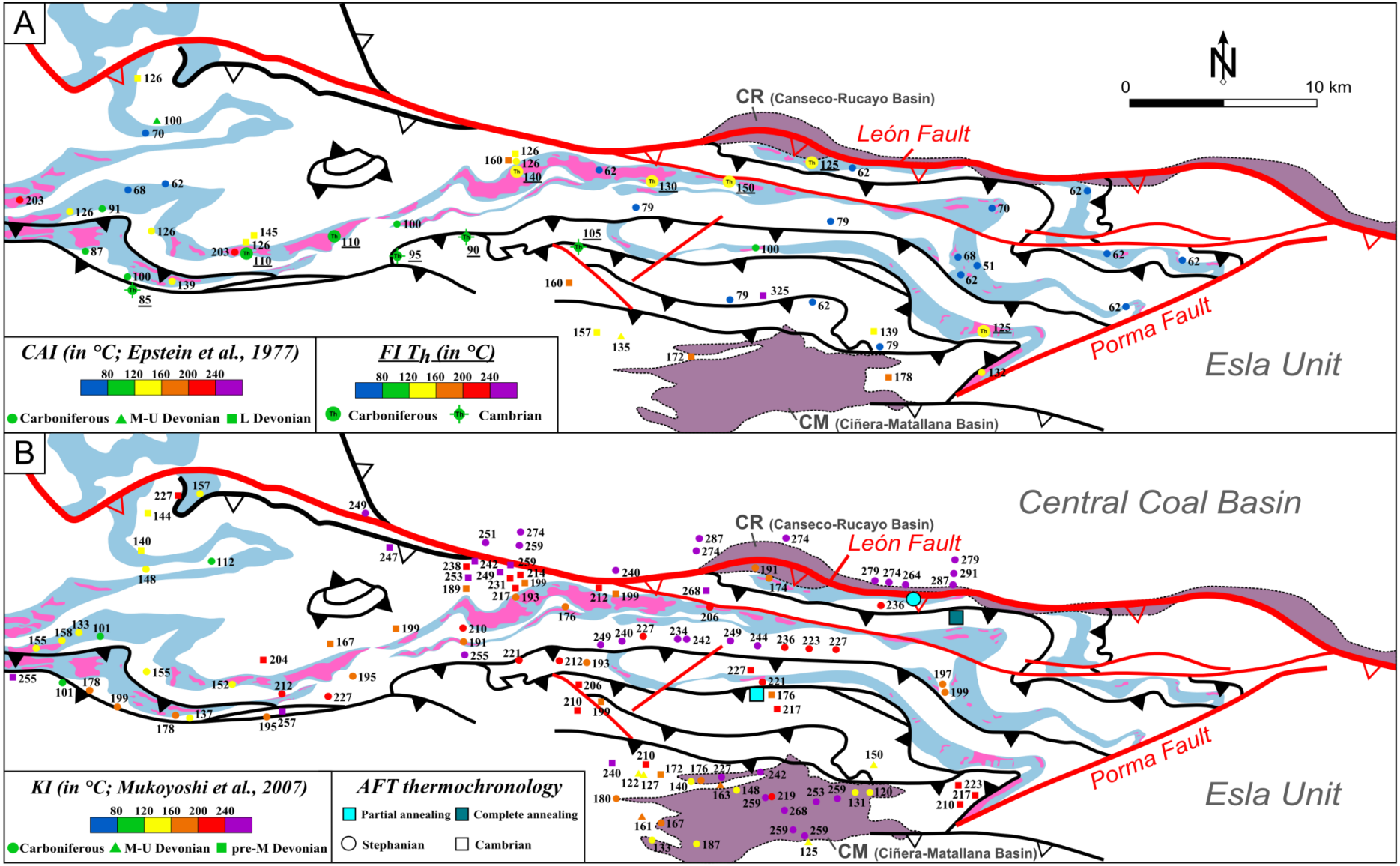

Figure 4.3: Geological map of the Bodón Unit with indication of **(A)** paleotemperatures based on conodont CAI data (Raven and van der Pluijm, 1986; Aller et al., 2005) and FI homogenization temperatures (Gasparrini et al., 2006a; Lapponi et al., 2013) and **(B)** paleotemperatures based on KI data (Marschik, 1992; Aller et al., 2005) and locations of AFT thermochronology (Carrière, 2006).

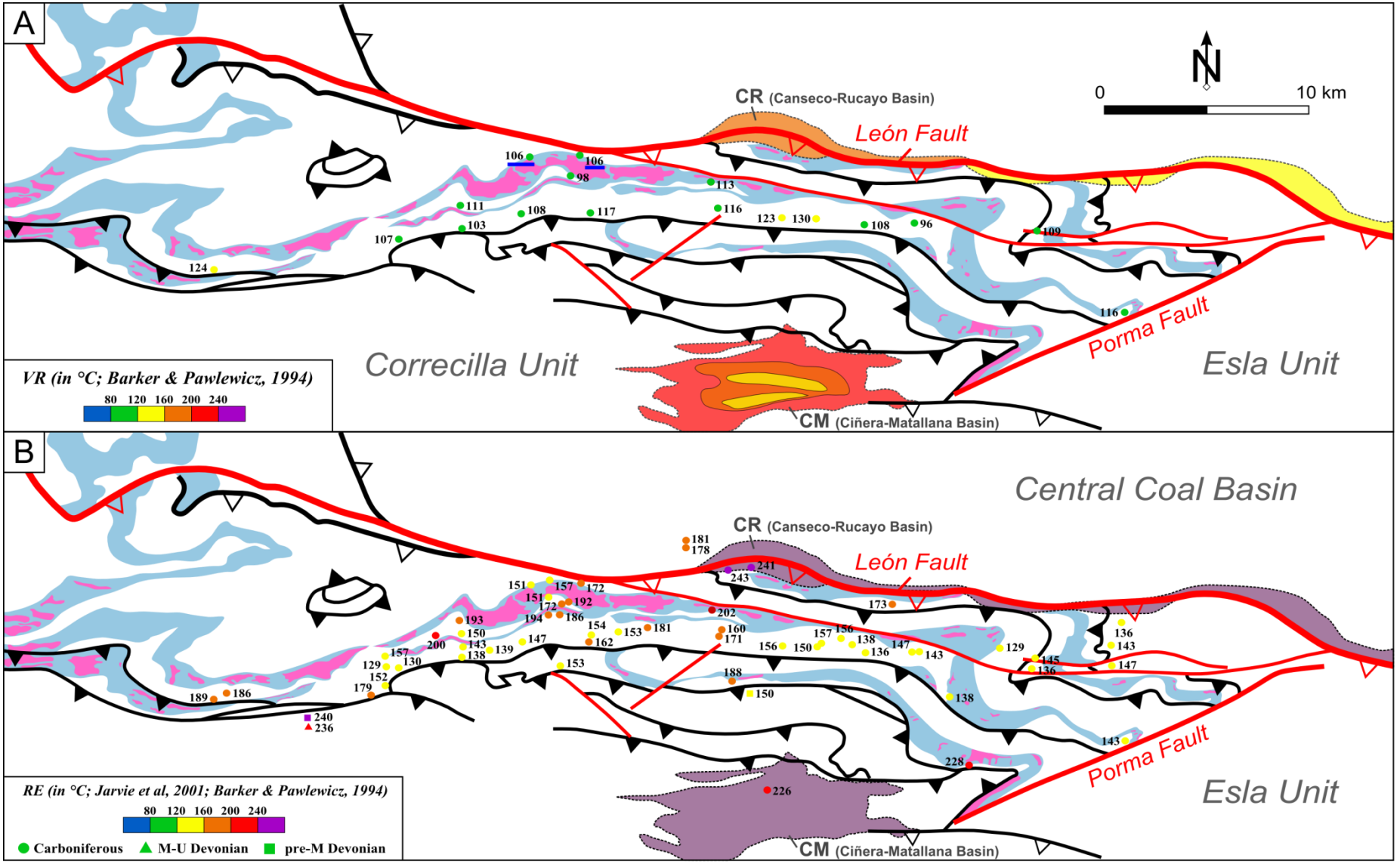

Figure 4.4: Geological map of the Bodón Unit with indication of **(A)** paleotemperatures based on VR analysis (Frings et al., 2004; Colmenero et al., 2008; this study) and **(B)** paleotemperatures based on RE pyrolysis (this study).

4.2.4. Results

In the following sections the temperatures obtained from literature datasets and from RE and VR measurements are reported. The regional distribution of paleotemperatures, calculated from each technique, is indicated on the geological map of the Bodón Unit (figures 4.3 & 4.4).

4.2.4.1. Published paleothermometry database

CAI data for Devonian and Carboniferous successions in the Bodón Unit range from 1 to 5 (Raven and van der Pluijm, 1986; Aller et al., 2005), corresponding to a wide range of diagenetic to anchizonal temperatures. The temperatures average around 60 °C for the Carboniferous precursor carbonates in the eastern part of the Bodón Unit, whereas precursor carbonates close to the dolomitized central and western parts are characterized by higher temperatures (up to 203 °C; figure 4.3A). These higher temperatures correlate with areas intensely affected by fracture-related dolomitization and ore mineralization.

Temperatures obtained from KI data from the ambient siliciclastic rocks are remarkably high compared to CAI temperatures (figure 4.3B). In the eastern part of the Bodón Unit temperatures approach 200 °C for samples from the San Emiliano Fm., while in the central part all KI data indicate temperatures between 200 and 250 °C, both for the San Emiliano Fm. and the pre-Carboniferous ambient rocks. In the central northern part of the Bodón Nappe, KI-derived paleotemperatures for pre-orogenic rock successions clearly increase towards the León Fault (figure 4.3B). The western part of the Bodón Unit is characterized by slightly lower temperatures, generally around 150 °C, but locally up to 200 °C. The southern part of the Central Coal Basin, north of the León Fault, is characterized by high temperatures between 250 and 300 °C.

VR data for both Stephanian CR and CM basins (Frings et al., 2004; Colmenero et al., 2008) correspond to temperatures ranging from 120 to 240 °C (figure 4.4A). These relatively high temperatures are believed to be restricted to the Stephanian pull-apart basins because of their fault-controlled settings and their association with intrusions of sills and dykes (Méndez, 1985; Frings et al., 2004).
FI trapping temperatures, derived from primary T_h values (indicated on figure 4.3A), range from 130 to 150 °C for dolomite cement in Carboniferous rocks (Gasparrini et al., 2006a). T_h values for dolomite cement in Cambrian rocks range between 85 and 105 °C (figure 4.3A) while true trapping temperatures lie approximately 5 to 10 degrees higher (Lapponi et al. 2013). Late diagenetic calcite cement is characterized by trapping temperatures between 115 and 130 °C (Gasparrini et al., 2006a). Partial re-equilibration to decrepitation of FIs is described by Ayllón et al. (2003) for quartz veins in the Stephanian CM Basin. Here, inclusions were trapped at temperatures between 110 and 120 °C and re-equilibrated by a short-lived thermal event recording temperatures as high as 300 °C. Ore mineralizations from the Bodón Unit are hosted by fracture-related dolomite and record trapping temperatures up to 200 °C (Paniagua et al., 1993), but did not result in reequilibration of the FIs in the dolomite cements.

In one of the Cambrian AFT samples, as well as in the Stephanian AFT sample, Carrière (2006) observed partial annealing of fission tracks at about 270 Ma, indicating insignificant duration of

peak thermal conditions to completely anneal the fission tracks (figure 4.3B). The other Cambrian AFT sample indicates complete annealing meaning that temperatures did exceed 110 ± 10 °C for more than 10 Ma. Most samples of the nearby Sabero Coalfield are completely annealed (Botor and Anczkiewicz, 2015).

4.2.4.2. RE pyrolysis and VR analysis

Tmax values obtained from RE pyrolysis show a very wide range from 449 to 608 °C (table 4.1), which corresponds to paleotemperatures of 130 to 250 °C (table 4.1; figure 4.4B). These data fall in a slightly cooler range of paleotemperatures as those derived from KI data, but are significantly higher compared to paleotemperatures deduced from CAI data in the study area. The 4 samples from the Vegamián Fm. show relatively low Tmax values with less variation (corresponding paleotemperatures: 129 – 172 °C), while the many samples from the San Emiliano Fm. and the Lena and Sama Groups show the maximum variability (paleotemperatures: 129 – 228 °C). The sample from the Devonian La Vid Group has a very high Tmax of 591 °C (paleotemperature: 236 °C). The maximum Tmax values, with very little variation, are recorded for the oldest sample, the Early Paleozoic Formigoso Fm. (Tmax: 602 °C; paleotemperature: 240 °C) and the youngest samples from the Stephanian CR Basin (Tmax: 603 – 608 °C; paleotemperature: 241 – 243 °C). Particularly the San Emiliano Fm. (and its equivalents) shows a very wide range of thermal maturity. Locations most intensely affected by fracture-related dolomitization show RE temperatures around 200 °C (e.g. the central, western and southeastern parts of the Bodón Unit).

Additionally to Tmax values, organic maturity was studied trough VR analysis on 18 samples. Tmax-derived VR values obtained for these samples (cfr. Jarvie et al., 2001), show a very wide range (0.92 – 2.29 Rm%; table 4.1). During VR analysis, two populations of kerogen particles were observed in the kerogen slides of all 15 samples from the San Emiliano Fm., as well as in the distribution of measured VR values (figure 4.5A). The first population consists of less mature organic matter, identified by light to medium brown colors (figure 4.6A). The second population contains higher mature organic matter, identified by dark brown to black colors (figures 4.5A & 4.6A). For the current maturity analysis, only the less mature vitrinite population was analyzed. This led to a narrow range of reflectance in all samples from the San Emiliano Fm. (0.61 – 0.93 Rm%; table 4.1), showing a much more homogeneous dataset compared to Tmax and Tmax-derived VR values. In the central part of the study area reflectance values range from 0.79 to 0.93 Rm% (corresponding paleotemperatures: 98 – 130 °C). Reflectance values are lower in the eastern part (0.61 – 0.72 Rm%; paleotemperatures: 96 – 109 °C). At the very western end of the study area, reflectance is high (0.87 Rm%; paleotemperature: 124 °C), as well as in the southeastern end, where reflectance increases to 0.79 Rm% (paleotemperature: 116 °C). The total vitrinite assemblage for five samples from the San Emiliano Fm. has been analyzed to compare with the Tmax-derived VR values (table 4.1). Reflectance data from the total vitrinite assemblages are close to the VR values calculated from Tmax. Except for one sample, all measured VR values are slightly lower. The difference between calculated and measured VR values seems to increase towards higher maturity.

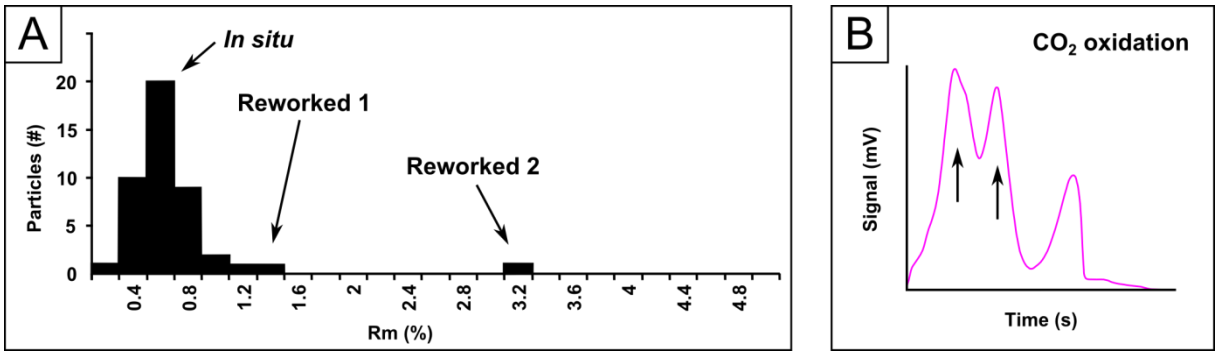

Figure 4.5: (A) Histogram illustrating VR data expressed as Rm(%) for sample 46, showing a large population of *in situ* material and two groups of reworked higher mature material. **(B)** CO_2 oxidation pattern from RE analysis for sample 46, showing the occurrence of two types of OM (black arrows). The third peak to the right corresponds to the carbonate content of the sample.

Samples from the Vegamián Fm. show strongly altered, poorly preserved organic matter (figure 4.6B). The alteration leads to lower reflectance values compared to the well preserved vitrinite in other samples. In one sample all organic matter, including vitrinite, is strongly altered. Therefore the reflectance value is much lower (0.45 Rm%) compared to the other samples and was excluded from the maturity analysis. In the two other samples (underlined in blue in figure 4.4A) vitrinite was poorly to moderately preserved. Careful selection of the few relatively well preserved vitrinite particles, and avoiding the altered particles, led to usable VR values, which still might be slightly lower than in well preserved samples.

The paleotemperatures calculated from VR values of the less mature vitrinite population range from 96 to 130 °C, which is significantly lower compared to the temperatures derived from RE pyrolysis and previous VR data of the CM and CR basins (figure 4.4A; Frings et al., 2004; Colmenero et al., 2008). It has to be taken into account, however, that these Stephanian pull-apart basins experienced a different depositional and diagenetic history due to their fault-controlled setting (Méndez, 1985; Frings et al., 2004; Botor and Anczkiewicz, 2015).

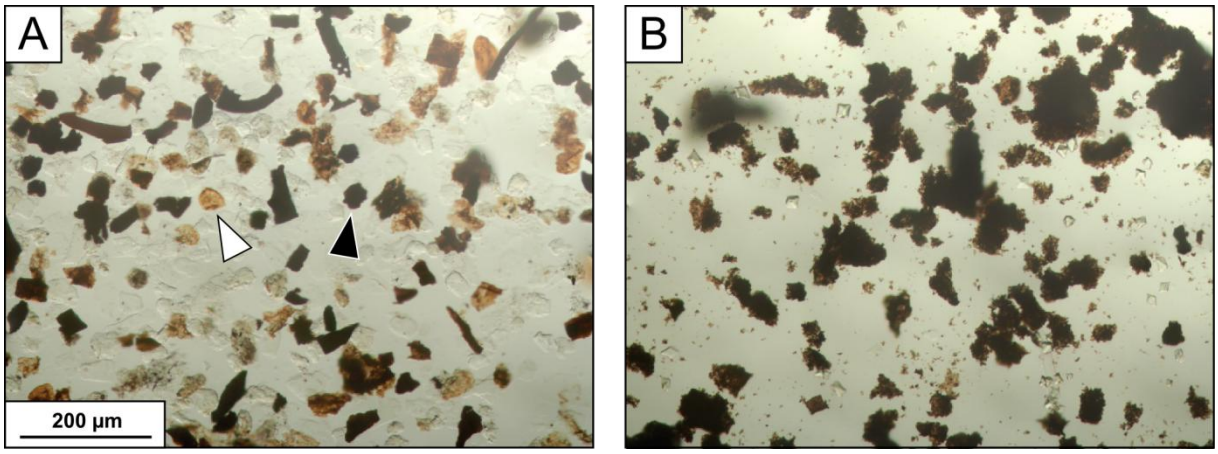

Figure 4.6: Kerogen photomicrographs. **(A)** Two populations of kerogen can be recognized in this sample from the San Emiliano Fm. Light brown colors (white arrow) characterize the least mature population, interpreted as *in situ*, whereas dark brown to black colors (black arrow) characterize the reworked most mature population. **(B)** Strongly altered OM in a sample from the Vegamián Fm.

4.2.5. Discussion

4.2.5.1. RE pyrolysis versus VR analysis

The less mature population of kerogen particles identified through optical kerogen analysis represents *in situ* organic matter recording the *in situ* basin maturity, while the higher mature population represents reworked organic matter showing the thermal overprint of previous depositional systems. Reflectance values of the total vitrinite population in the 5 analyzed samples from the San Emiliano Fm. are always higher compared to values of the corresponding *in situ* vitrinite population, but the differences show a significant variation (table 4.1). These differences seem to be controlled mainly by different proportions of highly mature reworked kerogen and less mature *in situ* kerogen, as observed in the kerogen slides (figure 4.6). This can also explain the difference between the less mature *in situ* VR data and the higher mature Tmax-derived VR data, as Tmax (and Tmax-derived VR) is based on whole rock samples, including both the less mature *in situ* OM and the higher mature reworked OM. The differences between Tmax-derived VR data and *in situ* VR data are thus controlled by changes in the proportions of higher mature reworked vitrinite and less mature *in situ* vitrinite.

The occurrence of highly mature reworked OM in the samples from the San Emiliano Fm. supports the hypothesis of reworked detrital illite influencing the KI data recorded for synorogenic successions in the CZ, which has been proposed in several studies (Bastida et al., 1999; Brime et al., 2001; Aller et al., 2005). Indeed, KI-derived temperatures for the San Emiliano Fm. (figure 4.3B) are distinctly higher compared to the temperatures obtained from both *in situ* (VR) and bulk rock paleothermometers (RE), and are even higher compared to fluid inclusion trapping temperatures in dolomite and quartz gangue minerals. The KI-derived paleotemperatures clearly represent overestimations of the true thermal maturity, most likely due to incorporation of detrital illite. The synorogenic San Emiliano Fm. is composed of siliciclastic sediments filling the foredeep of the Variscan Orogen (Brouwer and van Ginkel, 1964). The highly mature detrital illite and the reworked kerogen most likely represent eroded sediments, derived from the deformed and metamorphosed Variscan Orogen to the southwest composed of older pre-orogenic rocks (Julivert, 1978; Bastida et al., 1999). The importance of sediment reworking in pre-orogenic siliciclastic successions cannot be assessed for in this study. Nevertheless, also for these successions, the KI data indicate very high paleotemperatures not in agreement with the real thermal maturity of the sediments. Next to sediment reworking, additional causes for the anomalously high KI-derived temperatures are related to data measurement and processing, and to the empirical equation used for paleotemperature calculation. The KI data of Marschik (1992) were obtained by X-ray diffraction analysis of air-dried samples (Aller et al., 2005). This may result in an overestimation of the KI, as the presence of mixed-layer illite/smectite will modify the X-ray diffractograms in air-dried samples (Bastida et al., 1999; Junfeng and Browne, 2000). Empirical equations used to calculate KI-derived temperatures are not widespread in literature, and most of these equations are bound by specific preconditions. The equation of Mukoyoshi et al. (2007) yields the most realistic paleotemperatures for the range of KI data of Marschik (1992) and Aller et al. (2005).

The incorporation of reworked OM and detrital illite limits the interpretation of RE and KI data of the Carboniferous formations for paleothermometry purposes, since they represent synorogenic successions (figure 4.2; Marcos and Pulgar, 1982). Maturity analyses and paleothermal studies based on bulk rock techniques such as RE pyrolysis and the KI of illite crystallinity have a high risk of failure and erroneous interpretations in most sedimentary systems due to sediment reworking. Ideally, additional data are needed to cross-check the consistency and reliability of these bulk rock techniques. In this study, the presence of two populations of OM with different maturity levels, as observed through optical kerogen analysis, identified the problematic effect of reworking. Next to optical analysis, reworking can also be observed in the pattern of CO_2 produced during oxidation, following RE pyrolysis (figure 4.5B). The occurrence of two peaks in the oxidation patterns indicates the occurrence of two types of organic matter. Although RE pyrolysis can be used for fast screening of thermal maturity levels, additional maturity data are needed to verify the results from RE pyrolysis. This study indicates that a comparison with optical kerogen analysis of vitrinite is needed for more accurate interpretations, especially for the analysis of synorogenic sediments. Through VR analysis, reworked or altered vitrinite particles can be excluded, leading to more reliable and precise information on the thermal maturity of *in situ* vitrinite.

4.2.5.2. Comparison with paleothermal data from literature

The highest temperatures recorded for dolomitization and ore mineralization in the Variscan basement rocks of the Bodón Unit are derived from fluid inclusions in dolomite (130 – 150 °C: Gasparrini et al., 2006b) and in quartz gangue minerals in the central part of the study area (200 °C; Paniagua et al., 1993). Trapping temperatures of fluid inclusions indicate the maximum temperatures of hydrothermal fluid flow related to the Post-Variscan thermal event, as they provide a snapshot of the temperature during dolomitization and ore mineralization (e.g. Middleton et al., 2001). Hydrothermal fluid flow must have been most important in the central and western parts of the Bodón Unit, as well as in the southeastern part, given the abundance of dolomite and ore mineral deposits in these areas (figure 2.4). The occurrence of high CAI-derived paleotemperatures in carbonate precursors close to dolomitized and mineralized areas (figure 4.3A) attests of the importance of hydrothermal fluid flow in these parts of the Bodón Unit. The episodes of fluid flow must have been sufficiently long to allow the conodont fragments to equilibrate. Likewise, RE-derived temperatures of the Early Carboniferous Vegamián Fm. are higher in the central part of the Bodón Unit (151 – 172 °C) compared to the eastern part (129 °C).

Paleotemperatures derived from the *in situ* VR dataset of the Vegamián and San Emiliano Fm. are significantly lower compared to published data for the Stephanian CM and CR basins (figure 4.4A; Frings et al., 2004; Colmenero et al., 2008), highlighting their different thermal histories. They have been more intensely affected by hydrothermal fluid flow and volcanic intrusions due to their fault-controlled setting (Méndez, 1985; Frings et al., 2004), and due to the relatively high porosity and permeability of their sedimentary successions compared to the tight Paleozoic basement rocks making up the Bodón Unit (Duddy et al., 1994). Although the RE and KI-derived temperatures have to be treated with caution given the possible influence of reworked sediments, they seem to confirm the higher thermal maturity of the Stephanian basins (figures 4.3B & 4.4B).

Temperatures obtained from CAI data for precursor carbonates show baseline values around 60 °C in the eastern part of the study area, which was less affected by fracture-related hydrothermal dolomitization and ore mineralization (figures 2.4 & 4.3A). VR data yield temperatures around 100 °C for siliciclastics in the same area. This difference of approximately 40 °C can have several causes related to either the alteration of conodonts or the reflectance of vitrinite. The variety of empirical equations to calculate paleotemperatures from VR data yields divergent paleotemperatures (table 4.2), which results in an error range regarding VR-derived paleotemperatures. A possible suppression of vitrinite reflectance (Schito et al., 2016) cannot be assessed for in this study. Regarding the CAI data, it is known that they, compared to other paleothermometers, might be less sensitive. Zhang and Barnes (2007) state that CAI values changing from 1 to 1.5 (49 to 62 °C) are not as sensitive as corresponding VR or KI data. Moreover, Raven and van der Pluijm (1986) report a general range of uncertainty of ± 0.5, corresponding to a temperature range of ± 25 °C. Secondly, the applied heating time of 10 Ma might be an overestimation of the true time of heating. This is unlikely, given the AFT results of Carrière (2006) and Botor and Anckiewicz (2015) which indicate that following the Post-Variscan thermal event, temperatures remained high for a significant period of time. Even if the heating time is decreased to 1 Ma on the Arrhenius plot of Epstein et al. (1977), temperatures around 75 °C are obtained, which are still significantly lower compared to VR-derived temperatures. A third cause might be retardation of the color alteration process due to hydrothermal alteration. Hydrothermal alteration is usually accompanied by indicative textures and patinas (Voldman et al., 2008), which have indeed been observed in the CZ (Raven and van der Pluijm, 1986; Bastida et al., 1999; Blanco-Ferrera et al., 2016).

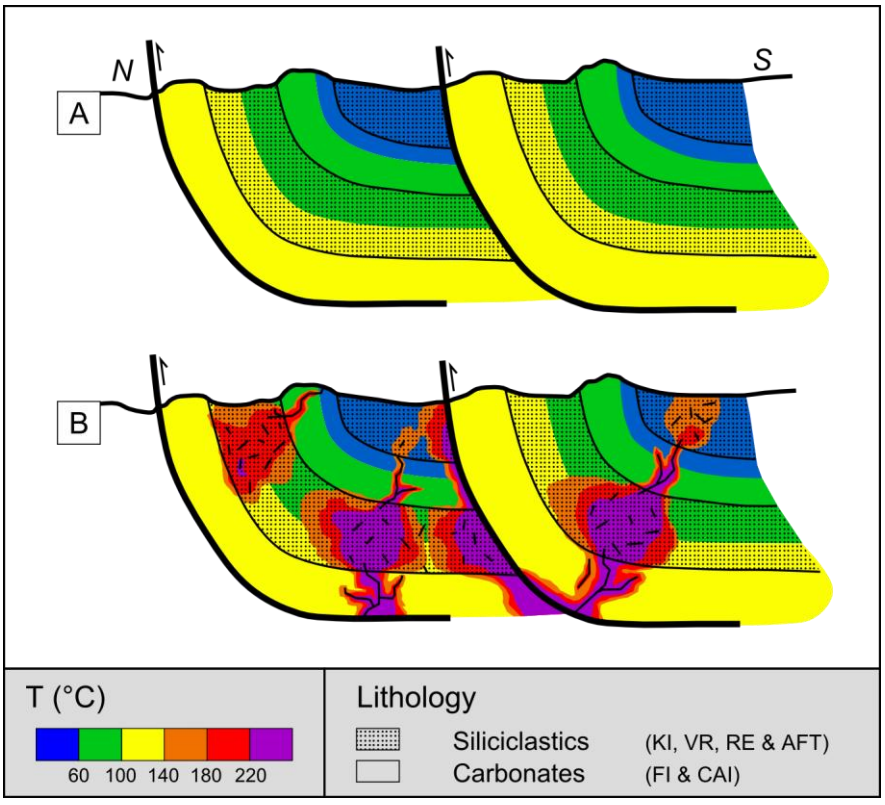

Figure 4.7: Sketch illustrating the principle of deformation partitioning in different mechanical units of the Variscan FFTB. **(A)** Paleothermal setting following Variscan thrusting. The thermal maturity experienced by the rock successions is caused by pre-Variscan peak burial. **(B)** Superimposed effects of Late- to Post-Variscan hydrothermal fluid circulation. Hydrothermal fluids circulated through rigid carbonates along spaced faults and fractures, while fluid circulation was more diffuse through the ambient siliciclastics where the heat transfer was more efficient.

Next to a lower sensitivity of the CAI technique, a secondary cause which might explain the observed differences between CAI- and VR-derived paleotemperatures, is the influence of deformation partitioning in different mechanical units of the Variscan FFTB (figure 4.7). CAI data are obtained from the thick Cambrian and Carboniferous carbonate successions representing rigid carbonate units. Hydrothermal fluid circulation was likely restricted to spaced fractures in these tight units, causing fracture-related dolomitization and ore mineralization, and resulting in a strong thermal overprint of nearby carbonate precursors. VR data on the other hand, are obtained from weak siliciclastic clay-rich successions which were more intensely deformed and might have allowed a more wide-spread circulation of hydrothermal fluids and a more effective heat dissipation in response to the Post-Variscan thermal event (see section 2.4).

In order to better understand the observed variation in paleotemperature between ambient siliciclastics and precursor limestones, the latter could be subject to clumped isotope paleothermometry (see section 4.3.2.2). According to recent experimental studies, the clumped isotope signature and corresponding paleotemperature of calcite crystals will be affected by solid state diffusion when the sample is heated to temperatures between 75 to 100 °C for 100 Ma (Henkes et al., 2014; Stolper and Eiler, 2015; Mangenot, 2017). Solid state diffusion is a process whereby atoms can migrate through a crystal when it is exposed to high temperatures (Dennis and Schrag, 2010; Passey and Henkes, 2012). Migration of atoms implies a resetting of the clumped isotope signature and thus corresponding paleotemperatures. If the maximum temperatures experienced by precursor limestones averaged around 60 °C, solid state diffusion should not have influenced the clumped isotope temperature. In this case, clumped isotope analyses of primary calcite from Carboniferous precursor limestones, e.g. a fragment of a crinoid, should yield temperatures corresponding to the temperature of crystallization of the crinoid (i.e. the depositional temperature). If the obtained clumped isotope temperature is higher, one can suspect that the precursor carbonates have experienced temperatures of 75 to 100 °C for a prolonged time, inducing the process of solid state diffusion. This could be an additional clue to understand the observed thermal variation between siliciclastics and limestones, which has important implications for thermal modeling. However, it is unlikely that the Paleozoic rocks of the Bodón Unit experienced temperatures of 75 to 100 °C for more than 10 Ma (Carrière, 2006).

4.2.5.3. Hydrothermal versus geothermal dolomitization

In the field of ore geology, hydrothermal activity refers to the action of hot waters directly related to igneous activity, in contrast with geothermal waters which are not related to igneous intrusions (Robb, 2005). In dolomitization studies, hydrothermal generally applies to dolomitization by fluids with temperatures at least 10 °C higher than those experienced by the surrounding rocks, including both carbonate precursors and ambient siliciclastics (Stearns et al., 1935; White, 1957; Machel and Lonnee, 2002). The current dolomitization model for the dolomite geobodies in the Bodón Unit assumes that thermal convection of hydrothermal marine-derived brines resulted in fracture-related porous dolomites (Gasparrini et al., 2006b). This was based on the difference between FI trapping temperatures of 130 to 150 °C (Gasparrini et al., 2006b) and CAI-derived paleotemperatures of 70 to 95 °C in Carboniferous carbonate formations (Raven and van der Pluijm, 1986).

This study indicates that in the eastern part of the study area, CAI-derived paleotemperatures of undolomitized precursor carbonate rocks average around 60 °C, which is likely an underestimation of their true thermal maturity. Siliciclastic ambient rocks are characterized by VR-derived temperatures around 100 °C. Since dolomitization and ore mineralization were more important in the central and western parts of the study area, one can assume that these lower temperatures are the result of Pre-Variscan burial and high crustal heat flow during the Post-Variscan thermal event. It confirms the hydrothermal nature of dolomitization (130 to 150 °C) and ore mineralizations (up to 200 °C) which are clearly related to positive temperature anomalies in the central and western parts of the study area.

4.2.6. Conclusion

The thermal maturity of Paleozoic rocks exposed in the Bodón Unit has been investigated to better constrain the thermal conditions of Late- to Post-Variscan fluid flow which caused widespread dolomitization and ore mineralization. Maximum temperatures experienced by both carbonate precursor and ambient siliciclastic rocks have been assessed based on a compilation of published paleothermal data (CAI, KI, VR, FI) combined with newly acquired RE pyrolysis and VR analysis data.

Both RE and KI data from synorogenic successions yield paleotemperatures that are anomalously high compared to *in situ* VR data and CAI data. Optical kerogen analysis of VR samples revealed an important amount of reworked highly mature kerogen, giving evidence for significant input of reworked sediments in these synorogenic units. The presence of reworked sediments, most likely eroded material from higher metamorphic zones of the Variscan Orogen, critically affects maturity analysis through bulk rock techniques like RE pyrolysis, KI and VR analysis of total vitrinite populations. This is a general problem in many sedimentary systems, where maturity analyses based on bulk rock data are limited by uncertainties and the risk of erroneous misinterpretations. During optical kerogen analysis, *in situ* and reworked kerogen populations can be identified. Using only the reflectance values of *in situ* populations significantly increases the accuracy and reliability of the maturity data and minimizes the risk of failure of maturity analyses.

CAI-derived paleotemperatures for carbonate precursor rocks not affected by intense fluid circulation average around 60 °C and are attributed to burial and increased crustal heat flow following lithospheric delamination. Paleotemperatures within these carbonate rock units increase towards dolomitized and mineralized zones, which formed during Post-Variscan fluid flow at temperatures up to 200 °C (Paniagua et al., 1993). Siliciclastic ambient rocks affected by burial and high crustal heat fluxes have a higher average thermal maturity, corresponding to temperatures around 100 °C (based on *in situ* VR data). The different thermal maturity of carbonate and siliciclastic rocks is likely caused by a difference in analytical techniques used to obtain CAI and VR data and their corresponding paleotemperatures. Conodont fragments were likely not as sensitive to the thermal overprint compared to VR, and the color alteration process might have suffered from hydrothermal alteration. A secondary cause to explain the difference in thermal maturity might be a different response to Variscan compression and orocline formation of rigid precursor carbonates and softer ambient siliciclastics which caused the hot fluids to circulate in a different manner. Circulation was localized along spaced fractures through the carbonates, and was more widespread through the siliciclastics, resulting in more efficient heat transport.

Massive fracture-related dolomitization of Cambrian and Carboniferous carbonates of the southern Cantabrian Zone occurred at temperatures between 90 and 150 °C (based on FIs). Undisturbed ambient siliciclastic rocks experienced temperatures around 100 °C, whereas this temperature might have been lower for precursor carbonates. Dolomitization was thus caused by hydrothermal fluids, circulating in thermal disequilibrium with the precursor carbonate rocks. The positive temperature anomalies recorded in the precursor carbonate rocks by CAI data broadly correlate with the occurrence of dolomitization and ore mineralization. This implies that in similar settings, mapping the thermal maturity anomalies within carbonate precursors could be used as an exploration tool for porous hydrothermal dolomite geobodies and ore mineralization.

4.3. Dolomite paleothermometry

4.3.1. Introduction

The study of clumped isotopes (CI) is concerned with the state of ordering of rare and heavy isotopes in natural materials and blessed the scientific world with the introduction of a new carbonate paleothermometer (Eiler and Schauble, 2004; Ghosh et al., 2006; Eiler, 2007). Approximately 10 years ago, Ghosh et al. (2006) reported that bonding between heavy O and C isotopes (e.g. ^{18}O and ^{13}C) in the carbonate mineral lattice is directly related to crystallization temperature and independent of the isotopic composition of the precipitating fluid. The amount of carbonate ions containing two or more heavy isotopes thus provides a direct approach to paleothermometry which, in contrast to the classical $\delta^{18}O$ thermometer (Urey, 1947; Epstein et al., 1953), does not require assumptions about the isotopic composition of the water from which the mineral grew.

Most CI paleothermal studies so far have focused on low-temperature (< 100 °C) calcite and dolomite (e.g. Ferry et al., 2011; Huntington et al., 2011; Dale et al., 2014; Swart et al., 2016; Mangenot et al., 2017). Measurements of higher temperature precipitates have been impeded by the lack of calibrations for high temperature ranges (see section 4.3.2.2). This part of the PhD thesis aims to use a set of HTD cement samples from the Bodón Unit as a test case for high-temperature CI paleothermometry. The obtained CI temperatures are compared to FI homogenization temperatures (T_h) derived from the same samples, allowing a comparative study between both paleothermometers.

Based on the thermal data derived from both thermometers, this chapter also introduces a new approach to geobarometry in carbonate minerals in sedimentary and diagenetic settings. Pressure is, like temperature, an important parameter to be considered when investigating a wide range of geological processes. Geobarometry can yield information on diagenesis, basin evolution, hydrocarbon generation and boiling of ore-forming fluids, among others. To date, only a limited number of geobarometers exist, only a few of which are applicable to sedimentary and diagenetic settings. Most of these geobarometers are, at least partly, based on the use of FI data (Roedder and Bodnar, 1980). One way to estimate pressure conditions during crystal growth is by combining information from two immiscible fluids which are trapped simultaneously (e.g. petroleum and aqueous fluids; Munz, 2001). This approach is hampered by the need for multiple cogenetic FI generations, which are not frequently encountered. If only one generation of inclusions is present, information on its homogenization temperature and composition can be used for geobarometry, but only in combination with an independent geothermometer which can provide the temperature of formation of the host crystal (e.g. chlorite thermometry; Schroyen and Muchez, 2000). An important assumption is that both FIs and mineral phases used as independent geothermometer are spatially and temporally associated, which is not easy to prove (Roedder and Bodnar, 1980). Estimating the pressure of carbonate crystallization by combining thermal information from FI microthermometry and CI paleothermometry provides a new approach to geobarometry. Pressures can now be measured on single carbonate crystals, without the need for cogenetic FI generations or other independent geothermometers, since FI and CI data are obtained from the same carbonate mineral phase.

4.3.2. Methodology

The dataset of dolomite samples used for this study consists of 9 samples of dolomite cement from which 2 samples came directly from the sample set used by Gasparrini et al. (2006b) for FI microthermometry. The other 7 samples were collected from the Barcaliente Fm. exposed in the Bodón Unit (figure 4.8). Samples were obtained specifically from the same locations corresponding to those of Gasparrini et al. (2006b) in order to allow a comparison with the newly obtained FI data. Samples and thin sections were stained and investigated with standard optical microscopy and additional cathodoluminescence microscopy (see section 3.2.3).

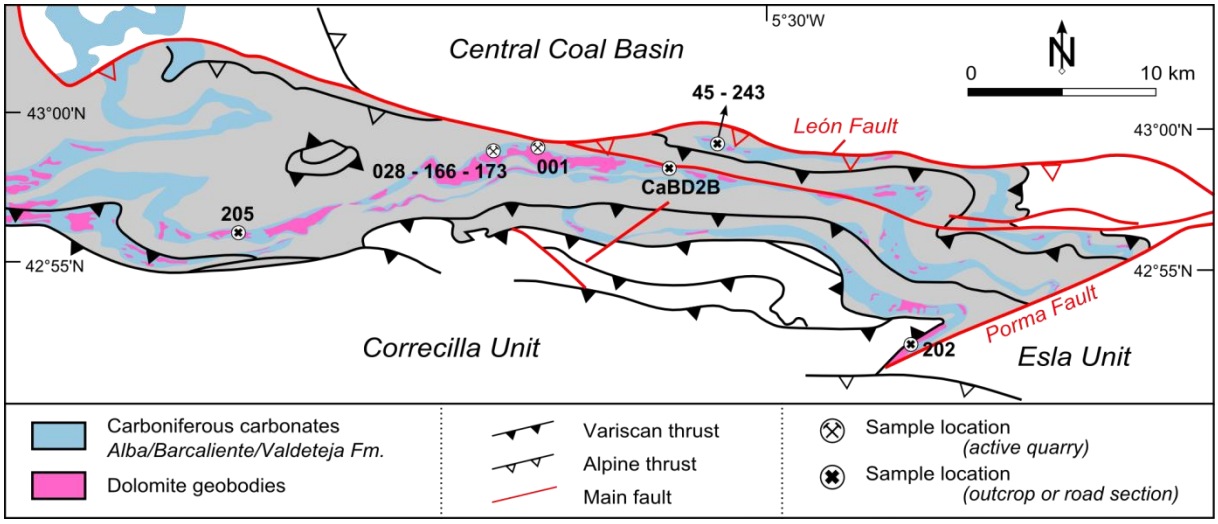

Figure 4.8: Geological map of the Bodón Unit adapted from Alonso et al. (2009) and Muñoz Quijano (2015). The map shows the locations of samples used for clumped isotope paleothermometry and FI microthermometry.

4.3.2.1. Fluid inclusion microthermometry

In order to obtain a precise comparison between T_h and clumped isotope temperatures, new FI measurements were performed on all samples, including those provided by Gasparrini et al. (2006b). Inclusions suitable for microthermometric analysis were selected based on a petrographic study of both thin sections and double polished thick sections (± 100 µm thick; cold-polishing technique; cfr. Muchez et al., 1994). Primary inclusions were selected from petrographically associated assemblages (FIA; Goldstein and Reynolds, 1994) and from growth zones within individual crystals. Measurements were carried out at KU Leuven on a Linkam MDS-600 heating/cooling stage mounted on an Olympus BX51 microscope. The stage was calibrated by synthetic Syn Flinc^{Tm} fluid inclusion standards. Isochores were calculated for each sample using salinity data from Gasparrini et al. (2006a, b) and the equation of state from Zhang and Frantz (1987). Salinity calculations were based on microthermometry coupled with cryo-Raman spectroscopy and revealed salinities around 26 eq. wt% $CaCl_2$ (see section 2.5). An overview of T_h frequency histograms and boxplots for each sample is provided in Appendix V. Raw T_h data for each sample are listed in Appendix VI.

4.3.2.2. Carbonate clumped isotope paleothermometry

CI analyses of carbonate minerals are performed on CO_2 extracted from the minerals by acid fractionation. The abundance of the $^{18}O^{13}C^{16}O$ isotopologue (isotopic variant of a molecule) in the extracted CO_2 is measured by gas-source isotope ratio mass spectrometry and expressed as Δ_{47}, which represents the offset (‰) of the amount of heavy bonds compared to a stochastic isotopic distribution, expressed in the Carbon Dioxide Equilibrium Scale (CDES) established by Dennis et al. (2011). CO_2 has 12 different isotopic variants (e.g. $^{16}O^{12}C^{16}O$, $^{17}O^{13}C^{18}O$,…), but clumped isotope measurements are performed on the isotopologue with mass 47 as it is the most abundant variant containing 2 heavy isotopes (i.e. ^{18}O and ^{13}C). A temperature decrease results in an increase in clumping between heavy isotopes and thus an increase in the Δ_{47}-value (figure 4.9). Ghosh et al. (2006) introduced the first experimental calibration to convert Δ_{47} to temperature, based on synthetic inorganic calcite precipitated in a laboratory environment. During the following years, several modified or new calibrations have been proposed, all of them focusing on materials precipitated below 100 °C (e.g. Ghosh et al., 2007; Eagle et al., 2010; Henkes et al., 2013; Came et al., 2014; Kele et al., 2015). Kluge et al. (2015) introduced the first high-temperature carbonate calibration (up to 250 °C) based on CI measurements of inorganic calcite precipitated in a laboratory environment. Bonifacie et al. (2017) recently created a high-temperature calibration for dolomite (up to 350 °C) based on CI measurements performed in two different laboratories using different methods for data acquisition and post-measurement processing. Inter-laboratory communication and cooperation are indispensable for the creation of universal calibrations, as the weak reproducibility between current calibrations is often attributed to the laboratory-specific nature of methodological procedures for data acquisition and post-measurement data processing (Bonifacie et al., 2017; Kelson et al., 2017).

CI analyses were performed in the Qatar Stable Isotope Lab at Imperial College London. The method used for the analyses is based on Dennis and Schrag (2010) and described for the Imperial College laboratory in Dale et al. (2014). Powder samples were drilled from rock slabs using a dental drilling device with a drilling bit 1.4 mm in diameter. On average 3 to 5 replicate measurements were performed for each sample using the same manual CO_2 purification line and mass spectrometer. Aliquots of 5 to 6 mg of dolomite powder were reacted online in a phosphoric acid (H_3PO_4) bath held at 90 °C for 20 minutes. The liberated CO_2 gas was subsequently purified from contaminants, such as hydrocarbons or sulfides, prior to mass spectrometric analysis. This is accomplished by cryogenic purification through a Porapak Q trap. Purification is a necessary step given the low natural abundance (45 ppm; Ghosh et al., 2006) of the CO_2 isotopologue with mass 47. Contaminants might produce gas molecules which can create significant isobaric interferences during mass spectrometry. The clean gas was measured on a Thermo Fisher MAT 253 isotope ratio mass spectrometer. Data processing was performed using the free software Easotope (John and Bowen, 2016), and processed using the 'Brand' parameters for ^{17}O correction (Daëron et al., 2016). Non-linearity corrections were done based on heated gases (Huntington et al., 2009), and the projection of the data into the absolute reference frame of Dennis et al. (2011) was performed using heated gases, and inter-laboratory standards ETH1, ETH2, and ETH3 (Meckler et al., 2014). All data are presented in the absolute reference frame CDES using the permil (‰) unit. Reliability of the measurements was assessed based on the Δ_{48} offset and 49 parameter (cfr. Huntington et al., 2009). The natural abundances of the 48 and 49 CO_2 isotopologues are too

small to be detectable during mass spectrometry. The presence of measurable signals of these isotopologues can thus be used as a sign of contamination. Δ_{47} values were converted into temperatures using the calibration of Kluge et al. (2015). The latter calibration has been established in the Qatar Stable Isotope Lab at Imperial College London and was the only high-temperature calibration available at the time of data acquisition and processing. The calibration has been recently adapted with the newly proposed 'Brand' parameters for ^{17}O correction (Daëron et al., 2016). Temperatures are reported at 1 standard error (SE) precision and at 95 % confidence level (CO). The measured clumped isotope signatures have also been converted based on the recent calibration of Bonifacie et al. (2017), which however does not take into account the new 'Brand' parameters (Daëron et al., 2016). In the remainder of this chapter, Δ_{47}-temperatures ($T\Delta_{47}$) obtained with the Kluge et al. (2015) calibration will be referred to as KL15 while Δ_{47}-temperatures obtained with the Bonifacie et al. (2017) calibration will be referred to as BO17. An overview of Δ_{47} and corresponding temperature for each sample can be found in table 4.3. Appendix VII provides a similar table, extended with raw data.

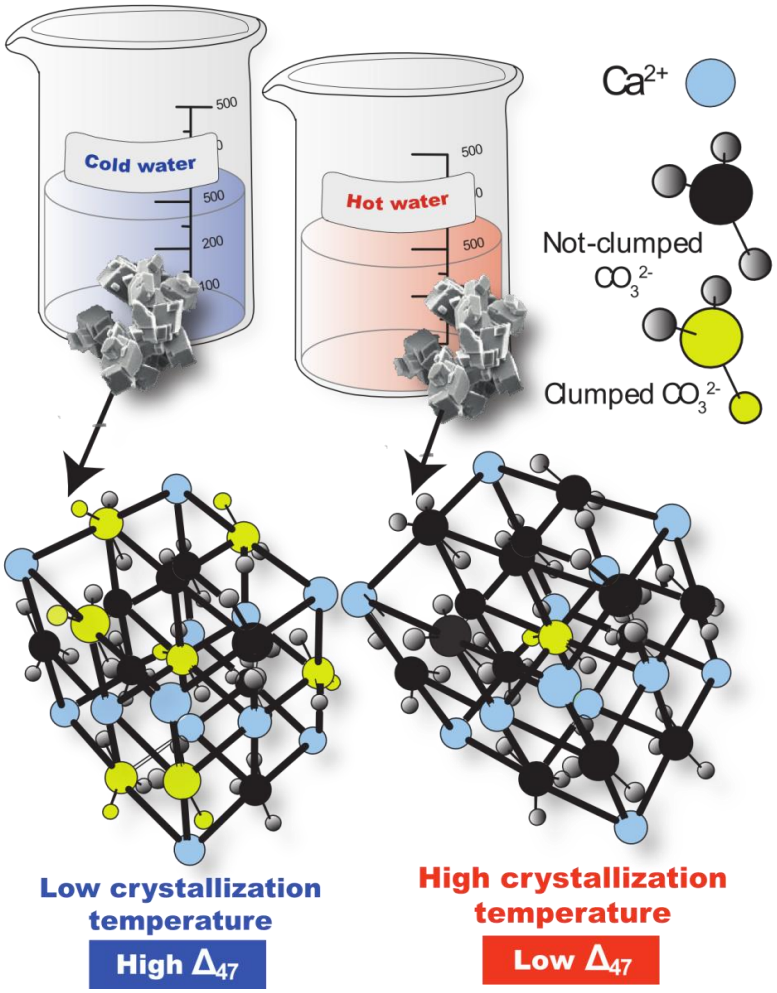

Figure 4.9: Illustration of the incorporation of carbonate ions in the crystal lattice of calcite as a function of temperature (Mangenot et al., 2017). Clumping between heavy and rare isotopes (yellow) in carbonate ions is promoted at low temperatures, resulting in the incorporation of heavy carbonate ions and a high Δ_{47} signature (left). At higher temperatures, clumping will be less important, resulting in lower Δ_{47} signatures (right). The amount of carbonate ions containing clumped isotopes is exaggerated for clarity.

4.3.3. Results

All 9 samples display either zebra or breccia textures. Zebra textures have been formerly interpreted as alternations of dark gray replacive and white dolomite cement filling voids developed by focused flow of overpressured basinal fluids (Nielsen et al., 1998; Vandeginste et al., 2005). The dolomite veins making up zebra sets in the samples used for this study consist of thin rims made up of idiotopic white dolomite crystals (figure 4.10A). They show a mottled appearance under luminescent light, except for a last growth zone exhibiting a dull luminescence (figure 4.10B). Breccia textures are composed of angular fragments of replacive dolomite in a matrix of dolomite and calcite cement (figure 4.10C). They are mostly clast-supported, with thick dolomite cement rims which show a similar luminescence as the rims observed in zebra veins (figure 4.10D). Individual dolomite crystals are larger compared to those making up the zebra veins, though they show stepwise crystal terminations. The dull rims in both zebra and breccia textures represent a change in fluid chemistry (see section 3.4.2.3). They often show signs of dedolomitization, and were avoided during sampling. Two breccia samples (samples 202 and CaBD2B) show replacive dolomite with large crystal sizes (around 250 µm) and abundant development of saddle dolomite crystals (figure 3.16B; up to 2000 µm). Both replacive and void-filling dolomite in these samples display no or low luminescence. Sample 202 is obtained from key outcrop 3 discussed in chapter 3 (see sections 3.3.3 & 3.7.3).

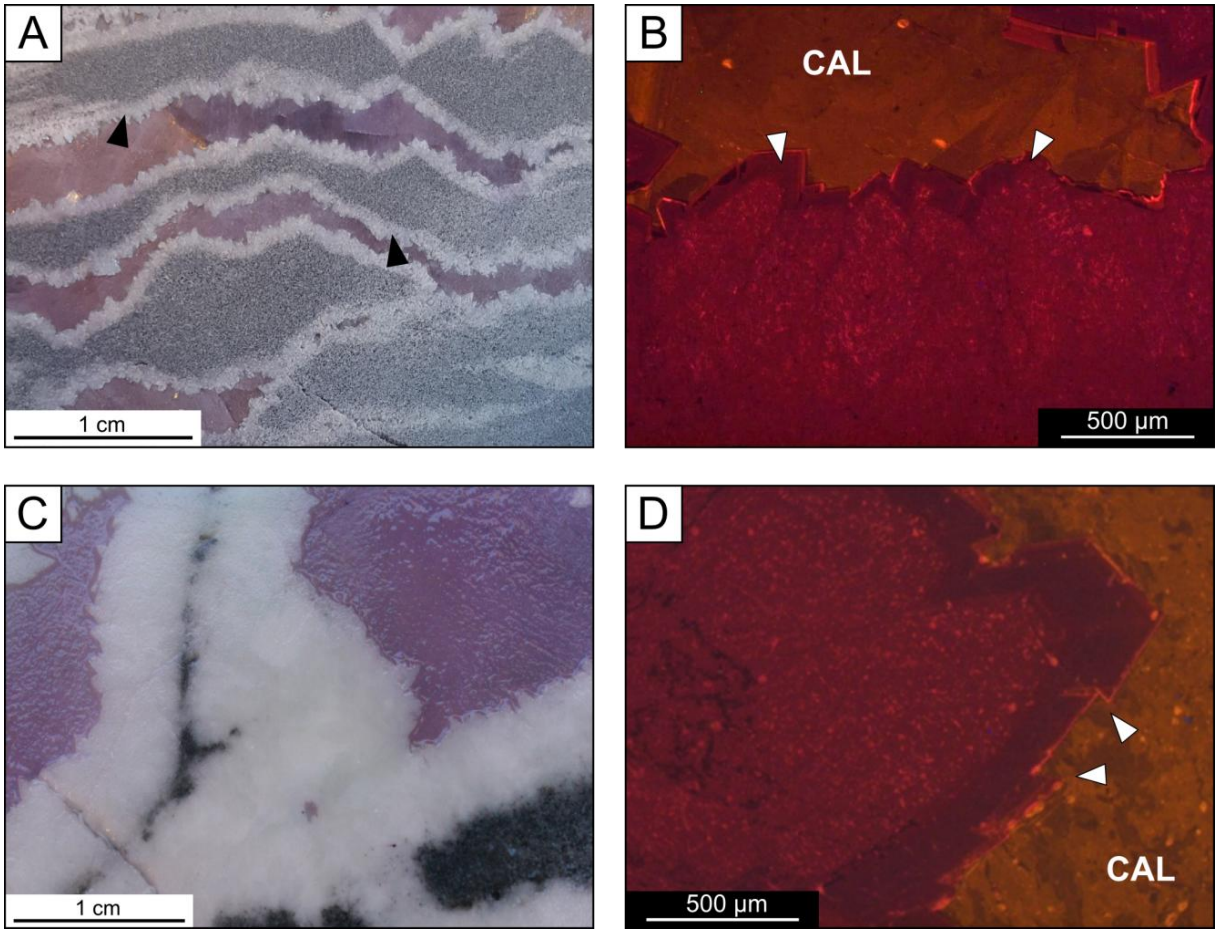

Figure 4.10: Petrography of samples used for fluid inclusion microthermometry and clumped isotope paleothermometry. **(A)** Zebra texture with thin white dolomite cement rims (black arrows). Calcite is stained red. **(B)** CL photomicrograph of dolomite cement crystals making up zebra texture. A last growth zone exhibiting dull luminescence is indicated with white arrows. Orange calcite cement is visible in the upper part of the image ('CAL'). **(C)** Breccia texture. Calcite is stained red. **(D)** CL photomicrograph of dolomite cement crystals in breccia. Note the large crystal size and stepwise crystal terminations (white arrows). Orange calcite cement is visible in the right part of the image ('CAL').

Frequency histograms of T_h data for individual samples show unimodal distributions (figure 4.11; see Appendix V). T_h modes of fluid inclusions for all 9 samples broadly correspond to those obtained by Gasparrini et al. (2006b) and range between 95 and 145°C (figure 4.12; table 4.3).

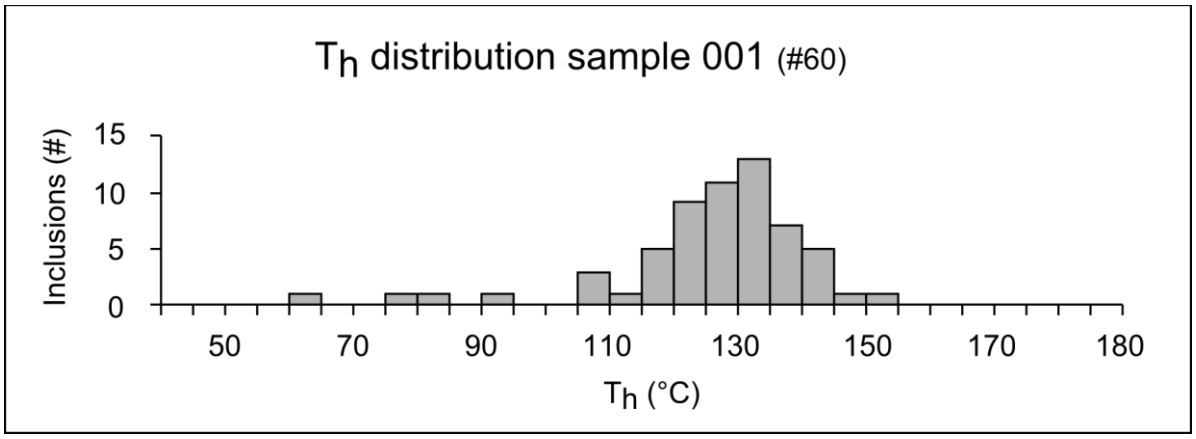

Figure 4.11: Frequency histogram for T_h values measured for 60 fluid inclusions in sample 001. The histogram shows a unimodal distribution, which suggests a primary nature for fluid inclusions and a lack of possible resetting. The inclusions characterized by lower temperatures possibly represent secondary or necked inclusions (change in shape).

CI temperatures obtained from dolomite crystals range between 107 and 168 °C (KL15, figure 4.12A) and between 102 and 154 °C (BO17; figure 4.12B). For all 9 samples investigated, KL15 yields slightly higher temperatures (6.1 % or 8 °C on average) compared to BO17 (figure 4.12; table 4.3). T_h-data are generally lower compared to Δ_{47}-temperatures, except for sample 028 (with both KL15 & BO17) and samples 166 and 173 (with BO17).

TABLE 4.3: Fluid inclusion and clumped isotope data

Sample	Texture	T_h (°C)	Δ_{47} (‰CDES)	# replicates	$T\Delta_{47}$ (°C)*	±1SE (°C)	±1CO (°C)	P (MPa)*	$T\Delta_{47}$ (°C)**	P (MPa)**
001	Zebra	133	0.462	3	149	8	34	32	138	9
028	Breccia	128	0.489	3	125	3	14	0	118	0
166	Breccia	130	0.48	4	133	4	14	7	125	0
173	Breccia	123	0.489	5	126	7	20	8	118	0
202	Breccia	105	0.494	3	121	2	7	37	115	35
205	Zebra	110	0.489	2	125	4	54	34	118	22
243	Zebra	95	0.513	3	107	1	3	29	102	26
45†	Zebra	100	0.482	3	131	5	22	72	123	53
CaBD2B†	Breccia	145	0.444	2	168	7	93	50	154	18

*Calculated using modified Kluge et al. (2015)

**Calculated using Bonifacie et al. (2017)

†Samples from Gasparrini et al. (2006a)

Table 4.3: Results from FI microthermometry and CI paleothermometry. $T\Delta_{47}$ and corresponding pressure data have been calculated based on Kluge et al. (2015; reprocessed with new 'Brand' parameters for ^{17}O correction) and Bonifacie et al. (2017). An extended table with raw data can be found in Appendix VII.

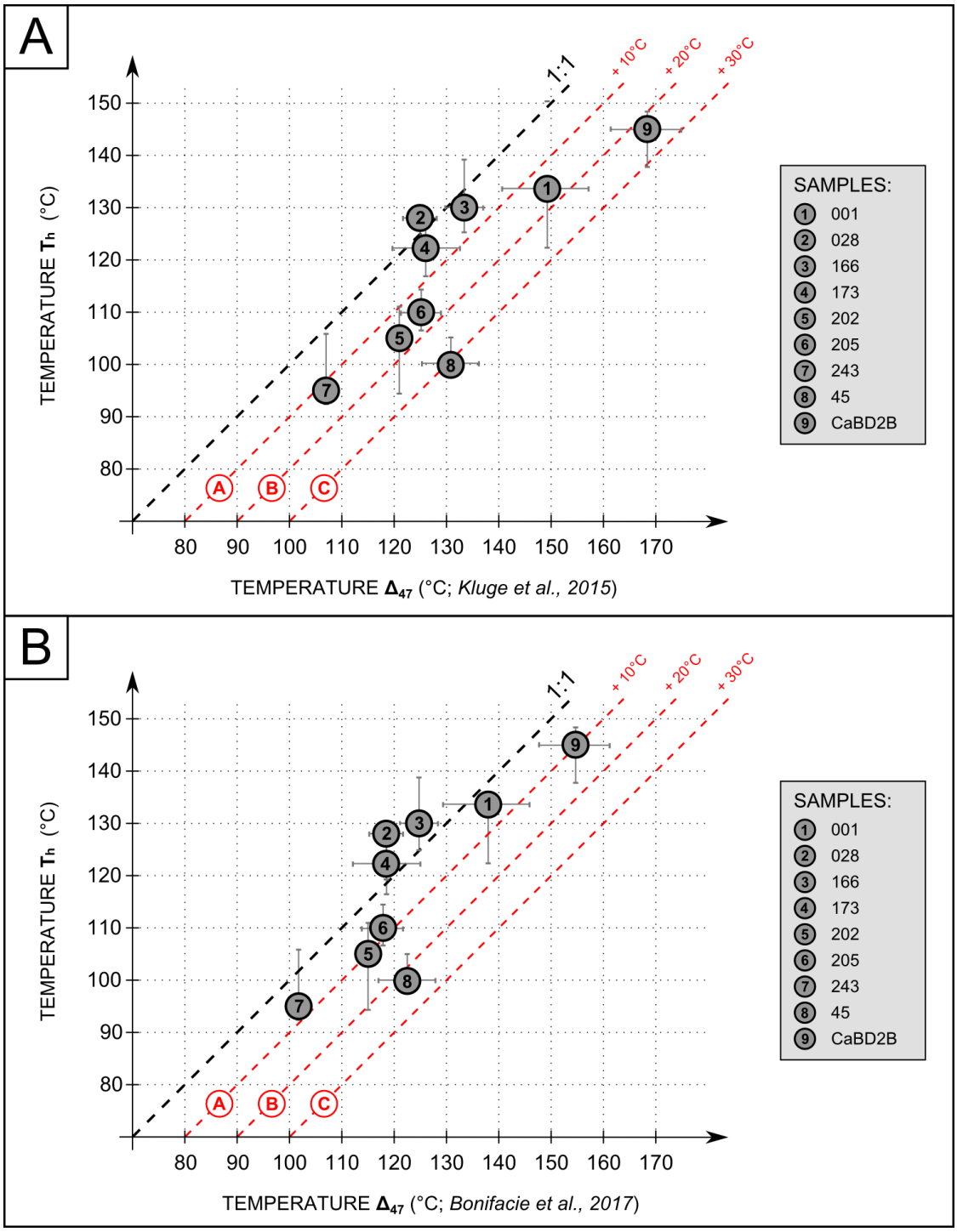

Figure 4.12: Graphs showing relationship between FI homogenization temperature (T_h) and CI (Δ_{47}) temperature. T_h-values range between 95 and 145 °C. Δ_{47}-temperatures range between 107 and 168 °C (Kluge et al., 2015; **A**) and between 102 and 154 °C (Bonifacie et al., 2017; **B**). Error bars for T_h-values correspond to Q1 – Q3 ranges (25^{th} – 75^{th} percentiles) which are enlisted in Appendices IV and VI. Error bars for Δ_{47}-temperatures correspond to ±1SE enlisted in table 4.3 (and in Appendix VI). The black dashed line represents a 1:1 fit between both temperatures, while the red dashed lines represent offsets in Δ_{47} temperature (A: +10 °C; B: +20 °C; C: +30 °C).

4.3.4. Discussion

4.3.4.1. Fluid inclusions versus clumped isotopes

Several sources of error can influence both FI and CI datasets and can result in significant variations. Firstly, FIs should be primary and not affected by post-entrapment processes such as thermal reequilibration or deformation of crystals (Goldstein and Reynolds, 1994). The FIs used for this study were selected from FIAs and growth zones within crystals, in order to avoid measuring secondary inclusions. Frequency histograms of T_h data for individual samples show unimodal distributions (figure 4.11; see Appendix V) which suggests that the inclusions are indeed primary and have not been affected by post-entrapment processes. Secondly, the carbonate crystals should not be affected by solid-state diffusion of O and C atoms, which could break bonds between heavy isotopes hereby inducing an overestimation of $T\Delta_{47}$ (e.g. Came et al., 2017; see section 4.2.5.2). Temperatures necessary for diffusion likely approach 300 °C for dolomite (Lloyd et al., 2017; MacDonald et al., 2017), which is significantly higher compared to calcite (see section 4.2.5.2). Circulation of hydrothermal fluids following lithospheric delamination was the hottest event affecting the Paleozoic rocks in the CZ (Carrière, 2006) minimizing the possibility of solid-state diffusion in dolomite crystals.

A third and important cause which could account for part of the temperature variation between CI paleothermometry and FI microthermometry is a difference in the sample volumes for both techniques. This is the most likely explanation for the occurrence of lower T_h compared to $T\Delta_{47}$ values for some samples (e.g. figure 4.12B). Powder samples used for clumped isotope analyses (± 30 mg for each sample) were drilled from dolomite crystals visible on rock slabs and are inevitably derived from a suite of crystals (Defliese and Lohmann, 2015). FI measurements, on the other hand, allow obtaining T_h-values for individual crystals and even growth zones within crystals. Hydrothermal systems are known to be episodically very dynamic (Eichhubl and Boles, 2000), which may account for rapid variations in temperature. FI data obtained from individual crystals might therefore differ from CI data which give an 'averaged' temperature. Analytical improvements resulting in increasingly smaller sample sizes (currently up to 1 mg for 1 replicate measurement) will allow more precise CI measurements (Hu et al., 2014; Müller et al., 2017). An additional source of error, which is related to the CI technique, is the use of laboratory-specific methods for data acquisition and post-measurement processing (see section 4.3.2.2; Bonifacie et al., 2017). In order to take this source of error into account, this study applies the two most accepted high-temperature calibrations (Kluge et al., 2015; Bonifacie et al., 2017).

4.3.4.2. Geobarometry

On the assumption that both FI and CI signatures are pristine and have not been reset, the offset (ΔT) between T_h and $T\Delta_{47}$ can be explained by the fact that T_h represents the minimum temperature of FI entrapment while $T\Delta_{47}$ represents the true temperature of crystallization of the host dolomite mineral (figure 4.13). ΔT is influenced by the pressure at the time of inclusion entrapment, referred to as the pressure correction (Goldstein, 2001). At low pressures, the crystallization temperature should be similar to the temperature of fluid inclusion entrapment and ΔT should be close to 0. At higher pressures, $T\Delta_{47}$ should theoretically be higher than T_h. The

dataset yields CI temperatures which are higher compared to FI homogenization temperatures, except for 1 sample (KL15; figure 4.12A) or 3 samples (BO17; figure 4.12B). A reason for this deviation could be the difference in sample volume and the episodic nature of dolomitization as mentioned above (section 4.3.4.1), or an underestimation of $T\Delta_{47}$ from the calibration of Bonifacie et al. (2017).

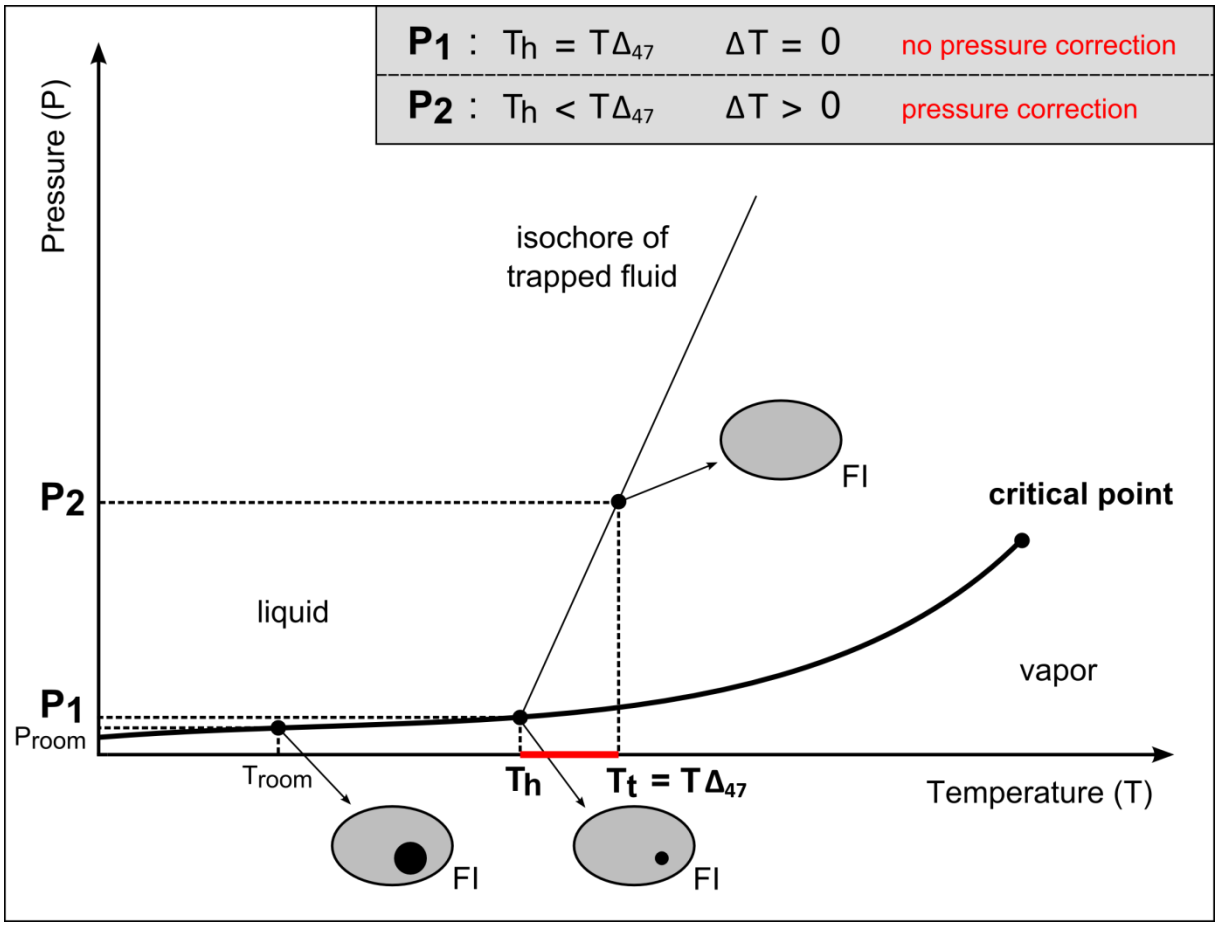

Figure 4.13: Pressure-temperature phase diagram of water illustrating the principle of geobarometry based on fluid inclusion T_h and clumped isotope $T\Delta_{47}$. In case of low pressure during carbonate precipitation, $T\Delta_{47}$ and T_h will be approximately similar (P_1). With increasing pressures (P_2), $T\Delta_{47}$ will increase compared to T_h, resulting in a temperature offset (ΔT). Phase diagram based on Gasparrini (2003).

The crystallization temperatures obtained with CI paleothermometry can be plotted on the isochores constructed for each sample based on their T_h mode and composition of their FIs (figure 4.14). Corresponding pressures range between 0 and 72 MPa (KL15, figure 4.14A; table 4.3) and between 0 and 53 MPa (BO17; figure 4.14B; table 4.3), which is significantly higher compared to a hydrostatic pressure of 10 MPa typically prevailing in rocks at 1000 m depth (Frings et al., 2004). Void-filling dolomite cement from breccia samples is characterized by low pressures (0-8 MPa KL15; 0 MPa BO17), while dolomite crystals in zebra veins formed at higher pressures, between 29 to 72 MPa (KL15) and 22 to 53 MPa (BO17). The lower pressures recorded by breccia cements could be related to an abrupt decrease in fluid pressure that results from the creation of open space following hydraulic brecciation (Knipe, 1993). The massive nature of the cements and their imperfect crystal morphologies support a model of fast precipitation in response to a sudden

decrease in fluid pressure. The higher overpressures recorded for dolomite crystals forming zebra veins support the idea that zebra textures form during a pre-seismic buildup of suprahydrostatic to supralithostatic pressures (Nielsen et al., 1998; Muchez and Sintubin, 2002). These overpressures are also in agreement with a new view on zebra textures introduced by Merino et al. (2006), stating that zebra textures are self-organized, pushing aside replacive dolomite through pressure-dissolution (see section 3.5.2). Dolomite rhombs displace the host constituents due to local induced stress generated by crystal growth. This induced stress can reach 47 MPa for dolomite crystals growing at 100 °C (Merino et al., 2006).

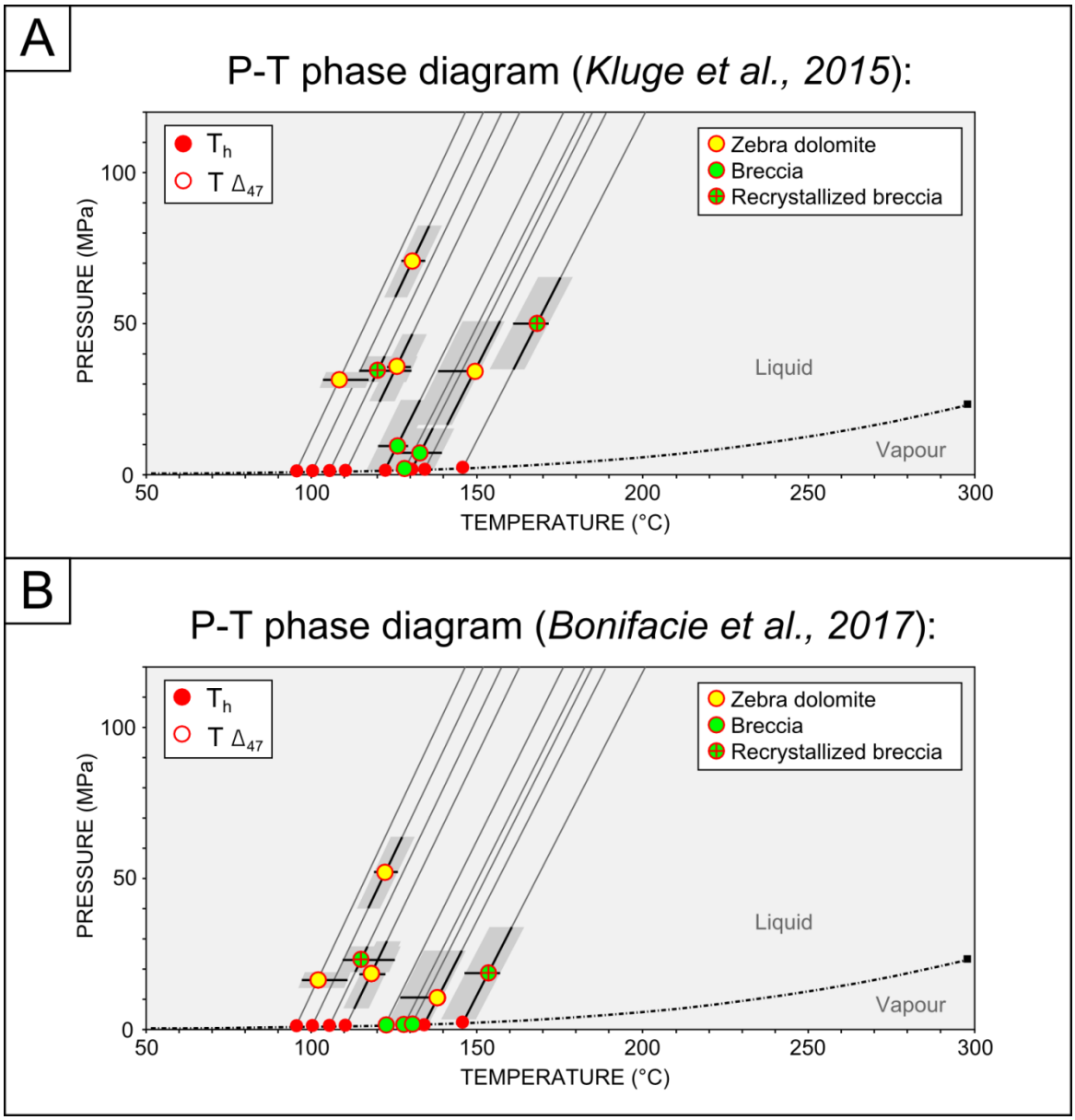

Figure 4.14: Pressure-temperature phase diagrams of saline water. T_h modes obtained for each sample are plotted on the liquid-vapor curve (dashed line), and corresponding isochores have been drawn (using Zhang and Frantz, 1987). Error bars for T_h-values correspond to Q1 – Q3 ranges (25^{th} – 75^{th} percentiles) which are enlisted in Appendices IV and VI. Δ_{47}-temperatures are reported along the isochores of the corresponding samples. Error bars for Δ_{47}-temperatures correspond to ±1SE enlisted in table 4.3 (and in Appendix VI). These temperatures are based on the calibration of Kluge et al. (2015; **A**) and Bonifacie et al. (2017; **B**).

The breccia samples (CaBD2B and 202) composed of coarse saddle crystals with low luminescence are characterized by higher pressures compared to pristine breccia (figure 4.14). These two samples likely represent overprinted and/or recrystallized dolomite cement, as described for key outcrop 3 in chapter 3 (see section 3.7.3.4). They originated from a separate episode of faulting and associated expulsion of dolomitizing fluids resulting in either coarse-crystalline dolomitization or recrystallization of the initial dolomite rocks. The observed temperatures and pressures are thus not representative of the initial crystallization process, but rather of a later pulse of dolomitization or dolomite recrystallization.

The size of the dataset used for this study is limited, and merely aims to illustrate the principle of geobarometry based on coupled fluid inclusion microthermometry and clumped isotope paleothermometry. It therefore does not allow a generalization towards regional processes, which could only be accomplished with additional measurements on dolomite exposures in different geodynamic settings.

4.3.5. Conclusion

Hydrothermal dolomite samples from the Bodón Unit have been used as a test case for high-temperature clumped isotope paleothermometry. Fluid inclusion homogenization temperatures of dolomite cement have been compared to clumped isotope temperatures obtained based on two well-known calibrations. Important provisos when comparing both temperature datasets are the primary nature of fluid inclusions and the absence of high-temperature resetting of clumped isotope signatures (i.e. solid state diffusion). The dataset yields clumped isotope temperatures (102 – 168 °C) which correlate with fluid inclusion homogenization temperatures (95 – 145 °C), confirming the validity of the new technique as a high-temperature carbonate paleothermometer. The new high-temperature clumped isotope calibration of Bonifacie et al. (2017) yields slightly lower temperatures (102 – 154 °C) compared to the calibration of Kluge et al. (2015; 107 – 168 °C). Although the last 10 years of technical progress made clumped isotope paleothermometry a reliable analytical technique, future challenges remain. Inter-laboratory communication and cooperation should increase in order to reduce variation in calibrations and increase data reproducibility.

The clumped isotope temperatures, representing the true temperatures of fluid inclusion entrapment, are regularly higher compared to fluid inclusion homogenization temperatures. The offset between both is defined by the pressure during carbonate crystallization. Comparing the thermal data derived from fluid inclusion microthermometry and clumped isotope paleothermometry thus allows an estimation of the pressure during crystallization of carbonate minerals, without the need for cogenetic generations of fluid inclusions or the use of independent geothermometers. Zebra dolomite likely formed during pre-seismic pressure buildup (22 – 72 MPa), while dolomite cement in breccia samples precipitated in response to a sudden decrease in fluid pressure upon fault rupture. Geobarometry based on fluid inclusion and clumped isotope thermometry is not only a promising tool for sedimentary and diagenetic studies, but could prove useful for a broad range of geological applications.

Chapter 5 Mg-isotope geochemistry

5.1. Introduction

The study of the distribution of stable Mg isotopes in carbonates is, like clumped isotope paleothermometry, a relatively new isotope technique which can be of interest for the reconstruction of depositional and diagenetic histories. Stable Mg isotopes contained in carbonate minerals can also be used as proxies for secular changes in continental weathering, ocean alkalinity and biochemical cycles (Higgins and Schrag, 2010; Higgins and Schrag, 2012; Pogge von Strandmann et al., 2014; Immenhauser et al., 2016). The advent of powerful mass spectrometers allows to study the distribution of stable isotopes of Mg (Galy et al., 2001), which is a major rock-forming element and an important driver in the dolomitization process. The first studies on the Mg-isotope signatures of dolomite were hopeful as to use the new isotope technique as a tracer to characterize and identify the source of Mg in dolomite, and hence the source of dolomitizing fluids allowing to refine the dolomitization model (see section 1.2.3; e.g. Lavoie et al., 2010). After these first years of excitement, realism got the upper hand. Most labs measuring Mg-isotope distributions in dolomite now agree that their Mg-isotope signatures cannot be used to pinpoint the exact dolomitization model, as the signatures of different types of dolomite tend to overlap (see section 5.2; Geske et al., 2015). Nevertheless, Mg-isotope geochemistry represents a new tool which can, in combination with the classical geochemical proxies and isotope systems, provide new insights into the nature and origin of dolomitizing fluids and the dolomitization process itself.

The HTD geobodies exposed in Paleozoic limestones in the Bodón Unit provide an ideal test case for Mg-isotope geochemistry as they have been characterized through a variety of geochemical and isotopic proxies in different studies (see section 2.5). The dolomitizing fluids were hypersaline marine-derived brines modified through water-rock interactions (Gasparrini et al., 2006a, b; Lapponi et al., 2013). In this chapter, the Mg-isotope signatures of carbonate powder samples are reported and discussed in light of the knowledge of the dolomitization process gathered in previous studies. Samples include precursor limestone, replacive dolomite and dolomite cement from both Cambrian and Carboniferous dolomitized limestones. The main aim of this study is to provide Mg-isotope data of well-studied dolomite exposures, which could provide new insights into the systematics of Mg isotopes in dolomite rocks. Important research goals are (1) to investigate the variation in signatures between precursor limestone, replacive dolomite and dolomite cement and (2) to understand the influence of precursor limestones on the Mg-isotope signature of dolomite rocks.

CHAPTER 5 ***HIGHLIGHTS:***

- This chapter reports and discusses the **Mg-isotope signatures** of **limestone and dolomite** samples collected in the Bodón Unit.
- The obtained Mg-isotope signatures for limestone samples correspond to average signatures reported in literature, while dolomite samples are **enriched in heavy Mg isotopes**.
- This enrichment is the result of **intense water-rock interactions** between dolomitizing hydrothermal fluids and **detrital siliciclastic rocks**.
- The signatures of dolomite cement overlap with those of replacive dolomite. However, some samples of dolomite cement have slightly less enriched Mg-isotope signatures compared to replacive dolomite, which suggests a slight **change in fluid chemistry** during dolomitization, or influence of additional parameters on fractionation.
- The sample set contains **1 outlier**. This is a coarse-crystalline and Fe-rich dolomite phase, which potentially **overprinted** and/or **recrystallized** the original dolomite rocks.
- An influence of the precursor limestone on the Mg-isotope signatures of hydrothermal dolomite rocks cannot be observed, possibly due to the limited size of the sample set.

5.2. Mg isotopes

Mg has three stable isotopes, ^{24}Mg (78.99 %), ^{25}Mg (10.00 %) and ^{26}Mg (11.01 %), for which differences in relative abundances are caused by mass-dependent fractionation (Galy et al., 2001; Young and Galy, 2004). Mg-isotope measurements on carbonates have not been performed before the early 21st century, partly due to the pioneer work of Catanzaro et al. (1966) who concluded that, at that time, analytical techniques were not powerful enough to measure Mg-isotope variations in terrestrial samples. Technological advances now allow measuring terrestrial samples with sufficient high precision through multiple-collector inductively coupled plasma-source mass spectrometry (MC-ICP-MS; Galy et al., 2001). Variations in the ratios ^{25}Mg/^{24}Mg and ^{26}Mg/^{24}Mg are measured in dissolved powder samples, and are expressed in δ notation (‰) relative to a standard material referred to as DSM3 (Dead Sea Magnesium), which consists of pure magnesium metal dissolved in nitric acid (Galy et al., 2003).

Recent studies on the Mg-isotope signatures of natural materials suggest that carbonates tend to incorporate light Mg isotopes and are depleted in heavy Mg isotopes (^{25}Mg and ^{26}Mg) compared to seawater and silicate rocks (figure 5.1; Hippler et al., 2009; Li et al., 2010; Tipper et al., 2010; Wombacher et al., 2011; Azmy et al., 2013; Mavromatis et al., 2014; Geske et al., 2015). Limestones are more depleted compared to dolomite (Geske et al., 2015; Walter et al., 2015). The Mg-isotope signatures of marine dolomite are mainly controlled by the signatures of the dolomitizing fluid which is generally seawater or evaporated seawater. For dolomite formed in burial environments, such as hydrothermal dolomite, the Mg-isotope signature is influenced to a large extent by water-rock interactions, which usually enrich fluids in heavy Mg isotopes (figure 5.1; Geske et al., 2015). The large spread in δ^{26}Mg signatures of hydrothermal dolomite (figure 5.1) is attributed to the large variety in Mg sources and sinks in a burial environment, temporally fluctuating fluid pulses and

complex variables affecting fractionation (Geske et al., 2015). So far, experimental data on fractionation of Mg isotopes in dolomite at high temperature (> 100 °C) have not been published. Fractionation during precipitation of burial dolomite can be influenced by a variety of parameters such as crystal growth rate, reaction kinetics or the replacement process associated with dolomitization (Immenhauser et al., 2010; Pearce et al., 2012; Mavromatis et al., 2013; Mavromatis et al., 2017). The dehydration of Mg aquo-complexes, which influences fractionation in low-temperature dolomite, is less significant at higher temperatures (Pearce et al., 2012). Several studies also indicate that temperature-induced fractionation between dolomitizing fluids and dolomite is insignificant in burial dolomite (Geske et al., 2012, 2015; Li et al., 2012; Azmy et al., 2013; Lavoie et al., 2014; Walter et al., 2015). Walter et al. (2015) observed no relationship between fluid salinity and the δ^{26}Mg signature of hydrothermal carbonates. At last, diagenetic alteration does not influence the Mg isotope signatures of large dolomite bodies (Geske et al., 2012; Immenhauser et al., 2016; Hu et al., 2017) although resetting can locally overprint original signatures (Geske et al., 2015; Chanda and Fantle, 2017).

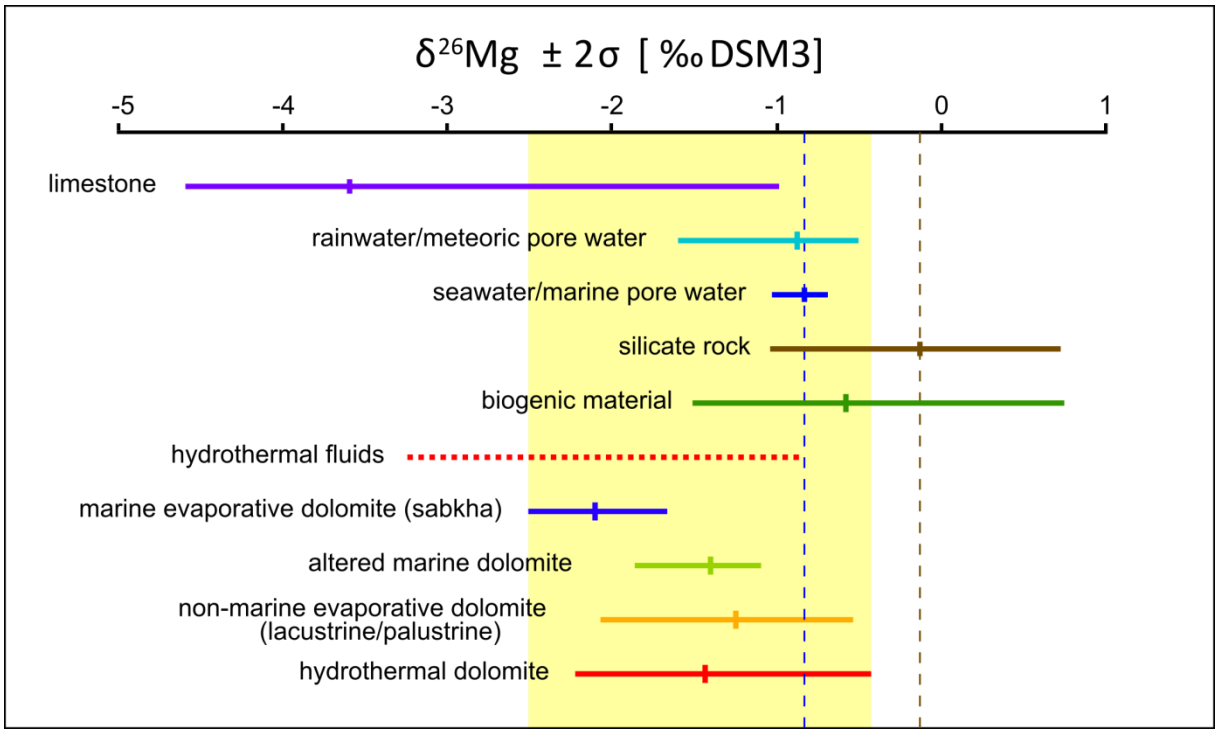

Figure 5.1: Overview of δ^{26}Mg signatures of natural materials. The last four materials correspond to different types of dolomite. The yellow shade shows the range of dolomite signatures. Vertical dashed lines represent the signatures of seawater/marine pore water (blue) and silicate rocks (brown). Modified from Geske et al. (2015), based on a compilation of several studies.

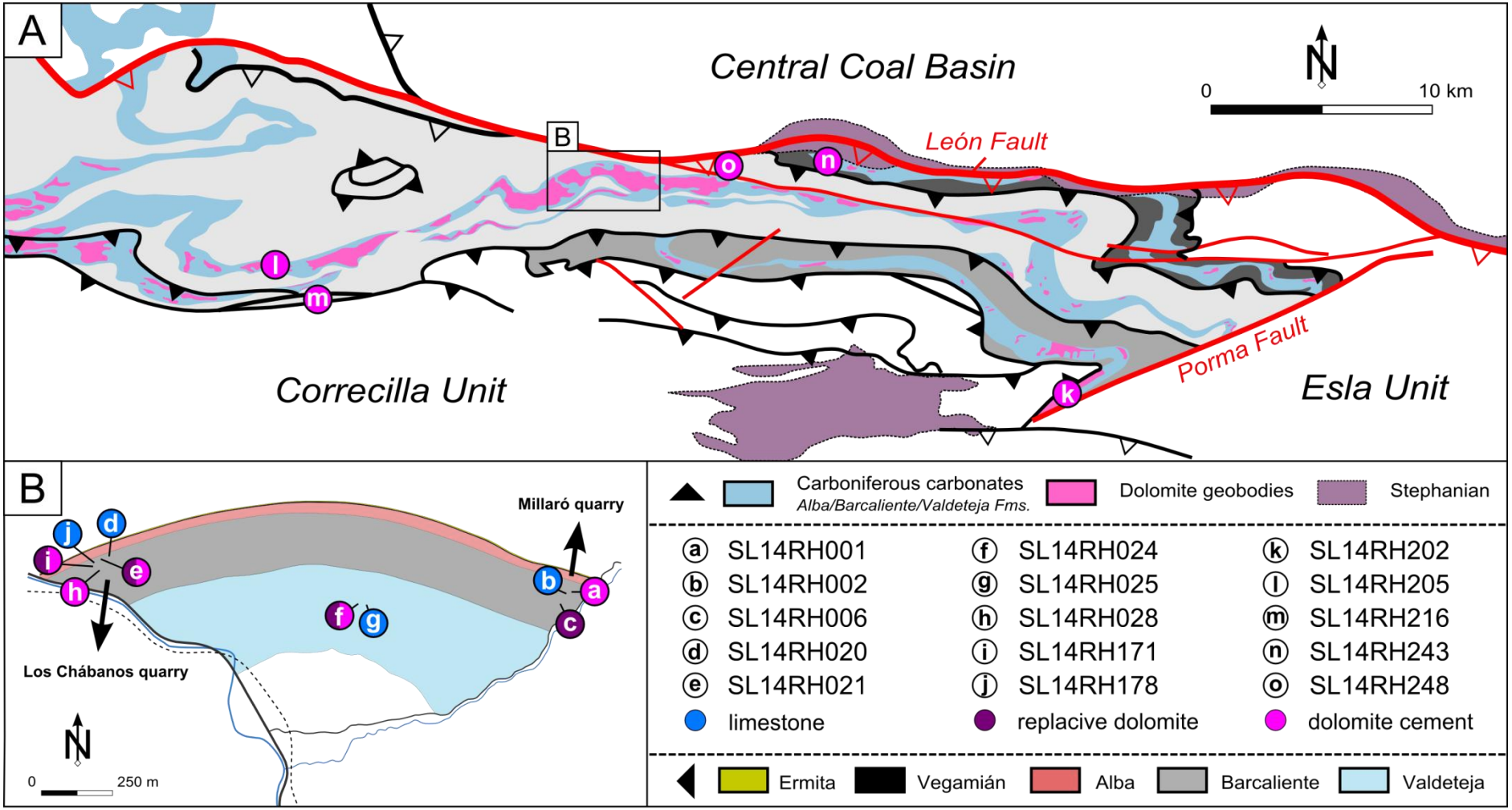

Figure 5.2: Sample locations. **(A)** Geological map of the Bodón Unit indicating the locations of 5 dolomite cement samples. The locations of dolomite geobodies (based on Muñoz-Quijano, 2015) exposed in Carboniferous successions have been indicated in pink. **(B)** Geological map of key outcrop 1 (see chapter 3), indicating the locations of the remaining 10 samples. Out of these 10 samples, 7 were collected in the Millaró and Los Chábanos quarries.

TABLE 5.1: Mg-isotope data

Sample (#15)	*Powder sample (#18)*	*Location*	*Formation*	$\delta^{25}Mg$ (‰)	±2σ	$\delta^{26}Mg$ (‰)	±2σ	$T\,\Delta_{47}$ (°C)	*Remark*
SL14RH001 (a)	Dolomite cement	42°58'38.52"N 5°38'52.58"W	Barcaliente	-0.32	0.01	-0.61	0.02	149	Zebra texture
SL14RH002 (b)	Limestone	42°58'38.30"N 5°38'53.30"W	Barcaliente	-1.72	0.02	-3.29	0.05		
SL14RH006 (c)	Replacive dolomite	42°58'37.97"N 5°38'53.92"W	Barcaliente	-0.26	0.03	-0.50	0.06		
SL14RH020 (d)	Limestone	42°58'40.89"N 5°40'50.64"W	Barcaliente	-1.85	0.02	-3.56	0.03		
SL14RH021 (e)	Replacive dolomite	42°58'40.17"N 5°40'51.69"W	Barcaliente	-0.31	0.02	-0.59	0.03		
	Dolomite cement			-0.31	0.02	-0.59	0.02		Zebra texture
SL14RH024 (f)	Replacive dolomite	42°58'32.85"N 5°39'47.25"W	Valdeteja	-0.25	0.01	-0.49	0.02		
	Dolomite cement			-0.32	0.01	-0.61	0.03		Normal replacive
SL14RH025 (g)	Limestone	42°58'32.55"N 5°39'45.65"W	Valdeteja	-1.95	0.02	-3.76	0.04		
SL14RH028 (h)	Dolomite cement	42°58'39.31"N 5°40'52.33"W	Barcaliente	-0.34	0.04	-0.66	0.06	125	Breccia
SL14RH171 (i)	Replacive dolomite	42°58'39.60"N 5°40'52.66"W	Barcaliente	-0.39	0.02	-0.75	0.03		
	Dolomite cement			-0.40	0.01	-0.77	0.02		Breccia
SL14RH178 (j)	Limestone	42°58'40.02"N 5°40'52.47"W	Barcaliente	-1.96	0.02	-3.76	0.04		
SL14RH202 (k)	Dolomite cement	42°53'17.24"N 5°22'55.96"W	Barcaliente	-0.61	0.03	-1.17	0.05	121	Recrystallized
SL14RH205 (l)	Dolomite cement	42°56'12.91"N 5°50'44.20"W	Barcaliente	-0.36	0.03	-0.67	0.04	125	Zebra texture
SL14RH216 (m)	Dolomite cement	42°54'48.72"N 5°49'30.34"W	Láncara	-0.34	0.03	-0.65	0.06		Zebra texture
SL14RH243 (n)	Dolomite cement	42°58'47.53"N 5°32'25.27"W	Barcaliente	-0.40	0.02	-0.77	0.02	107	Zebra texture
SL14RH248 (o)	Dolomite cement	42°58'43.01"N 5°34'49.09"W	Láncara	-0.51	0.02	-0.99	0.06		Zebra texture

Table 5.1: Results of Mg-isotope measurements on dolomite and limestone samples from the Bodón Unit. Corresponding clumped isotope temperatures have been added.

5.3. Samples and methodology

A set of 15 samples (table 5.1) was selected from the larger sample database collected for petrographic descriptions (see chapter 3) and for clumped isotope analyses (see chapter 4). The samples were selected following a detailed petrographic study of polished and stained rock slabs and thin sections (see section 3.2.3 for more details on methodology). The sample set is derived from exposures throughout the entire Bodón Unit (figure 5.2A), although most samples are derived from the Los Chábanos and Millaró quarries in a large key outcrop in the central part of the study area (key outcrop 1; figure 5.2B; see section 3.3.1). Mg-isotope measurements were performed on 18 powder samples drilled out of rock slabs from the 15 samples using a dental drilling device. A total amount of 16 powder samples was drilled from precursor limestone (4 samples), replacive dolomite (4 samples) and void-filling dolomite cement (8 samples) from the Barcaliente and Valdeteja Fm. (table 5.1). Two powder samples of void-filling dolomite cement from the Cambrian Láncara Fm. are also included.

Mg-isotope measurements were performed in the non-traditional stable isotope laboratory at Ruhr-University Bochum by Dr. Dieter Buhl, under supervision of Prof. Dr. Adrian Immenhauser. The measurements are preceded by an extraction and purification process which involves different steps. Approximately 0.5 mg of powder is first dissolved in HCl (6 M) after which it is evaporated on a hot plate at 125 °C to complete dryness. The samples are subsequently treated with a 1:1 mixture of H_2O_2 and HNO_3 (31 % : 65 %) to destroy organic compounds which might cause undesirable interferences during measurements. The samples are then again dried on a hot plate at 60 °C and re-dissolved in HCl (1.25 M). Next, the Mg fraction is recovered by cation exchange chromatography using BioRad ion exchange resin AG50W-X12 (200 to 400 mesh) and quartz glass columns. The column elution patterns are determined for each column using an IAPSO seawater test solution (diluted 1:1). The Mg yield exceeds 95 %.

Measurements of a 500 ppb Mg solution in 3.5 % HNO_3 were performed on a Thermo Fisher Scientific Neptune MC-ICP-MS. A standard sample bracketing technique was applied to calculate the $\delta^{25}Mg$ and $\delta^{26}Mg$ values (‰), which are given against DSM3 standard solution. Each sample measurement was repeated 5 times. Reference measurements of the elemental solution Cambridge1 were performed to assess the reproducibility of the Mg-isotope measurements. The obtained $\delta^{25}Mg$ signature ranges between -1.29 and -1.39 ‰ with an average of -1.33 ‰ and the $\delta^{26}Mg$ signature ranges between -2.50 and -2.64 ‰ with an average of -2.57 ‰.

The crystallization temperature of 5 Carboniferous samples used for Mg-isotope geochemistry has been measured through clumped isotope paleothermometry (see chapter 4). Corresponding Δ_{47}-derived temperatures have been added to table 5.1. The average Sr-isotope ($^{87}Sr/^{86}Sr$) ratios for dolomite in Carboniferous limestones in the Bodón Unit are 0.7087 for replacive dolomite and 0.7088 for dolomite cement (Gasparrini et al., 2006a; Pauwels, 2016). These ratios are higher than those of Early Permian seawater (between 0.7080 and 0.7085; Burke et al., 1982), which implies that the dolomitizing fluids were enriched in radiogenic ^{87}Sr derived from the radioactive decay of ^{87}Rb (Allan and Wiggins, 1993). The radiogenic ratios of dolomite in the Bodón Unit are attributed to interaction of the dolomitizing fluids with silicate minerals rich in Rb (Gasparrini et al., 2006a).

5.4. Results

Limestone samples from the Barcaliente Fm. consist of dark calcimudstones with limited fossil content (figures 2.3D & 5.3A). The sample of Valdeteja limestone was collected atop key outcrop 1 (figure 5.2B), in a depositional unit largely composed of calciturbidites (see section 3.3.1). The sample is a crinoid packstone, and the muddy matrix in between crinoid fragments was drilled for Mg-isotope analysis (figure 5.3B). Light gray replacive dolomite from the Barcaliente Fm. (figure 5.3A) is characterized by a mosaic of sub- to anhedral crystals. Each sample is characterized by a fairly unimodal crystal size distribution, although crystal size can be coarser in some samples. The same holds true for replacive dolomite in dolomitized crinoid packstones from the Valdeteja Fm. (figure 5.3C). Dolomite cement samples are derived from thick cement rims in hydrothermal breccia in the Barcaliente Fm. (figure 4.10C), or from thin cement layers making up zebra dolomite in the Barcaliente (figure 4.10A) and Láncara Fm. (figure 5.3D). Dolomite cement occurs locally in between crinoid fragments in dolomitized crinoid packstones of the Valdeteja Fm. (figure 5.3C). Void-filling dolomite crystals show a mottled appearance under luminescent light, except for a last dull rim which is often affected by dedolomitization or dissolution (figures 3.21L; 4.10B & D), and which was avoided during sampling. Sample SL14RH202 (figure 3.16B) is a sample from a distinct outcrop (KO 3) in the southeastern part of the Bodón Unit where dolomite is coarse-crystalline and characterized by high concentrations of Fe (see chapter 3). Here, dolomite cement sampled for Mg-isotope analysis is made up of large (up to several mm) feather-like saddle crystals (figure 3.16B), lacking luminescence. Sample SL14RH202 possibly represents an additional phase of dolomitization overprinting primary dolomite rocks, or a product of Fe-rich recrystallization.

Table 5.1 and figure 5.4 provide an overview of the δ^{25}Mg and δ^{26}Mg signatures obtained for limestone, replacive dolomite and dolomite cement. The limestone samples have δ^{25}Mg signatures ranging between -1.98 and -1.70 ‰ with an average of -1.87 ‰, and δ^{26}Mg ratios ranging between -3.80 and -3.24 ‰ with an average of -3.59 ‰ (figure 5.4A). Dolomite samples are more enriched in heavy Mg-isotopes compared to limestone (figures 5.4A & B), with a slight difference between replacive dolomite and dolomite cement (figure 5.4C). Replacive dolomite samples have δ^{25}Mg signatures ranging between -0.41 and -0.23 ‰ with an average of -0.31 ‰, and δ^{26}Mg signatures ranging between -0.78 and -0.44 ‰ with an average of -0.58 ‰. Dolomite cement samples are slightly less enriched, with δ^{25}Mg signatures ranging between -0.64 and -0.28 ‰ with an average of -0.38 ‰, and δ^{26}Mg signatures ranging between -1.22 and -0.53 with an average of -0.73 ‰. While the Mg-isotope signatures of limestone and replacive dolomite show very little variation, one outlier can be identified in the dolomite cement samples (δ^{25}Mg -0.64 ‰ and δ^{26}Mg -1.22 ‰; figures 5.4B & C). The outlier is dolomite cement sample SL14RH202, an Fe-rich sample from the southeastern part of the Bodón Unit (see chapter 3).

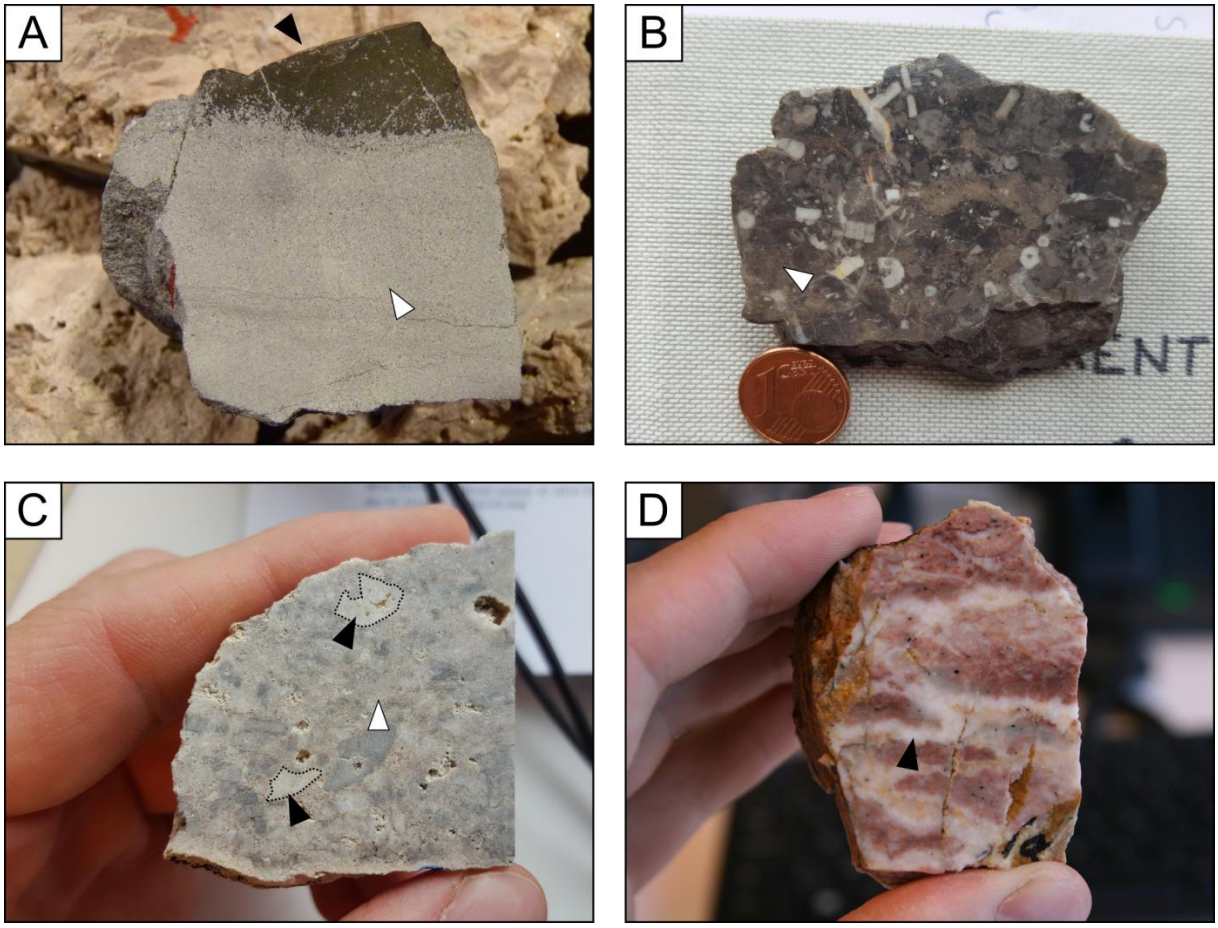

Figure 5.3: Selection of sample photographs. **(A)** Photograph of sample SL14RH006, which was obtained from a limestone-dolomite contact exposed in the Millaró quarry (figure 5.2B). The upper part of the sample (black arrow) is composed of dark mudstone from the Barcaliente Fm., while the lower part (white arrow) has been replaced by dolomite. The sample is approximately 4 cm wide. **(B)** Photograph of limestone sample SL14RH025 from successions of the Valdeteja Fm. exposed on top of KO 1. This is a crinoidal packstone, where a sample has been carefully drilled from the muddy matrix in between crinoid fragments (e.g. location indicated with white arrow). **(C)** Photograph of dolomite sample SL14RH024 from successions of the Valdeteja Fm. exposed on top of key outcrop 1. This particular sample has been treated with HCl (1 M) in order to remove calcite. Powder samples of matrix dolomite (white arrow) and small pockets of dolomite cement (black arrows and black dashed lines) were drilled from this sample. **(D)** Photograph of a sample (SL14RH248) of dolomitized limestone of Cambrian age (Láncara Fm.). The sample displays a zebra texture. The white cement (black arrow) has been sampled for Mg-isotope analyses.

5.5. Discussion

The Mg-isotope signatures of the 4 limestone samples analyzed in this study, correspond to the average signatures reported in literature (figure 5.4D; Azmy et al., 2013; Geske et al., 2015). HTD samples, although they plot within the wide range of reported dolomite signatures (figure 5.4D), are enriched in ^{25}Mg and ^{26}Mg relative to samples of HTD from literature (e.g. Azmy et al., 2013; Lavoie et al., 2014; Geske et al., 2015). The samples measured in this study in fact provide some of the most enriched values for burial dolomite reported to date.

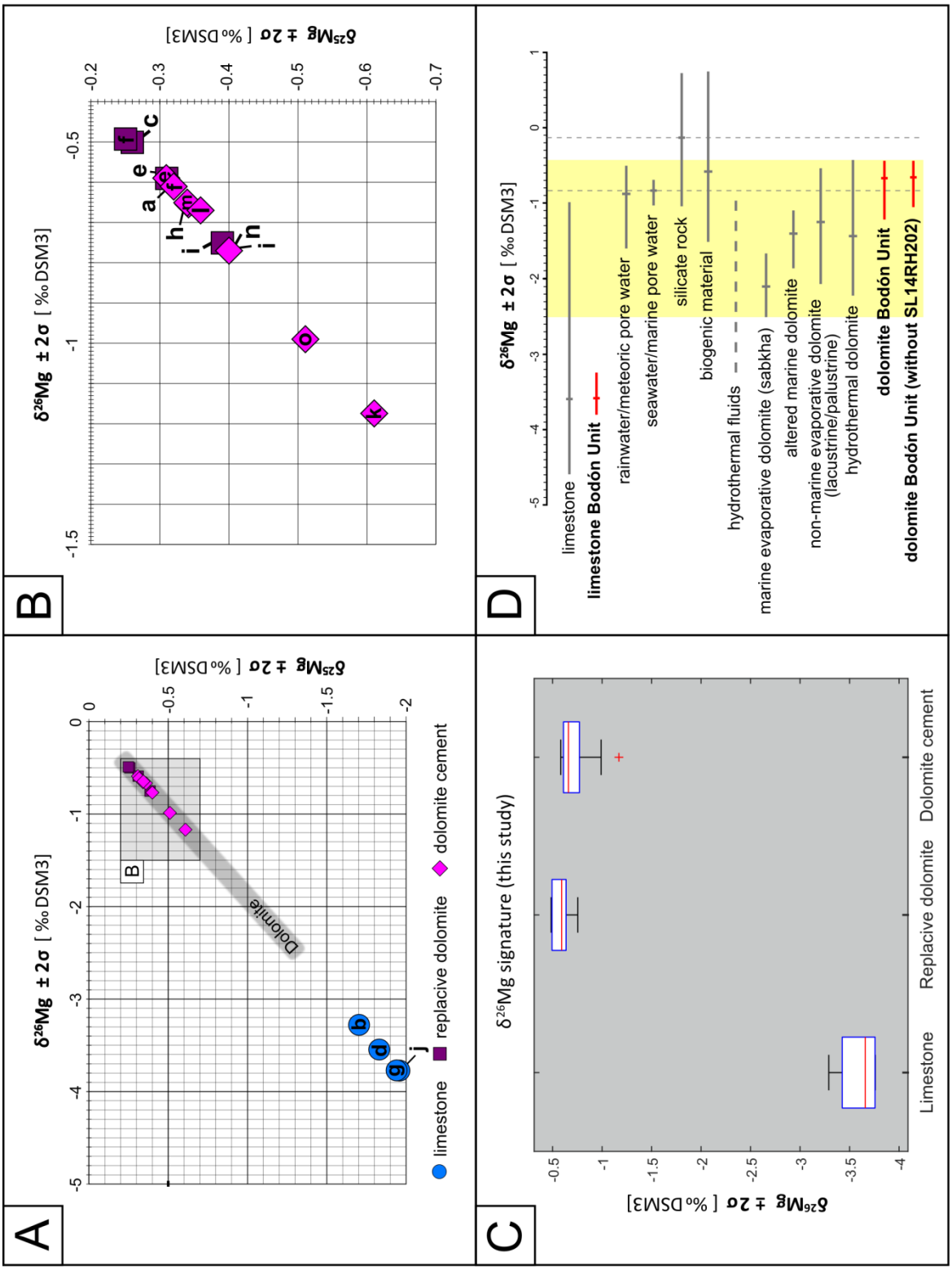

Figure 5.4: Overview of Mg-isotope data. **(A)** Three-isotope plot displaying $\delta^{25}Mg$ and $\delta^{26}Mg$ isotopic variations of measured samples. Refer to figure 5.2 and table 5.1 for sample numbers. The thick gray line ('Dolomite') corresponds to the range of Mg-isotope signatures as reported by Geske et al. (2015) for different types of dolomite (yellow shaded areas in figures 5.1 & 5.4D). **(B)** Detail of the three-isotope plot displayed in figure 5.4A, zooming in on replacive dolomite and dolomite cement samples. **(C)** Boxplots showing the $\delta^{26}Mg$ signatures of limestone, replacive dolomite and dolomite cement samples. **(D)** Overview of $\delta^{26}Mg$ signatures of natural materials and different types of dolomite. The data obtained for this study for limestone and dolomite samples have been added. Based on Geske et al. (2015).

The strong enrichment of heavy Mg isotopes in the HTD samples relative to the precursor limestone rocks suggests a strong control of the dolomitizing fluids on the Mg-isotope signature of the dolomite rocks. These fluids must have been enriched in heavy Mg isotopes, which was likely a result of important water-rock interactions between the dolomitizing fluids and silicate material. The burial domain is a rock-dominated domain where water-rock interactions strongly control fluid chemistry. Important water-rock interactions were proposed for dolomitizing fluids by Gasparrini et al. (2006a) and Lapponi et al. (2013) based on Sr-isotope signatures of dolomite rocks and the presence of Li in fluid inclusions in the Bodón Unit. The Sr-isotope signatures of these dolomite rocks are strongly radiogenic (0.7088 on average; Gasparrini et al., 2006a; Pauwels, 2016), indicating water-rock interaction with silicate material (see section 5.3). Reported Sr-isotope signatures of the sample set of HTD from Geske et al. (2015) are slightly more radiogenic (average value of 0.7089) which suggests that the strong enrichment of heavy Mg isotopes in dolomite from the Bodón Unit is not only caused by strong water-rock interactions. A difference between the dolomite rocks exposed in the Bodón Unit and the sample set of hydrothermal dolomite rocks discussed by Geske et al. (2015) is the high salinity of the former. Gasparrini et al. (2006b) reported salinities around 26 eq. mass % $CaCl_2$ for fluid inclusions in replacive dolomite and dolomite cement in the Bodón Unit. However, a study performed by Walter et al. (2015) found no relationship between salinity and $\delta^{26}Mg$. Moreover, seawater and rainwater have approximately similar Mg-isotope signatures, which suggests that Mg isotopes do not fractionate during evaporation. The additional enrichment in ^{25}Mg and ^{26}Mg must be due to additional factors, such as reaction kinetics and/or crystal size, which can currently not be assessed.

The $\delta^{25}Mg$ and $\delta^{26}Mg$ signatures of dolomite cement roughly correlate with the Mg-isotope signature range of replacive dolomite, which indicates buffering of dolomite cementation by replacive dolomite. This correlation is confirmed by ANOVA results, which indicate no significant variation between the Mg-isotope data of replacive dolomite and dolomite cement. Nevertheless, figures 5.4B and C suggest a slight decrease of heavy Mg isotopes in dolomite cement. Reported Sr-isotope signatures for dolomite cement (0.7088 on average; Gasparrini et al., 2006a; Pauwels, 2016) are slightly more radiogenic compared to signatures for replacive dolomite (0.7087 on average; Gasparrini et al., 2006a; Pauwels, 2016) which suggests that a decrease in water-rock interactions cannot be the cause for the slightly less heavy Mg-isotope signatures for dolomite cement. The creation of replacive dolomite might have preferentially incorporated heavy Mg isotopes, leaving the dolomitizing fluids relatively enriched in light isotopes. This, however, is very unlikely since it is generally accepted that carbonates preferentially incorporate light Mg isotopes (Mavromatis et al., 2014). The slightly less enriched signatures of dolomite cement samples potentially suggest small-scale fluctuations in fluid chemistry or concentration, the latter which is known to affect Mg-isotope fractionation (e.g. Mavromatis et al., 2011). Other indications of fluctuations in fluid chemistry during dolomite cementation are small growth zones displaying a dull cathodoluminescence (e.g. figures 4.10B & D) and the occurrence of a late phase of Fe-rich cementation (Gasparrini et al., 2006a; Lapponi et al., 2013). Additional parameters, such as crystal growth rate, crystal size and specific reaction kinetics, could have affected fractionation, but cannot be assessed for in this study.

The Mg-isotope data of the dolomite samples measured in this study show an outlier, i.e. sample SL14RH202 from an outcrop in the southeastern part of the Bodón Unit, which is less enriched in heavy Mg isotopes. This confirms the hypothesis postulated in chapter 3 about the distinct nature of the dolomite geobodies exposed in this particular outcrop (see section 3.7.3.4). The dolomitizing

fluids must have experienced a different circulation history resulting in a different chemical composition. It is not clear whether these geobodies represent recrystallized dolomite, but if this is the case, the data from this study suggest that Mg isotopes recorded in the dolomite rocks from the Bodón Unit can distinguish samples affected by recrystallization. Similar observations have been reported by Chanda and Fantle (2017), who observed a decline in δ^{26}Mg for marine carbonates affected by diagenetic recrystallization.

In the dataset compiled for this study, the Mg-isotope signature of precursor limestones seemingly did not influence the signature of corresponding dolomite samples. Neither is there a clear difference in signatures between dolomite samples from Cambrian and Carboniferous successions. However, the dataset of limestone samples used in this study is rather small, and a more extended dataset might give a higher chance for revealing the influence of precursor rocks.

5.6. Conclusion

Mg-isotope geochemistry provides a new geochemical proxy which might help to better understand the depositional and diagenetic environment in which dolomite forms. Although several studies during the last decade have shown that the Mg-isotope signature of dolomite cannot be used to pinpoint the dolomitization model, the new technique can be of great value to better understand the dolomitization process and the nature and evolution of dolomitizing fluids. Mg-isotope measurements on well-studied dolomite exposures allow to better understand Mg-isotope systematics. This chapter introduced and discussed Mg-isotope data for hydrothermal dolomite rocks from the Bodón Unit, for which the dolomitization model and the nature of the dolomitizing fluids have been well-constrained in previous studies.

The Mg-isotope signatures of limestone samples correspond to values reported in literature, while dolomite samples, both replacive dolomite and dolomite cement, are enriched in heavy Mg isotopes compared to signatures reported in previous studies. This highlights the strong control of the dolomitizing fluids on the Mg-isotope signature of dolomite rocks in a burial environment. The Mg-isotope composition of hydrothermal dolomite rocks from the Bodón Unit is more enriched compared to signatures of hydrothermal dolomite reported in previous studies. The high enrichment is likely caused by a combination of strong water-rock interactions with detrital siliciclastics and additional factors such as reaction kinetics. The Mg-isotope signatures of dolomite cement crystals partly overlap with the signatures of replacive dolomite, but some cement samples are slightly depleted in heavy Mg isotopes. This suggests a strong control of replacive dolomite on the signature of dolomite cement, and a possible slight change in fluid chemistry during dolomitization.

One outlier in the dataset corresponds to a cement sample derived from an exposure of coarse-crystalline and Fe-rich dolomite. This illustrates the potential benefit of Mg isotopes over other proxies, such as stable O and C isotopes, as the latter did not allow to quantify this divergent exposure (Pauwels, 2016). In the sample set from the Bodón Unit, dolomite cement is slightly less enriched in heavy Mg isotopes compared to replacive dolomite, which might be a result of a change in fluid chemistry during the dolomitization process, or other parameters affecting fractionation such as crystal size or reaction kinetics. An influence of the precursor limestone rocks on the Mg-isotope

signature of dolomite has not been observed in this study, but this could be an artifact related to the limited size of the dataset.

Chapter 6 General conclusions and future perspectives

Subsurface dolomite geobodies constitute potential reservoirs for hydrocarbon accumulation and provide storage capacity for captured CO_2 and for geothermal projects. Dolomite rocks, which often represent the most porous lithologies in carbonate systems, are investigated through outcrop analogue studies in order to understand and predict their genesis and reservoir architecture. Spectacular dolomite outcrop analogues are exposed in the Cantabrian Mountains in Northern Spain. These mountains constitute the Variscan foreland fold-and-thrust belt on the Iberian Peninsula and are referred to as the Cantabrian Zone. The latter is made up of Paleozoic successions, of which the limestones have been affected by hydrothermal dolomitization following Late- to Post-Variscan orocline formation and associated lithospheric delamination (Gasparrini et al., 2006a). Dolomite geobodies exposed in the Bodón Unit, an important thrust unit in the Cantabrian Zone, have been investigated in several petrographic and geochemical studies (Gasparrini et al., 2006a; Lapponi et al., 2013). The geobodies were formed by circulation of hydrothermal dolomitizing fluids, affected by intense water-rock interactions, through thermal convection.

Chapter 2 of this PhD thesis provided a short introduction to the geodynamic evolution, stratigraphy and thermal history of the Bodón Unit. The geometry and petrophysical properties of hydrothermal dolomite (HTD) rocks exposed in Carboniferous successions of the Bodón Unit are underexplored, and have been subject to a detailed study in chapter 3. An extended paleothermal study of the HTD rocks and their precursor and ambient rocks has been the subject of the first part of chapter 4. The exceptional exposures of HTD in the Bodón Unit have been characterized in previous studies through an array of techniques such as stable isotope geochemistry, multi-element analysis and fluid inclusion microthermometry (Gasparrini et al., 2006a, b; Lapponi et al., 2013; Muñoz Quijano, 2015). These studies provide a detailed geoscientific framework which makes the exposed dolomite rocks the ideal targets for new and innovative proxies in carbonate sedimentology and diagenesis. Hence, the second part of chapter 4 used the dolomite rocks as a test case for high-temperature clumped isotope paleothermometry, while chapter 5 investigated the Mg-isotope signatures of the dolomite rocks. This chapter finally provides concise conclusions of the previous chapters, and discusses applications and future perspectives for the obtained results.

6.1. HTD geometry and porosity distribution

The geometry and matrix porosity and permeability of HTD exposed in Carboniferous carbonate successions in the Bodón Unit were studied in 3 key outcrop areas. The latter show exposed dolomite geobodies with divergent properties such as massive *versus* fracture-associated geometries and porous *versus* tight dolomite rocks. Dolomitization was primarily fracture-controlled, but secondary controlling factors strongly influenced the size, geometry and pore networks of the HTD geobodies. These secondary factors relate to the nature of fluid-migration pathways, the available volume of dolomitizing fluids and the initial lithology and sedimentary framework of the dolomitized limestone successions.

Throughout the Bodón Unit, fluid circulation was typically focused around dense fracture networks. Limited fluid circulation along such fracture networks, likely due to a low availability of dolomitizing

fluids, resulted in narrow fracture-associated dolomite geobodies. These are usually tight (average matrix porosity 1.8 %), as many of these fracture zones have been the main loci of reactivations with associated fluid flow and calcite cementation. Massive dolomitized limestone successions, resulting from a higher availability of dolomitizing fluids, are more porous (average matrix porosity 3.8 %). In these massive dolomite geobodies, the lithology and sedimentary framework of the precursor limestone rocks affect the petrophysical properties of the resulting dolomite. Uniform dolomitized mudstones from the Barcaliente Fm. show abundant zebra textures, while the complex platform limestones of the Valdeteja Fm. are characterized by a large variety of dolomite pore types. The latter limestones can be subdivided into three depositional units of which the first and third units have been completely dolomitized. The middle depositional unit is only partly dolomitized, as a result of fine-grained siliciclastic intercalations and chert nodules baffling fluid circulation. An exceptional dolomite geobody occurs in the eastern part of the Bodón Unit, where fluids migrated along a deeply-rooted thrust fault. These fluids had a different composition as they migrated through a multitude of deeply buried stratigraphic successions and experienced a variety of water-rock interactions. The resulting dolomitized fault breccia of the thrust is coarse-crystalline, highly enriched in Fe and the fault gouge is exceptionally porous (average matrix porosity 9.6 %). This phase of Fe-rich and coarse-crystalline dolomite might represent a secondary phase which has locally overprinted and/or recrystallized the primary dolomite phase exposed in the study area. The secondary phase could be related to the Late- to Post-Variscan phase of dolomitization omnipresent in the Bodón Unit, but could also be associated with an important Mesozoic episode of Fe-rich fluid circulation affecting Aptian and Albian carbonates in the Basque-Cantabrian Basin (Dewit et al., 2014). For most of the dolomite textures and associated pore networks in the 3 key outcrops, small plug measurements allowed to quantify the matrix porosity and permeability. An exception is dolomitized microbial boundstone and synsedimentary breccia, of which the size of some pores exceeds the size of small plugs (diameter of ± 3.3 cm). The representative elementary volume for petrophysical measurements of these dolomite textures is larger than the size of the small plugs, and should be quantified in order to obtain representative petrophysical data from plug measurements. All petrophysical measurements performed on dolomite rocks in the Bodón Unit indicate a very low permeability (average matrix permeability 0.10 mD). This result can to some extent be explained by the small size of the plugs used for petrophysical measurements, which results in an underestimation of the influence of fractures. Nevertheless, the results of fieldwork and log analysis reveal a higher fracture abundance in dolomite compared to their precursor limestone rocks.

The 3 key outcrop areas studied in chapter 3 provide analogues for the numerous HTD geobodies exposed in the Bodón Unit, of which several show similar characteristics compared to the studied key outcrops. The HTD rocks in the Bodón Unit constitute seismic-scale geobodies. Understanding the relationship between geometry and size on the one hand, and the distribution of matrix porosity on the other hand, allows to better predict the reservoir quality of similar geobodies in subsurface environments, such as Variscan foreland fold-and-thrust belts. In order to fully quantify the reservoir quality of dolomite rocks exposed in the Bodón Unit, the importance of fractures should be quantified and the representative elementary volume for petrophysical measurements of dolomitized microbial boundstone and synsedimentary breccia should be elaborated.

The petrographic study in chapter 3 illustrates the variety of diagenetic modifications which have affected the carbonate rock successions of the Bodón Unit and which are directly related to the long and complex geodynamic history of the Cantabrian Mountains. These modifications and overprints

had important consequences for the petrophyiscal characteristics of the precursor limestones and dolomite rocks. Further research on the geodynamic and thermal evolution of carbonate rocks in the Bodón Unit would benefit from *in situ* U-Pb dating of diagenetic carbonate phases, in order to allow a more detailed understanding of the geodynamic and thermal processes (in case of coupled Δ_{47} measurements) affecting the Bodón Unit. Certainly the Late-Paleozoic and Mesozoic history of the Cantabrian Zone are currently underexplored, due to a lack of preserved sediments. As an example, several episodes of Post-Variscan tectonic reactivation of fracture zones could be directly dated based on corresponding calcite cement phases.

6.2. Paleothermometry

Chapter 4 aimed to provide a coherent interpretation of the paleothermal data available for the southern Cantabrian Zone, which allows to better constrain the thermal conditions of dolomitization. The thermicity of precursor and ambient rocks has been studied based on a detailed literature study with additional Rock-Eval pyrolysis and vitrinite reflectance measurements, while the dolomite rocks have been subject to carbonate clumped isotope paleothermometry.

The thermicity of precursor limestones and ambient siliciclastic rocks has been investigated in the first section of chapter 4 (section 4.2). It was found that bulk rock paleothermometers, such as Rock-Eval pyrolysis and the crystallinity of illite, significantly overestimate the thermal maturity of ambient siliciclastic rocks, because of the incorporation of detrital reworked sediments. Detailed optical kerogen analysis during vitrinite reflectance studies provide a qualitative way to determine the thermal maturity of synorogenic deposits. Paleotemperatures based on vitrinite reflectance analysis of *in situ* kerogen in ambient siliciclastic rocks average around 100 °C, which is significantly higher compared to paleotemperatures obtained through the color alteration index of conodont fragments in precursor limestones (around 60 °C). This dispersion in temperature between precursor limestone and ambient siliciclastic rocks is attributed to differences in analytical techniques and empirical equations applied to obtain corresponding temperatures. A secondary reason for this variation in temperature could be a different response to mechanical deformation between rigid limestones and fractured siliciclastic successions, which allowed more intense fluid circulation and heat dissipation in the latter. In order to better understand the observed variation in paleotemperature between the different lithologies, clumped isotope paleothermometry could be performed on primary carbonate components in precursor limestones, such as pristine crinoid or bivalve fragments. If the clumped isotope signatures are primary and not affected by solid state diffusion, they would provide an additional argument to justify the lower temperatures experienced by precursor limestones.

The temperatures experienced by precursor limestone and ambient siliciclastic rocks indicate that dolomite formation (at temperatures between 100 to 170 °C) was hydrothermal. Regional variations in thermal maturity throughout the Bodón Unit suggest the existence of positive temperature anomalies associated with hydrothermal dolomite, which can be used as an exploration tool for hydrothermal carbonate geobodies in analogue sub-surface settings.

The thermicity of the dolomite rocks exposed in the Bodón Unit has been the subject of fluid inclusion microthermometry studies (Gasparrini et al., 2006b; Lapponi et al., 2013). These dolomite rocks have now been used as a test case for high-temperature carbonate clumped isotope paleothermometry. Several studies have proven the potential of low-temperature (< 100 °C)

clumped isotope paleothermometry, and an extension towards higher temperatures opens up a new field of applications for this innovative paleothermometer. Two calibrations are currently available for the conversion of clumped isotope signatures of high-temperature carbonate phases. These two calibrations have been compared in chapter 4 (section 4.3). The investigated set of dolomite cement samples yields fluid inclusion homogenization temperatures between 95 and 145 °C. The clumped isotope calibration of Kluge et al. (2015) yields temperatures between 107 and 168 °C, while the calibration of Bonifacie et al. (2017) yields slightly lower temperatures (102 – 154 °C). The correlation between the obtained fluid inclusion and clumped isotope temperature data confirm the validity of clumped isotope paleothermometry towards higher temperature ranges. Increasing numbers of clumped isotope labs will increase the accessibility to this new technique and will allow clumped isotopes to become a standard proxy in sedimentary and diagenetic studies. Towards the future, clumped isotope measurements will benefit from increasingly smaller sample sizes, which will allow more detailed analyses. In order to reduce variation between clumped isotope data from different labs, a universal calibration for high-temperature clumped isotope paleothermometry should be established, based inter-laboratory communication and cooperation. The calibration of Bonifacie et al. (2017) has been introduced as a potential universal calibration for high-temperature (> 100 °C) carbonate clumped isotope paleothermometry. Nevertheless, specific points of discussion, such as parameters applied for ^{17}O correction (see section 4.3.2.2), are still causing considerable debate in the clumped isotope community.

To conclude, chapter 4 introduced a new and innovative approach to geobarometry in carbonate minerals. Combining thermal information derived from fluid inclusions (with known composition) and clumped isotope paleothermometry possibly allows to calculate the pressure at which single carbonate minerals formed. The thermal data presented in this PhD thesis yield higher pressures for dolomite crystals in zebra textures compared to dolomite crystals in breccia. The geobarometric difference between both textures reflects their formation conditions. Zebra textures formed during pressure buildup, while the thick cement rims in breccia likely formed in response to a sudden decrease in fluid pressure. This new approach opens up the possibility of routinely estimating the pressure of carbonate crystallization and has potential applications in diagenesis, basin analysis, ore geology and continental tectonics. Additional experimental studies on other dolomite and carbonate exposures should confirm the validity of the new approach.

6.3. Mg-isotope geochemistry

The Mg-isotope geochemistry of dolomite rocks has been put forward as a new and promising proxy to decipher the origin of Mg in dolomite and in diagenetic products in general. Although Mg-isotope geochemistry has not (yet) been able to establish its position amongst the more traditional diagenetic proxies, it can provide interesting insights into the process(es) of dolomitization and the nature of dolomitizing fluids.

A set of limestone and hydrothermal dolomite samples from the Bodón Unit has been used as a test case for Mg-isotope geochemistry in chapter 5. The signatures obtained for limestone samples compare to average signatures reported in literature, while HTD samples (both replacive dolomite and cement) are characterized by some of the most enriched signatures for dolomite reported to date. The signatures of dolomite cement correlate to those of replacive dolomite, but some cement

samples are slightly less enriched in heavy Mg isotopes, which could have been caused by a slight change in fluid chemistry during dolomitization. The strong enrichment of HTD samples in heavy Mg isotopes compared to precursor limestones is likely related to strong water-rock interactions between dolomitizing fluids and siliciclastic material. Hence, the results illustrate the importance of the dolomitizing fluids as a primary control on the Mg-isotope signature of dolomite samples in a burial environment. The dataset presented in chapter 5 shows one outlier, which is a sample of Fe-rich coarse-crystalline dolomite likely representing an additional dolomitization phase.

The Mg-isotope study presented in this PhD thesis illustrates the current position of the new approach in the series of traditional and new proxies used in carbonate sedimentology and diagenesis. Although currently the new isotope system apparently does not have the potential to distinguish the source of Mg in dolomite rocks and hence the source of dolomitizing fluids, it allows a carbonate sedimentologist to infer additional information regarding the nature of Mg-rich fluids in dolomite rocks which have been characterized petrographically as well as geochemically. Additional experimental studies regarding fractionation kinetics of Mg isotopes, and increasing datasets of different types of dolomite rocks, will lead to an increasing applicability of this new isotope system in carbonate sedimentology and diagenesis.

Bibliography

A

Adrados-González, L. Alonso-Alonso, V., Bahamonde, J.R., Farias-Arquer, P., Fernández-González, L.P., Gutiérrez-Claverol, H., Heredia, N., Jiménez-Sánchez, M., Meléndez-Asensio, M., Merino-Tomé, Ó.A. & Villa-Otero, E. (2010) *Parque Nacional de los Picos de Europa: Guía Geológica*. Instituto Geológico y Minero de España (IGME), Serie Guía Geológicas de Parques Nacionales, 337 p.

Aguilera, R. (1995) *Naturally Fractured Reservoirs*. PannWell, Tulsa, 521 p.

Al-Awadi, M., Clark, W.J., Moore, W.R., Herron, M., Zhang, T., Zhao, W., Hurley, N., Kho, D., Montaron, B. & Sadooni, F. (2009) *Dolomite: Perspectives on a Perplexing Mineral*. Oilfield Review, 21(3):32-45.

Allan, J.R. & Wiggins, W.D. (1993) *Dolomite reservoirs : chemical techniques for evaluating origin and distribution*. AAPG Continuing Education Course Note Series 36, 129 p.

Aller, J. & Brime, C. (1985) *Deformación y metamorfismo en la parte Sur de la Cuenca Carbonífera Central (NO de España)*. C R X Congres Int Strat Geol Carbonifere, 3:541-548.

Aller, J., Bastida, F., Brime, C. & Pérez-Estaún, A. (1987) *Cleavage and its relation with metamorphic grade in the Cantabrian Zone (Hercynian of North-West Spain)*. Sciences Géologiques Bulletin, 40:255-272.

Aller, J., Valín, M.L., García-López, S., Brime, C. & Bastida. F. (2005) *Superposition of tectono-thermal episodes in the southern Cantabrian Zone (foreland thrust and fold belt of the Iberian Variscides, NW Spain)*. Bulletin de la Société Géologique de France, 176:487-498.

Alonso, J.L., Suárez-Rodríguez, A., Rodríguez-Fernández, L.R., Farias, P. & Villegas, F.J. (1990) *Hoja del Mapa Geológico Nacional de España (1:50000), Memoria 104 (La Pola de Gordón)*. IGME, Madrid.

Alonso, J.L., Pulgar, F.J., García-Ramos, J.C. & Barba, P. (1996) *Tertiary Basins and Alpine Tectonics in the Cantabrian Mountains*. In: Friend, P.F. & Dabrio, C.J. (eds.) *Tertiary basins of Spain: The stratigraphic record of crustal kinematics*. Cambridge University Press, Cambridge, 214-227.

Alonso, J.L., Marcos, A. & Suárez, A. (2009) *Paleogeographic inversion resulting from large out of sequence breaching thrusts : The León Fault (Cantabrian Zone, NW Iberia). A new picture of the external Variscan Thrust Belt in the Ibero-Armorican Arc*. Geologica Acta, 7:451-473.

Arp, G., Reimer, A. & Reitner, J. (2003) *Microbialite in seawater of increased alkalinity, Satonda Crater Lake, Indonesia*. Journal of Sedimentary Research, 73:105-127.

Arvidson, R.S. & Mackenzie, F.T. (1999) *The dolomite problem: control of precipitation kinetics by temperature and saturation state*. American Journal of Science, 299:257-288.

Ayllón, F., Bakker, R.J. & Warr, L.N. (2003) *Re-equilibration of fluid inclusions in diagenetic-anchizonal rocks of the Ciñera-Matallana coal basin (NW Spain)*. Geofluids, 3:49-68.

Azmy, K., Lavoie, D., Wang, Z., Brand, U., Al-Aasm, I., Jackson, S. & Girard, I. (2013) *Magnesium-isotope and REE compositions of Lower Ordovician carbonates from eastern Laurentia: Implications for the origin of dolomites and limestones*. Chemical Geology, 356:64-75.

B

Bahamonde, J.R., Colmenero, J.R. & Vera, C. (1997) *Growth and demise of Late Carboniferous carbonate platforms in the eastern Cantabrian Zone, Asturias, northwestern Spain*. Sedimentary Geology, 110:99-122.

Bahamonde, J.R., Merino-Tomé, O.A. & Heredia, N. (2007) *A Pennsylvanian microbial boundstone-dominated carbonate shelf in a distal foreland margin (Picos de Europa Province, NW Spain)*. Sedimentary Geology, 198:167-193.

Bahamonde, J.R., Martín, L. & Fernández, L.P. (2014) *The Pennsylvanian microbial-dominated carbonate platform of the El Sueve Massif : Contribution to the reconstruction of the Variscan foreland basin of the Cantabrian Zone (N Spain)*. Revista de la Sociedad Geológica de España. 27(1):47-62.

Bahamonde, J.R., Merino-Tomé, O., Della Porta, G. & Villa, E. (2015) *Pennsylvanian carbonate platforms adjacant to deltaic systems in an active marine foreland basin (Escalada Fm., Cantabrian Zone, NW Spain)*. Basin Research, 27(2):208-229.

Ballesteros, D., Jiménez-Sánchez, M., Giralt, S., García-Sansegundo, J. & Giralt, S. (2011) *Geological methods applied to speleological research in vertical caves: the example of Torca Teyera shaft (Picos de Europa, N Spain)*. Carbonates and Evaporites, 26:29-40.

Barker, C.E. & Pawlewicz, M.J. (1994) *Calculation of vitrinite reflectance from thermal histories and peak temperatures. A comparison of methods*. In: Mukhopadhyay, P.K. & Dow, W.G. (eds.) *Vitrinite reflectance as a maturity parameter: applications and limitations*. ACS Symp Series, 570:216-229.

Bastida, F., Brime, C., García-López, S. & Sarmiento, G.N. (1999) *Tectono-thermal evolution in a region with thin-skinned tectonics: the western nappes in the Cantabrian Zone (Variscan belt of NW Spain)*. International Journal of Earth Sciences, 88:38-48.

Bastida, F., Brime, C., García-López, S., Aller, J., Valín, M.L. & Sanz-López, J. (2002) *Tectono-thermal evolution of the Cantabrian Zone (NW Spain)*. Cuadernos del Museo Geominero Madrid, 1:105-123.

Bathurst, R.G. (1966) *Boring algae, micritic envelopes and lithification of molluscan biosparites*. Geological Journal, 5(1):15-32.

Beckert, J., Vandeginste, V. & John, C.M. (2015) *Exploring the geological features and processes that control the shape and internal fabrics of late diagenetic dolomite bodies (Lower Khuff equivalent – Central Oman Mountains)*. Marine and Petroleum Geology, 68:325-340.

Bertani, R. (2016) *Geothermal power generation in the world 2010-2014 update report*. Geothermics, 60:31-43.

Blanco-Ferrera, S., Sanz-López, J., García-López, S. & Bastida, F. (2017) *Tectonothermal evolution of the northeastern Cantabrian Zone (Spain)*. International Journal of Earth Sciences, 106(5):1539-1555.

Boni, M., Parente, G., Bechstädt, T., De Vivo, B. & Iannace, A. (2000) *Hydrothermal dolomites in SW Sardinia (Italy): evidence for a widespread late-Variscan fluid flow event*. Sedimentary Geology, 131:181–200.

Bonifacie, M., Calmels, D., Eiler, J.M., Horita, J., Chaduteau, C., Vasconcelos, C., Agrinier, P., Katz, A., Passey, B.H., Ferry, J.M. & Bourrand, J.J. (2017) *Calibration of the dolomite clumped isotope thermometer from 25 to 350°C, and implications for a universal calibration for all (Ca, Mg, Fe)CO_3 carbonates*. Geochimica et Cosmochimica Acta, 200:255-279.

Botor, D. (2012) *Hydrothermal fluids influence on the thermal evolution of the Stephanian sequence, the Sabero Coalfield (NW Spain)*. Geology, Geophysics and Environment, 38:369-393.

Botor, D. & Anczkiewicz, A.A. (2015) *Thermal history of the Sabero Coalfield (Southern Cantabrian Zone, NW Spain) as revealed by apatite fission track analyses from tonstein horizons: implications for timing of coalification*. International Journal of Earth Sciences, 104:1779-1793.

Bowman, M.B.J. (1982) *The stratigraphy of the San Emiliano Formation and its relationship to other Namurian/Westphalian A sequences in the Cantabrian Mts, NW Spain*. Trabajos de Geologia, 12:23-35.

Brime, C. (1981) *Postdepositional transformations of clays in Palaeozoic rocks of Northwest Spain*. Clay Minerals, 16:421-424.

Brime, C., García-López, S., Bastida, F., Valín, M.L, Sanz-López, J. & Aller, J. (2001) *Transition from Diagenesis to Metamorphism Near the Front of the Variscan Regional Metamorphism (Cantabrian Zone, Northwestern Spain)*. The Journal of Geology, 109:363-379.

Brouwer, A. & van Ginkel, A.C. (1964) *La succession Carbonifère dans la partie méridionale des montagnes Cantabriques (Espagne Nord-Ouest)*. Comptes Rendus, 5ème Congrès sur le Carbonifère, Paris 1963, 1:301-319.

Brunton, F.R. & Dixon, O.A. (1994) *Siliceous sponge-microbe biotic associations and their recurrence through the Phanerozoic as reef mound constructors*. Palaios, 9:370-387.

Burke, W.H., Denison, R.E., Hetherington, E.A., Koepnick, R.B., Nelson, H.F. & Otto, J.B. (1982) *Variation of seawater $^{87}Sr/^{86}Sr$ throughout Phanerozoic time*. Geology, 10:516-519.

C

Came, R.E., Brand, U. & Affek, H.P. (2014) *Clumped isotope signatures in modern brachiopod carbonate*. Chemical Geology, 377:20-30.

Came, R.E., Azmy, K., Tripati, A. & Olanipekun, B.J. (2017) *Comparison of clumped isotope signatures of dolomite cements to fluid inclusion thermometry in the temperature range of 73-176 °C*. Geochimica et Cosmochimica Acta, 199:31-47.

Cantrell, D., Swart, P.K. & Hagerty, R.M. (2004) *Genesis and characterization of dolomite, Arab-D Reservoir, Ghawar Field, Saoudi Arabia*. GeoArabia, 9:11-36.

Carrière, K.L. (2006) *Neoproterozoic to Holocene tectonothermal evolution of the southern Cantabrian Mountains NW Iberia, revealed by apatite fission-track thermochronology*. Unpublished PhD thesis, University of Heidelberg, 270 p.

Catanzaro, E.J., Murphy, T.J., Garner, E.L. & Shields, W.R. (1966) *Absolute isotopic abundance ratios and atomic weight of magnesium*. Journal of Research of the NBS, 70(A):453-458.

Chanda, P. & Fantle, M.S. (2017) *Quantifying the effect of diagenetic recrystallization on the Mg isotopic composition of marine carbonates*. Geochimica et Cosmochimica Acta, 204:219-239.

Chesnel, V., Samankassou, E., Merino-Tomé, Ó., Fernández, L.P. & Villa, E. (2015) *Facies, geometry and growth phases of the Valdorria carbonate platform (Pennsylvanian, Northern Spain)*. Sedimentology, 63:60-104.

Chesnel, V., Merino-Tomé, Ó., Fernández, L.P., Villa, E. & Samankassou, E. (2017) *Spatial and temporal distribution of microbial carbonates, skeletal and non-skeletal grains in a Pennsylvanian carbonate platform* (Valdorria, Northern Spain). Palaeogeography, Palaeoclimatology, Palaeoecology, 476:106-139.

Choh, S.J. & Kirkland, B.L. (2006) *Sedimentologic role of microproblematica Donezella in a lower Pennsylvanian Donezella-siliceous sponge-dominated carbonate buildup, frontal Ouachita thrust belt, Oklahoma, U.S.A*. Journal of Sedimentary Research, 76:152-161.

Choquette, P.W. & Pray, L.C. (1970) *Geologic Nomenclature and Classification of Porosity in Sedimentary Carbonates*. AAPG Bulletin, 54(2):207-250.

Colmenero, J.R. & Prado, J.G. (1993) *Coal basins in the Cantabrian Mountains, Northwestern Spain*. International Journal of Coal Geology, 23:215-229.

Colmenero, J.R., Suárez-Ruiz, I., Fernández-Suárez, J., Barba, P. & Llorens, T. (2008) *Genesis and rank distribution of Upper Carboniferous coal basins in the Cantabrian Mountains, Northern Spain*. International Journal of Coal Geology, 76:187-204.

Comte, P. (1959) *Recherches sur les terrains anciens de la Cordillère Cantabrique*. Memorias del Instituto Geológico de España, 60:1-440.

Copard, Y., Disnar, J.R. & Becq-Giraudon, J.F. (2002) *Erroneous maturity assessment given by Tmax and HI Rock-Eval parameters on highly mature weathered coals*. International Journal of Coal Geology, 49:57-65.

Corretgé, L.G. & Suárez, O. (1990) *Igneous rocks of the Cantabrian/Palentine Zone*. In: Dallmeyer, R.D. & Martínez-García, E. (eds.) Pre-Mesozoic Geology of Iberia. Springer-Verlag, Berlin, 72-79.

Crain, E.R. (2001) *Crain's petrophysical handbook*. Spectrum, 193 p.

Crespo. J.L., Moro, M.C., Fadón, O., Cabrera, R. & Fernández, A. (2000) *The Salamón gold deposit (León, Spain)*. Journal of Geochemical Exploration, 71:191-208.

D

Daëron, M., Blamart, D., Peral, M. & Affek, H.P. (2016) *Absolute isotopic abundance ratios and the accuracy of Δ47 measurements*. Chemical Geology, 442:83-96.

Dale, A., John, C.M., Mozley, P.S., Smalley, P.C. & Muggeridge, A.H. (2014) *Time-capsule concretions: Unlocking burial diagenetic processes in the Mancos Shale using carbonate clumped isotopes*. Earth and Planetary Science Letters, 394:30-37.

Dallmeyer, R.D. & Martínez-García, E. (1990) *Pre-Mesozoic Geology of Iberia*. Springer-Verlag, Berlin, 416 p.

Davies, G.R. & Smith, L.B. (2006) *Structurally controlled hydrothermal dolomite reservoir facies: An overview*. AAPG Bulletin, 90:1641-1690.

Deffeyes, K.S., Lucia, F.J. & Weyl, P.K. (1965) *Dolomitization of recent and Plio-Pleistocene sediments by marine evaporite waters on Bonaire, Netherlands Antilles*. In: Pray, L.C. & Murray, R.C. (eds.) *Dolomitization and Limestone Diagenesis*, SEPM Spec. Publ., 28:71-88.

Defliese, W.F. & Lohmann, K.C. (2015) *Non-linear mixing effects on mass-47 CO_2 clumped isotope thermometry: Patterns and implications*. Rapid Communications in Mass Spectrometry, 29:901-909.

Della Porta, G., Kenter, J.A.M., Bahamonde, J.R., Immenhauser, A. & Villa, E. (2003) *Microbial Boundstone Dominated Carbonate Slope (Upper Carboniferous, N Spain): Microfacies, Lithofacies Distribution and Stratal Geometry*. Facies, 49:175-208.

Dennis, K.J. & Schrag, D.P. (2010) *Clumped isotope thermometry of carbonatites as an indicator of diagenetic alteration*. Geochimica et Cosmochimica Acta, 74:4110-4122.

Dennis, K.J., Affek, H.P., Passey, B.H., Schrag, D.P. & Eiler, J.M. (2011) *Defining an absolute reference frame for 'clumped' isotope studies of CO_2*. Geochimica et Cosmochimica Acta, 75:7117-7131.

Dewit, J. (2012) *Genesis and reservoir properties of hydrothermal dolomites (HTD), Ramales platform (northern Spain)*. Unpublished PhD thesis, KU Leuven, 183 p.

Dewit, J., Foubert, A., El Desouky, H.A., Muchez, Ph., Hunt, D., Vanhaecke, F. & Swennen, R. (2014) *Characteristics, genesis and parameters controlling the development of a large stratabound HTD body at Matienzo (Ramales Platform, Basque-Cantabrian Basin, northern Spain)*. Marine and Petroleum Geology, 55:6-25.

Della Porta, G., Kenter, J.A.M., Bahamonde, J.R., Immenhauser, A. & Villa, E. (2003) *Microbial Boundstone Dominated Carbonate Slope (Upper Carboniferous, N Spain): Microfacies, Lithofacies Distribution and Stratal Geometry*. Facies, 49:175-208.

Dickson, J.A.D. (1966) *Carbonate identification and genesis as revealed by staining*. Journal of Sedimentary Research, 36(2):491-505.

Dietrich, B. (2005) *Numerical modeling as a Means to Enhance Genetic Sedimentary Basin Interpretation: A Case Study of the Southern Cantabrian Basin (NW Spain)*. Unpublished PhD thesis, University of Heidelberg, 263 p.

de Dolomieu, D. (1791) *Sur un genre de Pierres calcaires très-peu effervescentes avec les Acides, & phosphorescentes par la collision*. Journal de Physique, 39:3-10. Translation of Dolomieu's paper with notes reporting his discovery of dolomite by Carozzi, A.V. & Zenger, D.H. (1981) Journal of Geological Education, 29:4-10.

Dubois, C., Quinif, Y., Baele, J.M., Barriquand, L., Bini, A., Bruxelles, L., Dandurand, G., Havron, C., Kaufmann, O., Lans, B., Maire, R., Martin, J., Rodet, J., Rowberry, M.D., Tognini, P. & Vergari, A. (2014) *The process of ghost-rock karstification and its role in the formation of cave systems*. Earth-Science Reviews, 131:116-148.

Duddy, I.R., Green, P.F., Bray, R.J. & Hegarty, K.A. (1994) *Recognition of the thermal effects of fluid flow in sedimentary basins*. In: Parnel, J. (ed.) *Geofluids: Origin, Migration and Evolution of Fluids in Sedimentary Basins*. Geological Society Special Publication, 78:325-345.

E

Eagle, R.A., Schauble, E.A., Tripati, A.K., Tütken, T., Hulbert, R.C. & Eiler, J.M. (2010) *Body temperature of modern and extinct vertebrates from ^{13}C-^{18}O bond abundances in bioapatite*. Proceedings of the National Academy of Sciences of the United States of America, 107(23):10377-10382.

Eberl, D.D. (1993) *Three zones for illite formation during burial diagenesis and metamorphism*. Clay and Clay Minerals, 41:26-37.

Eichhubl, P. & Boles, J.R. (2000) *Rates of fluid flow in fault systems – Evidence for episode rapid fluid flow in the Miocene Monterey Formation, coastal California*. American Journal of Science, 300:571-600.

Eichmüller, K. (1985) *Die Valdeteja Formation: Aufbau und Geschichte einer oberkarbonischen Karbonatplattform (Kantabrisches Gebirge, Nordspanien)*. Facies, 13:45-154.

Eichmüller, K. (1986) *Some Upper Carboniferous (Namurian; Westphalian) Lithostratigraphic Units in Northern Spain: Results and Implications of an Environmental Interpretation*. Boletín Geológico y Minero, 97:590-607.

Eiler, J.M. & Schauble, E. (2004) *$^{18}O^{13}C^{16}O$ in Earth's atmosphere*. Geochimica et Cosmochimica Acta, 68(23):4767-4777.

Eiler, J.M. (2007) *"Clumped-isotope" geochemistry – The study of naturally-occurring, multiply-substituted isotopologues*. Earth and Planetary Science Letters, 262:309-327.

Epstein, S., Buchsbaum, R., Lowestam, H.A. & Urey, H.C. (1953) *Revised carbonate-water isotopic temperature scale*. Geological Society of America Bulletin, 64(11): 1315-1326.

Epstein, A.G., Epstein, J.B. & Harris, L.D. (1977) Conodont color alteration – an index to organic metamorphism. US Geological Survey Professional Paper, 995:1-27.

Espitalié, J., Deroo, G. & Marquis, F. (1985a) *La pyrolyse Rock-Eval et ses applications. Première Partie.* Revue Inst. Français du Pétrol, 40:563-579.

Espitalié, J., Deroo, G. & Marquis, F. (1985b) *La pyrolyse Rock-Eval et ses applications. Deuxième Partie.* Revue Inst. Français du Pétrol, 40:755-784.

Espitalié, J., Deroo, G. & Marquis, F. (1985c) *La pyrolyse Rock-Eval et ses applications. Troisième Partie.* Revue Inst. Français du Pétrol, 41:73-89.

Espitalié, J., Laporte, J.L., Madec, M., Marquis, F., Leplat, P. & Paulet, J. (1977) *Méthode rapide de caractérisation des roches mères, de leur potentiel pétrolier et de leur degré d'évolution*. Revue Inst. Français du Pétrol, 32:23-45.

Evers, H.J. (1967) *Geology of the Leonides between the Bernesga and Porma rivers, Cantabrian Moutains, NW Spain*. Leidse Geologische Mededelingen, 41:83-151.

F

Fernández-Martínez, E.M., Matías, R. & Domingo, J.M. (1996) *Minerales del área de Villamanín (Provincia de León, España) : Guía de identificación y utilización docente*. Enseñanza de las Ciencias de la Tierra, 99-109.

Ferry, J.M., Passey, B.H., Vasconcelos, C. & Eiler, J.M. (2011) *Formation of dolomite at 40-80 °C in the Latemar carbonate buildup, Dolomites, Italy, from clumped isotope thermometry*. Geology, 39(6):571-574.

Fillon, C., Pedreira, D., van der Beek, P.A., Huismans, R.S., Barbero, L. & Pulgar, J.A. (2016) *Alpine exhumation of the central Cantabrian Mountains, Northwest Spain*. Tectonics, 35:339-356.

Flügel, E. (2004) *Microfacies of carbonate rocks: Analysis, Interpretation and Application*. Springer-Verlag, Berlin, 976 p.

Fontboté, L. (1993) *Self-organization fabrics in carbonate-hosted ore deposits: Example of diagenetic crystallization rhythmites*. In: Fenoll Hach-Alí, P., Torres-Ruiz, J., Gervilla, F. (eds.) *Current Research in Geology Applied to Ore Deposits*, Granada, University of Granada, 11-14.

Frings, K., Lutz, R., de Wall, H. & Warr, L.N. (2004) *Coalification history of the Stephanian Ciñera-Matallana pull-apart basin, NW Spain: Combining anisotropy of vitrinite reflectance and thermal modeling*. International Journal of Earth Sciences, 93:92-106.

Fukuchi, R., Fujimoto, K., Kameda, J., Hamahashi, M., Yamaguchi, A., Kimura, G., Hamada, Y., Hashimoto, Y., Kitamura, Y. & Saito, S. (2014) *Changes in illite crystallinity within an ancient tectonic boundary thrust caused by thermal, mechanical, and hydrothermal effects: an example from the Nobeoka Thrust, southwest Japan*. Earth, Planets and Space, 66:116-127.

G

Gale, J.F.W., Laubach, S.E., Marrett, R.A., Olson, J.E., Holder, J. & Reed, R.M. (2004) *Predicting and characterizing fractures in dolostone reservoirs: using the link between diagenesis and fracturing.* Geological Society, London, Special Publications, 235:177-192.

Galy, A., Belshaw, N.S., Halicz, L. & O'Nions, R.K. (2001) *High-precision measurements of magnesium isotopes by multiple-collector inductively coupled plasma mass spectrometry*. International Journal of Mass Spectrometry, 208:89-98.

Galy, A., Yoffe, O., Janney, P.E., Williams, R.W., Cloquet, C., Alard, O., Halicz, L., Wadhwa, M., Hutcheo, I.D., Ramon, E. & Carignan, J. (2003) *Magnesium isotope heterogeneity of the isotopic standard SRM980 and new reference materials for magnesium-isotope-ratio measurements*. Journal of Analytical Atomic Spectrometry, 18:1352-1356.

García-López, S., Bastida, F., Brime, C., Aller, J., Valín, M.L., Sanz-López, J., Méndez, C.A. & Menéndez-Álvarez, J.R. (1999) *Los episodios metamórficos de la Zona Cantábrica y su contexto estructural*. Trabajos de Geología Universidad de Oviedo, 21:177-187.

Gasparrini, M. (2003) *Large-scale hydrothermal dolomitisation in the southwestern Cantabrian Zone (NW Spain): causes and controls of the process and origin of the dolomitising fluids*. Unpublished PhD thesis, University of Heidelberg, 193 p.

Gasparrini, M., Bechstädt, T. & Boni, M. (2006a) *Massive hydrothermal dolomites in the southwestern Cantabrian Zone (Spain) and their relation to the Late Variscan evolution*. Marine and Petroleum Geology, 23:543-568.

Gasparrini, M., Bakker, R.J. & Bechstädt, T. (2006b) *Characterization of dolomitizing fluids in the Carboniferous of the Cantabrian Zone (NW Spain): a fluid-inclusion study with cryo-raman spectroscopy*. Journal of Sedimentary Research, 76:1304-1322.

Gasparrini, M., López-Cilla, I., Blázquez-Fernández, S., Rosales, I., Lerat, O., Martín-Chivelet, J. & Doligez, B. (2017) *A multidisciplinary modeling approach to assess facies-dolomitization-porosity interdependence in a lower Cretaceous platform (Northern Spain)*. SEPM Special Publication, 109.

Geske, A., Zorlu, J., Richter, D.K., Buhl, D., Niedermayr, A. & Immenhauser, A. (2012) *Impact of diagenesis and low grade metamorphosis on isotope ($\delta^{26}Mg$, $\delta^{13}C$, $\delta^{18}O$ and $^{87}Sr/^{86}Sr$) and elemental (Ca, Mg, Mn, Fe and Sr) signatures of Triassic sabkha dolomites*. Chemical Geology, 332-333:45-64.

Geske, A., Goldstein, R.H., Mavromatis, V., Richter, D.K., Buhl, D., Kluge, T., John, C.M. & Immenhauser, A. (2015) *The magnesium isotope ($\delta^{26}Mg$) signature of dolomites*. Geochimica et Cosmochimica Acta, 149:131-151.

Ghosh, P., Adkins, J., Affek, H., Balta, B., Guo, W., Schauble, E.A., Schrag, D. & Eiler, J.M. (2006) *^{13}C-^{18}O bonds in carbonate minerals: A new kind of paleothermometer*. Geochimica et Cosmochimica Acta, 70:1439-1456.

Ghosh, P., Eiler, J., Campana, S.E. & Feeney, R.F. (2007) *Calibration of the carbonate "clumped isotope" paleothermometer for otoliths*. Geochimica et Cosmochimica Acta, 71:2736-2744.

Given, R.K. & Wilkinson, B.H. (1987) *Dolomite abundance and stratigraphic age: constraints on rates and mechanisms of Phanerozoic dolostone formation*. Journal of Sedimentary Petrology, 57(6):1068-1078.

Gleadow, A.J.W. & Duddy, I.R. (1981) *A natural long-term track annealing experiment for apatite*. Nuclear Tracks, 5:169-174.

Goldstein, R.H. (2001) *Fluid inclusions in sedimentary and diagenetic systems*. Lithos, 55:159-193.

Goldstein, R.H. & Reynolds, T.J. (1994) *Systematics of fluid inclusions in diagenetic minerals*. Society for Sedimentary Geology Short Course 31, 199 p.

Gómez, S., Vara, I., Álvarez, B. & Marcos, A. (1996) *Aula activa de la naturaleza Villamanín (León).* Junta de Castilla y León : Consejería de Educación y Cultura. Salamanca, 184 p.

Gómez-Fernández, F., Both, R.A., Mangas, J. & Arribas, A. (2000) *Metallogenesis of Zn-Pb carbonate-hosted mineralization in the southeastern region of the Picos de Europa (Central Northern Spain) Province: geologic, fluid inclusion, and stable isotopes studies*. Economic Geology, 95:19-40.

Gomez-Rivas, E., Corbella, M., Martín-Martín, J.D., Stafford, S.L., Teixell, A., Bons, P.D., Griera, A. & Cardellach, E. (2014) *Reactivity of dolomitizing fluids and Mg source evaluation of fault-controlled dolomitization at the Benicàssim outcrop analogue (Maestrat basin, E Spain)*. Marine and Petroleum Geology, 55:26-42.

Gong, Z., Langereis, C.G. & Mullender, T.A.T. (2008) *The rotation of Iberia during the Aptian and the opening of the Bay of Biscay*. Earth and Planetary Science Letters, 273:80-93.

Gregg, J.M., Bish, D.L., Kaczmarek, S.E. & Machel, H.G. (2015) *Mineralogy, nucleation and growth of dolomite in the laboratory and sedimentary environment: A review*. Sedimentology, 62:1749-1769.

Grammer, G.M., Harris, P.M. & Eberli, G.P. (2004) *Intergration of outcrop and modern analogs in reservoir modelling: Overview with examples from the Bahamas.* In: Grammer, G.M., Harris, P.M. & Eberli, G.P. (eds.) *Integration of outcrop and modern analogs in reservoir modelling*. American Association of Petroleum Geologists Memoirs, 80:1–22.

Grimmer, J.O.W., Bakker, R.J., Zeeh, S. & Bechstädt, T. (2000) *Dolomitisation and brecciation along fault zones in the Cantabrian mountains*. Journal of Geochemical Exploration, 69-70:153-158.

Guggenheim, S., Bain, D.C., Bergaya, F., Brigatti, M.F., Drits, V.A., Eberl, D.D., Formoso, M.L.L., Galán, E., Merriman, R.J., Peacor, D.R., Stanjek, H. & Watanabe, T. (2002) *Report of the Association Internationale pour l'Etude des Argiles (AIPEA) Nomenclature Committee for 2001: Order, disorder and crystallinity in phyllosilicates and the use of the 'Crystallinity Index'*. Clay Minerals, 37:389-393.

Gutiérrez-Alonso, G., Collins, A.S., Fernández-Suárez, J., Pastor-Galán, D., González-Clavijo, E., Jourdan, F., Weil, A.B. & Johnston, S.T. (2015) *Dating of lithospheric buckling: $^{40}Ar/^{39}Ar$ ages of syn-orocline strike-slip shear zones in northwestern Iberia*. Tectonophysics, 643:44-54.

Gutiérrez-Alonso, G., Fernández-Suárez, J. & Weil, A.B. (2004) *Orocline triggered lithospheric delamination*. Geological Society of America, 383:121-131.

Gutiérrez-Alonso, G., Johnston, S.T., Weil, A.B., Pastor-Galán, D. & Fernández-Suárez, J. (2012) *Buckling an orogen: The Cantabrian Orocline*. GSA Today, 22:4-9.

H

Handin, J. (1966) *Strength and ductility*. In: Clarke, S.P. (ed.) *Handbook of Physical Constraints*. Geological Society of America Memoirs, 97:223–289.

Henkes, G.A., Passey, B.H., Grossman, E.L., Shenton, B.J., Pérez-Huerta, A. & Yancey, T.E. (2014) *Temperature limits for the preservation of primary calcite clumped isotope paleotemperatures*. Geochimica et Cosmochimica Acta, 139:362-382.

Henkes, G.A., Passey, B.H., Wanamaker, A.D., Grossman, E.L., Ambrose, W.G. & Carroll, M.L. (2013) *Carbonate clumped isotope compositions of modern marine mollusk and brachiopod shells*. Geochimica et Cosmochimica Acta, 106:307-325.

Higgins, J.A. & Schrag, D.P. (2010) *Constraining magnesium cycling in marine sediments using magnesium isotopes*. Geochimica et Cosmochimica Acta, 74:5039-5053.

Higgins, J.A. & Schrag, D.P. (2012) *Records of Neogene seawater chemistry and diagenesis in deep-sea carbonate sediments and pore fluids*. Earth and Planetary Science Letters, 357:386-396.

Hippler, D., Buhl, D., Witbaard, R., Richter, D.K. & Immenhauser, A. (2009) *Towards a better understanding of magnesium-isotope ratios from marine skeletal carbonates*. Geochimica et Cosmochimica Acta, 73:6134-6146.

Honlet, R., Gasparrini, M., Jäger, H., Muchez, Ph. & Swennen, R. (in press) *Precursor and ambient rock paleothermometry to assess the thermicity of burial dolomitization in the southern Cantabrian Zone (northern Spain)*. International Journal of Earth Sciences.

Hu, Z., Hu, W., Wang, X., Lu, Y., Wang, L., Liao, Z. & Li, W. (2017) *Resetting of Mg isotopes between calcite and dolomite during burial metamorphism: Outlook of Mg isotopes as geothermometer and seawater proxy*. Geochimica et Cosmochimica Acta, 208:24-40.

Hu, B., Radke, J., Schlüter, H.J., Heine, F.T., Zhou, L. & Bernasconi, S.M. (2014) *A modified procedure for gas-source isotope ratio mass spectrometry: the long-integration dual-inlet (LIDI) methodology and implications for clumped isotope measurements*. Rapid Communications in Mass Spectrometry, 28:1413-1425.

Hugman, R.H.H. III & Friedman, M. (1979) *Effects of texture and composition on mechanical behaviour of experimentally deformed carbonate rocks*. AAPG Bulletin, 63:1478–1489.

Huntington, K.W., Eiler, J.M., Affek, H.P., Guo, W., Bonifacie, M., Yeung, L.Y., Thiagarajan, N., Passey, B., Tripati, A., Daëron, M. & Came, R. (2009) *Methods and limitations of 'clumped' CO_2 isotope (Δ_{47}) analysis by gas-source isotope ratio mass spectrometry*. Journal of Mass Spectrometry, 44:1318-1329.

Huntington, K.W., Budd, D.A., Wernicke, B.P. & Eiler, J.M. (2011) *Use of clumped-isotope thermometer to constrain the crystallization temperature of diagenetic calcite*. Journal of Sedimentary Research, 81:656-669.

I

IEA (2017) *World Energy Outlook 2017 - Executive summary*. International Energy Agency, 8 p.

Immenhauser, A., Buhl, D., Richter, D., Niedermayr, A., Richelmann, D., Dietzel, M. & Schulte, M. (2010) *Magnesium-isotope fractionation during low-Mg calcite precipitation in a limestone cave-field study and experiments*. Geochimica et Cosmochimica Acta, 74:4346-4364.

Immenhauser, A., Buhl, D., Lokier, S., Geske, A., Walter, B.F., Markl, G., Mavromatis, V. & Dietzel, M. (2016) *Magnesium isotope geochemistry of dolomites: Recent developments*. Abstract Book, Dolomieu Conference on Carbonate Platforms and Dolomite, Selva di Val Gardena (Italy), October 4-7, 2016, 71.

J

Jacquemyn, C. (2013) *Diagenesis and application of LIDAR in reservoir analogue studies: Karstification in the Cretaceous Apulia carbonate platform – Dolomitization in the Triassic Latemar carbonate buildup*. Unpublished PhD thesis, KU Leuven, 192 p.

Jacquemyn, C., Huysmans, M., Hunt, D., Casini, G. & Swennen, R. (2015) *Multi-scale three-dimensional distribution of fracture- and igneous intrusion-controlled hydrothermal dolomite from digital outcrop model, Latemar platform, Dolomites, northern Italy*. AAPG Bulletin, 99(5):957-984.

Jacka, A.D. (1974) *Replacement of fossils by length-slow chalcedony and associated dolomitization*. Journal of Sedimentary Petrology, 44:421-427.

Jarvie, D.M., Claxton, B.L., Henk, F.B. & Breyer, J.T. (2001) *Oil and Shale Gas from the Barnett Shale, Ft. Worth Basin, Texas*. AAPG National Convention, Denver, CO June 3-6, 2001, 28 p.

Jiménez-Sánchez, M., Ballesteros, D., Rodríguez-Rodríguez, L. & Domínguez-Cuesta, M.J. (2014) *The Picos de Europa National and Regional Parks*. In: Gutiérrez, F. & Gutiérrez, M. (eds.) *Landscapes and Landforms of Spain*. World Geomorphological Landscapes. Springer-Verlag, Berlin, 155-163.

John, C.M. & Bowen, D. (2016) *Community software for challenging isotope analysis: First applications of 'Easotope' to clumped isotopes*. Rapid Communications in Mass Spectrometry, 30:2285-2300.

Julivert, M. (1971) *Décollement tectonics in the Variscan Cordillera of northwest Spain*. American Journal of Science, 270:1-29.

Julivert, M. (1978) *Hercynian orogeny and Carboniferous palaeogeography in northwestern Spain: a model of deformation–sedimentation relationships*. Zeitschrift der Deutschen geologischen Gesellschaft, 29:565-592.

Junfeng, J. & Browne, P.R.L. (2000) *Relationschip between illite crystallinity and temperature in active geothermal systems of New Zealand*. Clay and Clay Minerals, 48:139-144.

K

Kaczmarek, S.E., Gregg, J.M., Bish, D.L., Machel, H.G. & Fouke, B.W. (2017) *Dolomite, very high-magnesium calcite, and microbes – Implications for the microbial model of dolomitization*. SEPM Special Publication, 109.

Karweil, J. (1956) *Die Metamorphose der Kohlen vom Standpunkt der physikalischen Chemie*. Zeitschrift der Deutschen geologischen Gesellschaft, 107:132-139.

Kastner, M., Keene, J.B. & Gieskens, J.M. (1977) *Diagenesis of siliceous oozes. I. Chemical controls on the rate of opal-A to opal-CT transformation – an experimental study*. Geochimica et Cosmochimica Acta, 41:1041-1059.

Kearey, P. (2001) *The New Penguin Dictionary of Geology (second edition)*. Penguin Books, London, England, 327 p.

Kele, S., Breitenbach, S.F.M., Capezzuoli, E., Meckler, A.N., Ziegler, M., Millan, I.M., Kluge, T., Deák, J., Hanselmann, K., John, C.M., Yan, H., Liu, Z. & Bernasconi, S.M. (2015) *Temperature dependence of oxygen- and clumped isotope fractionation in carbonates: A study of travertines and tufas in the 6-95°C temperatures range*. Geochimica et Cosmochimica Acta, 168:172-192.

Kelson, J.R., Huntington, K.W., Schauer, A.J., Saenger, C. & Lechler, A.R. (2017) *Toward a universal carbonate clumped isotope calibration: Diverse synthesis and preparatory methods suggest a single temperature relationship*. Geochimica et Cosmochimica Acta, 197:104-131.

Kenter, J.A.M., Van Hoeflaken, F., Bahamonde, J.R., Bracco Gartner, G.L., Keim, L. & Besems, R.E. (2002) *Anatomy and lithofacies of an intact and seismic-scale carboniferous carbonate platform (Asturias, NW Spain): analogues of hydrocarbon reservoirs in the Pricaspian Basin (Kazakhstan)*. In: Zempolich, W.G. & Cook, H.E. (eds.) *Paleozoic Carbonates of the Commonwealth of Independent States (CIS): Subsurface Reservoirs and Outcrop Analogs*. SEPM Special Publication, 77:181-203.

Kirwan, R. (1794) *Elements of mineralogy*. J. Nichols, London, 510 p.

Kluge, T., John, C.M., Jourdan, A.L., Davis, S. & Crawshaw, J. (2015) *Laboratory calibration of the calcium carbonate clumped isotope thermometer in the 25-250°C temperature range*. Geochimica et Cosmochimica Acta, 157:213-227.

Knauth, L.P. (1979) *A model for the origin of chert in limestone*. Geology, 7:274-277.

Knipe, R.J. (1993) *The influence of fault zone processes and diagenesis on fluid flow*. In: Horbury, A.D. & Robinson, A.G. (eds.) *Diagenesis and Basin Development*. AAPG Studies in Geology, 36:135-151.

Kübler, B. (1967) *La cristallinité de l'illite et les zones tout à fait supérieures du métamorphisme*. In: Etages Tectoniques, Colloque de Neuchâtel 1966, à la Baconnière, Neuchâtel, 105-121.

Kübler, B. (1968) *Evaluation quantitative du métamorphisme par cristallinité de l'illite*. Bulletin du Centre de recherches de Pau, 2:385-397.

L

Lafargue, F., Marquis, F. & Pillot, D. (1998) *Rock-Eval 6 applications in hydrocarbon exploration, production, and soil contamination studies*. Revue Inst. Français du Pétrol, 53:421-437.

Land, L.S. (1985) *The origin of massive dolomite*. Journal of Geological Education, 33:112-125.

Land, L.S. (1998) *Failure to Precipitate Dolomite at 25°C from Dilute Solution Despite 1000-Fold Oversaturation after 32 Years*. Aquatic Geochemistry, 4:361-368.

Lapponi, F., Bakker, R.J. & Bechstädt, T. (2007) *Low temperature behavior of natural saline fluid inclusions in saddle dolomite (Paleozoic, NW Spain)*. Terra Nova, 19(6):440-444.

Lapponi, F., Casini, G., Sharp, I., Blendiger, W., Fernández, N., Romaire, I. & Hunt, D. (2011) *From outcrop to 3D modelling : a case study of a dolomitized carbonate reservoir, Zagros Mountains, Iran*. Petroleum Geoscience, 17:283-307.

Lapponi, F., Bechstädt, T., Boni, M., Banks, D.A. & Schneider, J. (2013) *Hydrothermal dolomitization in a complex geodynamic setting (Lower Palaeozoic, northern Spain)*. Sedimentology, 61:411-443.

Lavoie, D. & Morin, C. (2004) *Hydrothermal dolomitization in the Lower Silurian Sayabec Formation in northern Gaspé – Matapédia (Québec): constraint on timing of porosity and regional significance for hydrocarbon reservoirs*. Bulletin of Canadian Petroleum Geology, 52(3):256-269.

Lavoie, D., Jackson, S. & Girard, I. (2010) *Mg isotopes and hydrothermal saddle dolomites; current data for Paleozoic dolomites of eastern Canada and implications for Mg source*. Conference abstract, GeoConvention 2010, Calgary.

Lavoie, D., Jackson, S. & Girard, I. (2014) *Magnesium isotopes in high-temperature saddle dolomite cements in the lower Paleozoic of Canada*. Sedimentary Geology, 305:58-68.

Leung, D.Y.C., Caramanna, G. & Maroto-Valer, M.M. (2014) *An overview of current status of carbon dioxide capture and storage technologies*. Renewable and Sustainable Energy Reviews, 39:426-443.

Li, W., Teng, F.Z., Ke, S., Rudnick, R.L., Gao, S., Wu, F.Y. & Chappel, B.W. (2010) *Heterogeneous magnesium isotopic composition of the upper continental crust*. Geochimica et Cosmochimica Acta, 74(23):6867-6884.

Li, W., Chakraborty, S., Beard, B.L., Romanek, C.S. & Johnson, C.M. (2012) *Magnesium isotope fractionation during precipitation of inorganic calcite under laboratory conditions*. Earth and Planetary Science Letters, 333-334:304-316.

Lloyd, M.K., Eiler, J.M. & Nabelek, P.I. (2017) *Clumped isotope thermometry of calcite and dolomite in a contact metamorphic environment*. Geochimica et Cosmochimica Acta, 197:323-344.

Lobato, L., García-Alcalde, J.L., Sánchez de Posada, L.C., Truylos, J. & Villegas, F.J. (1984) *Hoja del Mapa Geológico Nacional de España (1:50000), Memoria 104 (Boñar)*. IGME, Madrid.

López-Horgue M.A., Iriarte E., Schroder S., Fernández-Mendiola, P.A., Caline B., Corneyllie H., Fremont J., Sudrie M. & Zerti S. (2010) *Structurally controlled hydrothermal dolomites in Albian carbonates of the Asón valley, Basque Cantabrian Basin, Northern Spain*. Marine and Petroleum Geology, 27(5):1069-1092.

Lucia, F.J. (1983) *Petrophysical parameters estimated from visual description of carbonate rocks: a field classification of pore space*. Journal of Petroleum Technology, 35:626-637.

Lund, J.W. & Boyd, T.L. (2015) *Direct Utilization of Geothermal Energy 2015 Worldwide Review*. Proceedings World Geothermal Congress 2015, Melbourne, Australia, 31 p.

M

MacDonald, J.M., John, C.M. & Girard, J.P. (2017) *Testing clumped isotopes as a reservoir characterization tool: a comparison with fluid inclusions in a dolomitized sedimentary carbonate reservoir buried to 2-4 km*. In: Lawson, M. (ed.) *From Source to Seep: Geochemical Applications in Hydrocarbon Systems*. Geological Society of London, *accepted for publication*.

Machel, H.G. (2004) *Concepts and models of dolomitization: a critical reappraisal*. In: Braithwaite, C.J.R., Rizzi, G. & Darke, G. (eds.) *The geometry and Petrogenesis of Dolomite Hydrocarbon Reservoirs*. Geological Society, London, Special Publications, 235:7-63.

Machel, H.G. & Lonnee, J. (2002) *Hydrothermal dolomite – a product of poor definition and imagination*. Sedimentary Geology, 152:163-171.

Mangenot, X. (2017) *Contributions du thermomètre Δ_{47} et du chronomètre U-Pb à l'étude de l'histoire diagénétique, thermique, et hydrogéologique des réservoirs carbonatés du Jurassique Moyen du bassin de Paris*. Unpublished PhD thesis, Université Sorbonne Paris, 193 p.

Mangenot, X., Bonifacie, M., Gasparrini, M., Götz, A., Chaduteau, C., Ader, M. & Rouchon, V. (2017) *Coupling Δ_{47} and fluid inclusion thermometry on carbonate cements to precisely reconstruct the temperature, salinity and $\delta^{18}O$ of paleo-groundwater in sedimentary basins*. Chemical Geology, *accepted for publication*.

Mansour, A.S.M. (2004) *Diagenesis of Upper Cretaceous Rudist Bivalves, Abu Roash Area, Egypt: A Petrographic Study*. Geologia Croatica, 57(1):55-66.

Marcos, A. (1968) *La tectónica de la Unidad de la Sobia-Bodón*. Trabajos de Geología Universidad de Oviedo, 2:59-87.

Marcos, A. & Pulgar, J.A. (1982) *An approach to the tectonostratigraphic evolution in the Cantabrian Foreland thrust and fold belt, Hercynian Cordillera of NW Spain*. Neues Jahrbuch für Geologie und Paläontologie, 163:256-260.

Marín, J.A. (1997) *Estructura del Domo de Valsurbio y borde suroriental de la Región del Pisuerga-Carrión (Zona Cantábrica, NO de España)*. Unpublished PhD thesis, Oviedo University, 181 p.

Martín-Martín, J.D., Gomez-Rivas, E., Gómez-Gras, D., Travé, A., Ameneiro, R., Koehn, D. & Bons, P.D. (2017) *Activation of stylolites as conduits for overpressured fluid flow in dolomitized platform carbonates*. Geological Society of London Special Publications, 459:1-25.

Martínez-García, E. (1983) *Permian mineralizations in the Cantabrian Mountains (North-West Spain)*. In: Schneider, H.J. (ed.) *Mineral deposits of the Alps and of the Alpine epoch in Europe*. Springer-Verlag, Berlin, 259-274.

Martín-González, F., Barbero, L., Capote, R., Heredia, N. & Gallastegui, G. (2012) *Interaction of two successive Alpine deformation fronts: constraints from low-temperature thermochronology and structural mapping (NW Iberian Peninsula)*. International Journal of Earth Sciences, 101:1331-1342.

Marschik, R. (1992) *Der Übergang von Diagenese zur sehr niedergradigen Metamorphose im externen Variszikum (Kantabrische Zone), NW Spanien*. Unpublished PhD thesis, University of Heidelberg, 70 p.

Mavromatis, V., Gautier, Q., Schott, J. & Oelkers, E.H. (2011) *Effect of aqueous organic ligands on Mg-isotope fractionation during magnesite precipitation*. Conference abstract, Goldschmidt conference Prague.

Mavromatis, V., Gautier, Q., Bosc, O. & Schott, J. (2013) *Kinetics of Mg partition and Mg stable isotope fractionation during its incorporation in calcite*. Geochimica et Cosmochimica Acta, 114:188-203.

Mavromatis, V., Meister, P. & Oelkers, E.H. (2014) *Using stable Mg isotopes to distinguish dolomite formation mechanisms: A case study from the Peru Margin*. Chemical Geology, 385:84-91.

Mavromatis, V., Immenhauser, A., Buhl, D., Purgstaller, B., Baldermann, A. & Dietzel, M. (2017) *Effect of organic ligands on Mg partitioning and Mg isotope fractionation during low-temperature precipitation of calcite in the absence of growth rate effects*. Geochimica et Cosmochimica Acta, 207:139-153.

McKenzie, J.A. (1981) *Holocene dolomitization of calcium carbonate sediments from coastal sabkhas of Abu Dhabi, U.A.E.: a stable isotope study*. Journal of Geology, 89:185-198.

McKenzie, J.A. & Vasconcelos, C. (2009) *Dolomite Mountains and the origin of the dolomite rock of which they mainly consist: historical developments and new perspectives*. Sedimentology, 56:205-219.

Meckler, A., Ziegler, M., Millán, M., Breitenbach, S. & Bernasconi, S. (2014) *Long-term performance of the Kiel carbonate device with a new correction scheme for clumped isotope measurements*. Rapid Communications in Mass Spectrometry, 28:1705-1715.

Méndez, A. (1985) *Estudio de la evolución de los carbones de la Cuenca Ciñera-Matallana, León*. Unpublished PhD thesis, University of Oviedo, 269 p.

Merino, E., Canals, A. & Fletcher, R.C. (2006) *Genesis of self-organized zebra textures in burial dolomites: Displacive veins, induced stress, and dolomitization*. Geologica Acta, 4(3):383-393.

Merino, E. & Canals, A. (2011) *Self-accelerating dolomite-for-calcite replacement: self-organized dynamics of burial dolomitization and associated mineralization*. American Journal of Science, 311:573-607.

Merriman, R.J. & Frey, M. (1999) *Patterns of very low-grade metamorphism in metapelitic rocks*. In: Frey, M. & Robinson, D. (eds.) *Low-grade metamorphism*. Blackwell Science Limited, London, 61-107.

Middleton, D.W.J., Parnell, J., Green, P.F., Xu, G. & McSherry, M. (2001) *Hot fluid flow events in Atlantic margin basins: an example from the Rathlin Basin*. In: Shannon, P.M., Haughton, P.D.W. & Corcoran, D.V. (eds.) *The Petroleum Exploration of Ireland's Offshore Basins*. Geological Society, London, Special Publications, 188:91-105.

Moore, C.H. (1989) *Carbonate Diagenesis and Porosity*. Developments in Sedimentology 46. Elsevier Science, 337 p.

Muchez, Ph., Marshall, J.D., Touret, J.L.R. & Viaene, W.A. (1994) *Origin and migration of palaeofluids in the Upper Visean of the Campine Basin, northern Belgium*. Sedimentology, 41(1):133-145.

Muchez, Ph. & Sintubin, M. (2002) *Palaeofluid flow within the evolution of sedimentary basins: principles and examples from the Carboniferous of Belgium*. Aardkundige Mededelingen, 12:161-164.

Mukoyoshi, H., Hara, H. & Omori, K. (2007) *Quantitative estimation of temperature conditions for illite crystallinity: comparison to vitrinite reflectance from the Chichibu and Shimanto accretionary complexes, eastern Kyushu, Southwest Japan*. Bulletin of the geological survey of Japan, 58:23-31.

Müller, I.A., Fernandez, A., Radke, J., van Dijk, J., Bowen, D., Schwieters, J. & Bernasconi, S.M. (2017) *Carbonate clumped isotope analyses with the long-integration dual-inlet (LIDI) workflow: scratching at the lower sample weight boundaries*. Rapid Communications in Mass Spectrometry, 31:1057-1066.

Muñoz-Quijano, I.N. & Gutiérrez-Alonso, G. (2007) *Modelo de evolución topográfica en el NO de la Península Ibérica durante la delaminación litosférica al final de la Orogenia Varisca*. Geogaceta, 43:43-46.

Muñoz-Quijano, I.N. (2015) *Hydrothermal dolomitization of Paleozoic successions in Northern Spain : petrophysical properties and structural control*. Unpublished PhD thesis, University of Heidelberg, 130 p.

Munz, I.A. (2001) *Petroleum inclusions in sedimentary basins: systematics, analytical methods and applications*. Lithos, 55:195-212.

N

Nader, F.H., López-Horgue, M.A., Shah, M.M., Dewit, J., Garcia, D., Swennen, R., Iriarte, E., Muchez, Ph. & Caline, B. (2012) *The Ranero Hydrothermal Dolomites (Albian, Karrantza Valley, Northwest Spain): Implications on Conceptual Dolomite Models*. Oil & Gas Science and Technology – Rev. IFP Energies nouvelles, 67(1):9-29.

Nielsen, P., Swennen, R., Muchez, Ph. & Keppens, E. (1998) *Origin of Dinantian zebra dolomites south of the Brabant-Wales Massif, Belgium*. Sedimentology, 45:727-743.

P

Paniagua, A., Fontboté, L., Fenoll Hach-Alí, P., Fallick, AE., Moreiras, D.B. & Corretgé, L.G. (1993) *Tectonic setting, mineralogical characteristics, geochemical signatures and age dating of a new type of epithermal carbonate-hosted, precious metal-five element deposits: the Villamanín area (Cantabrian Zone, northern Spain)*. In: Fennoll Hach-Alí, P., Torres-Ruiz, J. & Gervilla, F. (eds.) *Current research in geology applied to ore deposits*. Proceedings of the 2nd SGA Biennial Meeting, Granada, Spain, 531-534.

Paniagua, A., Rodríguez-Pevida, L.S., Loredo, J., Fontboté, L. & Fenoll Hach-Ali, P. (1996) *Un yacimiento de Au en carbonatos del Orógeno Hercínico: el área de Salamón (N León)*. Geogaceta, 20(7):1605-1608.

Passey, B.H. & Henkes, G.A. (2012) *Carbonate clumped isotope bond reordering and geospeedometry*. Earth and Planetary Science Letters, 351-352**:**223-236.

Pauwels, J. (2016) *Studying the internal variation (textures, geochemistry and reservoir characteristics) of fracture-related hydrothermal dolostones (Cantabrian Zone, N. Spain).* Unpublished master thesis, KU Leuven, 115 p.

Pearce, C.R., Saldi, G.D., Schott, J. & Oelkers, E.H. (2012) *Isotopic fractionation during congruent dissolution, precipitation and at equilibrium: Evidence from Mg isotopes*. Geochimica et Cosmochimica Acta, 92:170-183.

Pérez-Estaún, A., Bastida, F., Alonso, J.L., Marquinez, J., Aller, J., Alvarez-Marrón, J., Marcos, A. & Pulgar, J.A. (1988) *A thin-skinned tectonics model for an arcuate fold and thrust belt: the Cantabrian Zone (Variscan Ibero-Armorican Arc)*. Tectonics, 7(3):517-537.

Pogge von Strandmann, P.A.E., Forshaw, J. & Schmidt, D.N. (2014) *Modern and Cenozoic records of magnesium behaviour from foraminiferal Mg isotopes*. Biogeosciences Discuss., 11:7451-7484.

Potent, S. & Reuther, C.D. (2000) *Kinematik der Faltungs- und Überschiebungsprozesse der variszisch angelegten Montuerto-Struktur im südlichen Kantabrischen Gebirge, Nord-Spanien*. Mitt. Geol.-Paläont. Inst. Univ. Hamburg, 84:83-110.

Price, P.B. & Walker, R.M. (1963) *Fossil tracks of charged particles in mica and the age of minerals*. Journal of Geophysical Research, 68(16):4847-4862.

Pulgar, J.A., Alonso, J.L., Espina, R.G. & Marín, J.A. (1999) *La deformación alpina en al basamento varisco de la Zona Cantábrica*. Trabajos de Geología Universidad de Oviedo, 21:283-294.

Purser, B.H., Brown, A. & Aissaoui, D.M. (1994) *Nature, origins and evolution of porosity in dolomites*. Special Publication of the International Association of Sedimentologists, 21:283-308.

Q

Quijada, E., Díaz-García, I, Merino-Tomé, O., Bahamonde, J.R., Fernández, L.P., Della Porta, G., Samankassou, E., Ortí, F., Javier, F.-L., Gutiérrez-Alonso, G., Valenzuela, M. & Martín-LLaneza, J. (2017) *Evaporite deposits and intraclastic breccias in the remnant of the Rheic Ocean during the Mid-Carboniferous boundary (Barcaliente Fm., Cantabrian Zone, NW Spain)*. International Meeting of Sedimentology, conference abstracts, 735.

R

Radke, B.M. & Mathis, R.L. (1980) On *the formation and occurrence of saddle dolomite*. Journal of Sedimentary Petrology, 50(4):1149-1168.

Raven, J.G.M. (1983) *Conodont biostratigraphy and depositional history of the Middle Devonian to Lower Carboniferous in the Cantabrian Zone (Cantabrian Mountains, Spain)*. Leidse Geologische Mededelingen, 52:265-339.

Raven, J.G.M. & van der Pluijm, B.A. (1986) *Metamorphic fluids and transtension in the Cantabrian Mountains of northern Spain: an application of the conodont color alteration index*. Geological Magazine, 123:673-681.

Rejebian, V.A., Harris, A.G. & Huebner, J.S. (1987) *Conodont color and textural alteration: An index to regional metamorphism, contact metamorphism, and hydrothermal alteration*. GSA Bulletin, 99:471-479.

Robb, L. (2005) *Introduction to Ore-Forming Processes*. Blackwell, Oxford, 373 p.

Robertson, E.C. (1955) *Experimental study of the strength of rocks*. Geological Society of America Bulletin, 66:1275-1314.

Roduit, N. (2007) *JMicroVision: un logiciel d'analyse d'images pétrographiques polyvalent*. Unpublished PhD thesis, Université de Genève, 116 p.

Roedder, E. & Bodnar, R.J. (1980) *Geological pressure determinations from fluid inclusion studies*. Annual Review of Earth and Planetary Sciences, 8:263-301.

Ronchi, P., Masetti, D., Tassan, S. & Camocino, D. (2012) *Hydrothermal dolomitization in platform and basin carbonate successions during thrusting: A hydrocarbon reservoir analogue (Mesozoic of Venetian Southern Alps, Italy)*. Marine and Petroleum Geology, 29:68-89.

S

Samankassou, E. (2001) *Internal structure and depositional environment of Late Carboniferous mounds from the San Emiliano Formation, Cármenes Syncline, Cantabrian Mountains, Northern Spain*. Sedimentary Geology, 145:235-252.

Samankassou, E., Von Allmen, K. & Bahamonde, J.R. (2013) *Growth dynamics of Pennsylvanian carbonate mounds from a mixed terrigenous-carbonate ramp in the Puebla de Lillo area, Cantabrian Mountains, Northern Spain*. Journal of Sedimentary Research, 83:1099-1112.

Sanchez de Posada, L.C., Martinez Chacon, M.L., Mendez Fernandez, C., Menendez Alvarez, J.R., Truyols, J. & Villa, E. (1990) *Carboniferous Pre-Stephanian Rocks of the Asturian-Leonese Domain (Cantabrian Zone)*. In: Dallmeyer, R.D. & Martínez-García, E. (eds.) *Pre-Mesozoic geology of Iberia*. Springer-Verlag, Berlin, 24-33.

de Saussure, N.T. (1792) *Analyse de la dolomie*. Journal de Physique, 40:161-172.

Schito, A., Corrado, S., Aldega, L. & Grigo, D. (2016) *Overcoming pitfalls of vitrinite reflectance measurements in the assessment of thermal maturity: the case history of the lower Congo basin*. Marine and Petroleum Geology, 74:59-70.

Schlumberger (2017) *Carbonate Reservoirs*. http://www.slb.com/services/technical_challenges/carbonates.aspx

Schmoker, J.W. & Halley, R.B. (1982) *Carbonate porosity versus depth: a predictable relation for South Florida*. AAPG Bulletin, 66:2561-2570.

Schneider, J., Bakker, R.J., Bechstädt, T. & Littke, R. (2008) *Fluid evolution during burial diagenesis and subsequent orogenic uplift: the La Vid Group (Cantabrian Zone, Northern Spain)*. Journal of Sedimentary Research, 78:282-300.

Schoeller, W.R. & Powell, A.R. (1920) *Villamaninite, a new mineral*. Mineralogical Magazine, 19-14-18.

Scholle, P.A. & Ulmer-Scholle, D.S. (2003) *A Color Guide to the Petrography of Carbonate Rocks: Grains, textures, porosity, diagenesis*. AAPG Memoir 77, AAPG, Tulsa, U.S.A., 459 p.

Schroyen, K. & Muchez, Ph. (2000) *Evolution of metamorphic fluids at the Variscan fold-and-thrust belt in eastern Belgium*. Sedimentary Geology, 131:163-180.

Searl, A. (1989) *Saddle dolomite: a new view of its nature and origin*. Mineralogical Magazine, 53:547-555.

Seibert, L. (1986) *Fazies und Paläogeographie des Unter-Karbon (Alba Formation) im Kantabrischen Gebirge (Nordspanien)*. Unpublished PhD thesis, University of Tübingen, 208 p.

Shah, M.M., Nader, F.H., Dewit, J., Swennen, R. & Garcia, D. (2010) *Fault-related hydrothermal dolomites in Cretaceous carbonates (Cantabria, northern Spain): Results of petrographic, geochemical and petrophysical studies*. Bulletin de la Société Géologique de France, 181(4):391-407.

Sharp, I., Gillespie, P., Morsalnezhad, D., Taberner, C., Karpuz, R., Vergés, J., Horbury, A., Pickard, N., Garland, J. & Hunt, D. (2010) *Stratigraphic architecture and fracture-controlled dolomitization of the Cretaceous Khami and Bangestan groups: an outcrop case study, Zagros Mountains, Iran*. Geological Society, London, Special Publications, 329:343-396.

Shrock, R.R. (1948) *A classification of sedimentary rocks*. Journal of Geology, 56:118-129.

Smith, L.B. (2006) *Origin and reservoir characteristics of Upper Ordovician Trenton-Black River hydrothermal dolomite reservoirs in New York*. AAPG Bulletin, 90:1691-1718.

Stearns, N.D., Stearns, H.T. & Waring, G.A. (1935) *Thermal springs in the United States*. Contributions to the hydrology of the United States, Water Supply Paper 679-B:59-191.

Stolper, D.A. & Eiler, J.M. (2015) *The kinetics of solid-state isotope-exchange reactions for clumped isotopes; a study of inorganic calcites and apatites from natural and experimental samples*. American Journal of Science, 315(5):363-411.

Suárez Rodríguez, A., Heredia, N., López Díaz, F., Toyos, J.M., Rodríguez Fernández, L.R. & Gutiérrez, G. (1991) *Hoja del Mapa Geológico Nacional de España (1:50000), Memoria 102 (Los Barrios de Luna)*. IGME, Madrid.

Suchý, V., Rozkosny, I., Zák, K. & Francu, J. (1996) *Epigenetic dolomitization of the Prídolí Formation (Upper Silurian), the Barrandian basin, Czech Republic: implications for burial history of Lower Paleozoic strata*. Geologische Rundschau, 85:264–277.

Suggate, R.P. (1959) *New Zealand coals, their geological setting and its influence on their properties*. In: Owen, R.E. (ed.) New Zealand Department of Scientific and Industrial Research Bulletin, 13:1-112.

Sun, Q. (1995) *Dolomite reservoirs: Porosity evolution and reservoir characteristics*. AAPG Bulletin, 79:186-204.

Swart, P.K., Cantrell, D.L., Arienzo, M.M. & Murray, S.T. (2016) *Evidence for high temperature and 18O-enriched fluids in the Arab-D of the Ghawar Field, Saudi Arabia*. Sedimentology, 63:1739-1752.

Swennen, R., Dewit, J., Fierens, E., Muchez, Ph., Shah, M., Nader, F. & Hunt, D. (2012) *Multiple dolomitization events along the Pozalagua Fault (Pozalagua Quarry, Basque-Cantabrian Basin, Northern Spain)*. Sedimentology, 59(4):1345-1374.

Symons, D.T.A., Tornos, F., Kawasaki, K., Velasco, F. & Rosales, I. (2015) *Genetic constraints from paleomagnetic dating for the Aliva zinc-lead deposit, Picos de Europa Unit, northern Spain*. Mineralium Deposita, 50(8):953-966.

T

Teichmüller, M. (1982) *Application of coal petrological methods in geology including oil and natural gas prospecting*. In: Stach, E., Mackowsky, M.T., Teichmüller, M., Taylor, G.H., Chandra, D. & Teichmüller, R. (eds.) *Stach's textbook of coal petrology*. Gebrüder Borntraeger, Berlin, 381-413.

Teichmüller, M. (1987) *Organic material and very low grade metamorphism*. In: Frey, M. (ed.) *Low-temperature Metamorphism*. Chapman and Hall, Glasgow, 114-161.

Tipper, E.T., Gaiullardet, J., Louvat, P., Campas, F. & White, A.F. (2010) *Mg isotope constraints on soil pore-fluid chemistry: evidence from Santa Cruz, California*. Geochimica et Cosmochimica Acta, 47:3883-3896.

Tissot, B.P. & Welte, D.H. (1978) *Petroleum Formation and Occurrence. A new approach to oil and gas exploration*. Springer-Verlag, Berlin, 538 p.

U

Urey, H.C. (1947) *Thermodynamic properties of isotopic substances*. Journal of the Chemical Society, 562-581.

V

Vandeginste, V., Swennen, R., Gleeson, S.A., Ellam, R.M., Osadetz, K. & Roure, F. (2005) *Zebra dolomitization as a result of focused fluid flow in the Rocky Mountains Fold and Thrust Belt, Canada*. Sedimentology, 52:1067-1095.

Vandeginste, V., John, C.M., Cosgrove, J.W. & Manning, C. (2014) *Dimensions, texture-distribution, and geochemical heterogeneities of fracture-related dolomite geobodies hosted in Ediacaran limestones, northern Oman*. AAPG Bulletin, 98(9):1789-1809.

van Ginkel, A.C. (1965) *Carboniferous fusulinids from the Cantabrian Mountains (Spain)*. Leidse Geologische Mededelingen, 34:1-255.

Vasconcelos, C. & McKenzie, J.A. (1997*) Microbial mediation of modern dolomite precipitation and diagenesis under anoxic conditions (Lagoa Vermalha, Rio de Janeiro, Brazil)*. Journal of Sedimentary Research, 67:378-390.

Voldman, G.G., Albanesi, G.L. & Do Campo, M. (2008) *Conodont palaeothermometry of contact metamorphism in Middle Ordovician rocks from the Precordillera of western Argentina*. Geological Magazine, 145:449-462.

W

Wagner, R.H., Winkler Prins, C.F. & Riding, R.E. (1971) *Lithostratigraphic units of the lower part of the Carboniferous in Northern León, Spain*. Trabajos de Geología Universidad de Oviedo, 4:603-663.

Wagner, R.H. & Bowman, M.B.J. (1983) *The position of the Bashkirian/Moscovian boundary in West European chronostratigraphy*. Newsletters on Stratigraphy, 12:132-161.

Wagner, G.A. & van den Haute, P. (1992) *Fission-Track Dating*. Enke, Stuttgart, 238 p.

Walter, B.F., Immenhauser, A., Geske, A. & Markl, G. (2015) *Exploration for hydrothermal carbonate magnesium isotope signatures as tracers for continental fluid aquifers, Schwarzwald mining district, SW Germany*. Chemical Geology, 400:87-105.

Warren, J. (2000) *Dolomite: occurrence, evolution and economically important associations*. Earth-Science Reviews, 52:1-81.

Weh, A., Krumm, S., Clauer, N. & Keller, M. (2001) *The late orogenic history of the southeastern Cantabrian Mountains: illite-crystalllinity and K-Ar data*. EUGX1 abstract.

Weil, A.B., Gutiérrez-Alonso, G., Johnston, S.T. & Pastor-Galán, D. (2013) *Kinematic constraints on buckling a lithospheric-scale orocline along the northern margin of Gondwana: A geologic synthesis*. Tectonophysics, 582:25-49.

White, D.E. (1957) *Thermal waters of volcanic origin*. Geological Society of America Bulletin, 68:1637-1658.

Williams, D.M. & McNamara, K. (1992) *Limestone to dolomite to dedolomite conversion and its effect on rock strength: a case study*. Quaterly Journal of Engineering Geology and Hydrogeology, 25:131-135.

Wilson, M.E.J., Evans, M.J., Oxtoby, N.H., Satria Nas, D., Donnelly, T. & Thirlwall, M. (2007) *Reservoir quality, textural evolution, and origin of fault-associated dolomites*. AAPG Bulletin, 91(9):1247-1272.

Winkler Prins, C.F. (1968) *Carboniferous Productidina and Chonetidina of the Cantabrian Mountains (NW Spain): Systematics, Stratigraphy and Palaeoecology.* Leidse Geologische Mededelingen, 43:41-126.

Wombacher, F., Eisenhauer, A., Boehm, F., Gussone, N., Regenberg, M., Dullo, W.C. & Rueggeberg, A. (2011) *Magnesium stable isotope fractionation in marine biogenic calcite and aragonite*. Geochimica et Cosmochimica Acta, 75:5797-5818.

Wood, R. (1999) *Reef Evolution*. Oxford University Press, Oxford, 426 p.

Wright, W.R., Somerville, I.D., J.M., G. & Shelton, K.L. (1999) *Dolomite CL and $\delta^{18}O$ $\delta^{13}C$ data from Irish Midlands and Dublin Basin, Carboniferous*. In: Stanley et al. (eds.), *Mineral Deposits: Processes to Processing*, 913-916.

Y

Young, E.D. & Galy, A. (2004) *The Isotope Geochemistry and Cosmochemistry of Magnesium*. Reviews in Mineralogy & Geochemistry, 55:197-230.

Z

Zamarreño, I. (1972) *Las lithofacies carbonatadas del Cámbrico de la Zona Cantábrica (NW España) y su distributión paleogeográfica*. Trabajos de Geología Universidad de Oviedo, 5:3-118.

Zenger, D.H., Dunham, J.B. & Ethington, R.L. (1980) *Concepts and models of dolomitization*. SEPM Special Publication 28, 320 p.

Zhang, S. & Barnes, C.R. (2007) *Late Ordovician-Early Silurian conodont biostratigraphy and thermal maturity, Hudson Bay Basin*. Bulletin of Canadian Petroleum Geology, 55:179-216.

Zhang, Y.G. & Frantz, J.D. (1987) *Determination of the homogenization temperatures and densities of supercritical fluids in the system NaCl-KCl-$CaCl_2$-H_2O using synthetic fluid inclusions*. Chemical Geology, 64:335-350.

Appendix I Logs key outcrop 1

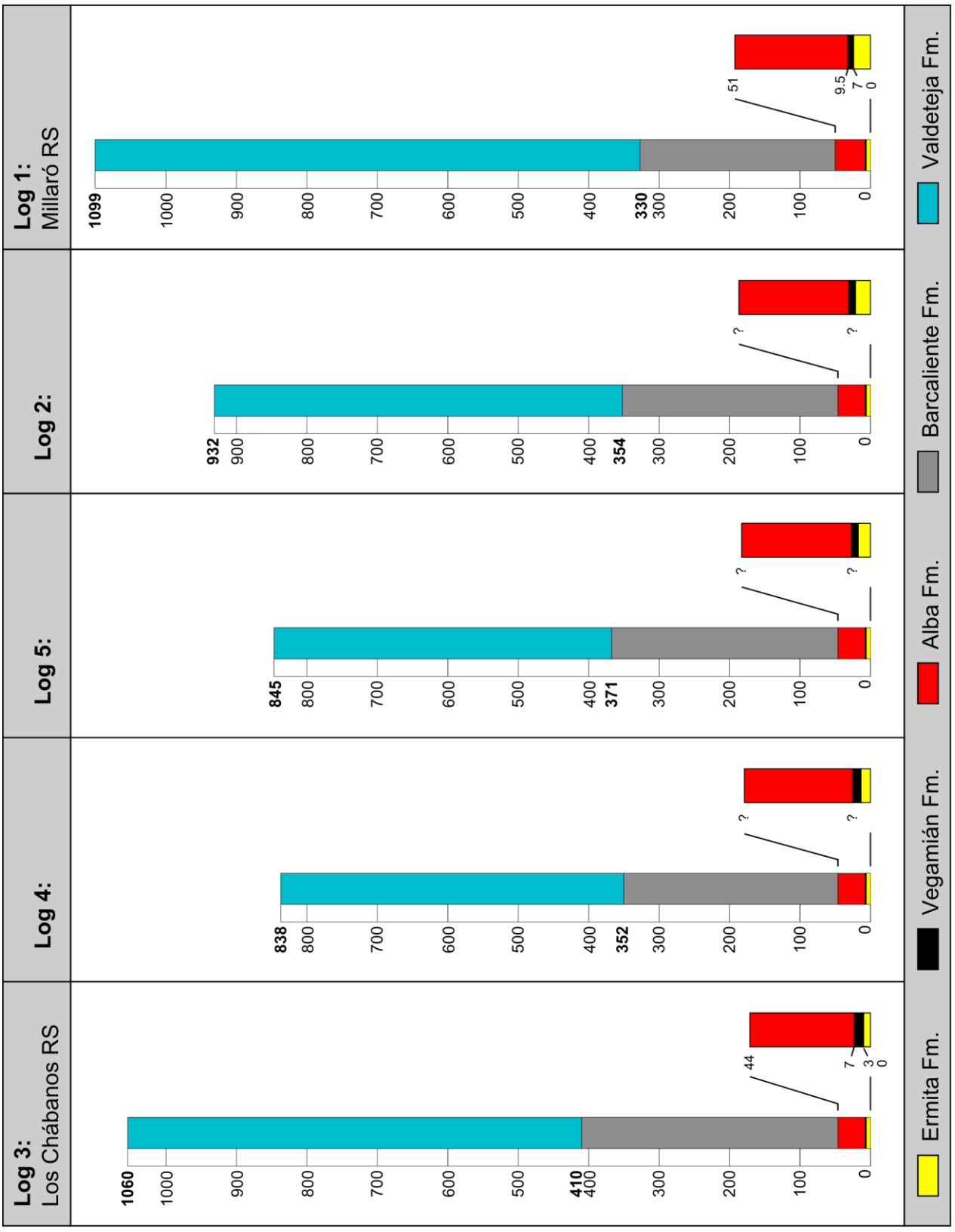

Appendix I: Logs (in m) for the 5 stratigraphic sections in key outcrop 1. The locations of the stratigraphic sections have been indicated on figures 3.1 and 3.3.

Appendix II Easytrace histograms

Easytrace histograms illustrating the relationships between dolomitization and fracture abundance (A), the stratigraphic formation and dolomitization (B), dolomite textures and the Barcaliente Fm. (C), gray- and beige-colored dolomite in the Barcaliente Fm. (D) and pore size distribution and precursor depositional facies (E). All data are based on the 5 logged sections in KO 1.

A

Easytrace histogram illustrating the fracture abundance in limestone and dolomite rocks along the logged sections. Fracture abundance has been visually assessed during logging and has been assigned to 3 classes: low, medium and high fracture abundance. A high fracture abundance (in blue) is more important in dolomitized sections of the logs.

Low fracture abundance
Medium fracture abundance
High fracture abundance

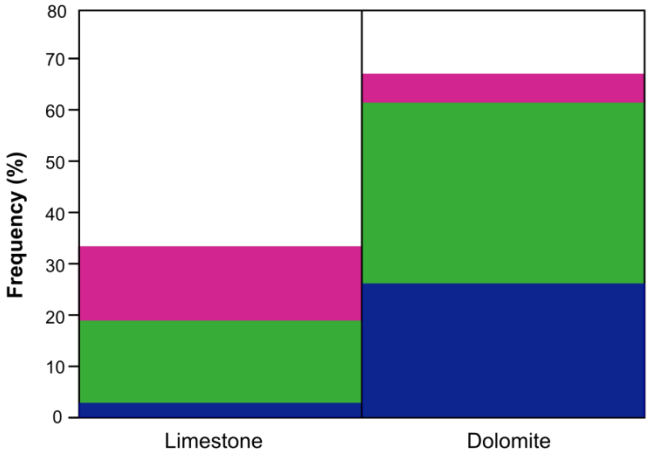

B

Easytrace histogram illustrating the occurrence of dolomite (in red) in both the Barcaliente and Valdeteja Fm. Of the logged sections, 33 % corresponds to the Barcaliente Fm. while 67 % corresponds to the Valdeteja Fm. 75 % of the Barcaliente Fm. has been dolomitized, while 62 % of the Valdeteja Fm. has been dolomitized.

Undolomitized precursor limestone
Dolomite

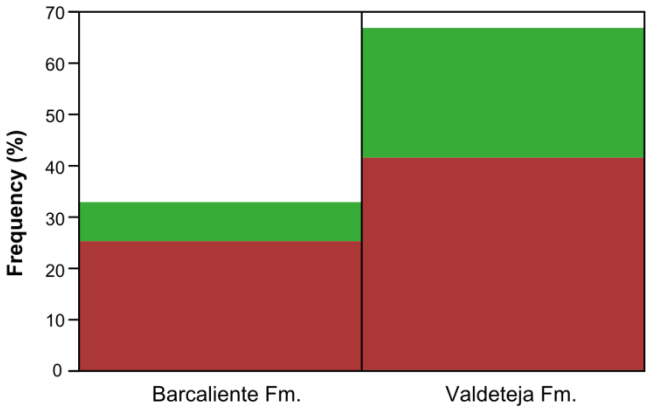

C

Easytrace histogram illustrating the abundance of different dolomite textures in the Barcaliente Fm. Approximately 45 % of the dolomite rocks in the Barcaliente Fm. display zebra textures (in blue).

Undolomitized precursor limestone
Breccia texture
Replacive dolomite with zebra textures
Replacive dolomite

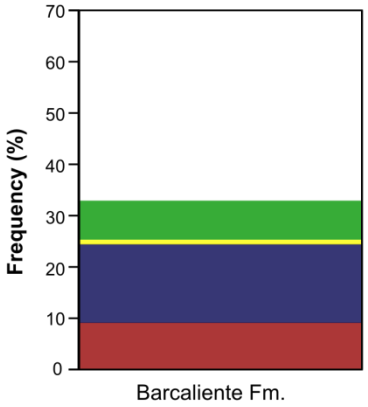

D

Easytrace histogram illustrating the abundance of beige-colored dolomite (in beige) compared to the total abundance of the Barcaliente Fm. along the logged sections. Approximately 33 % of the Barcaliente Fm. is dolomitized and has a typical beige color.

- Undolomitized precursor limestone
- Gray-colored dolomite
- Beige-colored dolomite

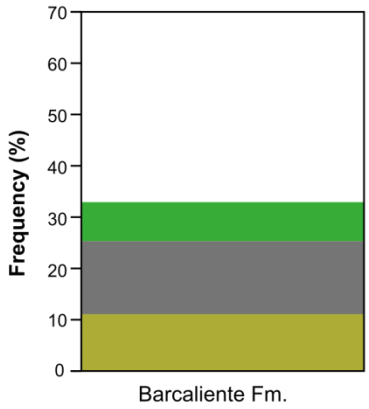

E

Easytrace histogram illustrating the pore size distribution in dolomite rocks of both the Barcaliente and Valdeteja Fm. logged in KO 1. Pore size has been visually assessed during logging and has been assigned to 3 classes: small (< 1 mm), medium (1-10 mm) and large (> 10 mm). A large pore size is more abundant in dolomitized boundstones.

- Large pores
- Medium pores
- Small pores

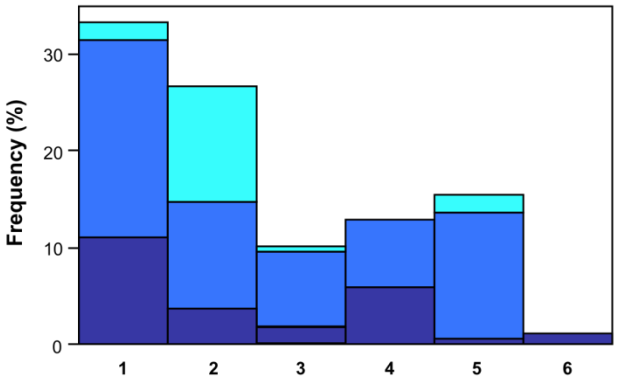

1. Muddy texture (Barcaliente & Valdeteja Fm.)
2. Boundstones (Valdeteja Fm.)
3. Grainy textures (Valdeteja Fm.)
4. Calciturbidites (Valdeteja Fm.)
5. Synsedimentary breccia (Valdeteja Fm.)
6. Other (e.g. karstification)

Appendix III Petrophysical data

He Ø: Helium porosity – **WS Ø**: Water saturation porosity – **E.K.κ**: Empirical Klinkenberg permeability – **mCT Ø**: porosity obtained from medical CT scanning – **µCT Ø** : porosity obtained from microfocus CT scanning.

PART I. Key outcrop 1

Sample	*Type*	*Location*	*Formation*	*Plug*	*He Ø (%)*	*W.S. Ø (%)*	*E.K.κ (mD)*	*mCT Ø (%)*	*µCT Ø (%)*	*Remark*
SL14RH123	Core	42°58'29.21"N 5°39'00.89"W	Valdeteja		-	-	-	0.9	-	Hydrothermal breccia
SL14RH124	Core + plug	42°58'27.05"N 5°39'01.86"W	Valdeteja	a	2.4	2.9	0.01	1.8	-	
				b	-	3.0	-	1.8	-	
SL14RH125	Core	42°58'21.64"N 5°39'10.31"W	Valdeteja		-	-	-	6.6	-	
SL14RH127	Core + plug	42°58'20.39"N 5°39'14.91"W	Valdeteja	a	-	7.3	-	0.5	-	Hydrothermal breccia
SL16RH003	Plug	42°58'39.16"N 5°38'50.31"W	Alba	a	-	1.1	-	-	-	
SL16RH005	Plug	42°58'38.81"N 5°38'51.07"W	Alba	a	-	0.7	-	-	-	
SL16RH008	Plug	42°58'36.03"N 5°38'52.47"W	Barcaliente	a	2.1	2.4	0.02	-	-	
SL16RH010	Plug	42°58'33.52"N 5°38'55.41"W	Barcaliente	a	-	10.4	-	-	-	
SL16RH011	Plug	42°58'32.29"N 5°39'01.69"W	Barcaliente	a	4.4	5.3	0.51	-	-	
SL16RH012	Plug	42°58'26.93"N 5°39'01.98"W	Valdeteja	a	-	7.2	-	-	-	
SL16RH013	Plug	42°58'24.94"N 5°39'03.61"W	Valdeteja	a	3.3	3.7	0.01	-	-	
				b	-	6.5	-	-	-	
SL16RH014	Plug	42°58'25.82"N 5°39'02.76"W	Valdeteja	a	-	3.0	-	-	-	
SL16RH015	Plug	42°58'22.95"N 5°39'07.89"W	Valdeteja	a	5.9	5.7	0.02	-	4.4	
SL16RH016	Plug	42°58'21.43"N 5°39'11.54"W	Valdeteja	a	6.9	6.7	0.02	-	-	
SL16RH017	Plug	42°58'19.20"N 5°39'16.49"W	Valdeteja	a	-	1.8	-	-	-	
				b	-	3.6	-	-	-	
SL16RH018	Plug	42°58'18.54"N 5°39'17.32"W	Valdeteja	a	5.6	5.8	0.02	-	-	
SL16RH020	Plug	42°58'15.87"N 5°39'23.34"W	Valdeteja	a	4.1	2.4	0.01	-	-	
SL16RH021	Plug	42°58'14.71"N 5°39'27.81"W	Valdeteja	a	6.3	5.5	0.42	-	4.5	
SL16RH022	Plug	42°58'43.31"N 5°39'16.20"W	Barcaliente	a	-	4.2	-	-	-	

SL16RH023	Plug	42°58'41.45"N 5°39'15.92"W	Barcaliente	a	-	4.0	-	-	-	
SL16RH024	Plug	42°58'39.47"N 5°39'18.24"W	Barcaliente	a	-	4.3	-	-	-	
SL16RH026	Plug	42°58'34.55"N 5°39'20.92"W	Valdeteja	a	-	4.5	-	-	-	
SL16RH027	Plug	42°58'32.79"N 5°39'23.62"W	Valdeteja	a	-	7.7	-	-	-	
				b	-	6.7	-	-	-	
SL16RH028	Plug	42°58'29.45"N 5°39'25.71"W	Valdeteja	a	-	4.5	-	-	2.7	
SL16RH030	Plug	42°58'26.78"N 5°39'24.24"W	Valdeteja	a	-	5.9	-	-	-	
				b	-	4.0	-	-	-	
SL16RH031	Plug	42°58'26.01"N 5°39'26.28"W	Valdeteja	a	-	4.1	-	-	-	
				b	-	4.2	-	-	-	
SL16RH032	Plug	42°58'24.59"N 5°39'27.04"W	Valdeteja	a	-	1.8	-	-	-	
SL16RH033	Plug	42°58'24.22"N 5°39'27.37"W	Valdeteja	a	-	2.7	-	-	-	
SL16RH035	Plug	42°58'21.53"N 5°39'28.56"W	Valdeteja	a	-	2.0	-	-	-	
SL16RH036	Plug	42°58'20.68"N 5°39'29.31"W	Valdeteja	a	-	2.8	-	-	-	
				b	-	3.1	-	-	4.0	
SL16RH040	Plug	42°58'42.84"N 5°40'43.53"W	Barcaliente	a	-	1.1	-	-	-	
				b	-	1.1	-	-	-	
SL16RH041	Plug	42°58'42.47"N 5°40'43.60"W	Barcaliente	a	-	3.4	-	-	-	
SL16RH042	Plug	42°58'42.68"N 5°40'43.57"W	Barcaliente	a	-	1.1	-	-	-	
SL16RH043	Plug	42°58'39.06"N 5°40'52.50"W	Barcaliente	a	-	2.3	-	-	-	
SL16RH044	Plug	42°58'38.66"N 5°40'52.34"W	Barcaliente	a	-	4.8	-	-	-	
SL16RH045	Plug	42°58'37.49"N 5°40'52.60"W	Barcaliente	a	4.6	3.9	0.09	-	2.9	
				b	-	5.7	-	-	-	
SL16RH046	Plug	42°58'37.21"N 5°40'52.05"W	Barcaliente	a	-	5.5	-	-	-	
SL16RH047	Plug	42°58'36.76"N 5°40'51.13"W	Barcaliente	a	-	2.7	-	-	-	
SL16RH048	Plug	42°58'35.95"N 5°40'50.60"W	Barcaliente	a	-	3.5	-	-	-	
				b	-	5.8	-	-	-	
				c	-	7.0	-	-	-	
SL16RH049	Plug	42°58'35.01"N 5°40'52.13"W	Barcaliente	a	-	2.8	-	-	-	

SL16RH050	Plug	42°58'35.01"N 5°40'51.57"W	Barcaliente	a	-	3.7	-	-	-	
SL16RH051	Plug	42°58'34.93"N 5°40'50.69"W	Barcaliente	a	-	4.0	-	-	-	
				b	1.9	2.6	0.01	-	1.2	
SL16RH052	Plug	42°58'34.72"N 5°40'49.94"W	Barcaliente	a	-	2.2	-	-	-	
SL16RH054	Plug	42°58'34.23"N 5°40'47.45"W	Barcaliente	a	-	2.2	-	-	-	
				b	0.2	1.3	-	-	-	
				c	1.4	1.5	0.02	-	-	
				d	-	2.5	-	-	-	
SL16RH055	Plug	42°58'33.19"N 5°40'44.55"W	Barcaliente	a	-	1.7	-	-	-	
SL16RH056	Plug	42°58'31.85"N 5°40'42.62"W	Valdeteja	a	3.7	2.7	0.01	-	-	
SL16RH057	Plug	42°58'29.88"N 5°40'39.61"W	Valdeteja	a	4.8	4.6	0.02	-	-	
				b	-	4.7	-	-	-	
SL16RH058	Plug	42°58'28.47"N 5°40'37.83"W	Valdeteja	a	4.6	4.6	0.13	-	-	
SL16RH059	Plug	42°58'27.69"N 5°40'36.49"W	Valdeteja	a	-	3.7	-	-	-	
SL16RH060	Plug	42°58'26.97"N 5°40'32.29"W	Valdeteja	a	2	2.3	0.01	-	-	
				b	-	3.6	-	-	-	
SL16RH061	Plug	42°58'26.89"N 5°40'31.25"W	Valdeteja	a	-	1.6	-	-	-	
SL16RH063	Plug	42°58'26.09"N 5°40'29.99"W	Valdeteja	a	6.9	7.2	0.18	-	2.0	
				b	-	4.6	-	-	-	
SL16RH065	Plug	42°58'25.97"N 5°40'27.09"W	Valdeteja	a	1.9	2.3	0.01	-	-	
				b	-	2.7	-	-	-	
SL16RH067	Plug	42°58'25.02"N 5°40'17.80"W	Valdeteja	a	-	2.7	-	-	-	
				b	-	8.3	-	-	-	
SL16RH068	Plug	42°58'22.18"N 5°40'14.15"W	Valdeteja	a	-	2.8	-	-	-	
SL16RH069	Plug	42°58'46.70"N 5°40'01.66"W	Barcaliente	a	-	3.9	-	-	-	
SL16RH070	Plug	42°58'40.70"N 5°40'01.71"W	Valdeteja	a	-	2.8	-	-	-	
SL16RH071	Plug	42°58'40.15"N 5°40'02.72"W	Valdeteja	a	-	3.0	-	-	-	
SL16RH072	Plug	42°58'37.66"N 5°39'59.29"W	Valdeteja	a	-	3.4	-	-	-	
SL16RH073	Plug	42°58'36.70"N 5°39'59.29"W	Valdeteja	a	-	5.3	-	-	-	

				b	-	6.8	-	-	-	
				c	-	5.6	-	-	-	
SL16RH074	Plug	42°58'30.60"N 5°40'00.87"W	Valdeteja	a	-	3.0	-	-	-	
				b	-	2.0	-	-	-	
SL16RH075	Plug	42°58'28.18"N 5°40'01.00"W	Valdeteja	a	-	2.6	-	-	-	
				b	-	2.9	-	-	-	
SL16RH076	Plug	42°58'26.35"N 5°40'00.69"W	Valdeteja	a	-	1.6	-	-	-	
				b	-	1.2		-	-	
SL16RH077	Plug	42°58'41.42"N 5°40'00.27"W	Barcaliente	a	4.2	4.9	0.09	-	-	
				b	-	3.5	-	-	-	
SL16RH078	Plug	42°58'42.43"N 5°40'00.61"W	Barcaliente	a	-	3.0	-	-	-	
				b	-	4.1	-	-	-	
SL16RH079	Plug	42°58'45.95"N 5°40'02.55"W	Barcaliente	a	-	4.4	-	-	-	
SL16RH081	Plug	42°58'45.06"N 5°39'58.05"W	Barcaliente	a	-	5.4	-	-	-	
SL16RH082	Plug	42°58'43.93"N 5°39'39.13"W	Barcaliente	a	-	8.6	-	-	-	
				b	-	9.1	-	-	-	
SL16RH083	Plug	42°58'39.83"N 5°39'42.29"W	Barcaliente	a	-	1.8	-	-	-	
				b	-	2.5	-	-	-	
SL16RH084	Plug	42°58'40.55"N 5°39'41.66"W	Barcaliente	a	-	2.1	-	-	-	
SL16RH093	Plug	42°58'37.39"N 5°39'41.72"W	Valdeteja	a	-	5.5	-	-	-	
				b	-	4.6	-	-	-	
SL16RH095	Plug	42°58'35.31"N 5°39'43.64"W	Valdeteja	a	-	2.6	-	-	-	
				b	-	2.3	-	-	-	
				c	-	3.0	-	-	-	
SL16RH096	Plug	42°58'28.18"N 5°39'45.54"W	Valdeteja	a	-	2.7	-	-	-	
				b	-	1.6	-	-	-	
SL16RH097	Plug	42°58'25.82"N 5°39'45.63"W	Valdeteja	a	-	0.9	-	-	-	
SL16RH100	Plug	42°58'33.15"N 5°39'49.61"W	Valdeteja	a	-	2.3	-	-	-	
				b	-	3.4	-	-	-	

SL16RH101	Plug	42°58'34.00"N 5°40'05.88"W	Valdeteja	a	-	3.5	-	-	-	
				b	-	4.7	-	-	-	

PART II: Key outcrop 2

Sample	*Type*	*Location*	*Formation*	*Plug*	*He por. (%)*	*W.S. Ø (%)*	*E.K.κ (mD)*	*mCT Ø (%)*	*µCT Ø (%)*	*Remark*
SL14RH122	Core	42°53'52.94"N 5°24'00.50"W	Valdeteja		-	-	-	1.5	-	
SL15JP014	Core + 2 plugs	42°53'55.36"N 5°23'52.16"W	Valdeteja	a	0.4	0.9	0.36	< 0.1	-	Limestone
				b	0.2	0.4	0.00	< 0.1	-	Limestone
SL15JP015	Core + 2 plugs	42°53'55.36"N 5°23'51.98"W	Valdeteja	a	1.5	2.3	0.03	0.3	-	
				b	1.6	2.1	0.07	0.3	-	
SL15JP016	Core + 2 plugs	42°53'55.37"N 5°23'51.91"W	Valdeteja	a	1.8	2.2	0.02	0.1	-	
				b	2.8	2.9	0.15	0.1	-	
SL15JP017	Core + 2 plugs	42°53'55.38"N 5°23'51.82"W	Valdeteja	a	1.1	0.7	0.02	< 0.1	-	
				b	1.7	0.9	0.01	< 0.1	-	
SL15JP018	Core + 2 plugs	42°53'55.37"N 5°23'51.66"W	Valdeteja	a	0.5	0.5	0.01	0.8	-	Limestone
				b	0.6	0.5	0.00	0.8	-	Limestone

PART III: Key outcrop 3

Sample	*Type*	*Location*	*Formation*	*Plug*	*He por. (%)*	*W.S. Ø (%)*	*E.K.κ (mD)*	*mCT Ø (%)*	*µCT Ø (%)*	*Remark*
SL15JP034	Core + plug	42°53'09.93"N 5°23'22.89"W	Láncara	a	6.3	5.7	0.02	-	6.6	
SL15JP036	Core + 2 plugs	42°53'08.96"N 5°23'22.66"W	Fault gouge	a	8.7	6.3	0.01	4.7	6.3	
				b	9.5	7.6	0	4.7	-	
SL15JP037	Core + 2 plugs	42°53'08.08"N 5°23'22.63"W	Fault	a	11	9.6	0.07	4.7	6.1	

			gouge							
				b	9.5	8.4	0.09	4.7	5.5	
SL15JP038	Core + 2 plugs	42°53'07.21"N 5°23'23.79"W	Barcaliente	a	3	2.6	3.21	0.1	0.7	
				b	3.6	2.9	0.06	0.1	-	
SL15JP042	Core + plug	42°53'16.36"N 5°22'57.12"W	Fault gouge	a	2.2	2.0	0.02	< 0.1	-	Reactivated breccia
SL15JP043	Core + 2 plugs	42°53'15.67"N 5°22'57.18"W	Fault gouge	a	15.4	15.3	0.21	1.1	15.2	
				b	2.4	2.2	0.01	1.1	-	
SL15JP044	Core + 2 plugs	42°53'15.40"N 5°22'56.83"W	Fault gouge	a	8.6	6.6	0.02	4.5	-	
				b	4.3	3.8	0.08	4.5	1.8	

Appendix IV Comparison porosimetry techniques

This appendix provides a comparison between the different methods used to obtain porosity values for the small plugs (diameter of ± 3.3 cm). The first graph shows boxplots of the porosity values for a selection of 12 plugs on which He porosimetry, water saturation (WS) porosimetry and microfocus CT (µCT) porosimetry have been performed. ANOVA suggests that there is no significant variation between the results of these three techniques ($p > 0.05$). Nevertheless, the graph seems to indicate lower average porosities associated with µCT porosimetry, which is likely caused by the limited resolution of the technique (voxel size 16*16*16 µm). Possible variations between He and WS porosimetry are influenced by the vacuum conditions and pressure attained during measurements.

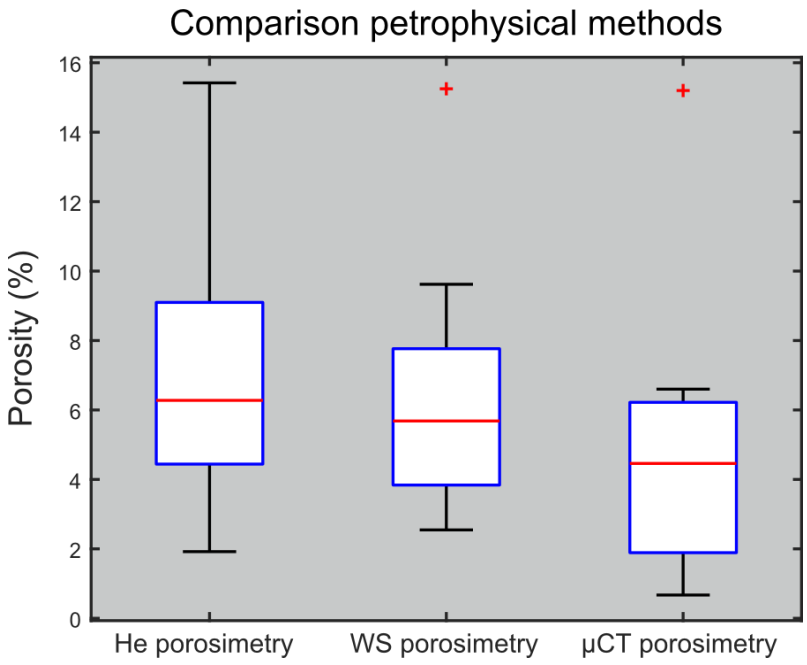

The second graph shows a good correlation between the porosity values obtained for small plugs through both He and WS porosimetry. The correlation between both techniques might be lower for porosity values around and below 2 %, which is attributed to a decrease in precision of WS porosimetry for tight material.

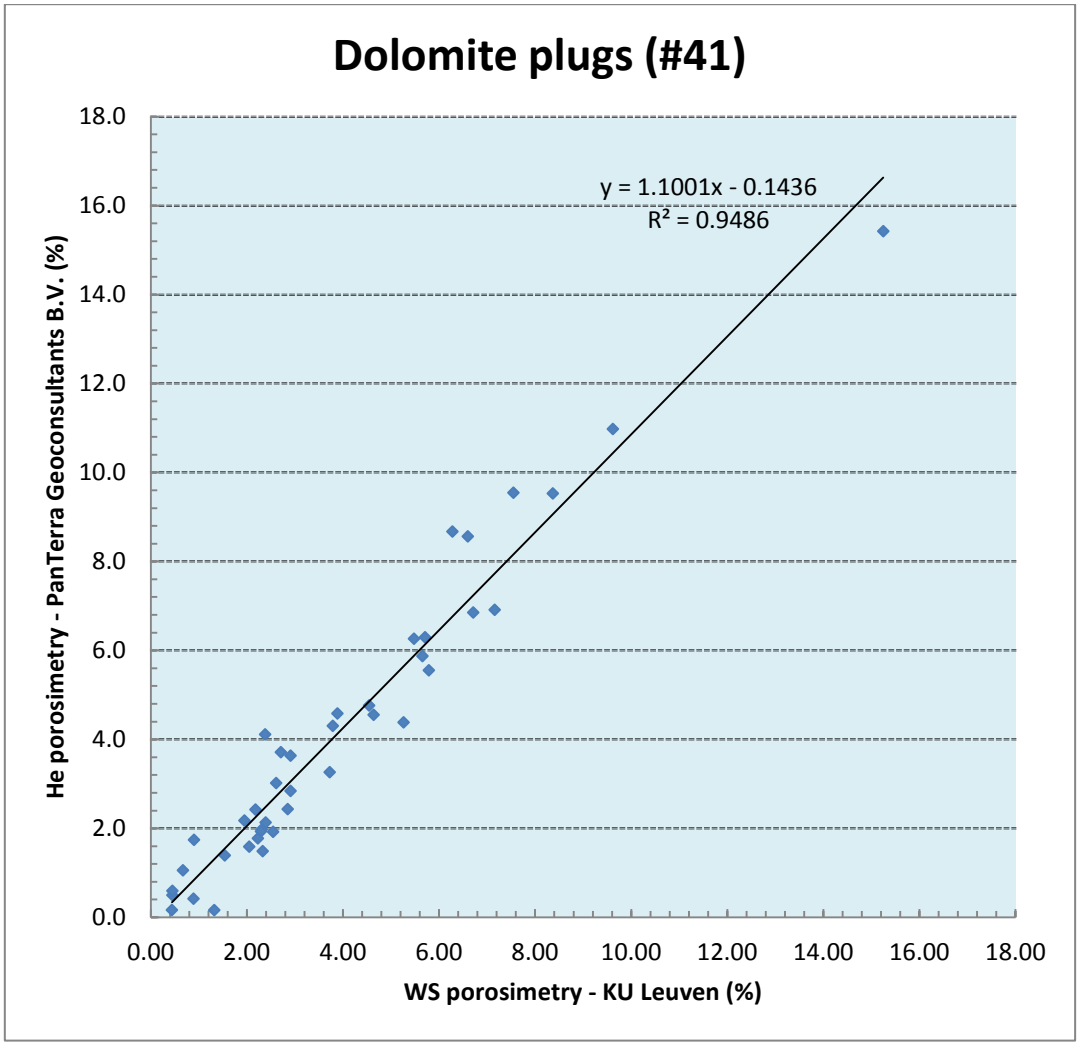

Appendix V Fluid inclusion microthermometry (T_h histograms)

Sample 001:

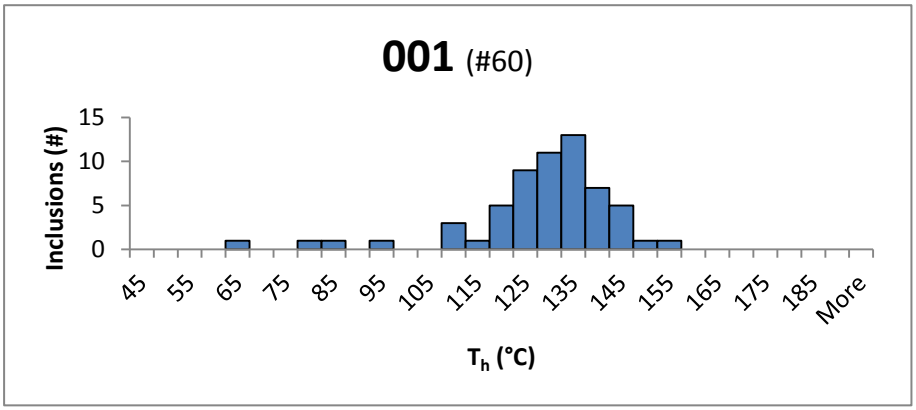

Mode (°C)	133
Range (°C)	65 - 151
Q1 (°C)	122
Q2 (°C)	129
Q3 (°C)	135
Inclusions (#)	60

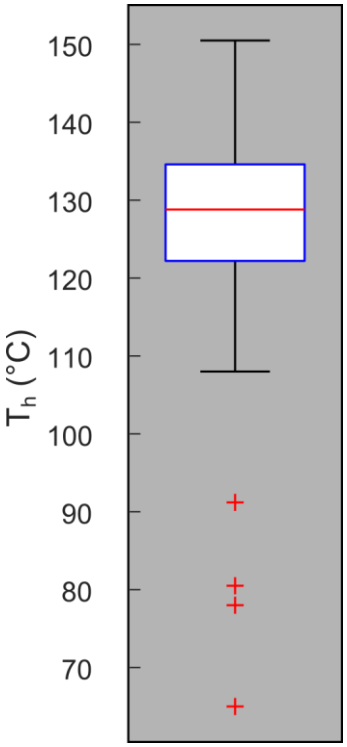

Sample 028:

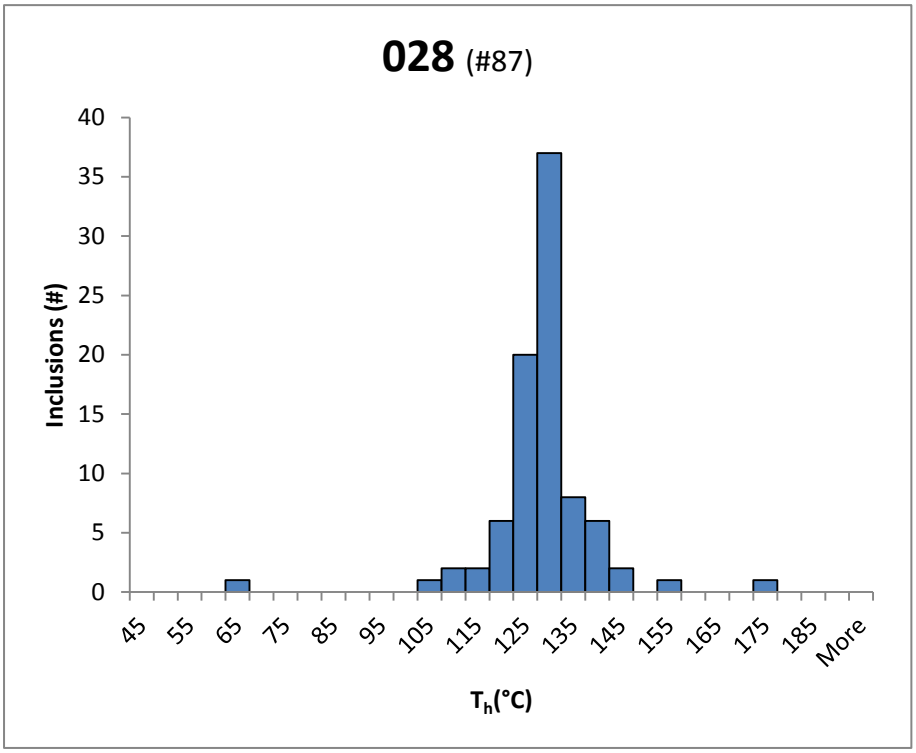

Mode (°C)	128
Range (°C)	65 - 173
Q1 (°C)	124
Q2 (°C)	126
Q3 (°C)	129
Inclusions (#)	87

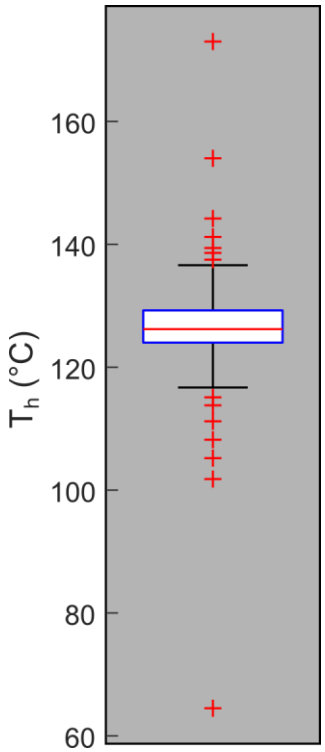

Sample 166:

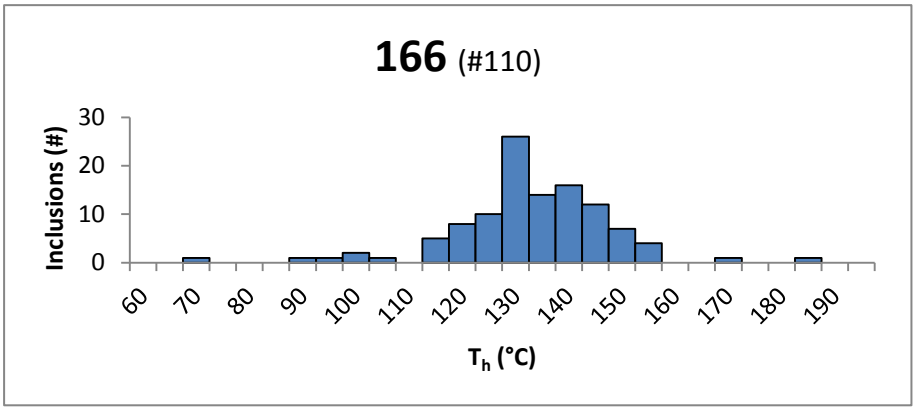

Mode (°C)	130
Range (°C)	67 - 181
Q1 (°C)	125
Q2 (°C)	130
Q3 (°C)	139
Inclusions (#)	110

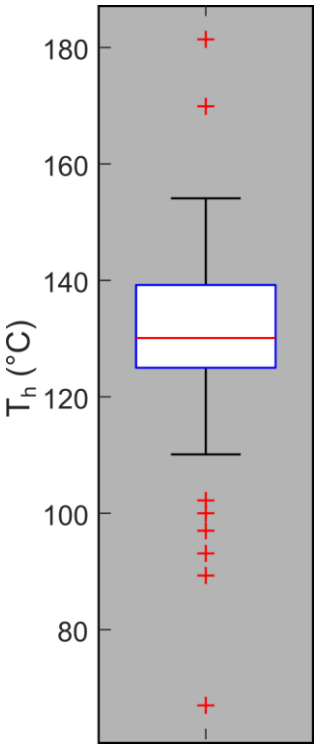

Sample 173:

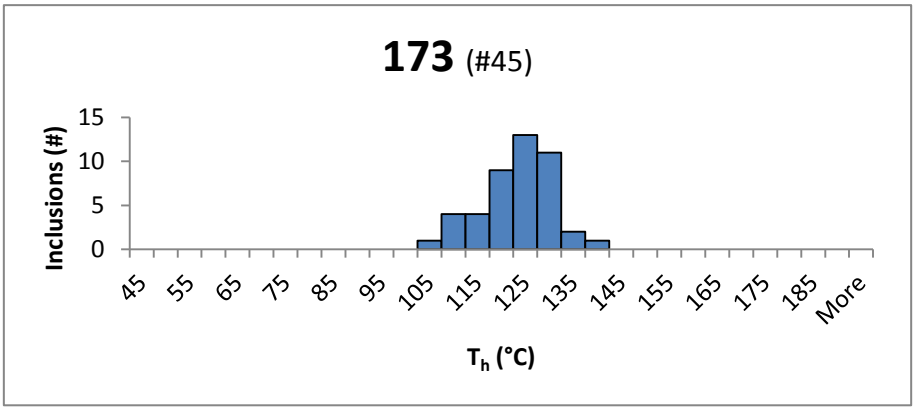

Mode (°C)	123
Range (°C)	104 - 138
Q1 (°C)	117
Q2 (°C)	122.3
Q3 (°C)	126
Inclusions (#)	45

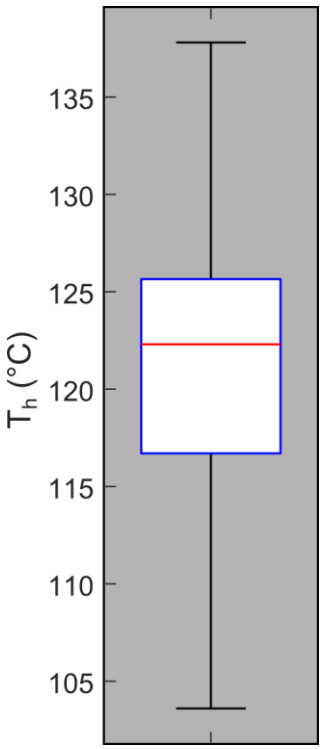

Sample 202:

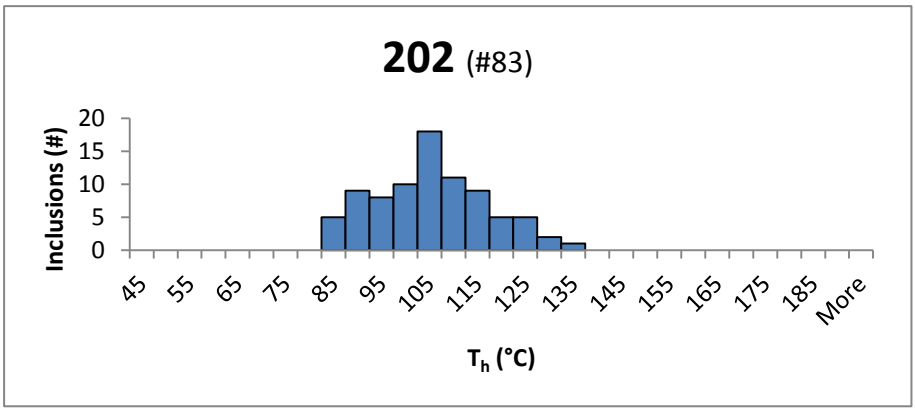

Mode (°C)	105
Range (°C)	81 - 131
Q1 (°C)	95
Q2 (°C)	103
Q3 (°C)	111
Inclusions (#)	83

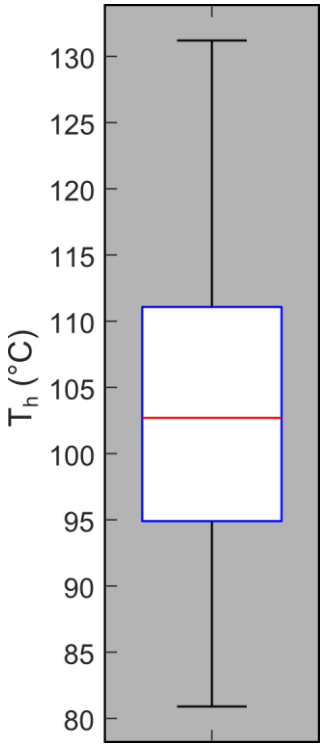

Sample 205:

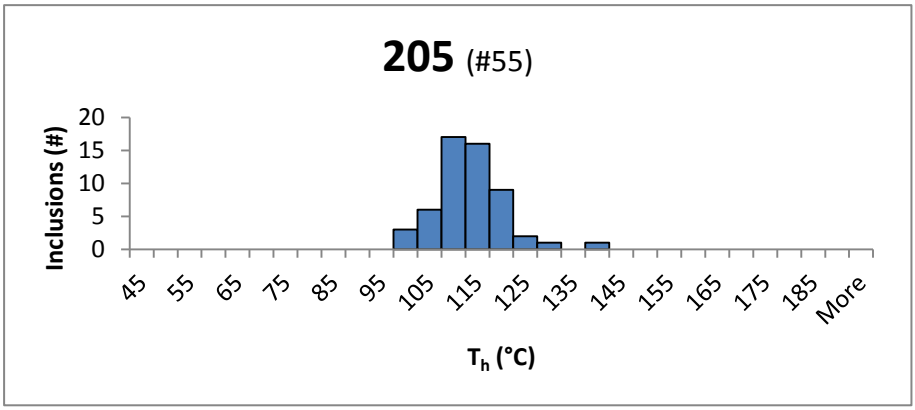

Mode (°C)	110
Range (°C)	99 - 138
Q1 (°C)	107
Q2 (°C)	110
Q3 (°C)	115
Inclusions (#)	55

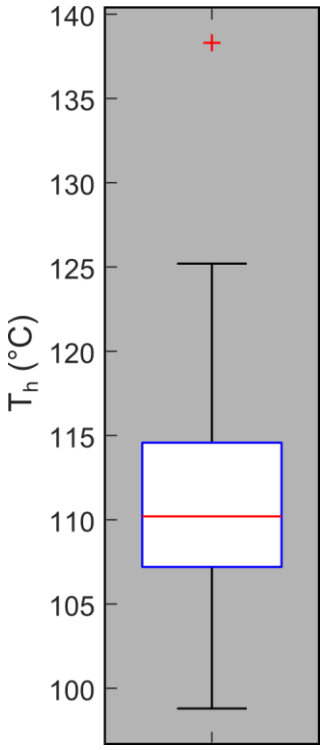

Sample 243:

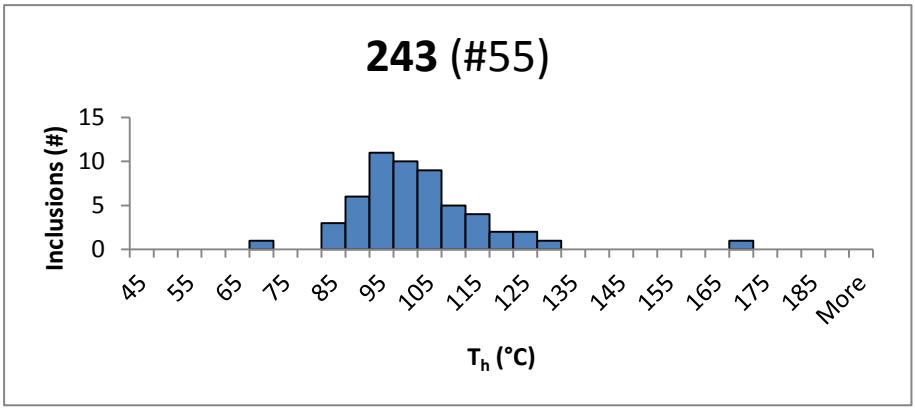

Mode (°C)	95
Range (°C)	70 - 167
Q1 (°C)	93
Q2 (°C)	99
Q3 (°C)	108
Inclusions (#)	55

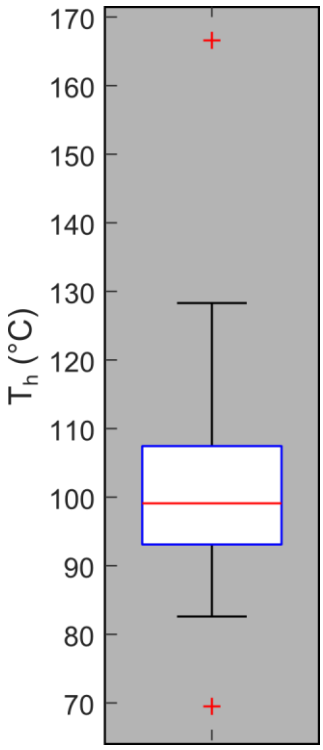

Sample 45:

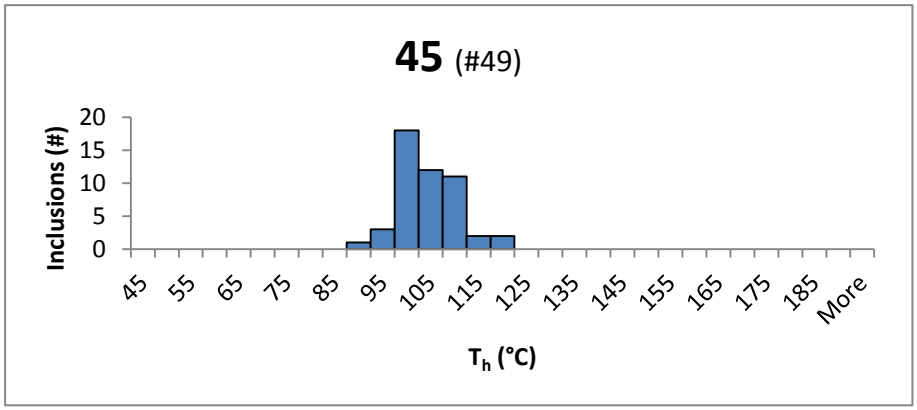

Mode (°C)	100
Range (°C)	88 - 117
Q1 (°C)	98
Q2 (°C)	102
Q3 (°C)	106
Inclusions (#)	49

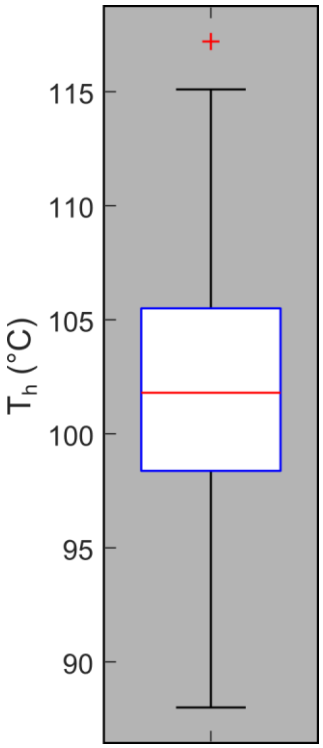

Sample CaBD2B:

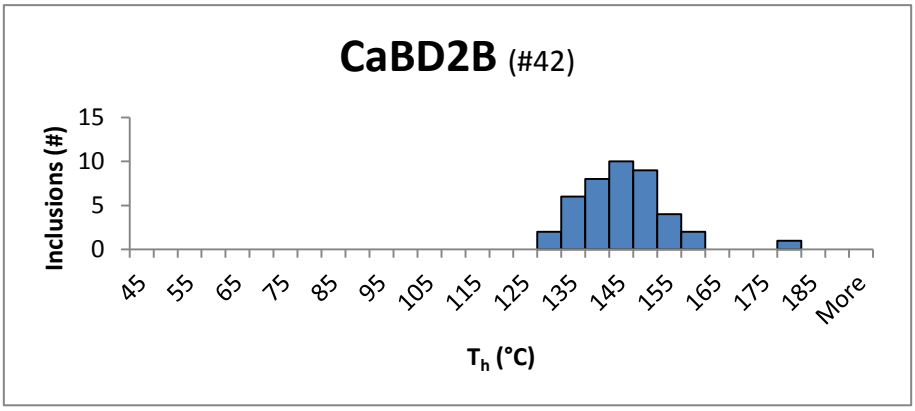

Mode (°C)	145
Range (°C)	129 - 176
Q1 (°C)	138
Q2 (°C)	143
Q3 (°C)	148
Inclusions (#)	42

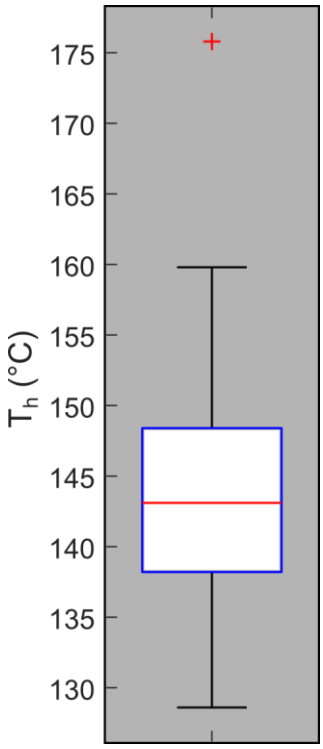

Appendix VI Fluid inclusion microthermometry (T_h raw data)

Sample 001		Sample 028		Sample 166		Sample 173		Sample 202		Sample 205		Sample 243		Sample 45		Sample CaBD2B	
Inclusion	**T_h**	**Inclusion**	**T_h**	**Inclusion**	**T_h**	**Inclusion**	**T_h**	**Inclusion**	**T_h**	**Inclusion**	**T_h**	**Inclusion**	**T_h**	**Inclusion**	**T_h**	**Inclusion**	**T_h**
1	131	1	128	1	142	1	121	1	103	1	105	1	91	1	93	1	141
2	126	2	125	2	124	2	121	2	86	2	108	2	103	2	101	2	160
3	132	3	125	3	136	3	130	3	85	3	113	3	112	3	98	3	145
4	122	4	126	4	110	4	126	4	88	4	114	4	120	4	100	4	147
5	91	5	124	5	130	5	130	5	85	5	110	5	94	5	98	5	143
6	132	6	128	6	136	6	130	6	86	6	114	6	110	6	99	6	143
7	132	7	125	7	142	7	133	7	81	7	119	7	103	7	100	7	141
8	142	8	125	8	151	8	117	8	85	8	109	8	117	8	100	8	153
9	116	9	129	9	126	9	117	9	90	9	113	9	97	9	98	9	137
10	137	10	126	10	137	10	117	10	90	10	124	10	115	10	109	10	141
11	139	11	124	11	124	11	122	11	90	11	110	11	112	11	109	11	158
12	141	12	124	12	110	12	117	12	90	12	125	12	90	12	102	12	150
13	133	13	129	13	135	13	128	13	85	13	112	13	104	13	100	13	150
14	142	14	124	14	147	14	116	14	103	14	118	14	98	14	101	14	139
15	65	15	125	15	89	15	117	15	100	15	107	15	105	15	112	15	145
16	130	16	126	16	154	16	123	16	90	16	107	16	93	16	106	16	153
17	144	17	124	17	136	17	116	17	113	17	116	17	107	17	109	17	148
18	126	18	126	18	97	18	108	18	100	18	109	18	90	18	106	18	136
19	108	19	124	19	93	19	114	19	102	19	109	19	102	19	96	19	148
20	109	20	128	20	147	20	108	20	102	20	100	20	124	20	103	20	154
21	108	21	136	21	131	21	127	21	88	21	114	21	95	21	108	21	140
22	126	22	136	22	115	22	126	22	95	22	109	22	95	22	93	22	147
23	128	23	126	23	134	23	122	23	115	23	110	23	95	23	109	23	140
24	128	24	128	24	125	24	122	24	116	24	107	24	100	24	112	24	144
25	118	25	126	25	134	25	122	25	120	25	104	25	104	25	102	25	147
26	131	26	139	26	116	26	127	26	124	26	104	26	108	26	96	26	147
27	130	27	126	27	126	27	127	27	116	27	107	27	90	27	102	27	154
28	130	28	132	28	130	28	126	28	124	28	111	28	100	28	105	28	134
29	138	29	124	29	136	29	126	29	115	29	107	29	123	29	104	29	134
30	138	30	128	30	128	30	125	30	120	30	117	30	102	30	103	30	134
31	124	31	128	31	130	31	113	31	115	31	113	31	91	31	105	31	131
32	123	32	126	32	129	32	108	32	127	32	121	32	84	32	99	32	134
33	144	33	134	33	125	33	125	33	124	33	119	33	86	33	98	33	129
34	136	34	128	34	142	34	122	34	124	34	112	34	95	34	105	34	140
35	136	35	128	35	146	35	114	35	116	35	107	35	99	35	105	35	138
36	126	36	128	36	138	36	107	36	127	36	104	36	99	36	105	36	140

37	112
38	81
39	125
40	151
41	122
42	122
43	120
44	149
45	132
46	130
47	135
48	125
49	132
50	78
51	122
52	130
53	125
54	118
55	128
56	116
57	135
58	128
59	137
60	135

37	125
38	144
39	126
40	126
41	125
42	126
43	135
44	114
45	129
46	128
47	125
48	135
49	121
50	135
51	126
52	127
53	127
54	129
55	127
56	127
57	118
58	126
59	127
60	105
61	124
62	118
63	129
64	125
65	115
66	119
67	129
68	125
69	122
70	127
71	134
72	137
73	139
74	132
75	129
76	141
77	132

37	148
38	152
39	125
40	134
41	132
42	146
43	148
44	140
45	118
46	125
47	126
48	124
49	136
50	154
51	145
52	135
53	139
54	136
55	143
56	144
57	170
58	139
59	110
60	113
61	119
62	136
63	127
64	141
65	102
66	110
67	119
68	67
69	126
70	181
71	100
72	140
73	122
74	138
75	127
76	129
77	135

37	122
38	133
39	112
40	125
41	125
42	120
43	138
44	104
45	120

37	131
38	112
39	124
40	109
41	111
42	110
43	109
44	93
45	109
46	103
47	98
48	110
49	111
50	108
51	102
52	89
53	86
54	107
55	104
56	102
57	110
58	103
59	95
60	103
61	103
62	95
63	103
64	100
65	100
66	100
67	109
68	92
69	103
70	104
71	110
72	109
73	90
74	99
75	99
76	104
77	99

37	111
38	115
39	107
40	110
41	116
42	110
43	105
44	99
45	112
46	138
47	105
48	99
49	103
50	119
51	116
52	116
53	109
54	115
55	112

37	88
38	99
39	86
40	93
41	167
42	104
43	110
44	93
45	102
46	70
47	93
48	96
49	93
50	110
51	113
52	128
53	83
54	83
55	95

37	98
38	98
39	88
40	97
41	97
42	102
43	97
44	117
45	115
46	99
47	91
48	102
49	110

37	142
38	143
39	131
40	129
41	146
42	176

78	173
79	122
80	138
81	65
82	111
83	108
84	102
85	154
86	117
87	117

78	119
79	131
80	133
81	135
82	126
83	137
84	135
85	140
86	142
87	144
88	127
89	122
90	129
91	122
92	125
93	122
94	137
95	125
96	128
97	115
98	115
99	136
100	140
101	125
102	128
103	128
104	129
105	140
106	129
107	125
108	128
109	125
110	132

78	102
79	107
80	113
81	102
82	99
83	104

Appendix VII Clumped isotope paleothermometry (raw data)

Sample	Texture	T_h (°C) mode	T_h (°C) Q1 – Q3	# inclusions	$\delta^{13}C$ (‰VPDB)	$\delta^{18}O$ (‰VPDB)	Δ_{47} (‰CDES)	Δ_{47} average	# replicates	T Δ_{47} (°C)*	±1SE (°C)	±1CO (°C)	P (MPa)*	T Δ_{47} (°C)**	P (MPa)**
001	Zebra	133	122-135	60	4.1	-10.2	0.466	0.462	3	149	8	34	32	138	9
							0.474								
							0.447								
028	Breccia	128	124-130	87	4.4	-9.6	0.495	0.489	3	125	3	14	0	118	0
							0.491								
							0.481								
166	Breccia	130	125-139	110	4.5	-8.2	0.482	0.48	4	133	4	14	7	125	0
							0.483								
							0.487								
							0.467								
173	Breccia	123	117-126	45	3.6	-9.5	0.495	0.489	5	126	7	20	8	118	0
							0.52								
							0.467								
							0.479								
							0.483								
202	Breccia	105	95-111	83	3.3	-6.1	0.489	0.494	3	121	2	7	37	115	35
							0.495								
							0.497								
205	Zebra	110	107-115	55	3.5	-11.3	0.494	0.489	2	125	4	54	34	118	22
							0.484								
243	Zebra	95	70-167	55	3.4	-8.3	0.515	0.513	3	107	1	3	29	102	26
							0.514								
							0.511								
45[†]	Zebra	100	98-106	49	3.6	-8.6	0.481	0.482	3	131	5	22	72	123	53
							0.471								
							0.493								
CaBD2B[†]	Breccia	145	138-148	42	4.2	-9.7	0.438	0.444	2	168	7	93	50	154	18
							0.45								

*Calculated using Kluge et al. (2015), reprocessed with new parameters for ^{17}O correction (Daëron et al., 2016)

**Calculated using Bonifacie et al. (2017)

[†]Samples from Gasparrini et al. (2006a)

Pain is temporary. Glory is forever.

FACULTY OF SCIENCE
DEPARTMENT OF EARTH AND ENVIRONMENTAL SCIENCES
GEOLOGY DIVISION
Celestijnenlaan 200E
B-3001 HEVERLEE, BELGIUM
tel. + 32 16 32 78 00
robin.honlet@kuleuven.be
aow.kuleuven.be/gi/